

# Quantum-State-Engineering for Spin-Quantum-Computing

Von der Fakultät Mathematik und Physik der Universität Stuttgart  
zur Erlangung der Würde eines  
Doktors der Naturwissenschaften (Dr. rer. nat.)  
genehmigte Abhandlung

Vorgelegt von  
**Andreas Heidebrecht**  
aus Stuttgart

Hauptberichter: Prof. Dr. M. Mehring  
Mitberichter: Prof. Dr. J. Wrachtrup

Eingereicht am: 24.11.2006  
Tag der mündlichen Prüfung: 20.12.2006

2. Physikalisches Institut der Universität Stuttgart  
**2006**



Meinen Eltern



# Contents

<b>Preface</b>	<b>1</b>
<b>1 Entanglement in the Three-Qubit Deutsch-Josza Algorithm</b>	<b>5</b>
1.1 2,3,4-Trifluoroaniline as a Three-Qubit Quantum Processor . . . . .	6
1.2 Pseudo-pure States . . . . .	8
1.2.1 Pure versus Pseudo-pure States . . . . .	9
1.2.2 Preparation of Pseudo-pure States . . . . .	10
1.2.3 Density Matrix Tomography . . . . .	14
1.3 Implementation of the Deutsch-Josza Algorithm . . . . .	15
1.3.1 Collins Version of the D.-J. Algorithm . . . . .	15
1.3.2 Deutsch-Josza Oracle Transformations for Three Qubits .	16
1.3.3 NMR Implementation of the Three-Qubit D.-J. Algorithm	18
1.3.4 Entanglement in the D.-J. Algorithm . . . . .	20
<b>2 Selective Excitation under Averaging</b>	<b>27</b>
2.1 The Magic Echo Sequence . . . . .	27
2.2 Chemical Shift Scaling under the Magic Echo Sequence . . . . .	30
2.3 Elimination of the Dipolar Coupling . . . . .	32
2.4 Selective Excitation under Continuous Averaging . . . . .	34
<b>3 Visualization of Unitary Transformations</b>	<b>37</b>
3.1 Representing Unitary Transformations in $R^3$ . . . . .	38
3.1.1 Vector Representation of Unitary Transformations . . . . .	38
3.1.2 Rules for Successive Transformations . . . . .	40
3.2 Examples of Visual Pulse Sequence Analysis . . . . .	41
3.2.1 Composite $\pi$ -Pulse . . . . .	41
3.2.2 Continously Shaped Pulses . . . . .	45
3.2.2.1 Constant Rectangular $\frac{\pi}{2} _y$ -Pulse . . . . .	45
3.2.2.2 $\frac{\pi}{2} _y$ -Pulse with Fermi-like Envelope . . . . .	47
3.2.2.3 $\frac{\pi}{2} _y$ -Pulse with Gaussian Envelope . . . . .	48
3.2.2.4 $\frac{\pi}{2} _y$ -Pulse with $\sin x/x$ Envelope . . . . .	49
3.2.3 Selective Alternating $\frac{\pi}{2} _y$ -Pulse . . . . .	50

---

<b>4</b>	<b>Detailed Implementation of the <math>S</math>-Bus Concept with <math>\text{CaF}_2:\text{Ce}</math></b>	<b>53</b>
4.1	The $S$ -Bus Concept for Spin Quantum Computing . . . . .	53
4.1.1	General Features . . . . .	53
4.1.2	Density Matrices in the $S$ -Bus . . . . .	55
4.1.2.1	Preparation of a Correlated Qubit Register . . . . .	56
4.1.2.2	Reduced Density Matrix . . . . .	58
4.1.2.3	Manipulation and Detection . . . . .	59
4.2	The $S$ -bus cluster in $\text{CaF}_2:\text{Ce}$ . . . . .	60
4.2.1	Crystalline Structure . . . . .	60
4.2.2	The $S$ -Bus Hamiltonian . . . . .	62
4.2.3	Manipulation of Spins . . . . .	63
4.2.4	$\text{CaF}_2:\text{Ce}$ as a Testbed for the $S$ -Bus . . . . .	63
4.3	EPR Spectra and Sample Alignment . . . . .	64
4.3.1	Coordinate Transformations . . . . .	64
4.3.2	Modeling of the EPR Spectra . . . . .	65
4.3.3	Fitting of the EPR Spectra . . . . .	66
4.4	ENDOR Spectra . . . . .	69
4.4.1	ENDOR Spectra and Hyperfine Parameters . . . . .	70
4.4.2	TRIPLE Spectra and $m_S$ Assignment . . . . .	72
4.5	Numeric Modeling of the 10-Spin $S$ -Bus System . . . . .	75
4.5.1	Construction and Diagonalization of the Hamiltonian . . . . .	75
4.5.1.1	The Zeeman Terms . . . . .	75
4.5.1.2	The Hyperfine Interaction Term . . . . .	76
4.5.1.3	The Dipole-Dipole Coupling Term . . . . .	76
4.5.1.4	Diagonalization of the Hamiltonian . . . . .	77
4.5.2	The Fictitious Eigenframe Hamiltonian . . . . .	78
4.5.3	The Sorting Problem . . . . .	78
4.5.4	ENDOR Spectrum . . . . .	80
4.5.5	Spin-Spin Couplings . . . . .	82
4.5.6	Computation Time . . . . .	84
4.6	Simulation of Pulse Experiments . . . . .	85
4.6.1	Transformation to the Rotating Frame of Reference . . . . .	85
4.6.1.1	Standard Treatment . . . . .	85
4.6.1.2	Generalized Transformation to the Rotating Frame . . . . .	86
4.6.2	Initial State and Measurement Operators . . . . .	88
4.6.3	Rabi Oscillations . . . . .	88
4.6.4	Pulse and Free Evolution Propagators . . . . .	90
4.6.5	Free Induction Decay . . . . .	90
4.6.6	Electron Spin Echoes . . . . .	91
4.6.7	Electron Spin Echo Envelope Modulation . . . . .	93
4.7	Detailed Evolution of Density Matrix Components . . . . .	97

4.7.1	Multi-Quantum ENDOR and PPS Preparation . . . . .	97
4.7.1.1	Phase Encoding of the Nuclear Spin State (MQE)	97
4.7.1.2	Preparation of Pseudo-Pure States . . . . .	99
4.7.2	Density Matrix Evolution during Two-Qubit Gates . . . . .	103
4.7.2.1	The SEDOR Sequence . . . . .	103
4.7.2.2	The INEPT Sequence . . . . .	105
4.7.2.3	The Controlled Not Sequence . . . . .	106
4.7.3	Quantitative Evaluation of the <i>S</i> -Bus Model . . . . .	109
4.8	Entanglement of Distant Qubits in the <i>S</i> -Bus . . . . .	114
4.8.1	Distant Qubits . . . . .	114
4.8.2	Creation of Entanglement . . . . .	115
4.8.3	Implementation and Tomography of the <i>CNOT</i> gate . . . . .	116
4.8.4	Creation and Direct Detection of Entangled States . . . . .	122
4.8.5	Detection of Entanglement through “Disentanglement” . . . . .	124
4.8.6	Decay of Entangled States . . . . .	125
<b>5</b>	<b>Spin-Spin Interactions in a Hostile Environment</b>	<b>127</b>
5.1	Spin-Spin Couplings . . . . .	127
5.2	Single Nuclear Spin Decoherence . . . . .	128
5.3	Recoupling of Selected Spin-Pairs . . . . .	131
5.3.1	SEDOR Sequence . . . . .	131
5.3.2	Carr-Purcell-Meiboom-Gill Sequence . . . . .	132
5.3.3	Simultaneous Spin-Locking . . . . .	134
5.3.4	The $8\pi$ -Sequence . . . . .	135
5.4	Conclusions . . . . .	136
	<b>Summary</b>	<b>137</b>
	<b>Zusammenfassung</b>	<b>141</b>
	<b>Appendices</b>	
<b>A</b>	<b>Basics of Magnetic Resonance</b>	<b>153</b>
A.1	Spin Evolution . . . . .	153
A.1.1	Spin Hamiltonian . . . . .	153
A.1.2	Evolution in Static Field . . . . .	154
A.1.3	Evolution in a Static and an Oscillating Magnetic Field . . . . .	155
A.1.4	Bloch Equations . . . . .	156
A.2	The Principle of Pulsed Magnetic Resonance . . . . .	157
A.2.1	Rotating Frame of Reference . . . . .	157
A.2.2	Rotation Pulses . . . . .	157
A.2.3	FID . . . . .	158
A.2.4	Hahn Echo . . . . .	158

---

A.3 Pulsed Nuclear Magnetic Resonance . . . . .	158
A.4 Electron Spin Resonance . . . . .	159
<b>B Density Matrix Formalism and Notation</b>	<b>161</b>
B.1 Fundamental Properties of the Density Operator . . . . .	161
B.2 Spin Operator Component Basis . . . . .	163
B.3 Density Matrices of Multi-Particle Systems . . . . .	164
B.4 Notation of Pulses . . . . .	165
B.5 Useful Formulae . . . . .	166
<b>C Tensor Product Algorithms</b>	<b>167</b>
C.1 Tensor Product of General Matrices . . . . .	168
C.2 Tensor Multiplication Algorithms . . . . .	169
C.2.1 Addition of Single Spin Operators . . . . .	169
C.2.2 Addition of a Spin $I = 1/2$ Operator . . . . .	171
C.2.3 Addition of a Product of Operators . . . . .	172
<b>Bibliography</b>	<b>173</b>
<b>List of figures</b>	<b>181</b>
<b>List of tables</b>	<b>185</b>



# Preface

At the time of my graduation, “quantum computing” has, for some time, been one of the buzzwords among the physicists. A tremendous amount of research activity and whole new avenues of inquiry have sprung up around the concept of quantum information processing. I believe, this enormous interest is primarily motivated by two factors.

First, of course, is the excitement about the ability to manipulate nature at the scale of single quanta, to access matter at its innermost level, where phenomena are governed by laws defying the common sense. The second – and I think more important reason for this great interest – is the fact that study of quantum information processing turns a spotlight on fundamental interpretational problems at the heart of quantum mechanics, a theory which we have been using with spectacular success for almost a century.

Those difficulties were first hinted at by Einstein, Podolski, and Rosen [1], when the phenomenon of entanglement, which we now recognize as being central to quantum information, was first identified. Feynman in 1982 was the first to express the idea that quantum systems could be used to solve hard problems about quantum systems [2].

Feynman’s ideas were put into precise mathematical form, when Deutsch rigorously demonstrated that a computational device whose elements are governed by quantum mechanical principles is capable of solving a mathematical problem in exponentially less time than a computer restricted to classical behavior [3–5]. Deutsch’s paradigm of quantum computing is based on the Turing machine [6,7]. This approach has, so far, been the most fruitful. Although the Deutsch problem has no practical utility, it has inspired a search for more practically useful algorithms. Apart from Deutsch’s algorithm, the best known algorithms for quantum computers are Grover’s search algorithm [8,9] and, of course, Shor’s algorithm for prime factorization [10].

The theoretical advances in the field have by far outpaced the experimental implementations. Besides the three famous algorithms there has been extensive work on error correction, quantum simulation, teleportation etc. Main cause of the slow pace of experimental realization are the difficulties connected with such an endeavor summarized in the five DiVincenzo criteria [11,12] of (i) well-defined (ii) initializable qubits with (iii) slow decoherence for which (iv) a universal set of quantum gates and (v) high quantum efficiency measurements are available.

The first experimental technique used to demonstrate quantum computing [13] was Nuclear Magnetic Resonance (NMR) in liquid state at room temperature. Nuclear spins of small, rapidly tumbling molecules in solution are ideally suited

to serve as qubits. NMR provides unprecedented coherent control of the quantum state of these qubits through the use of rf pulses, gates are implemented utilizing the scalar  $J$ -coupling, decoherence times are long and gradient pulses together with diffusion are efficient coherence erasers. The only item missing from the NMR quantum computing toolkit is the ability to implement hard projective measurements. The early achievements in the implementation of quantum computing with liquid state NMR already included the implementation of the Deutsch [13–17] and Grover [18–21] algorithms, the quantum Fourier transform [22,23], quantum simulations [24,25], entanglement transfer [26], and quantum error correction [27]. They culminated in the experimental factorization of the number 15 with the Shor algorithm [28].

These fast advances were afforded by the high level of sophistication of experimental techniques in NMR. However, liquid state NMR quantum computing is not scalable beyond at most a few dozen qubits [29]. The range of chemically available resonance frequencies limits the number of selectively addressable qubits and the ratio of gate time to relaxation time is only sufficient for proof-of-principle demonstrations. More importantly, ensemble spin quantum computing suffers from exponential loss of efficiency of pseudo-pure state preparation with growing system size. Clearly, other approaches are needed, if quantum computers are to actually compete with classical computers.

A large number of possible implementations of quantum computing has been proposed. The range of ideas includes cold cavity quantum electrodynamics, trapped ions, ultra-cold Rydberg atoms, molecular magnets, charge and spin qubits on quantum dots, charge and flux qubits in superconducting boxes, nuclear and electron spins implanted in diamond or semiconductor heterostructures and so on. Ultimately, only time will tell, which of these approaches will make the race to building a quantum computer useful beyond the study of fundamental questions of quantum information itself.

All of the quantum computing schemes intending to use spins as qubits have in common the basic methods of manipulating and observing the quantum state of those spins and controlling their interactions. My own work has been chiefly concerned with several of these methodic aspects of quantum computing. In particular, procedures for creation, tomography, and control of the quantum states of spin qubits were studied and refined.

First, I report on the observation of intermediate entanglement in the experimental implementation of the Deutsch-Josza algorithm. Together with O. Mangold in the course of his master's thesis research [30,31], we implemented the Deutsch-Josza algorithm using the three  $^{19}\text{F}$  nuclear spins of 2,3,4-Trifluoroaniline as qubits. It turns out, that the possible test functions and associated oracle transforms can be subdivided into several equivalence classes according to the spin-basis operator structure of the oracles. Some but not all of these oracles produce partially or maximally entangled states in the course of their application. This entanglement can be made visible by applying local (i.e., one-qubit) operations to the output states of the algorithm.

On the experimental side, the highlights were the preparation of three-qubit pseudo-pure states as input to the algorithm and a method for full tomography of density matrix of the spin system. The tomography is used

---

to access the entire density matrix which is only rarely done in NMR implementations of quantum computing. This extended information allows the fidelity of implementation to be quantified. Also, with this data, it is possible to demonstrate the difference arising from the use of pseudo-pure states as input to the algorithm instead of the sometimes used Boltzmann state.

Control of interactions between the qubits is one of the goals of every quantum computing scheme. Many proposals suggest to actually move the particles in space to achieve this. Another possibility to tailor the interaction Hamiltonian consists of applying a suitably designed sequence of strong rf pulses to average out interactions when they are not desired. In particular, interactions must be switched off during the application of single-qubit gates. The question now is, whether it is still possible to selectively manipulate the single qubits under the thus tailored Hamiltonian.

Chapter 2 presents some proof-of-principle measurements. 2,3-Difluoroaniline was placed in a liquid crystal matrix in order to partially align the molecules and thus partially reintroduce the dipole-dipole coupling between the fluorine nuclei. Protons were decoupled by strong continuous irradiation. A variant of the magic echo pulse sequence was used to turn this dipolar coupling on and off. Selective manipulation of qubits under the modified Hamiltonian was then demonstrated by applying soft excitation pulses on top of the averaging pulse sequence.

One of the major parts of experimental work in Magnetic Resonance is the design of pulse sequences to achieve a particular goal. Especially in the case of homonuclear spin systems, where all spins are to some degree affected by all pulses, it is sometimes difficult to grasp these influences. In standard NMR, pulses are usually designed to transform the polarization of a spin ensemble from one particular state to another state. Because spins frequently enter the quantum algorithms in superimposed or even entangled states, the pulses must implement particular unitary transformations instead of point-to-point rotations. Rotations of spins-1/2 have a simple classical representation based on the Bloch sphere construction. It is, however, not immediately obvious, how to imagine a unitary transformation affected by an rf-pulse. Thinking about unitary transformations resulting from an rf pulse is further complicated when some or all pulse parameters are varied during the pulse. Chapter 3 presents a technique for visualizing one-qubit time-dependent unitary transformations without looking at their effect on particular spin components.

Some of the solid state proposals for quantum computing are certainly among the most interesting candidates: They hold a great scalability promise and draw upon highly developed fabrication techniques. In our group we have worked on the implementation of the *S*-bus concept of spin quantum computing developed by M. Mehring [32–34]. Many aspects of this concept are relevant to other proposals for spin quantum computing in solid state.

The *S*-bus concept is based on an electron spin coupled via hyperfine interaction to a number of nuclear spins. The nuclear spins serve as qubits carrying quantum information, while the electron spins serves as “quantum bus” which connects the qubits with each other. Such clusters can then be coupled over longer

distances to each other via the dipole-dipole interaction between their bus spins. In addition to its role as a bus, the electron spin can be used to create highly correlated states of nuclear qubits. Also, the use of the electron spin to detect the state of the nuclear spins affords a large sensitivity enhancement. Direct observation of the nuclear qubits is not feasible because of the necessarily low concentration of paramagnetic centers.

In the course of his PhD work in our group [35,36], J. Mende was able to find a system with suitable properties in cerium doped  $\text{CaF}_2$  single crystals. He has experimentally characterized the system and performed the basic demonstrations of its fitness as a testbed for the  $S$ -bus concept by preparing pseudo-pure states of two and three qubits, implementing the two-qubit Deutsch algorithm and a first attempt at creating a two-qubit entangled state. The general  $S$ -bus theory does approximate the paramagnetic cluster in  $\text{CaF}_2:\text{Ce}$  reasonably well. It does not, however, provide detailed and, in particular, quantitative understanding. The missing pieces must be filled in by further theoretical treatment and experimental study.

To improve qualitative and quantitative understanding, I have performed a full numeric simulation of this ten-spin system. It gives access to many experimentally relevant quantities and allows the simulation of some experiments. In addition, I studied the evolution of various components of truncated density matrices under a number of pulse sequences relevant to quantum computing with this system. When taken as a basis, the perturbation model features a number of coefficients which can not be calculated from that model itself. Measurements of the evolution of the density matrix components allow experimental access to these quantities.

The work on  $\text{CaF}_2:\text{Ce}$  culminated in the implementation and tomography of a  $CNOT$ -gate. Also, experiments toward creation of entangled states of distant qubits were performed. Finally, measurements of decoherence properties of these Bell-states were done. The quantum computing work on  $\text{CaF}_2:\text{Ce}$  is presented in Chapter 4.

Chapter 5 describes a series of experiments on  $\text{CaF}_2:\text{Ce}$  which are also relevant outside the realm of quantum computing. Fluorine nuclei are abundant in  $\text{CaF}_2$  and form an extended spin network via dipole-dipole interaction. This neighborhood is a strong source of decoherence and, in this sense, presents the paramagnetic cluster with very hostile environment. When no measures are taken, the highly correlated state of the cluster decays too quickly to implement even a single two-qubit gate. Even, if that environment could be neglected, the cluster itself has  $2^{10}$  possible states and the coupling between the participating spins must be carefully controlled.

Decoupling experiments showed that a single qubit can be effectively decoupled from all other spins. To utilize the coupling of a selected qubit pair for a two-qubit gate, however, it must be restored while the decoupling from the environment is still effective. Variants of known and a newly designed pulse sequence were tested regarding their utility for this purpose. As a side-effect, these sequences allow spin-spin couplings to be measured accurately [37].

# Chapter 1

## Entanglement in the Three-Qubit Deutsch-Josza Algorithm

The technique of *nuclear magnetic resonance* (NMR) was the first experimental method to be used to approach the implementation of quantum computing (QC) [13]. The milestones where the implementation of various basic logic gates [14, 15, 38–41], the demonstration of the Deutsch-Josza [15, 41–44], Grover [18, 19, 45] and ultimately Shor [28] algorithms. In addition, a great variety of the many aspects of quantum computing ranging from the evaluation of various error correcting protocols to the investigation of decoherence effects and questions of entanglement has been and still remains under active investigation.

The magnetic Hamiltonian of a molecule in liquid state has the most simple form due to the fact that all anisotropic interactions are averaged out because of the rapid tumbling motion of the molecules in solution. For a molecule containing  $N$  nuclear spins the Hamiltonian has the form

$$\mathcal{H} = \sum_i^N \omega_{0_i} \mathbf{I}_{z_i} + \sum_{i \neq j} J_{ij} \mathbf{I}_i \mathbf{I}_j \quad (1.1)$$

The Larmor frequencies  $\omega_{0_i}$  are determined by the chemical shift of the local field seen by the nuclear spin due to the shielding effect of the molecules electrons. The  $J$ -couplings  $J_{ij}$  are the scalar spin-spin interactions mediated by those electrons. In the case of large differences in the resonance frequency, off-diagonal parts of the coupling term can be neglected:

$$\mathcal{H} = \sum_i^N \omega_{0_i} \mathbf{I}_{z_i} + \sum_{i \neq j} J_{ij} \mathbf{I}_{z_i} \mathbf{I}_{z_j} \quad \text{for } |\omega_{0_j} - \omega_{0_k}| \gg J_{ij} \quad (1.2)$$

We<sup>1</sup> have used *2,3,4-Trifluoroaniline* – which at room temperature is liquid –

---

<sup>1</sup>Most of the measurements were performed by O. Mangold in the course of his master's

to implement the three-qubit Deutsch-Josza algorithm by the means of NMR. For input into the algorithm, refined pseudo-pure states of three qubits were prepared. Extensive tomography was deployed to measure all 64 elements of the density matrix.

## 1.1 2,3,4-Trifluoroaniline as a Three-Qubit Quantum Processor

The molecular structure of 2,3,4-Trifluoroaniline and its free induction decay (FID) spectrum at 7.8 T are shown in Figure 1.1. The lines are nearly equally separated by 2 kHz and the  $J$ -couplings are unresolved.

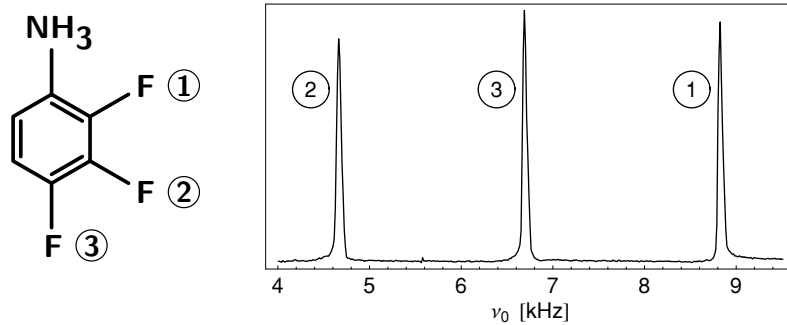


**Figure 1.1:** Molecular structure and FID-spectrum of 2,3,4-Trifluoroaniline at  $B_0 = 7.8$  T. Note that the numbering of spins used here is different from the chemical nomenclature.

The coupling network of the fluorine nuclei of this molecule has been determined by a *two-dimensional echo modulation* measurement [46]. The pulse sequence for this type of measurement is shown Figure 1.2.

The result of applying this pulse sequence is most easily demonstrated using an example with two spins  $\mathbf{I}_a$  and  $\mathbf{I}_b$ . The full time-dependent Hamiltonian of such a system in the laboratory frame is given by

$$\mathcal{H} = \omega_{0_a} \mathbf{I}_{z_a} + \omega_{0_b} \mathbf{I}_{z_b} + J_{ab} \mathbf{I}_{z_a} \mathbf{I}_{z_b} \quad (1.3)$$

where  $\omega_{0_j}$  is the Larmor frequency of spin  $j$  and  $J_{ab}$  is the scalar coupling between the two spins. The unitary transform describing the evolution under the echo modulation sequence is then given by

$$U(t_1, t_2) = \exp(-it_2 \mathcal{H}) \cdot \exp\left(-i\frac{t_1}{2} \mathcal{H}\right) \cdot \exp(-i\pi (\mathbf{I}_{y_a} + \mathbf{I}_{y_b})) \cdot \exp\left(-i\frac{t_1}{2} \mathcal{H}\right) \cdot \exp\left(-i\frac{\pi}{2} (\mathbf{I}_{y_a} + \mathbf{I}_{y_b})\right) \quad (1.4)$$

Applying this sequence to the initial Boltzmann state  $\rho_B = \mathbf{I}_{z_a} + \mathbf{I}_{z_b}$  yields the expression for the density matrix of the spin system dependent on the two

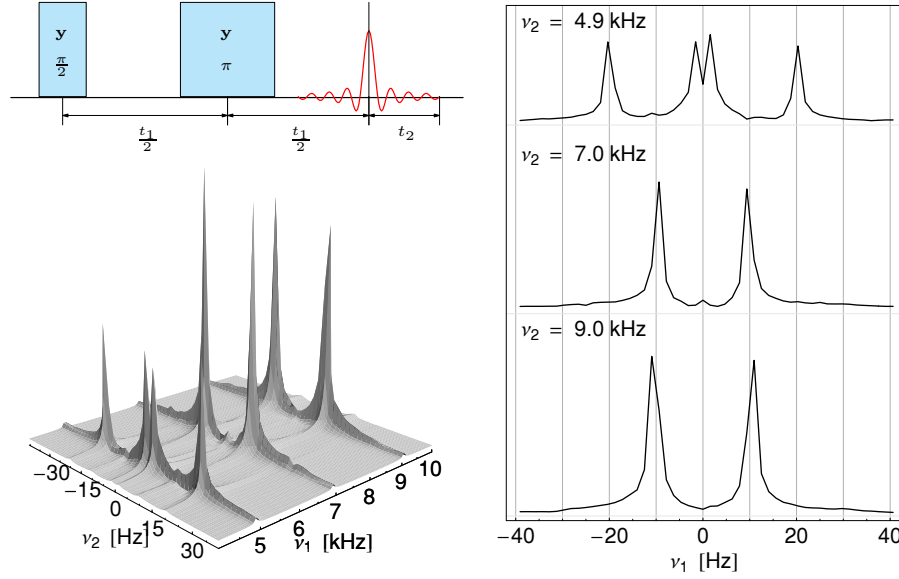


**Figure 1.2:** Two-dimensional echo modulation measurement on 2,3,4-Trifluoroaniline at 7.8 T. Top left: The pulse sequence. All pulses are wide-band and applied to all spins simultaneously. Bottom left: Two-dimensional Fourier transform of the experimental data. Right: Slices of the spectrum along the  $\nu_2$ -direction, showing the splittings due to  $J$ -couplings between the three  $^{19}\text{F}$  spins.

parameters  $t_1$  and  $t_2$ :

$$\rho(t_1, t_2) = U(t_1, t_2) \cdot \rho_B \cdot U^\dagger(t_1, t_2) \quad (1.5)$$

The complex amplitude recorded by the quadrature detection of the NMR spectrometer is given by the trace of the density matrix with the measurement operator  $P_M = \mathbf{I}_{-a} + \mathbf{I}_{-b}$ :

$$\begin{aligned} A(t_1, t_2) = \text{tr} \{ \rho(t_1, t_2) P_M \} = & \\ & \exp \left\{ i \left( -\frac{1}{2} J_{ab} t_1 + \left( \omega_{0_a} - \frac{1}{2} J_{ab} t_2 \right) \right) \right\} + \\ & \exp \left\{ i \left( +\frac{1}{2} J_{ab} t_1 + \left( \omega_{0_a} + \frac{1}{2} J_{ab} t_2 \right) \right) \right\} + \\ & \exp \left\{ i \left( -\frac{1}{2} J_{ab} t_1 + \left( \omega_{0_b} - \frac{1}{2} J_{ab} t_2 \right) \right) \right\} + \\ & \exp \left\{ i \left( +\frac{1}{2} J_{ab} t_1 + \left( \omega_{0_b} + \frac{1}{2} J_{ab} t_2 \right) \right) \right\} \end{aligned} \quad (1.6)$$

A two-dimensional Fourier transform of such a signal will yield a spectrum with four peaks. Since the  $J$ -coupling is much smaller than the Larmor frequencies of the spins, the lines corresponding to spin  $j$  will be aligned roughly at  $\omega_{0_j}$  along the  $\omega_2$ -axis. The splitting along the  $\omega_1$ -axis indicates the  $J$ -coupling to another spin. The results for the 2,3,4-Trifluoroaniline are shown in Figure 1.2. The spectrum clearly shows that  $J_{12} \approx J_{23} \approx 20$  Hz while the third coupling is

very weak  $J_{13} \leq 2$  Hz. The results of detailed evaluation of this measurement are shown in table Table 1.1. For more details on the measurement of the  $J$ -

<b>I</b>	2	3	1
2	0 ppm	20.00 Hz	19.30 Hz
3		6.48 ppm	1.50 Hz
1			13.28 ppm

**Table 1.1:** Chemical shifts and  $J$ -couplings of the  $^{19}\text{F}$  in 2,3,4-Trifluoroaniline. Chemical shifts are given relative to spin number 2.

couplings see [21]. The NMR-Hamiltonian for this molecule is therefore given by

$$\mathcal{H} = \sum_{j=1}^3 \omega_{0_j} \mathbf{I}_{z_j} + 2\pi J (\mathbf{I}_{z_1} \mathbf{I}_{z_2} + \mathbf{I}_{z_2} \mathbf{I}_{z_3}) \quad (1.7)$$

The missing coupling  $\mathbf{I}_{z_1} \mathbf{I}_{z_3}$  represents a challenge and leads to some interesting aspects as discussed below.

Line widths were dominated by the inhomogeneity of the static field  $B_0$  and lay between 100 Hz and 140 Hz. Longitudinal relaxation time  $T_1$  for all three spins was around 3 s dependent on sample preparation. No splitting due to scalar coupling to protons was observed and proton decoupling was not necessary.

## 1.2 Pseudo-pure States

The liquid state NMR operates with large ( $> 10^{20}$ ) ensembles of spins at room temperature. In the Boltzmann equilibrium, the density matrix of such an ensemble is given by

$$\rho_B = \exp\left(-\frac{\mathcal{H}}{k_B T}\right) \quad (1.8)$$

For the typical fields in modern NMR magnets, Larmor frequencies lie in the range of tens to hundreds of MHz. The Boltzmann factor for such splittings is in the order of magnitude of  $10^{-4}$  and the exponential function in Equation (1.8) can be expanded in a series and truncated after the first term:

$$\rho_B \approx \mathbf{1} + \frac{\hbar\omega_0}{k_B T} \mathbf{I}_z = \mathbf{1} + \epsilon \mathbf{I}_z \quad (1.9)$$

This density matrix represents a highly mixed quantum state. This observation has led to an intense debate over whether liquid state NMR experiments can properly be considered to be valid implementations of quantum computing. In fact, it has been shown, that any state which can be reached by standard liquid state NMR procedures starting from the Boltzmann state is fully separable [47–52]. Thus, no entanglement occurs and the NMR experiments can in principle be described in classical terms. A more severe implication is that the signal-to-noise ratio deteriorates exponentially with the number of qubits, thus, limiting the scalability of liquid state NMR quantum computing.



### 1.2.1 Pure versus Pseudo-pure States

Liquid state NMR is still a very useful technique for studies of the quantum computing with small systems (i.e., at most 10 to 20 qubits). The dominant mixed part of the density matrix in Equation (1.9) is invariant under unitary transformations and therefore under most operations used in magnetic resonance techniques. For the formal treatment of experiments, the density matrix of the spin ensemble can be separated in two parts:

$$\rho = (1 - \epsilon)\mathbf{1} + \epsilon\rho_{PPS} \quad (1.10)$$

Under the assumption that the single molecules do not interact with each other magnetically, the dimension of the density matrix  $\rho_{PPS}$  can be reduced to represent only the magnetically non-equivalent spins on a single molecule. Furthermore, it is possible to choose the factor  $\epsilon$ , such that the matrix  $\rho_{PPS}$  satisfies the condition for pure quantum states:

$$\text{tr} \{ \rho_{PPS}^2 \} = 1 \quad (1.11)$$

Such a density matrix is formally equivalent to a density matrix of a pure state and is, therefore, called the density matrix of *pseudo-pure state*. Crucially, this part of the total density matrix in Equation (1.10) is sufficient to describe all unitary transformations in magnetic resonance. This concept allows to implement quantum computing algorithms with the means of magnetic resonance far from the pure states, since all operations and measurements yield the same quantitative results as they would for an isolated quantum mechanical system.

The most important aspects of QC with liquid state NMR that arise from the use of large ensembles in nearly maximally mixed states are the lack of projective measurements and the ability to measure the expectation values of non-commuting operators simultaneously [47, 53–55].

The inability to project the state on chosen basis presents a problem for a class of procedures which require the destruction of coherence. An example of such a procedure is given in the following section. The *weak measurement* common in magnetic resonance is a direct consequence of the large ensemble size; the MR literature is full of plots of experimental data showing the expectation values of the  $\mathbf{I}_x$  and  $\mathbf{I}_y$  spin operators measured simultaneously.

Intuitively, the ensemble of isolated quantum systems may be thought of as an ensemble of quantum computers undergoing identical evolutions and performing identical quantum computations simultaneously. This has the advantage that the averaging over many measurements that is necessary to obtain the expectation value of an observable on an single isolated quantum system is replaced by an ensemble average. The sample size of this average is many orders of magnitude larger than any practicable sample achieved by the repetition of a particular measurement. Furthermore, the variations that can occur between the consecutive repetitions of a single measurement are eliminated, since all experimental parameters are identical for each copy of the quantum computer in an ensemble. The major problem for this interpretation is that the initial state of each copy of the quantum computer is poorly defined and certainly not the same. The way to solving this problem is in seeking systems and methods that allow to obtain an almost fully polarized spin ensemble. Several proposals in this direction have

been made. For NMR, for instance, this could be achieved by dynamic nuclear polarization (DNP) [56, 57]. In solid state magnetic resonance the quantum limit separating sufficiently pure from highly mixed states may be reached at experimentally viable temperatures [33].

## 1.2.2 Preparation of Pseudo-pure States

There have been two approaches to quantum computing with liquid state NMR. One way to demonstrate the implementation of algorithms is to prepare parts of the pseudo-pure state separately and run the experiments on the different parts consecutively, superimposing the obtained data after the measurement. The other method is to manipulate the spin system, such that the non-unity part of it's density matrix shows the desired structure of a pure state. The latter approach was chosen here.

For the implementation of the Deutsch-Josza algorithm described below, three-qubit pseudo-pure states were prepared in 2,3,4-Trifluoroaniline. The density matrix of a pseudo-pure state of three qubits consists of zeroes with only one "1" at the main diagonal. The density matrices and spin-operator expressions for the eight pseudo-pure states are as follows:

$$\begin{aligned} \rho_{000} &= \begin{pmatrix} 1 & 0 & 0 & 0 & 0 & 0 & 0 & 0 \\ 0 & 0 & 0 & 0 & 0 & 0 & 0 & 0 \\ 0 & 0 & 0 & 0 & 0 & 0 & 0 & 0 \\ 0 & 0 & 0 & 0 & 0 & 0 & 0 & 0 \\ 0 & 0 & 0 & 0 & 0 & 0 & 0 & 0 \\ 0 & 0 & 0 & 0 & 0 & 0 & 0 & 0 \\ 0 & 0 & 0 & 0 & 0 & 0 & 0 & 0 \\ 0 & 0 & 0 & 0 & 0 & 0 & 0 & 0 \end{pmatrix} = \\ &= \frac{1}{8}\mathbf{I}_0 + \frac{1}{4}(\mathbf{I}_{z_1} + \mathbf{I}_{z_2} + \mathbf{I}_{z_3}) + \frac{1}{2}(\mathbf{I}_{z_1}\mathbf{I}_{z_2} + \mathbf{I}_{z_2}\mathbf{I}_{z_3} + \mathbf{I}_{z_3}\mathbf{I}_{z_1}) + \mathbf{I}_{z_1}\mathbf{I}_{z_2}\mathbf{I}_{z_3} \quad (1.12a) \end{aligned}$$

$$\begin{aligned} \rho_{001} &= \begin{pmatrix} 0 & 0 & 0 & 0 & 0 & 0 & 0 & 0 \\ 0 & 1 & 0 & 0 & 0 & 0 & 0 & 0 \\ 0 & 0 & 0 & 0 & 0 & 0 & 0 & 0 \\ 0 & 0 & 0 & 0 & 0 & 0 & 0 & 0 \\ 0 & 0 & 0 & 0 & 0 & 0 & 0 & 0 \\ 0 & 0 & 0 & 0 & 0 & 0 & 0 & 0 \\ 0 & 0 & 0 & 0 & 0 & 0 & 0 & 0 \\ 0 & 0 & 0 & 0 & 0 & 0 & 0 & 0 \end{pmatrix} = \\ &= \frac{1}{8}\mathbf{I}_0 + \frac{1}{4}(\mathbf{I}_{z_1} + \mathbf{I}_{z_2} - \mathbf{I}_{z_3}) + \frac{1}{2}(\mathbf{I}_{z_1}\mathbf{I}_{z_2} - \mathbf{I}_{z_2}\mathbf{I}_{z_3} - \mathbf{I}_{z_3}\mathbf{I}_{z_1}) - \mathbf{I}_{z_1}\mathbf{I}_{z_2}\mathbf{I}_{z_3} \quad (1.12b) \end{aligned}$$

$$\begin{aligned} \rho_{010} &= \\ &= \frac{1}{8}\mathbf{I}_0 + \frac{1}{4}(\mathbf{I}_{z_1} - \mathbf{I}_{z_2} + \mathbf{I}_{z_3}) + \frac{1}{2}(-\mathbf{I}_{z_1}\mathbf{I}_{z_2} - \mathbf{I}_{z_2}\mathbf{I}_{z_3} + \mathbf{I}_{z_3}\mathbf{I}_{z_1}) - \mathbf{I}_{z_1}\mathbf{I}_{z_2}\mathbf{I}_{z_3} \quad (1.12c) \end{aligned}$$

$$\begin{aligned} \rho_{011} = & \\ \frac{1}{8}\mathbf{I}_0 + \frac{1}{4}(\mathbf{I}_{z_1} - \mathbf{I}_{z_2} - \mathbf{I}_{z_3}) + \frac{1}{2}(-\mathbf{I}_{z_1}\mathbf{I}_{z_2} + \mathbf{I}_{z_2}\mathbf{I}_{z_3} - \mathbf{I}_{z_3}\mathbf{I}_{z_1}) + \mathbf{I}_{z_1}\mathbf{I}_{z_2}\mathbf{I}_{z_3} \end{aligned} \quad (1.12d)$$

$$\begin{aligned} \rho_{100} = & \\ \frac{1}{8}\mathbf{I}_0 + \frac{1}{4}(-\mathbf{I}_{z_1} + \mathbf{I}_{z_2} + \mathbf{I}_{z_3}) + \frac{1}{2}(-\mathbf{I}_{z_1}\mathbf{I}_{z_2} + \mathbf{I}_{z_2}\mathbf{I}_{z_3} - \mathbf{I}_{z_3}\mathbf{I}_{z_1}) - \mathbf{I}_{z_1}\mathbf{I}_{z_2}\mathbf{I}_{z_3} \end{aligned} \quad (1.12e)$$

$$\begin{aligned} \rho_{101} = & \\ \frac{1}{8}\mathbf{I}_0 + \frac{1}{4}(-\mathbf{I}_{z_1} + \mathbf{I}_{z_2} - \mathbf{I}_{z_3}) + \frac{1}{2}(-\mathbf{I}_{z_1}\mathbf{I}_{z_2} - \mathbf{I}_{z_2}\mathbf{I}_{z_3} + \mathbf{I}_{z_3}\mathbf{I}_{z_1}) + \mathbf{I}_{z_1}\mathbf{I}_{z_2}\mathbf{I}_{z_3} \end{aligned} \quad (1.12f)$$

$$\begin{aligned} \rho_{110} = & \\ \frac{1}{8}\mathbf{I}_0 + \frac{1}{4}(-\mathbf{I}_{z_1} - \mathbf{I}_{z_2} + \mathbf{I}_{z_3}) + \frac{1}{2}(\mathbf{I}_{z_1}\mathbf{I}_{z_2} - \mathbf{I}_{z_2}\mathbf{I}_{z_3} - \mathbf{I}_{z_3}\mathbf{I}_{z_1}) + \mathbf{I}_{z_1}\mathbf{I}_{z_2}\mathbf{I}_{z_3} \end{aligned} \quad (1.12g)$$

$$\begin{aligned} \rho_{111} = & \\ \frac{1}{8}\mathbf{I}_0 + \frac{1}{4}(-\mathbf{I}_{z_1} - \mathbf{I}_{z_2} - \mathbf{I}_{z_3}) + \frac{1}{2}(\mathbf{I}_{z_1}\mathbf{I}_{z_2} + \mathbf{I}_{z_2}\mathbf{I}_{z_3} + \mathbf{I}_{z_3}\mathbf{I}_{z_1}) - \mathbf{I}_{z_1}\mathbf{I}_{z_2}\mathbf{I}_{z_3} \end{aligned} \quad (1.12h)$$

The task consists of preparing such a density matrix from the Boltzmann state which has the following shape:

$$\rho_B = \frac{1}{8}\mathbf{I}_0 + \epsilon(\mathbf{I}_{z_1} + \mathbf{I}_{z_2} + \mathbf{I}_{z_3}) \quad (1.13)$$

It is easily seen, that there is no unitary transformation able to achieve this goal. Due to the lack of projective measurement in ensemble NMR, the non-unitary operations are implemented by means of *gradient pulses* [58]. Such pulses effectively delete all off-diagonal components of the density matrix. Combined with one-spin rotations by appropriate angles, they allow the amplitude of linear  $z$ -terms to be adjusted.

The second challenge is to produce the bilinear and trilinear terms in Equation (1.12) from the linear terms available in the Boltzmann state in Equation (1.13). Such sequences must utilize the coupling between qubits. Regular time evolution under the unperturbed Hamiltonian is capable of producing such terms from transverse linear components. The term  $\mathbf{I}_{x_1}$ , for instance produces:

$$\begin{aligned} e^{-it\mathcal{H}}\mathbf{I}_{x_1}e^{it\mathcal{H}} = & \cos\left(\frac{Jt}{2}\right)\cos(\omega_{0_1}t)\mathbf{I}_{x_1} + \cos\left(\frac{Jt}{2}\right)\sin(\omega_{0_1}t)\mathbf{I}_{y_1} \\ & - 2\sin\left(\frac{Jt}{2}\right)\sin(\omega_{0_1}t)\mathbf{I}_{x_1}\mathbf{I}_{z_2} + 2\sin\left(\frac{Jt}{2}\right)\cos(\omega_{0_1}t)\mathbf{I}_{y_1}\mathbf{I}_{z_2} \end{aligned} \quad (1.14)$$

This shows, also, that evolution under different chemical shifts produces many undesired terms. To avoid such complications, the standard refocusing and

decoupling technique based on the *Hahn echo* can be used. This sequence introduces a  $\pi$ -pulse in the middle of the free evolution period. With the initial and final  $\pi/2$ -pulses to rotate the magnetization into the  $xy$ -plane and back, the corresponding propagator is

$$U_{1\leftrightarrow 12} = P_{x_1} \left( \frac{\pi}{2} \right) e^{-i\frac{t}{2}\mathcal{H}} P_{x_{1,2}}(\pi) e^{-i\frac{t}{2}\mathcal{H}} P_{y_1} \left( \frac{\pi}{2} \right) \quad (1.15)$$

The  $\pi$ -pulse effectively inverts the time for the evolution under the chemical shift leaving only the  $J$ -coupling effective:

$$U_{1\leftrightarrow 12} \mathbf{I}_{z_1} U_{1\leftrightarrow 12}^\dagger = \cos \left( \frac{Jt}{2} \right) \mathbf{I}_{x_1} + 2 \sin \left( \frac{Jt}{2} \right) \mathbf{I}_{z_1} \mathbf{I}_{z_2} \stackrel{Jt=\pi}{=} 2 \mathbf{I}_{z_1} \mathbf{I}_{z_2} \quad (1.16)$$

Selecting  $t$  such that  $2Jt = \pi$  achieves a full transfer from the linear to the bilinear term. Applying the  $\pi$ -pulse only to two of the three spins additionally cancels out the evolution under the coupling of each of the two spins to the third one. The term  $\mathbf{I}_{z_2} \mathbf{I}_{z_3}$  can be obtained analogously from  $\mathbf{I}_{z_3}$ .

When  $\mathbf{I}_{z_2}$  is used as input, a slightly modified sequence allows creation of the trilinear term  $\mathbf{I}_{z_1} \mathbf{I}_{z_2} \mathbf{I}_{z_3}$ :

$$U_{2\leftrightarrow 123} = P_{y_2} \left( \frac{\pi}{2} \right) e^{-i\frac{t}{2}\mathcal{H}} P_{x_{1,2,3}}(\pi) e^{-i\frac{t}{2}\mathcal{H}} P_{y_2} \left( \frac{\pi}{2} \right) \quad (1.17)$$

and

$$U_{2\leftrightarrow 123} \mathbf{I}_{z_2} U_{2\leftrightarrow 123}^\dagger = -\frac{1}{2} (1 + \cos(Jt)) \mathbf{I}_{z_2} + \sin(Jt) (\mathbf{I}_{z_1} \mathbf{I}_{y_2} + \mathbf{I}_{y_2} \mathbf{I}_{z_3}) + 4 \sin^2 \left( \frac{Jt}{2} \right) \mathbf{I}_{z_1} \mathbf{I}_{z_2} \mathbf{I}_{z_3} \stackrel{Jt=\pi}{=} 4 \mathbf{I}_{z_1} \mathbf{I}_{z_2} \mathbf{I}_{z_3} \quad (1.18)$$

The term  $\mathbf{I}_{z_1} \mathbf{I}_{z_3}$  cannot be created in this simple fashion, because the two spins are not coupled directly. However, applying  $U_{2\leftrightarrow 123}$  and  $U_{1\leftrightarrow 12}$  in succession yields the desired result.

Combining these operations with single-spin rotations and gradient pulses allows a pulse sequence for creation of pseudo-pure states to be constructed. Such a sequence is shown in Figure 1.3. It utilizes three evolution periods with refocussing  $\pi$ -pulses and four gradient pulses to achieve the goal. Each of the eight different pseudo-pure states in Equation (1.12) can be selected by the appropriate choice of rotation angles for some pulses as indicated in Table 1.2 and Figure 1.3.

A typical signature of a pseudo-pure state is shown in Figure 1.4. It is obtained by recording the decay of the magnetization after the last gradient pulse and applying a Fourier transform. Such signatures, though commonly used in literature as indicators of particular quantum states, do not, in fact, provide the full information about the density matrix. Particularly under the conditions of unresolved  $J$ -coupling, the signature only shows the terms of the density matrices in Equation (1.12) which are linear in spin operators. To obtain the complex amplitudes of bilinear and trilinear terms, special pulse sequences must be applied which are, in a sense, inverse to the above mentioned sequence for creation of higher order terms.

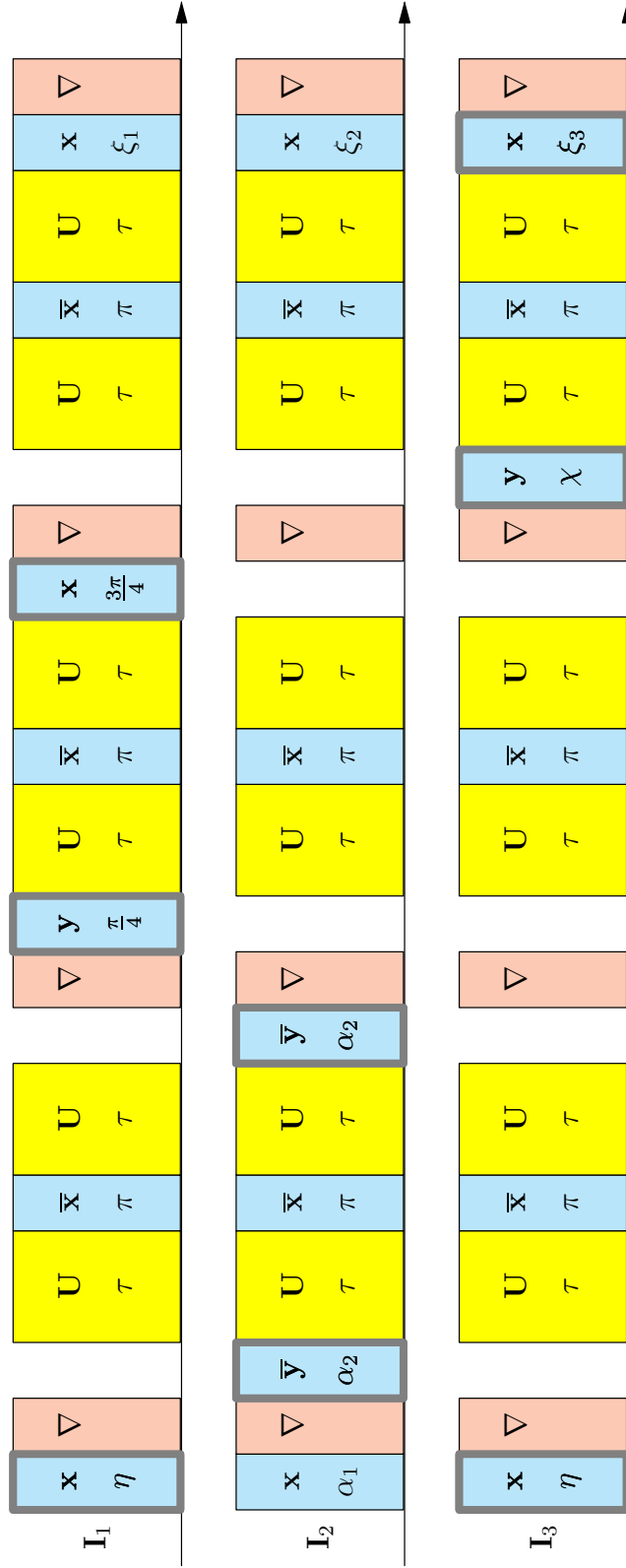


**Figure 1.3:** Pulse sequence for the preparation of the eight 3-qubit pseudo-pure states in 2,3,4-Trifluoroaniline. Rf and gradient pulses are shown in blue and red respectively. Yellow indicates periods of free evolution. The rotation angles  $\alpha_i$  are constant and given by  $\alpha_1 = \arccos \frac{2}{4}$  and  $\alpha_2 = \arccos \frac{1}{\sqrt{3}}$ . The selection of specific states is achieved through the choice of parameters shown in Table 1.2. The Pulses adjusted to correct for relaxation and pulse imperfections are highlighted with thick frames.

$\rho$	000	001	010	011	100	101	110	111
$\eta$	$\pi/3$	$\pi/3$	$\pi/3$	$\pi/3$	$2\pi/3$	$2\pi/3$	$\pi/3$	$\pi/3$
$\chi$	$\pi/4$	$\pi/4$	$\pi/4$	$\pi/4$	$-3\pi/4$	$\pi/4$	$\pi/4$	$\pi/4$
$\xi_1$	0	0	0	0	0	0	$\pi$	$\pi$
$\xi_2$	$\pi$	$\pi$	0	0	$\pi$	$\pi$	0	0
$\xi_3$	$-3\pi/4$	$\pi/4$	$-3\pi/4$	$\pi/4$	$-3\pi/4$	$-3\pi/4$	$-3\pi/4$	$\pi/4$

**Table 1.2:** Parameters of the preparation sequence for the eight three-qubit pseudo-pure states in 2,3,4-Trifluoroaniline. The pulse sequence is shown in Figure 1.3.

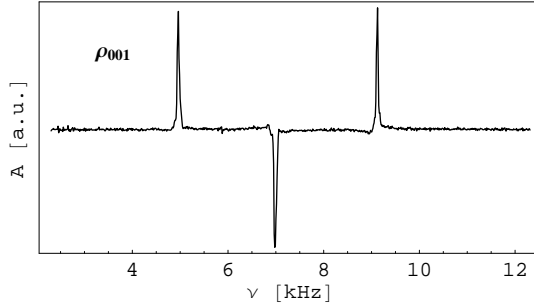


**Figure 1.4:** Example of a spectral signature of a pseudo-pure state ( $\rho_{001}$ ) in 2,3,4-Trifluoroaniline. Notice that the qubits in the spectrum appear in the order 2, 3, 1 (cf. Figure 1.1)

### 1.2.3 Density Matrix Tomography

Only linear transverse components  $\mathbf{I}_{x_j}$  and  $\mathbf{I}_{y_j}$  of the density matrix are directly observable by NMR.  $\mathbf{I}_{z_j}$  is readily transformed to one of the former by a simple  $\pi/2$ -pulse. Higher order components of the form  $\mathbf{I}_{\alpha_j}\mathbf{I}_{\beta_k}$  (and higher orders) are not directly accessible, because their products with the NMR measurement operator are traceless:

$$\text{tr} \{ \mathbf{I}_- \mathbf{I}_{\alpha_j} \mathbf{I}_{\beta_k} \} = 0 \quad (1.19)$$

for any choice of  $\alpha, \beta$  and  $j \neq k$ . The information about such terms can, under suitable conditions, be extracted from two-dimensional measurements [59]. In the present case, however, the spin interactions are not resolved and a more generally applicable procedure must be deployed. It consists of transforming higher order contributions to linear terms, which can then be observed directly. This task can be achieved by the same basic sequence which was described in the last section. The various sequences required for the different terms of the density matrix are discussed in detail in [31]. Applying this tomography procedure, it is possible to gain the knowledge of all the 64 complex elements of the density matrix. In the case of the pseudo-pure states, the final gradient pulse in the preparation sequence eliminates all off-diagonal elements, such that only the eight diagonal components must be measured.

The knowledge of the density matrix allows the *fidelity* of the prepared state to the theoretical expectation to be computed. This is a measure of the deviation

of the theoretically expected density matrix from the experimentally obtained result which utilizes the scalar product in the Hilbert space.

$$\mathcal{F} = 1 - \frac{1}{2} \text{tr} \left\{ |\rho_{exp} - \rho_{theo}|^2 \right\}. \quad (1.20)$$

The preparation sequence described above is designed under the assumption of non-existent relaxation and perfect  $\delta$ -pulses. In practice, there are, of course, deviations from such idealized conditions. The analysis of the intermediate states produced during the preparation allows the sequence to be optimized by adjusting the rotation angles of some pulses to take advantage of the non-unitary nature of the entire transformation to compensate for the experimental imperfections as described in [30]. The pulses used for optimization are highlighted in Figure 1.3.

This procedure results in pseudo-pure states of much higher fidelity. Figure 1.5 shows a comparison of the real parts of the measured density matrices for the state  $\rho_{000}$  before and after the optimization of the preparation sequence. The fidelity improves from 0.953 the former case to 0.999 in the latter. Thorough optimization, it was possible to prepare all eight pseudo-pure states with fidelities  $\mathcal{F} > 0.95$ .

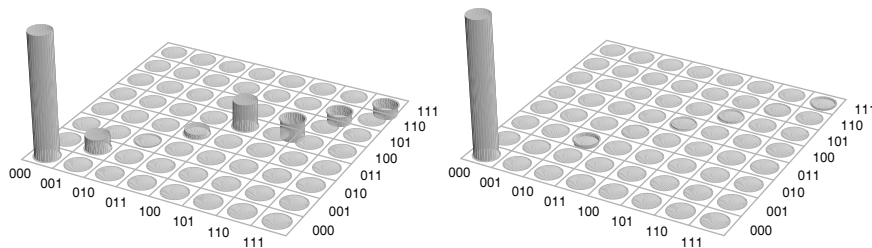


**Figure 1.5:** Real part of the density matrix of the pseudo-pure state  $\rho_{000}$  prepared without the compensation for pulse errors and relaxation (left) and after such optimization (right).

## 1.3 Implementation of the Deutsch-Josza Algorithm

### 1.3.1 Collins Version of the D.-J. Algorithm

The first concrete form of quantum computing algorithm was given by Deutsch and Josza [5]. It considers a set of functions which map a binary string of length  $N$  to a single bit:

$$f : \mathbb{Z}_{2^N} \mapsto \mathbb{Z}_2 \quad (1.21)$$

These functions are divided into two classes according to the following property:

- i)*  $f$  is *constant*, i.e., it yields the same value for all inputs, or
- ii)* it is *balanced*, meaning that applied to all possible inputs it returns 0 exactly as often as 1.

Functions  $f$  in Equation (1.21) which do not satisfy one of the above criteria are explicitly excluded. Deutsch and Jozsa have shown that, for a reasonable model of the oracle  $U_f$ , a quantum computer can solve this problem exponentially faster than a classical computer.

The original version of the algorithm required  $N + 1$  qubits for a  $N$ -bit function and two applications of  $U_f$ . Later, Cleve, Ekert, Macchiavello, and Mosca (CEMM) modified the Deutsch-Jozsa algorithm by reducing the number of evaluations of  $U_f$  to one [60]. Collins, Kim, and Holton removed the requirement of an ancilla qubit [61].

The block diagram for this extended version of the algorithm is shown in Fig. 1.6.  $|0\rangle_N$  is the initial state with all  $N$  qubits in state  $|0\rangle$ . Application of  $U_f$  is

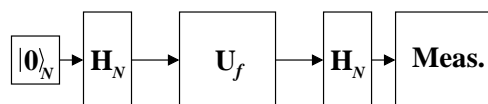


**Figure 1.6:** Block diagram of the CEMM version of the Deutsch-Josza algorithm for  $N$  qubits.

defined by

$$\begin{aligned}
 |0\rangle_N &\xrightarrow{H_N} \frac{1}{\sqrt{2^N}} \sum_{k=0}^{2^N-1} |k\rangle_N \\
 &\xrightarrow{U_f} \frac{1}{\sqrt{2^N}} \sum_{k=0}^{2^N-1} (-1)^{f(k)} |k\rangle_N \\
 &\xrightarrow{H_N} \frac{1}{2^N} \sum_{k=0}^{2^N-1} (-1)^{f(k)} \sum_{m=0}^{2^N-1} (-1)^{\sum_{j=0}^{N-1} m_j k_j} |m\rangle_N
 \end{aligned} \tag{1.22}$$

$H_N = H \otimes H \otimes \cdots \otimes H \otimes H$  is the *Hadamard* transform applied to all  $N$  qubits simultaneously. The Hadamard transform of one qubit is defined by

$$H = \frac{1}{\sqrt{2}} \begin{pmatrix} 1 & 1 \\ 1 & -1 \end{pmatrix} \tag{1.23}$$

and is equal to its inverse. The decision on the class of the test function is based upon the amplitude of the state  $|0\rangle_N$  in the output state:

$$P(|0\rangle_N) = \frac{1}{2^N} \left| \sum_{k=0}^{2^N-1} (-1)^{f(k)} \right| = \begin{cases} 1 & \text{if } f \text{ constant} \\ 0 & \text{if } f \text{ balanced} \end{cases} \tag{1.24}$$

### 1.3.2 Deutsch-Josza Oracle Transformations for Three Qubits

In the case of three qubits, there are 256 possible functions 70 of which are balanced and 2 are constant. Not all of these, however, are essentially different from the experimental point of view. First of all, there is the freedom of reversing



the states  $|0\rangle$  and  $|1\rangle$  to *spin up* and *spin down* resulting in a mirror image function. This halves the number of functions.

In order to further reduce the number of functions to a feasibly small set of interesting candidates, it is instructive to analyze the operator structure of the oracle transformations associated with them. Given a function which maps the input sequence of natural numbers  $S_i = \{1, 2, \dots, 8\}$  to the sequence of outputs such as  $S_o = \{1, 0, 1, 0, 1, 0, 0, 1\}$ , the unitary transformation representing the oracle for this test function is obtained by replacing the zeroes in the output sequence with  $-1$  and using this list for the diagonal of an  $8 \times 8$  matrix with otherwise vanishing elements<sup>2</sup>:

$$U_8 = \begin{pmatrix} +1 & 0 & 0 & 0 & 0 & 0 & 0 & 0 \\ 0 & -1 & 0 & 0 & 0 & 0 & 0 & 0 \\ 0 & 0 & +1 & 0 & 0 & 0 & 0 & 0 \\ 0 & 0 & 0 & -1 & 0 & 0 & 0 & 0 \\ 0 & 0 & 0 & 0 & +1 & 0 & 0 & 0 \\ 0 & 0 & 0 & 0 & 0 & -1 & 0 & 0 \\ 0 & 0 & 0 & 0 & 0 & 0 & -1 & 0 \\ 0 & 0 & 0 & 0 & 0 & 0 & 0 & +1 \end{pmatrix} \quad (1.25)$$

This transformation can be represented in the basis of spin component operators in the following way:

$$U_8 = \mathbf{I}_{z_3} + 2\mathbf{I}_{z_1}\mathbf{I}_{z_3} + 2\mathbf{I}_{z_2}\mathbf{I}_{z_3} - 4\mathbf{I}_{z_1}\mathbf{I}_{z_2}\mathbf{I}_{z_3} \quad (1.26)$$

It turns out, that the oracle transformations consist of linear combinations of certain sets of basis operators. There are seven such sets:

$$\mathbf{I}_0 \quad (1.27a)$$

$$\begin{aligned} &\mathbf{I}_{z_1} \\ &\mathbf{I}_{z_2} \\ &\mathbf{I}_{z_3} \end{aligned} \quad (1.27b)$$

$$\begin{aligned} &\mathbf{I}_{z_1}\mathbf{I}_{z_2} \\ &\mathbf{I}_{z_1}\mathbf{I}_{z_3} \\ &\mathbf{I}_{z_2}\mathbf{I}_{z_3} \end{aligned} \quad (1.27c)$$

$$\mathbf{I}_{z_1}\mathbf{I}_{z_2}\mathbf{I}_{z_3} \quad (1.27d)$$

$$\mathbf{I}_{z_1}, \quad \mathbf{I}_{z_2}, \quad \mathbf{I}_{z_3}, \quad \mathbf{I}_{z_1}\mathbf{I}_{z_2}\mathbf{I}_{z_3} \quad (1.27e)$$

$$\begin{aligned} &\mathbf{I}_{z_1}, \quad \mathbf{I}_{z_2}, \quad \mathbf{I}_{z_1}\mathbf{I}_{z_3}, \quad \mathbf{I}_{z_2}\mathbf{I}_{z_3} \\ &\mathbf{I}_{z_1}, \quad \mathbf{I}_{z_3}, \quad \mathbf{I}_{z_1}\mathbf{I}_{z_2}, \quad \mathbf{I}_{z_3}\mathbf{I}_{z_2} \\ &\mathbf{I}_{z_2}, \quad \mathbf{I}_{z_3}, \quad \mathbf{I}_{z_1}\mathbf{I}_{z_2}, \quad \mathbf{I}_{z_2}\mathbf{I}_{z_3} \end{aligned} \quad (1.27f)$$

<sup>2</sup>For simplicity, the numbering of the oracle transformations was chosen to be identical to the scheme used by Arvind *et al.* in [44]. See below for more details.

$$\begin{aligned}
& \mathbf{I}_{z_1}, & \mathbf{I}_{z_1}\mathbf{I}_{z_2}, & \mathbf{I}_{z_1}\mathbf{I}_{z_3}, & \mathbf{I}_{z_1}\mathbf{I}_{z_2}\mathbf{I}_{z_3} \\
& \mathbf{I}_{z_2}, & \mathbf{I}_{z_1}\mathbf{I}_{z_2}, & \mathbf{I}_{z_2}\mathbf{I}_{z_3}, & \mathbf{I}_{z_1}\mathbf{I}_{z_2}\mathbf{I}_{z_3} \\
& \mathbf{I}_{z_3}, & \mathbf{I}_{z_1}\mathbf{I}_{z_3}, & \mathbf{I}_{z_2}\mathbf{I}_{z_3}, & \mathbf{I}_{z_1}\mathbf{I}_{z_2}\mathbf{I}_{z_3}
\end{aligned} \tag{1.27g}$$

The oracles within each set differ only in the signs of the constituting terms and can otherwise be mutually mapped onto each other by qubit permutations. Thus, the implementations of all transforms within a class will be essentially identical save for the trivial operations of sign reversal and qubit relabeling. The transformations in the first two classes (Equations (1.27a–d)) require only one-qubit gates and are readily implemented through  $z$ -rotations. Transforms in the class of Equation (1.27f) utilize effective three-qubit gates. The remaining two classes employ different combinations of two-qubit gates.

### 1.3.3 NMR Implementation of the Three-Qubit Deutsch-Josza Algorithm

The analysis in the previous section assumed a Hamiltonian that is invariant under permutation of spins. For the Hamiltonian of 2,3,4-Trifluoroaniline in Equation (1.7) this is not the case. It is symmetric under the exchange of spins  $1 \leftrightarrow 3$ , however, exchanges  $1 \leftrightarrow 2$  and  $2 \leftrightarrow 3$  break this symmetry. The lower symmetry of the Hamiltonian has interesting implications for the implementation of some of the oracle transformations. For instance, the second type of the class in Equation (1.27) requires a two-qubit gate between the qubits 1 and 3. This gate cannot be implemented directly, because the  $J$ -coupling between these two spins in 2,3,4-Trifluoroaniline is negligible. This gate must be composed of the other two-qubit gates using next-neighbor interactions in the coupling network (cf. Section 1.2.2).

Our work on implementing the three-qubit Deutsch-Josza Algorithm was inspired by results published by Arvind *et al.* [44]. Their implementation differed in several important aspects from our approach. However, their choice of oracle functions reasonably highlights the different aspects of implementation of oracle transformations from different classes described above. For easy comparison, we adopted their choice of test functions and corresponding transformations:

$$U_1 = \mathbf{I}_0 \tag{1.28a}$$

$$U_2 = 2\mathbf{I}_{z_1} \tag{1.28b}$$

$$U_3 = 2\mathbf{I}_{z_3} \tag{1.28c}$$

$$U_4 = 4\mathbf{I}_{z_1}\mathbf{I}_{z_2} \tag{1.28d}$$

$$U_5 = 4\mathbf{I}_{z_1}\mathbf{I}_{z_2}\mathbf{I}_{z_3} \tag{1.28e}$$

$$U_6 = \mathbf{I}_{z_1} + 2\mathbf{I}_{z_1}\mathbf{I}_{z_2} + 2\mathbf{I}_{z_1}\mathbf{I}_{z_3} - 4\mathbf{I}_{z_1}\mathbf{I}_{z_2}\mathbf{I}_{z_3} \tag{1.28f}$$

$$U_7 = \mathbf{I}_{z_2} + 2\mathbf{I}_{z_1}\mathbf{I}_{z_2} + 2\mathbf{I}_{z_2}\mathbf{I}_{z_3} - 4\mathbf{I}_{z_1}\mathbf{I}_{z_2}\mathbf{I}_{z_3} \tag{1.28g}$$

$$U_8 = \mathbf{I}_{z_3} + 2\mathbf{I}_{z_1}\mathbf{I}_{z_3} + 2\mathbf{I}_{z_2}\mathbf{I}_{z_3} - 4\mathbf{I}_{z_1}\mathbf{I}_{z_2}\mathbf{I}_{z_3} \tag{1.28h}$$

$$U_9 = \mathbf{I}_{z_1} + \mathbf{I}_{z_3} - 2\mathbf{I}_{z_1}\mathbf{I}_{z_2} + 2\mathbf{I}_{z_2}\mathbf{I}_{z_3} \tag{1.28i}$$

The defining output sequences of the corresponding test functions are listed in Table 1.3

$f$	000	001	010	011	100	101	110	111
$f_1$	0	0	0	0	0	0	0	0
$f_2$	0	0	0	0	1	1	1	1
$f_3$	0	1	0	1	0	1	0	1
$f_4$	0	0	1	1	1	1	0	0
$f_5$	0	1	1	0	1	0	0	1
$f_6$	0	0	0	1	1	1	1	0
$f_7$	0	0	1	1	0	1	1	0
$f_8$	0	1	0	1	0	1	1	0
$f_9$	0	1	0	0	0	1	1	1

**Table 1.3:** Definitions of the test functions implemented by the oracle transformations in Equation (1.28). The inputs are given in binary representation to facilitate the association with the eight possible pseudo-pure states.

The nine selected oracle transformations were implemented by appropriate NMR pulse sequences. The measurements consisted of the sequence for the preparation of the pseudo-pure state  $\rho_{000}$  followed by a Hadamard transform, then one of the oracles' pulse sequences and a second Hadamard transform. Instead of the Hadamard transform as defined in Equation (1.23), a variant implemented by simple  $\pi/2$ -pulses was used. This substitution has some effect on details of calculations but presents no qualitative alteration. The output state of the Deutsch-Josza algorithm for each test function was then subjected to full density matrix tomography as described in Section 1.2.3. This procedure allowed the evaluation of the decision criterion in Equation (1.24) in order to ascertain the correct discrimination between the constant and balanced functions by the algorithm.

The measured values of the decision parameter for the nine test functions are shown in Table 1.4 along the fidelity of the output states to their theoretically expected shape. The decision parameter clearly separates the constant function

	$U_1$	$U_2$	$U_3$	$U_4$	$U_5$	$U_6$	$U_7$	$U_8$	$U_9$
$\mathcal{F}$	<b>0.862</b>	0.874	0.879	0.897	0.905	0.891	0.819	0.862	0.646
$D$	<b>0.862</b>	0.206	0.121	0.051	-0.066	0.084	0.015	0.027	0.184

**Table 1.4:** Fidelity of the output states of the nine oracle transforms of the Deutsch-Josza algorithm ( $\mathcal{F}$ ) and corresponding values of the decision parameter ( $D$ ). The values for the identity transformation  $U_1$  are highlighted.

(oracle  $U_1$ ) from its balanced counterparts ( $U_2 - U_9$ ). The fidelity of the output states is satisfactory, especially, since the total pulse sequences (including the input state preparation and output state tomography) of some of the oracles involve upwards of 50 pulses. The implementation of the oracle transformation  $U_1$ , in principle, requires no pulses. However, a pulse sequence analogous to the sequences for the other “ $z$ -rotation” oracles was applied to insure comparability of results. This way, the results for  $U_1$  are an indicator of the overall performance

of the preparation and tomography procedure. The poor fidelity of the pulse sequence for  $U_9$  is notable. It can be attributed to the fact that an effective three-qubit gate used in it utilizes the two slightly different  $J$ -couplings at the same time resulting in an additional error.

### 1.3.4 Entanglement in the Deutsch-Josza Algorithm

It has been shown [43, 61] that entanglement between qubits does not always take place in the course of the Deutsch algorithm: Some oracles are entangling in nature others are not. Furthermore, entangling oracles only occur starting with at least three qubits. In addition, the comparison of the output states of the algorithm when pseudo-pure states are used as input as opposed to the Boltzmann state demonstrates the utility of pseudo-pure states in the context of ensemble quantum computing.

The oracle transforms for the first five test functions discussed here do not produce any entanglement and their output states when the pseudo-pure state  $\rho_{000}$  is used are again various pseudo-pure states:

$$\rho_1 = \left(\frac{1}{2}\mathbf{I}_0 + \mathbf{I}_{z_1}\right) \left(\frac{1}{2}\mathbf{I}_0 + \mathbf{I}_{z_2}\right) \left(\frac{1}{2}\mathbf{I}_0 + \mathbf{I}_{z_3}\right) = \rho_{000} \quad (1.29a)$$

$$\rho_2 = \left(\frac{1}{2}\mathbf{I}_0 - \mathbf{I}_{z_1}\right) \left(\frac{1}{2}\mathbf{I}_0 + \mathbf{I}_{z_2}\right) \left(\frac{1}{2}\mathbf{I}_0 + \mathbf{I}_{z_3}\right) = \rho_{100} \quad (1.29b)$$

$$\rho_3 = \left(\frac{1}{2}\mathbf{I}_0 + \mathbf{I}_{z_1}\right) \left(\frac{1}{2}\mathbf{I}_0 + \mathbf{I}_{z_2}\right) \left(\frac{1}{2}\mathbf{I}_0 - \mathbf{I}_{z_3}\right) = \rho_{001} \quad (1.29c)$$

$$\rho_4 = \left(\frac{1}{2}\mathbf{I}_0 - \mathbf{I}_{z_1}\right) \left(\frac{1}{2}\mathbf{I}_0 - \mathbf{I}_{z_2}\right) \left(\frac{1}{2}\mathbf{I}_0 + \mathbf{I}_{z_3}\right) = \rho_{110} \quad (1.29d)$$

$$\rho_5 = \left(\frac{1}{2}\mathbf{I}_0 - \mathbf{I}_{z_1}\right) \left(\frac{1}{2}\mathbf{I}_0 - \mathbf{I}_{z_2}\right) \left(\frac{1}{2}\mathbf{I}_0 - \mathbf{I}_{z_3}\right) = \rho_{111} \quad (1.29e)$$

Note, how, in this representation, it is particularly straight forward to evaluate the decision criterion in Equation (1.24). Since the pseudo-pure basis states  $\rho_{000} - \rho_{111}$  form an orthogonal set, the oracle  $U_1$  reveals it's test function to be constant whereas all the others are balanced.

As described in Section 1.2.1 the Boltzmann state is fundamentally mixed. It is reasonable to require a representation of this state to satisfy the normalization condition

$$\text{tr}(\rho_B) = 1 \quad (1.30)$$

A possible representation is then

$$\rho_B = \frac{1}{8}\mathbf{I}_0 + b(\mathbf{I}_{z_1} + \mathbf{I}_{z_2} + \mathbf{I}_{z_3}) \quad (1.31)$$

Using this representation the output sates corresponding to those in Equation (1.29) when the algorithm is applied to the input state  $\rho_B$  are given by:

$$\rho_1^B = \frac{1}{8}\mathbf{I}_0 + b(+\mathbf{I}_{z_1} + \mathbf{I}_{z_2} + \mathbf{I}_{z_3}) \quad (1.32a)$$

$$\rho_2^B = \frac{1}{8}\mathbf{I}_0 + b(-\mathbf{I}_{z_1} + \mathbf{I}_{z_2} + \mathbf{I}_{z_3}) \quad (1.32b)$$

$$\rho_3^B = \frac{1}{8}\mathbf{I}_0 + b(+\mathbf{I}_{z_1} + \mathbf{I}_{z_2} - \mathbf{I}_{z_3}) \quad (1.32c)$$

$$\rho_4^B = \frac{1}{8}\mathbf{I}_0 + b(-\mathbf{I}_{z_1} - \mathbf{I}_{z_2} + \mathbf{I}_{z_3}) \quad (1.32d)$$

$$\rho_5^B = \frac{1}{8}\mathbf{I}_0 + b(-\mathbf{I}_{z_1} - \mathbf{I}_{z_2} - \mathbf{I}_{z_3}) \quad (1.32e)$$

Because the oracles  $U_1 - U_5$  are non-entangling, no higher-order products of the spin operators are present in the output. The linear terms, however, do reproduce the situation in Equation (1.29) correctly. It is because of this, that the discrimination between balanced and constant functions is at all possible with the Boltzmann state as the input. The quantitative evaluation of the decision parameter  $D = \text{tr}(\rho_{out} \rho_{000})$ , however, shows the shortcomings of this approach:

$$D_1 = 1 \quad D_1^B = \frac{1}{8} + \frac{3}{2}b \quad (1.33a)$$

$$D_2 = 0 \quad D_2^B = \frac{1}{8} + \frac{1}{2}b \quad (1.33b)$$

$$D_3 = 0 \quad D_3^B = \frac{1}{8} + \frac{1}{2}b \quad (1.33c)$$

$$D_4 = 0 \quad D_4^B = \frac{1}{8} - \frac{1}{2}b \quad (1.33d)$$

$$D_5 = 0 \quad D_5^B = \frac{1}{8} - \frac{3}{2}b \quad (1.33e)$$

Though the balanced function is sufficiently separated from its constant counterparts, and the initial problem can thus be solved, more detailed understanding of the implementation must consider the entire density matrix prepared from a pseudo-pure input state.

The output states of the algorithm for the oracles  $U_6 - U_9$  are these<sup>3</sup> :

$$\begin{aligned} \rho_6 = \frac{1}{8}\mathbf{I}_0 - \frac{1}{4}\mathbf{I}_{z_1} + \frac{1}{2}\mathbf{I}_{y_2}\mathbf{I}_{y_3} - \frac{1}{2}\mathbf{I}_{z_2}\mathbf{I}_{x_3} - \frac{1}{2}\mathbf{I}_{x_2}\mathbf{I}_{z_3} \\ + \mathbf{I}_{z_1}\mathbf{I}_{z_2}\mathbf{I}_{x_3} + \mathbf{I}_{z_1}\mathbf{I}_{x_2}\mathbf{I}_{z_3} - \mathbf{I}_{z_1}\mathbf{I}_{y_2}\mathbf{I}_{y_3} \end{aligned} \quad (1.34a)$$

$$\begin{aligned} \rho_7 = \frac{1}{8}\mathbf{I}_0 - \frac{1}{4}\mathbf{I}_{z_2} + \frac{1}{2}\mathbf{I}_{y_1}\mathbf{I}_{y_3} - \frac{1}{2}\mathbf{I}_{z_1}\mathbf{I}_{x_3} - \frac{1}{2}\mathbf{I}_{x_1}\mathbf{I}_{z_3} \\ + \mathbf{I}_{x_1}\mathbf{I}_{z_2}\mathbf{I}_{z_3} + \mathbf{I}_{z_1}\mathbf{I}_{z_2}\mathbf{I}_{x_3} - \mathbf{I}_{y_1}\mathbf{I}_{z_2}\mathbf{I}_{y_3} \end{aligned} \quad (1.34b)$$

$$\begin{aligned} \rho_8 = \frac{1}{8}\mathbf{I}_0 - \frac{1}{4}\mathbf{I}_{z_3} + \frac{1}{2}\mathbf{I}_{y_1}\mathbf{I}_{y_2} - \frac{1}{2}\mathbf{I}_{z_1}\mathbf{I}_{x_2} - \frac{1}{2}\mathbf{I}_{x_1}\mathbf{I}_{z_2} \\ + \mathbf{I}_{z_1}\mathbf{I}_{x_2}\mathbf{I}_{z_3} + \mathbf{I}_{x_1}\mathbf{I}_{z_2}\mathbf{I}_{z_3} - \mathbf{I}_{y_1}\mathbf{I}_{y_2}\mathbf{I}_{z_3} \end{aligned} \quad (1.34c)$$

<sup>3</sup>Notice, that the experimental implementation uses a  $\pi/2$ -pulse instead of the Hadamard transform

$$\begin{aligned} \rho_9 = & \frac{1}{8}\mathbf{I}_0 - \frac{1}{2}\mathbf{I}_{z_1}\mathbf{I}_{x_2} + \frac{1}{2}\mathbf{I}_{x_2}\mathbf{I}_{z_3} - \frac{1}{2}\mathbf{I}_{z_1}\mathbf{I}_{z_3} \\ & + \mathbf{I}_{x_1}\mathbf{I}_{y_2}\mathbf{I}_{y_3} - \mathbf{I}_{y_1}\mathbf{I}_{y_2}\mathbf{I}_{x_3} + \mathbf{I}_{x_1}\mathbf{I}_{z_2}\mathbf{I}_{x_3} + \mathbf{I}_{y_1}\mathbf{I}_{z_2}\mathbf{I}_{y_3} \end{aligned} \quad (1.34d)$$

The entanglement content of these states is not immediately obvious. Although entanglement of bipartite systems is well understood [62, 63], the problem of general multipartite entanglement [64–66] still remains unsolved. Fortunately, for the output states above it is possible to find a small set of *local* (i.e., one-qubit) operations, which transform each of these output states into a form which reveals the entanglement structure:

$$\begin{aligned} P_{y_2}\left(-\frac{\pi}{2}\right)\rho_6 = & \left(\frac{1}{2}\mathbf{I}_0 - \mathbf{I}_{z_1}\right) \left(\frac{1}{4}\mathbf{I}_0 + \mathbf{I}_{x_2}\mathbf{I}_{x_3} + \mathbf{I}_{y_2}\mathbf{I}_{y_3} - \mathbf{I}_{z_2}\mathbf{I}_{z_3}\right) = \\ & \begin{pmatrix} 0 & 0 & 0 & 0 & 0 & 0 & 0 & 0 \\ 0 & 0 & 0 & 0 & 0 & 0 & 0 & 0 \\ 0 & 0 & 0 & 0 & 0 & 0 & 0 & 0 \\ 0 & 0 & 0 & 0 & 0 & 0 & 0 & 0 \\ 0 & 0 & 0 & 0 & 0 & 0 & 0 & 0 \\ 0 & 0 & 0 & 0 & 0 & \frac{1}{2} & \frac{1}{2} & 0 \\ 0 & 0 & 0 & 0 & 0 & \frac{1}{2} & \frac{1}{2} & 0 \\ 0 & 0 & 0 & 0 & 0 & 0 & 0 & 0 \end{pmatrix} = \\ & \begin{pmatrix} 0 & 0 \\ 0 & 1 \end{pmatrix}^{(1)} \otimes \begin{pmatrix} 0 & 0 & 0 & 0 \\ 0 & \frac{1}{2} & \frac{1}{2} & 0 \\ 0 & \frac{1}{2} & \frac{1}{2} & 0 \\ 0 & 0 & 0 & 0 \end{pmatrix}^{(2,3)} = \rho_1^{(1)} \otimes \rho_{\Psi^+}^{(2,3)} \end{aligned} \quad (1.35a)$$

$$\begin{aligned} P_{y_3}\left(-\frac{\pi}{2}\right)\rho_7 = & \left(\frac{1}{2}\mathbf{I}_0 - \mathbf{I}_{z_2}\right) \left(\frac{1}{4}\mathbf{I}_0 + \mathbf{I}_{x_1}\mathbf{I}_{x_3} + \mathbf{I}_{y_1}\mathbf{I}_{y_3} - \mathbf{I}_{z_1}\mathbf{I}_{z_3}\right) = \\ & \begin{pmatrix} 0 & 0 & 0 & 0 & 0 & 0 & 0 & 0 \\ 0 & 0 & 0 & 0 & 0 & 0 & 0 & 0 \\ 0 & 0 & 0 & 0 & 0 & 0 & 0 & 0 \\ 0 & 0 & 0 & \frac{1}{2} & 0 & 0 & \frac{1}{2} & 0 \\ 0 & 0 & 0 & 0 & 0 & 0 & 0 & 0 \\ 0 & 0 & 0 & 0 & 0 & 0 & 0 & 0 \\ 0 & 0 & 0 & \frac{1}{2} & 0 & 0 & \frac{1}{2} & 0 \\ 0 & 0 & 0 & 0 & 0 & 0 & 0 & 0 \end{pmatrix} = \\ & \begin{pmatrix} 0 & 0 \\ 0 & 1 \end{pmatrix}^{(2)} \otimes \begin{pmatrix} 0 & 0 & 0 & 0 \\ 0 & \frac{1}{2} & \frac{1}{2} & 0 \\ 0 & \frac{1}{2} & \frac{1}{2} & 0 \\ 0 & 0 & 0 & 0 \end{pmatrix}^{(1,3)} = \rho_1^{(2)} \otimes \rho_{\Psi^+}^{(1,3)} \end{aligned} \quad (1.35b)$$

$$\begin{aligned}
P_{y_3} \left( -\frac{\pi}{2} \right) \rho_8 &= \left( \frac{1}{2} \mathbf{I}_0 - \mathbf{I}_{z_3} \right) \left( \frac{1}{4} \mathbf{I}_0 + \mathbf{I}_{x_1} \mathbf{I}_{x_2} + \mathbf{I}_{y_1} \mathbf{I}_{y_2} - \mathbf{I}_{z_1} \mathbf{I}_{z_2} \right) = \\
&\quad \begin{pmatrix} 0 & 0 & 0 & 0 & 0 & 0 & 0 & 0 \\ 0 & 0 & 0 & 0 & 0 & 0 & 0 & 0 \\ 0 & 0 & 0 & 0 & 0 & 0 & 0 & 0 \\ 0 & 0 & 0 & \frac{1}{2} & 0 & \frac{1}{2} & 0 & 0 \\ 0 & 0 & 0 & 0 & 0 & 0 & 0 & 0 \\ 0 & 0 & 0 & \frac{1}{2} & 0 & \frac{1}{2} & 0 & 0 \\ 0 & 0 & 0 & 0 & 0 & 0 & 0 & 0 \\ 0 & 0 & 0 & 0 & 0 & 0 & 0 & 0 \end{pmatrix} = \\
&\quad \begin{pmatrix} 0 & 0 \\ 0 & 1 \end{pmatrix}^{(3)} \otimes \begin{pmatrix} 0 & 0 & 0 & 0 \\ 0 & \frac{1}{2} & \frac{1}{2} & 0 \\ 0 & \frac{1}{2} & \frac{1}{2} & 0 \\ 0 & 0 & 0 & 0 \end{pmatrix}^{(1,2)} = \rho_1^{(3)} \otimes \rho_{\Psi^+}^{(1,2)} \quad (1.35c)
\end{aligned}$$

$$\begin{aligned}
P_{y_1}(\pi) P_{y_2} \left( -\frac{\pi}{2} \right) \rho_9 &= \\
&\quad \frac{1}{8} \mathbf{I}_0 + \frac{1}{2} (\mathbf{I}_{z_1} \mathbf{I}_{z_2} + \mathbf{I}_{z_2} \mathbf{I}_{z_3} + \mathbf{I}_{z_1} \mathbf{I}_{z_3}) \\
&\quad + \mathbf{I}_{x_1} \mathbf{I}_{x_2} \mathbf{I}_{x_3} - \mathbf{I}_{x_1} \mathbf{I}_{y_2} \mathbf{I}_{y_3} - \mathbf{I}_{y_1} \mathbf{I}_{x_2} \mathbf{I}_{y_3} - \mathbf{I}_{y_1} \mathbf{I}_{y_2} \mathbf{I}_{x_3} = \\
&\quad \begin{pmatrix} \frac{1}{2} & 0 & 0 & 0 & 0 & 0 & 0 & \frac{1}{2} \\ 0 & 0 & 0 & 0 & 0 & 0 & 0 & 0 \\ 0 & 0 & 0 & 0 & 0 & 0 & 0 & 0 \\ 0 & 0 & 0 & 0 & 0 & 0 & 0 & 0 \\ 0 & 0 & 0 & 0 & 0 & 0 & 0 & 0 \\ 0 & 0 & 0 & 0 & 0 & 0 & 0 & 0 \\ 0 & 0 & 0 & 0 & 0 & 0 & 0 & 0 \\ \frac{1}{2} & 0 & 0 & 0 & 0 & 0 & 0 & \frac{1}{2} \end{pmatrix} = \rho_{\text{GHZ}} \quad (1.35d)
\end{aligned}$$

The matrix representation is given to facilitate the comparison with the experimental results shown in Figure 1.7. Shown there are the results of the tomography procedure applied to the output states of the algorithm for the oracles  $U_6 - U_9$ . To emphasize the entanglement, the data has been subjected to the local transformations described above. The states  $\rho_6$ ,  $\rho_7$ , and  $\rho_8$  show the entangled Bell [67] state  $\Psi^+$  in the subspace of the spins  $\{1,2\}$ ,  $\{1,3\}$ , and  $\{2,3\}$  respectively, whereas the third spin remains in the one-qubit pseudo-pure state  $\rho_1$ . The density matrix resulting from the application of the algorithm for  $U_9$  produces the maximally entangled three-qubit *Greenberger-Horne-Zeilinger* (GHZ) state [68].

Again, these properties of the oracle transformations are not revealed, when the

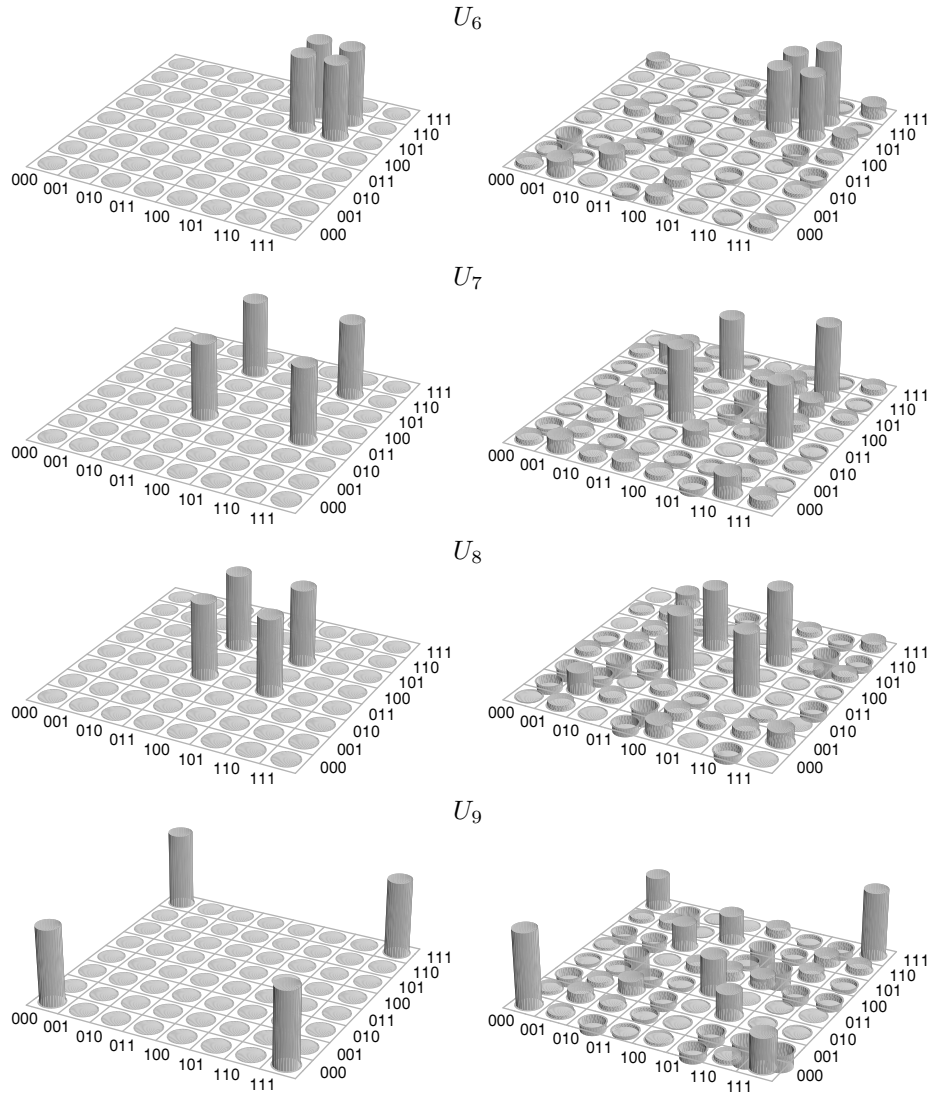


**Figure 1.7:** Partially and fully entangled output states of the three-qubit Deutsch-Josza algorithm. The theoretically expected (left) and experimentally obtained (right) real part of the density matrix is shown. The data has been subjected to local transformations to demonstrate the entanglement (see Equation (1.35)). The imaginary part is expected to vanish in all cases; the experimentally obtained elements of the imaginary parts show the same degree of deviation from the predicted behavior as the vanishing elements of the real parts.



Boltzmann state is used as input. The corresponding output states are:

$$P_{y_2} \left( -\frac{\pi}{2} \right) \rho_6^B = \frac{1}{8} \mathbf{I}_0 - b \mathbf{I}_{z_1} + 2b \mathbf{I}_{x_2} \mathbf{I}_{x_3} - 2b \mathbf{I}_{z_2} \mathbf{I}_{z_3} =$$

$$\begin{pmatrix} \frac{1}{8} - b & 0 & 0 & -\frac{b}{2} & 0 & 0 & 0 & 0 \\ 0 & \frac{1}{8} & -\frac{b}{2} & 0 & 0 & 0 & 0 & 0 \\ 0 & -\frac{b}{2} & \frac{1}{8} & 0 & 0 & 0 & 0 & 0 \\ -\frac{b}{2} & 0 & 0 & \frac{1}{8} - b & 0 & 0 & 0 & 0 \\ 0 & 0 & 0 & 0 & \frac{1}{8} & 0 & 0 & -\frac{b}{2} \\ 0 & 0 & 0 & 0 & 0 & \frac{1}{8} + b & -\frac{b}{2} & 0 \\ 0 & 0 & 0 & 0 & 0 & -\frac{b}{2} & \frac{1}{8} + b & 0 \\ 0 & 0 & 0 & 0 & -\frac{b}{2} & 0 & 0 & \frac{1}{8} \end{pmatrix} \quad (1.36a)$$

$$P_{y_3} \left( -\frac{\pi}{2} \right) \rho_7^B = \frac{1}{8} \mathbf{I}_0 - b \mathbf{I}_{z_2} + 2b \mathbf{I}_{x_1} \mathbf{I}_{x_3} - 2b \mathbf{I}_{z_1} \mathbf{I}_{z_3} =$$

$$\begin{pmatrix} \frac{1}{8} - b & 0 & 0 & 0 & 0 & \frac{b}{2} & 0 & 0 \\ 0 & \frac{1}{8} & 0 & 0 & \frac{b}{2} & 0 & 0 & 0 \\ 0 & 0 & \frac{1}{8} & 0 & 0 & 0 & 0 & \frac{b}{2} \\ 0 & 0 & 0 & \frac{1}{8} + b & 0 & 0 & \frac{b}{2} & 0 \\ 0 & \frac{b}{2} & 0 & 0 & \frac{1}{8} & 0 & 0 & 0 \\ \frac{b}{2} & 0 & 0 & 0 & 0 & \frac{1}{8} - b & 0 & 0 \\ 0 & 0 & 0 & \frac{b}{2} & 0 & 0 & \frac{1}{8} + b & 0 \\ 0 & 0 & \frac{b}{2} & 0 & 0 & 0 & 0 & \frac{1}{8} \end{pmatrix} \quad (1.36b)$$

$$P_{y_3} \left( -\frac{\pi}{2} \right) \rho_8^B = \frac{1}{8} \mathbf{I}_0 - b \mathbf{I}_{z_3} + 2b \mathbf{I}_{x_1} \mathbf{I}_{x_2} - 2b \mathbf{I}_{z_1} \mathbf{I}_{z_2} =$$

$$\begin{pmatrix} \frac{1}{8} - b & 0 & 0 & 0 & 0 & 0 & \frac{b}{2} & 0 \\ 0 & \frac{1}{8} & 0 & 0 & 0 & 0 & 0 & \frac{b}{2} \\ 0 & 0 & \frac{1}{8} & 0 & \frac{b}{2} & 0 & 0 & 0 \\ 0 & 0 & 0 & \frac{1}{8} + b & 0 & \frac{b}{2} & 0 & 0 \\ 0 & 0 & \frac{b}{2} & 0 & \frac{1}{8} & 0 & 0 & 0 \\ 0 & 0 & 0 & \frac{b}{2} & 0 & \frac{1}{8} + b & 0 & 0 \\ \frac{b}{2} & 0 & 0 & 0 & 0 & 0 & \frac{1}{8} - b & 0 \\ 0 & \frac{b}{2} & 0 & 0 & 0 & 0 & 0 & \frac{1}{8} \end{pmatrix} \quad (1.36c)$$

$$P_{y_1}(\pi) P_{y_2} \left( -\frac{\pi}{2} \right) \rho_9^B = \frac{1}{8} \mathbf{I}_0 + 4b \mathbf{I}_{x_1} \mathbf{I}_{x_2} \mathbf{I}_{x_3} + 2b \mathbf{I}_{z_1} \mathbf{I}_{z_2} + 2b \mathbf{I}_{z_2} \mathbf{I}_{z_3} =$$

$$\begin{pmatrix} \frac{1}{8} + b & 0 & 0 & 0 & 0 & 0 & 0 & \frac{b}{2} \\ 0 & \frac{1}{8} & 0 & 0 & 0 & 0 & \frac{b}{2} & 0 \\ 0 & 0 & \frac{1}{8} - b & 0 & 0 & \frac{b}{2} & 0 & 0 \\ 0 & 0 & 0 & \frac{1}{8} & \frac{b}{2} & 0 & 0 & 0 \\ 0 & 0 & 0 & \frac{b}{2} & \frac{1}{8} & 0 & 0 & 0 \\ 0 & 0 & \frac{b}{2} & 0 & 0 & \frac{1}{8} - b & 0 & 0 \\ 0 & \frac{b}{2} & 0 & 0 & 0 & 0 & \frac{1}{8} & 0 \\ \frac{b}{2} & 0 & 0 & 0 & 0 & 0 & 0 & \frac{1}{8} + b \end{pmatrix} \quad (1.36d)$$

Although these density matrices show certain symmetries, neither the operator structure, nor the matrix representation demonstrate the creation of entanglement in the course of the Deutsch-Josza algorithm. Similar to the non-entangling oracles, however, the decision parameter can be used to separate of the balanced functions from the constant one:

$$D_6 = 0 \quad D_6^B = \frac{1}{8} - \frac{1}{2}b \quad (1.37a)$$

$$D_7 = 0 \quad D_7^B = \frac{1}{8} - \frac{1}{2}b \quad (1.37b)$$

$$D_8 = 0 \quad D_8^B = \frac{1}{8} - \frac{1}{2}b \quad (1.37c)$$

$$D_9 = 0 \quad D_9^B = \frac{1}{8} \quad (1.37d)$$

These findings demonstrate the utility of the preparation of the pseudo-pure input states and full tomography of the output states, when implementing quantum computing algorithms in large ensembles.

## Chapter 2

# Selective Excitation under Continuous Averaging

It has long been known [69] that it is possible to modify the effective Hamiltonian of a spin system by continuous irradiation with strong rf fields. The spins are driven into a dynamic equilibrium state with a potentially different effective Hamilton operator. By carefully designing such a pulse sequence it is often possible to modify the Hamiltonian to satisfy particular needs. It is, for instance, possible to reduce or eliminate the dipole-dipole interaction of like nuclear spins in a solid sample [70, 71], to scale the chemical shifts of spins in a liquid [72], etc. As has been noted early on [29], this opens up the opportunity of tailoring a system's Hamiltonian to suit the requirements for the implementation of quantum computing.

The utility of such an approach depends on the ability to selectively manipulate the single spins of the system *while* the averaging is in effect. This chapter presents some proof-of-principle NMR experiments in this direction performed in 2002. The dipole-dipole coupling of two  $^{19}\text{F}$  nuclear spins offers a suitable test case. In normal liquids, this anisotropic interaction is averaged out due to fast random tumbling of the molecules. To avoid this cancellation, a liquid crystal matrix was used to align the molecules. The dipolar coupling has the additional advantage of being much stronger than the  $J$ -coupling which leads to potentially much shorter gate times.

### 2.1 The Magic Echo Sequence

The basis of the pulse sequences used here is the *magic echo* sequence [70, 71, 73, 74]. It was originally designed in the context of high resolution NMR in solids [75] to produce a free-standing echo in solid samples with an extended spin network. Under such conditions, the dipolar coupling amongst the ubiquitous spins leads to quick distribution of coherence among the spins and prevents the formation of an echo. The magic echo sequence as sketched in Figure 2.1 can be used to overcome this.

The *average Hamiltonian* theory, is commonly used to treat such *multi-pulse*

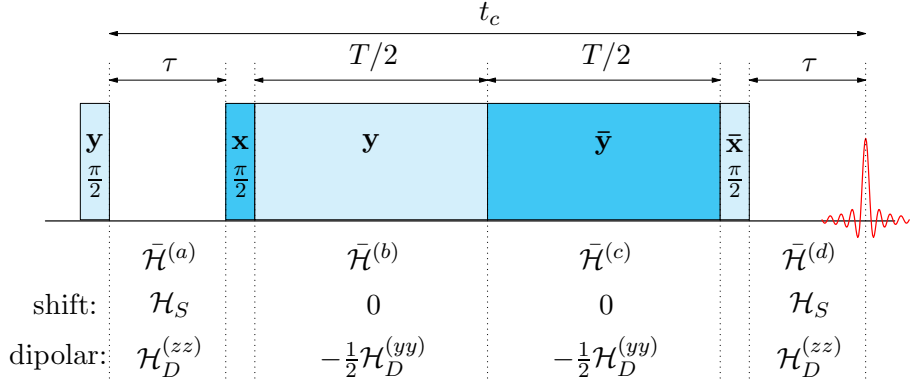


**Figure 2.1:** The magic echo pulse sequence for suppression of direct dipolar couplings between spins. All pulses are wide-band and affect all participating spins equally. The duration  $T$  of the magic echo sandwich and the ratio  $\tau/T$  must satisfy certain conditions (see text). Below the pulses, the chemical shift and dipolar Hamiltonians effective during that period are given.

sequences. It is assumed that the native Hamiltonian of the system is time-independent and the pulse sequence is periodic with period (cycle time)  $t_c$ . During the cycle time, the system may undergo complex evolution due to the interplay between the rf pulses and the native Hamiltonian. The effect of this evolution at  $t = t_c$  can be expressed by an average Hamiltonian which is *not* time-dependent. If the system is observed *stroboscopically* only at  $t = n t_c$ , it will appear to obey that average Hamiltonian. The average Hamiltonian<sup>1</sup> can be represented by an infinite sum of terms involving integrals of various combinations of commutators of the Hamiltonians at different times. The leading term is simply the average of the Hamiltonian over the cycle time:

$$\bar{\mathcal{H}}^{(0)} = \frac{1}{t_c} \int_0^{t_c} dt \mathcal{H}(t) \quad (2.1)$$

The power of this approach comes from the fact that the experimenter has – by judicious choice of pulse strength, phases, and timings – great influence on the average Hamiltonian’s shape. He may, for instance seek to hide some of its features while revealing others.

This formalism can be applied to calculate the 0-th order average Hamiltonian of the magic echo sequence. The free Hamiltonian of the system in the coordinate frame rotating with the frequency of rf irradiation

$$\mathcal{H} = \mathcal{H}_S + \mathcal{H}_D \quad (2.2)$$

contains two contributions: The chemical shift part given by

$$\mathcal{H}_S = \sum_j \omega_{0j} \mathbf{I}_{z_j} \quad (2.3)$$

<sup>1</sup>A concise but rigorous treatment is given in [75, 76].

and the dipole-dipole interaction part

$$\mathcal{H}_D = \sum_{j < k} D_{jk} (3\mathbf{I}_{z_j} \mathbf{I}_{z_k} - \mathbf{I}_j \mathbf{I}_k) \quad (2.4)$$

where  $\omega_{0_j}$  is the offset of the resonance frequency of the spin  $\mathbf{I}_j$  from the spectrometer frequency and  $D_{jk}$  is the dipole-dipole coupling constant. To simplify the notation, it is useful to define dipolar Hamiltonians quantized along the three Cartesian axes:

$$\begin{aligned} \mathcal{H}_D^{(xx)} &= \sum_{j < k} D_{jk} (3\mathbf{I}_{x_j} \mathbf{I}_{x_k} - \mathbf{I}_j \mathbf{I}_k) \\ \mathcal{H}_D^{(yy)} &= \sum_{j < k} D_{jk} (3\mathbf{I}_{y_j} \mathbf{I}_{y_k} - \mathbf{I}_j \mathbf{I}_k) \\ \mathcal{H}_D^{(zz)} &= \sum_{j < k} D_{jk} (3\mathbf{I}_{z_j} \mathbf{I}_{z_k} - \mathbf{I}_j \mathbf{I}_k) \end{aligned} \quad (2.5)$$

They satisfy the relationship

$$\mathcal{H}_D^{(xx)} + \mathcal{H}_D^{(yy)} + \mathcal{H}_D^{(zz)} = 0 \quad (2.6)$$

The average Hamiltonians can now be derived for the different parts of the cycle by piecewise integration. During the initial (*a*) and final (*d*) free evolution periods  $\tau$ , the average Hamiltonian of the system is identical to the native form:

$$\bar{\mathcal{H}}^{(a)} = \bar{\mathcal{H}}^{(d)} = \mathcal{H}_S + \mathcal{H}_D^{(zz)} \quad (2.7)$$

During the first period (*b*) of evolution under continuous irradiation, the system is driven by the rf field of strength  $B_1 = \omega_1/\gamma$  applied in the *y*-direction:  $\omega_1 (\mathbf{I}_{y_1} + \mathbf{I}_{y_2})$ . The dipolar part of the average Hamiltonian is then

$$\begin{aligned} \bar{\mathcal{H}}_D^{(b)} &= \frac{1}{T/2} \int_0^{T/2} dt e^{-i\omega_1 t (\mathbf{I}_{y_1} + \mathbf{I}_{y_2})} \mathcal{H}_D^{(zz)} e^{i\omega_1 t (\mathbf{I}_{y_1} + \mathbf{I}_{y_2})} \\ &= \frac{1}{T/2} \int_0^{T/2} dt (3 (\mathbf{I}_{z_j} \cos \omega_1 t + \mathbf{I}_{x_j} \sin \omega_1 t) (\mathbf{I}_{z_k} \cos \omega_1 t + \mathbf{I}_{x_k} \sin \omega_1 t) - \mathbf{I}_j \mathbf{I}_k) \\ &= \frac{1}{2} (3\mathbf{I}_{z_j} \mathbf{I}_{z_k} - \mathbf{I}_j \mathbf{I}_k + 3\mathbf{I}_{x_j} \mathbf{I}_{x_k} - \mathbf{I}_j \mathbf{I}_k) \\ &= \frac{1}{2} (\mathcal{H}_D^{(zz)} + \mathcal{H}_D^{(xx)}) = -\frac{1}{2} \mathcal{H}_D^{(yy)} \end{aligned} \quad (2.8)$$

under the condition that the time  $T/2$  accommodates an integer number of full Rabi rotations:

$$T = n \frac{2\pi}{\omega_1}, \quad n = 2, 3, 4... \quad (2.9)$$

Analogously, it can be shown that the second period (*c*) of evolution under rf irradiation with inverted phase produces the same average Hamiltonian

$$\bar{\mathcal{H}}_D^{(c)} = \bar{\mathcal{H}}_D^{(b)} \quad (2.10)$$

The phase inversion corresponds to an inversion of the  $B_1$ -field in the rotating frame of reference. Although this has no influence on the dipolar average Hamiltonian, it does correct for the inhomogeneity of the  $B_1$  field.

The effect of the  $\frac{\pi}{2}|_{x,\bar{x}}$ -pulses at the beginning and the end of continuous irradiation is to rotate the Hamiltonian back into the  $z$ -direction:

$$P_{x_{1,2}}\left(\frac{\pi}{2}\right)\mathcal{H}_D^{(yy)}P_{\bar{x}_{1,2}}\left(\frac{\pi}{2}\right)=\mathcal{H}_D^{(zz)} \quad (2.11)$$

By a similar argument, it can be shown that the chemical shift contribution  $\mathcal{H}_S$  vanishes under continuous rf irradiation. The average Hamiltonian over the entire cycle  $t_c$  can now be assembled:

$$\begin{aligned} \bar{\mathcal{H}} &= \frac{1}{t_c} \left( \tau \left( \mathcal{H}_S + \mathcal{H}_D^{(zz)} \right) - T \frac{1}{2} \mathcal{H}_D^{(zz)} + \tau \left( \mathcal{H}_S + \mathcal{H}_D^{(zz)} \right) \right) \\ &= \frac{2\tau}{2\tau + T} \mathcal{H}_S + \frac{2\tau - T/2}{2\tau + T} \mathcal{H}_D^{(zz)} \\ &= \frac{1}{3} \mathcal{H}_S \end{aligned} \quad (2.12)$$

when the condition

$$T = 4\tau \quad (2.13)$$

is satisfied.

To summarize: The sequence in Figure 2.1, under the conditions in Equation (2.9) and Equation (2.13), produces an effective Hamiltonian with the following properties:

- (i) as desired, the dipolar part of the Hamiltonian is eliminated:  $D_{ij} (3\mathbf{I}_{z_i}\mathbf{I}_{z_j} - \mathbf{I}_i \cdot \mathbf{I}_j) \longrightarrow 0$
- (ii) as a side effect, the chemical shift part of the Hamiltonian is scaled by a factor of 1/3:  $\omega_0\mathbf{I}_z \longrightarrow \frac{1}{3}\omega_0\mathbf{I}_z$

The average Hamiltonian only accurately describes the stroboscopic evolution of the density matrix, if the cycle time is much shorter than the time scale of the evolution under the dipolar coupling.

Under these conditions an echo is formed at  $t = t_c$ . Applying a second magic echo period at that time, produces a second echo at time  $t = 2t_c$ . In this fashion, the modified form of the Hamiltonian operator can be maintained over periods of many hundreds  $t_c$  with echoes appearing at  $t = nt_c$ . By recording the echo amplitude, the evolution of the spin system can be monitored *during the excitation*.

## 2.2 Scaling of the Chemical Shift under the Magic Echo Pulse Train

To demonstrate the feasibility of this approach and the predicted scaling of the chemical shift under the magic echo, the sequence was applied it to a sample of Trifluoroacetic acid. As described in the last section, a train of magic echo cycles

was used to modify the Hamiltonian and simultaneously monitor the state of the system. The pulse sequence shown in Figure 2.2 consists of an initial  $\pi/2$ -pulse, which brings the magnetization into the  $x$ -direction, followed by the magic echo train. In this form, the measurement comprises an observation of an FID of the magnetization under the modified Hamilton operator.

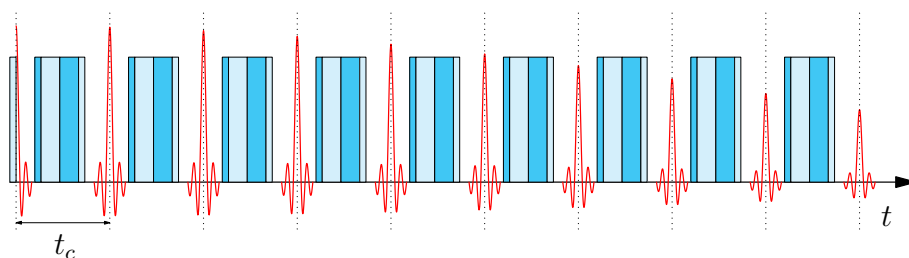


**Figure 2.2:** Magic echo pulse train used to demonstrate the scaling of the chemical shift part of the Hamilton operator. The data points were taken at the peak of the echos (shown in red) just before the following pulse sandwich.

The fluorinated methyl-group is attached to the molecule by a single carbon-carbon bond which allows fast and free rotation making all  $^{19}\text{F}$  nuclei magnetically equivalent. As a result, the high resolution liquid state  $^{19}\text{F}$ -NMR spectrum of this compound consists of a single sharp line.

Figure 2.3 shows on the left a comparison between the spectra under the two regimes: the native Hamiltonian of the molecule (green) and the average Hamiltonian created by the magic echo pulse train (red). To test the quantitative prediction of scaling by a factor of  $1/3$ , the native and scaled spectra were measured for a range of offsets of the resonance line with respect to the spectrometer frequency. Figure 2.3 shows on the right the plot of the two frequencies against

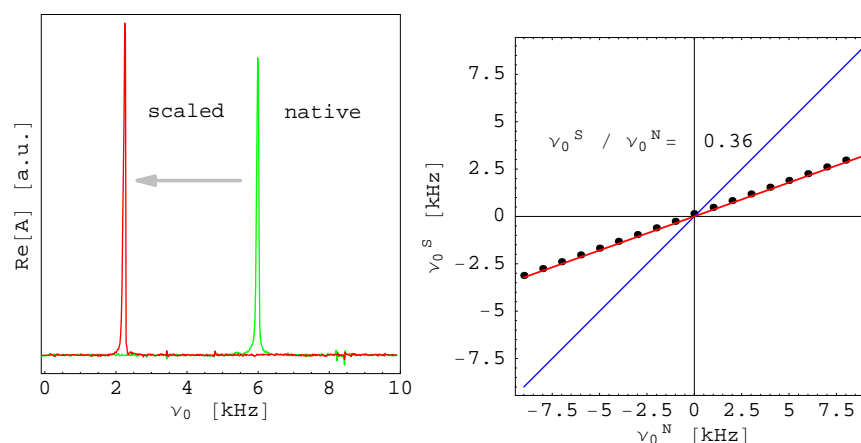


**Figure 2.3:** Scaling of the chemical shift part of the Hamiltonian under the magic echo pulse train. Left: FID-spectra of the Trifluoroacetic acid. Green: unmodified Hamiltonian. Red: average Hamiltonian produced by the magic echo pulse train. Right: Plot of scaled vs. native resonance frequency for different offsets with respect to the spectrometer frequency.  $B_0 = 7.8 \text{ T}$

each other. On the blue line, both frequencies would be equal. The red line represents a linear fit to the data points. The slope, which indicates the scaling factor of 0.36 is in good agreement with the predicted value of  $1/3$ .

## 2.3 Elimination of the Dipolar Coupling

The second prediction of the average Hamiltonian theory, namely the elimination of the dipole-dipole coupling was tested on *2,3-Difluoroaniline* embedded in a *liquid crystal matrix*. The liquid matrix used for this experiment was composed of the following three liquid crystals available from Merck KGaA:

- 33%wt S-1409 (Merck, BCH-52)
- 33%wt ZLI-1495 (Merck, D-501)
- 33%wt ZLI-1496 (Merck, D-302)

This mixture has been previously described as a host system suitable for alignment of small organic molecules for NMR [77]. Other liquid crystals have been used in early quantum computing experiments with NMR [20].

The chemical structure of 2,3-Difluoroaniline is shown in Figure 2.4. The spec-

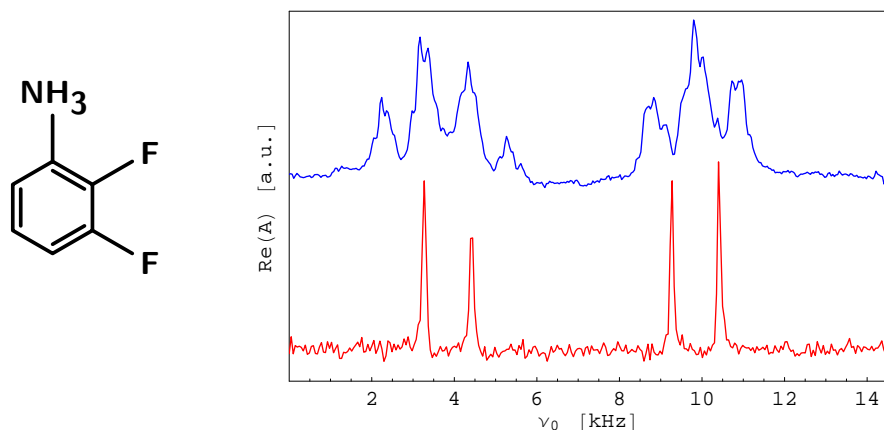


**Figure 2.4:** Left: Chemical structure of 2,3-Difluoroaniline. Right: Fluorine NMR-spectra of Difluoroaniline in a liquid crystal matrix. The blue plot shows the line splittings due to the interaction with the protons on the benzene ring. The red line shows the spectrum of the molecule with the protons decoupled through continuous irradiation. The splitting visible here is due to dipole-dipole coupling between fluorine nuclear spins of the partially aligned 2,3-Difluoroaniline molecules.  $B_0 = 7.8$  T,  $^1\text{H}$  Rabi frequency  $\approx 250$  kHz.

tra in this figure show the effect of the liquid crystal matrix upon the effective Hamiltonian of this system. In this situation, the free tumbling of the aniline molecule, which would otherwise average out all anisotropic interactions, is partially suppressed by the liquid crystal host. The dipole-dipole interaction of the  $^{19}\text{F}$ -nuclei with each other and with the protons on the benzene ring is therefore effective. This leads to multiple splittings of the two fluorine lines.



Heteronuclear interaction can be eliminated by strong continuous irradiation at the  $^1\text{H}$  resonance. This results in the proton decoupled spectrum shown in red in Figure 2.4. This spectrum reveals that the difference of the chemical shifts of the two fluorines is approximately 6 kHz. The line splitting shows that the dipole-dipole coupling is 1.8 kHz. This situation is well suited to demonstrate the effect of the magic echo sequence on the dipolar interaction.

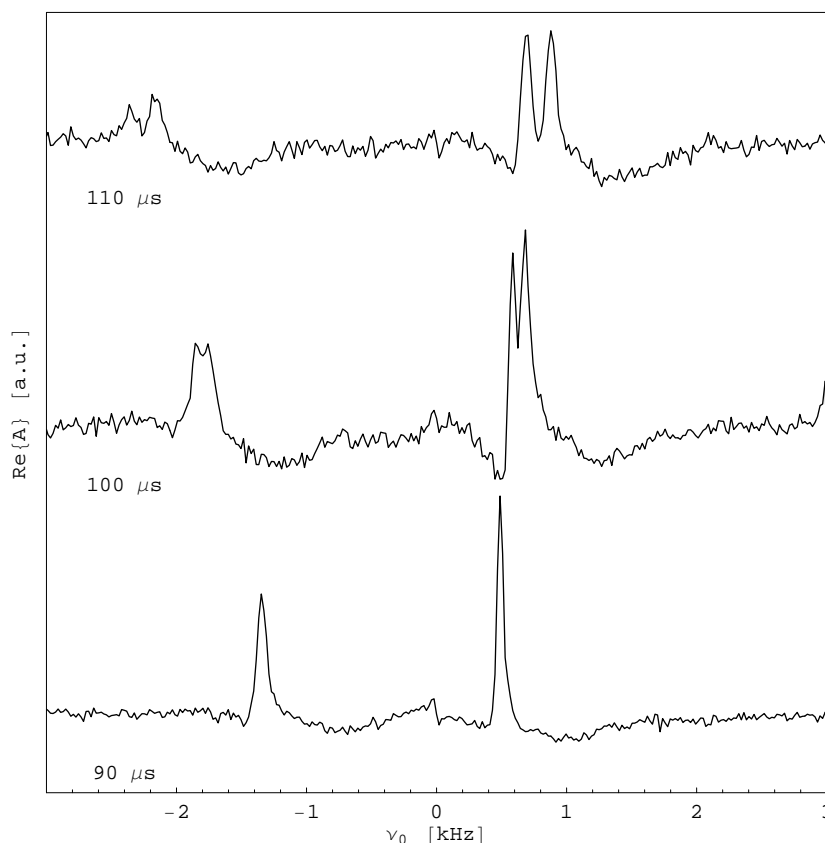


**Figure 2.5:** Suppression of the dipole-dipole coupling under the magic echo sequence. Spectra for three different cycle times  $t_c$  are shown, demonstrating the increasingly effective suppression. The strong baseline modulation is an experimental artifact.  $B_0 = 7.8 \text{ T}$ .

The sequence shown in Figure 2.2 and continuous proton decoupling were applied to the sample of Difluoroaniline in the liquid crystal matrix. Figure 2.5 shows the  $^{19}\text{F}$  FID spectra for three different cycle times of  $t_c = 110 \mu\text{s}$ ,  $100 \mu\text{s}$ , and  $90 \mu\text{s}$ . These spectra show the dependence of both the major features of the magic echo sequence on the cycle time  $t_c$ . The scaling of the chemical shift approaches the value of  $1/3$  expected for the limiting case of  $\tau \ll t_c$ . The most important finding is, that it was possible to achieve total suppression of the dipolar interaction between the two fluorene nuclei for  $t_c = 90 \mu\text{s}$  as seen in the bottom spectrum in Figure 2.5.

## 2.4 Selective Excitation under Continuous Averaging

As the previous sections have demonstrated, it is possible to tailor the Hamiltonian of a spin system by use of strong wide-band pulse trains. If such Hamiltonians are to be used for quantum computing, it must be possible to selectively address individual spins by means of soft pulses applied on top of the averaging sequence. To test the feasibility of such a procedure, we applied the sequence shown in Figure 2.6 to 2,3,4-Trifluoroaniline<sup>2</sup> in liquid state. It consists of a

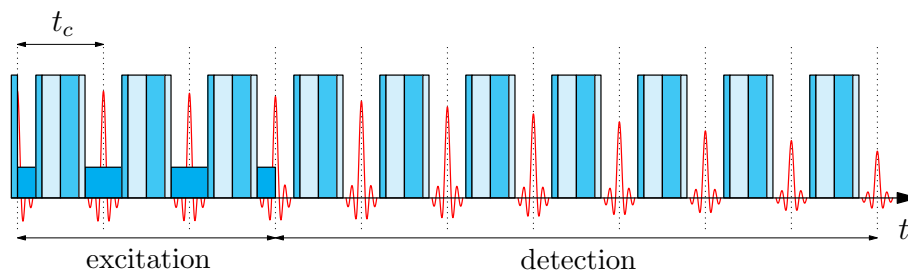


**Figure 2.6:** Pulse sequence for selective manipulation of a single spin under the action of the magic echo sequence. During the excitation phase, a soft selective rf pulse is applied in the windows of the magic echo block. In the detection phase, the sample response is sampled during the windows.

long train of magic echo cycles as described in Section 2.1. The first 80 cycles were used for the narrow-band selective excitation pulse. The Rabi frequency of the wide-band excitation channel was 67.6 kHz. A full Rabi rotation took  $14.8 \mu\text{s}$  and a  $\frac{\pi}{2}$ -pulse  $3.7 \mu\text{s}$ . Accordingly, the time unit was set to  $\tau = 7.4 \mu\text{s}$  and the full duration of the magic block (including the  $\frac{\pi}{2}$ -pulses) was  $37 \mu\text{s}$  resulting in a cycle time of  $t_c = 51.8 \mu\text{s}$ . The soft excitation pulse was applied in the windows during the excitation phase which spanned 4.144 ms.

The construction of the soft pulse deserves special attention. The individual qubit-spins have different resonance offsets  $\omega_{0j}$  with respect to the spectrometer frequency. This allows their selective excitation. As a sideeffect, due to the evolution under these offsets during the long quantum computing pulse sequences, different spins acquire appreciable phases. This accumulated phase must be taken into account, when applying pulses with specified phases to given spins. For instance, when two  $x$ -pulses are to be applied to the spin  $j$  at a distance  $\Delta t$  from each other, then the phase of the rf must be corrected by  $\Delta\varphi = -\omega_{0j}\Delta t$  for the first pulse. In general, a transformation into a rotating frame is used for each spin, such that at the beginning of observation rotating frames of all spins coincide. In the experiment described here, the evolution of spins under the resonance offset is suspended for the duration of the magic echo sandwich. Thus, the phase accumulated by a spin differs significantly from that acquired in the usual case. This is a crucial detail, since the omission of the phase correction results in a failure of the experiment.

The detection phase consisted of 512 magic echo cycles. The rotation angle of the soft excitation pulse was adjusted by varying the attenuation in the soft

<sup>2</sup>For more details on this molecule, see Chapter 1

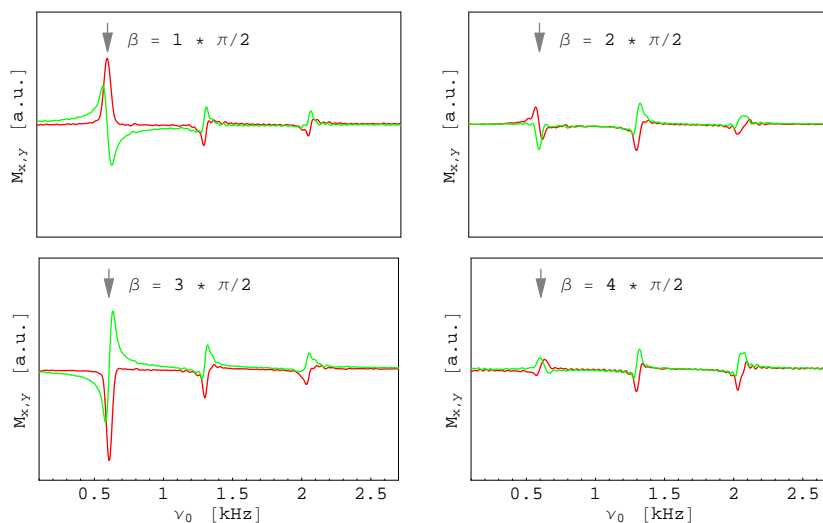


**Figure 2.7:** Selective excitation of a single spin under continuous action of the magic echo sequence. The plots show the x- (red) and y-component (green) of the NMR signal. The soft rotation pulse was applied at the frequency of the leftmost spin. The rotation angle of the pulse was adjusted by varying the pulse amplitude to be approximately multiple of  $90^\circ$ :  $\beta = n \times \pi/2$ ,  $n = 1, 2, 3, 4$ .

excitation channel until the rotation angle of  $\beta = \pi/2$  was found. Consecutively the attenuation was reduced in steps of 3 dB resulting in the doubling of the rf-field amplitude  $B_1$  with each step. Thus, rotation angles  $\beta = n \times \pi/2$  with  $n = 1, 2, 3, 4$  were expected. The corresponding spectra (for both the  $x$ - and the  $y$ -channel) are shown in Figure 2.7. The expected behavior is clearly visible for the spin  $\mathbf{I}_2$ .

These measurements demonstrate the feasibility of the original idea. However, for these overview measurements, no particular effort was made to carefully adjust the settings for optimal performance. This manifests itself especially in the strong cross-excitation of the other spins. With some additional effort, the amount of cross-excitation can be reduced significantly. Figure 2.8 shows as an example a selective  $\pi/2$ -pulse applied to spin  $\mathbf{I}_2$  under the continuous magic echo averaging after careful adjustment of timings and amplitudes. The plot represents the magnitude of the magnetization signal. This representation allows the comparison of the amplitude of the spectral lines without regard to the possible phase errors arising from a long “dead time” at the beginning of the transients.

Thus, it is shown that it is possible to tailor the Hamiltonian of a spin system through application of wide-band multi-pulse sequences and treat the resulting average Hamiltonian the same way as the native Hamiltonians. In particular, it is possible to apply soft shaped pulses on top of the averaging sequences in order to selectively address single spins.

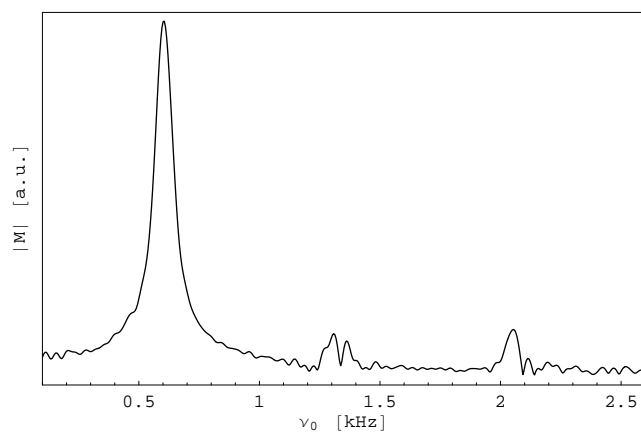


**Figure 2.8:** FID under magic echo averaging after selective  $\pi/2$  pulse on  $I_2$  (leftmost line) under continuous magic echo averaging in 2,3,4-Trifluoroaniline. Modulus of the magnetization is plotted to suppress the artefact of time-proportional phase shift.  $B_0 = 7.8$  T.

## Chapter 3

# Visualization of Unitary Transformations

Design of pulse sequences is a major part of implementing quantum computing by means of magnetic resonance. Such pulse sequences are subject to a number of partially competing constraints. Some of which are well known from traditional uses of magnetic resonance others become more important in the case of spin quantum computing.

A large variety of pulse sequences have been invented in the field over the decades to achieve an equally large variety of goals. They feature acronym names like INEPT, INADEQUATE, BURP and RE-BURP, WAHUHA and even HOHAHA.<sup>1</sup> Just the number of ways to invert the population of a particular spin – an operation commonly known as a  $\pi$ -rotation – is impressive [78–82]. Many of these methods however are targeted at preparing a desired state of the spin system; such as inverting the  $z$ -component of a particular spin species ( $\pi$ -pulse) or rotating the  $z$ -magnetization into the  $xy$ -plane ( $\pi/2$ -pulse). In many situations, what happens to the other spin operator components is usually not important. One might call such operations “point-to-point” transformations.

In spin quantum computing, the freedom of choice is much more constrained since the goal lies not so much in preparing particular states of the quantum system but in the production of a particular *unitary operation* which works regardless of the input spin state.

A good example is the implementation of *selective pulses* in liquid state NMR under the conditions of spectral crowding in homonuclear spin systems. Quantum algorithms call for well defined single qubit operations. Since the separation of the spectral lines is sometimes just a few ppm, very long and thus spectrally narrow pulses are commonly used. The spectral width of such pulses is however limited because pulses must be short on the time scale of evolution under the interactions coupling the spins. Which in turn must be fast on the time scale of decoherence and relaxation.

Under most circumstances it is therefore desirable to shorten the pulses as much as possible. At the same time, influence on the spectrally neighboring spins must

---

<sup>1</sup>For a list of NMR acronyms, see for instance <http://www.bmrb.wisc.edu/education/nmr.acronym.php>.

be suppressed. Clearly, this can only be achieved by varying the transformation's parameters as it proceeds. Although constrained numeric optimization can sometimes be used to obtain pulses that produce a desired transformation [83, 84], it is still necessary to understand pulse sequences constructed analytically.

Reasoning about the possible variations is, however, made difficult by the problem of imagining the temporal evolution of *transformations*. Evolution of spins is commonly visualized using the analogy between the components of the spin operator with the components of a vector in real space, which is utilized in the Bloch sphere construction. At least for evolution of single spins- $\frac{1}{2}$  particles, it is possible to visualize the unitary transformations themselves using a similar technique.

## 3.1 Representing Single-Spin Unitary Transformations in $\mathbb{R}^3$

### 3.1.1 Vector Representation of Unitary Transformations

Unitary transformations applied to spins are very closely related to rotations in ordinary space. This is most easily seen, when the density matrix of the spin and the unitary transformations applied to it are both written in the spin component basis.

Suppose that the spin state is represented by the pure state density matrix

$$\rho_0 = \frac{1}{2} \mathbf{I}_0 + \mathbf{I}_z = \begin{pmatrix} 1 & 0 \\ 0 & 0 \end{pmatrix} \quad (3.1)$$

classically corresponding to the spin pointing in  $z$ -direction. A unitary operation describing continuous irradiation along the  $y$ -direction in the rotating frame of reference is given by

$$U = \exp(-i\beta \mathbf{I}_y) = \mathbf{I}_0 \cos \frac{\beta}{2} - 2i \sin \frac{\beta}{2} \mathbf{I}_y = \begin{pmatrix} \cos \frac{\beta}{2} & -\sin \frac{\beta}{2} \\ \sin \frac{\beta}{2} & \cos \frac{\beta}{2} \end{pmatrix} \quad (3.2)$$

with  $\beta = \hbar\omega t$ .

Applying this transformation to the density matrix in Equation (3.1) yields the new density matrix

$$\rho(\beta) = U \rho_0 U^\dagger = \begin{pmatrix} \cos^2 \frac{\beta}{2} & \cos \frac{\beta}{2} \sin \frac{\beta}{2} \\ \cos \frac{\beta}{2} \sin \frac{\beta}{2} & \sin^2 \frac{\beta}{2} \end{pmatrix} = \frac{1}{2} \mathbf{I}_0 + \cos \beta \mathbf{I}_z + \sin \beta \mathbf{I}_x \quad (3.3)$$

This is readily interpreted as a rotation of magnetization around the  $y$ -axis which is the direction of the oscillating magnetic field, as seen in the term containing  $\mathbf{I}_y$  in Equation (3.2). The rotation angle is given by  $\beta$ .

This observation can be generalized as follows. A density matrix of a spin- $\frac{1}{2}$  may be represented in the basis of the spin operator components ( $\{\mathbf{I}_0, \mathbf{I}_x, \mathbf{I}_y, \mathbf{I}_z\}$ ) according to

$$\rho = s_1 \mathbf{I}_0 + s_x \mathbf{I}_x + s_y \mathbf{I}_y + s_z \mathbf{I}_z \quad (3.4)$$

with real coefficients  $s_j$ . Because of the normalization requirement  $\text{tr}(\rho^2) = 1$ , three real numbers are sufficient to fully describe  $\rho$ . Thus, one can define the 3-vector  $\mathbf{s} = (s_x, s_y, s_z)$  which describes the orientation of the spin in real space. Analogously, a given unitary transformation  $\mathbf{U}$  may be written as

$$\mathbf{U} = u_1 \mathbf{I}_0 - 2i(u_x \mathbf{I}_x + u_y \mathbf{I}_y + u_z \mathbf{I}_z) \quad (3.5)$$

with real coefficients  $u_j$  and the unitarity requirement

$$\mathbf{U} \mathbf{U}^\dagger = \mathbf{I}_0 \quad (3.6)$$

satisfied when

$$u_1^2 + u_x^2 + u_y^2 + u_z^2 = 1 \quad (3.7)$$

Again, this representation defines a 3-vector,  $\mathbf{u} = (u_x, u_y, u_z)$ . It can be shown that applying the transformation  $\mathbf{U}$  to the density matrix  $\rho$  corresponds to the rotation of the vector  $\mathbf{s}$  around the axis defined by the direction of  $\mathbf{u}$ . The magnitude of  $\mathbf{u}$  defines the rotation angle  $\beta = 2 \arcsin |\mathbf{u}|$  and the sign of the scalar component  $u_1$  determines the sense of rotation.

This construction provides the ingredients necessary for the visualization of unitary transformations by vectors in ordinary space. Such visualization is obtained by plotting the vector  $\mathbf{s}$  to represent the density matrix. Because of the normalization condition these vectors have unit length and end on the surface of the unit sphere.

The actual unitary transformations are represented by the vector  $\mathbf{u}$  with the sense of rotation given by the color used. As an example, Figure 3.1 demonstrates the situation described above for the case of the rotation angle  $\beta = \pi$ . The propagator (Equation (3.2)) extends from the origin in the direction of

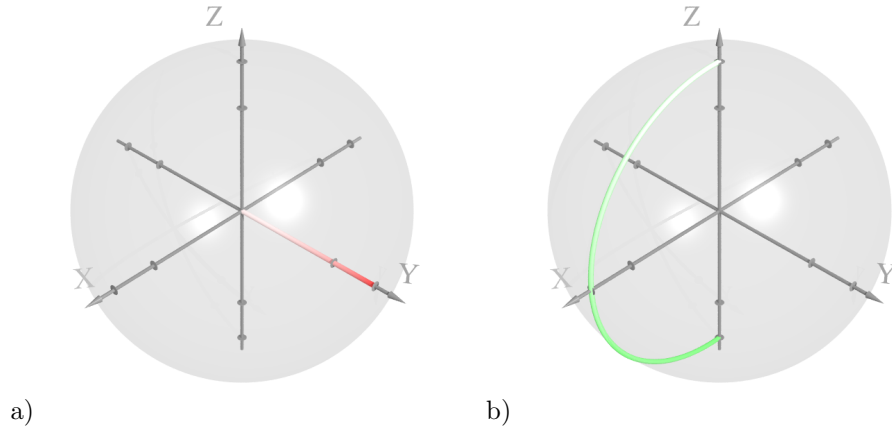


**Figure 3.1:** Representation of the propagator for a  $\pi$ -pulse applied in  $y$ -direction. a) The red line along the  $y$ -axis represents the propagator. b) The green trace represents the trajectory of the spin under the action of the propagator starting from the  $z$ -direction. Axes' ticks mark rotation angles of  $\pi/2$  and  $\pi$ .

the  $y$ -axis. The trajectory of the spin, which is initially oriented along the  $z$ -direction (Equation (3.1)), is a semicircle around the direction of the propagator (Equation (3.3)).

Simple pulses with constant frequency, amplitude, and phase always produce straight trajectories in the  $xy$ -plane when considered in isolation. The more interesting question is: What happens when, for example, a pulse in  $y$ -direction is followed by a pulse in  $x$ -direction?

### 3.1.2 Rules for Successive Transformations

To obtain a rule for successive application of transformations, consider two propagators  $\mathbf{U}$  and  $\mathbf{V}$  parameterized according to Equation (3.5):

$$\mathbf{U} = u_1 \mathbf{I}_0 - 2i(u_x \mathbf{I}_x + u_y \mathbf{I}_y + u_z \mathbf{I}_z) \quad (3.8)$$

$$\mathbf{V} = v_1 \mathbf{I}_0 - 2i(v_x \mathbf{I}_x + v_y \mathbf{I}_y + v_z \mathbf{I}_z) \quad (3.9)$$

The vectors representing these transformations in  $\mathbb{R}^3$  are given by

$$\mathbf{u} = \begin{pmatrix} u_x \\ u_y \\ u_z \end{pmatrix}, \quad \mathbf{v} = \begin{pmatrix} v_x \\ v_y \\ v_z \end{pmatrix} \quad (3.10)$$

The product transformation  $\mathbf{W}$  in terms of operator components is then

$$\begin{aligned} \mathbf{W} = \mathbf{V}\mathbf{U} = & (v_1 u_1 - v_x u_x - v_y u_y - v_z u_z) \mathbf{I}_0 \\ & - 2i(v_1 u_x + v_x u_1 + v_y u_z - v_z u_y) \mathbf{I}_x \\ & - 2i(v_1 u_y + v_y u_1 + v_z u_x - v_x u_z) \mathbf{I}_y \\ & - 2i(v_1 u_z + v_z u_1 + v_y u_x - v_y u_x) \mathbf{I}_z \end{aligned} \quad (3.11)$$

The scalar and vector parts of this composite propagator are thus found to be

$$w_1 = u_1 v_1 - (u_x v_x + u_y v_y + u_z v_z) \quad (3.12a)$$

$$\mathbf{w} = \begin{pmatrix} v_1 u_x + v_x u_1 + v_y u_z - v_z u_y \\ v_1 u_y + v_y u_1 + v_z u_x - v_x u_z \\ v_1 u_z + v_z u_1 + v_y u_x - v_y u_x \end{pmatrix} = v_1 \mathbf{u} + u_1 \mathbf{v} + \mathbf{v} \times \mathbf{u}. \quad (3.12b)$$

This rule produces the transformation arising from the combination of any two constant propagators.<sup>2</sup>

In order to visualize the trajectory of a propagator with a complicated continuous time dependence, the duration of the transformation  $T$  may be split into time slices such that the propagator can be approximated by a constant value during each time slice. The total transformation can then be represented by

$$\mathbf{U}(T) = \mathbf{U}_N \mathbf{U}_{N-1} \dots \mathbf{U}_j \dots \mathbf{U}_1 \mathbf{U}_0 \quad (3.13)$$

where  $\mathbf{U}_j$  is the propagator describing the evolution of the spin during  $j$ -th time slice. With such segmentation, it is possible to numerically obtain the trajectories of constant and varying pulses for visual representation.

The formula in Equation (3.12) implies some interesting properties of concatenation of propagators in special cases:

<sup>2</sup>Notice, that Equation (3.12) closely resembles multiplication rules for mathematical objects called *quaternions*. In fact, quaternions are used in several branches of physics instead of Euler angles to describe rotations. The corresponding formalism has also been used in the context of magnetic resonance [85–87].



- $\text{tr}(\mathbf{U}) \approx 1$

This is the region of weak initial propagators deep within the Bloch sphere around the coordinate origin, where

$$\mathbf{U} \approx \mathbf{1}, \quad u_1 \approx 1, \quad \mathbf{u} \approx \mathbf{0} \quad \Longrightarrow \quad \mathbf{w} \approx \mathbf{v}$$

When the initial propagator is weak, the vector  $\mathbf{v}$  immediately produces the total transformation.

- $\text{tr}(\mathbf{U}) \approx 0$

Edge of the Bloch sphere, region of strong initial propagators. Here,

$$u_1 \approx 0 \quad \Longrightarrow \quad \mathbf{w} \approx v_1 \mathbf{u} + \mathbf{v} \times \mathbf{u}. \quad (3.14)$$

The step in  $\mathbb{R}^3$  produced by  $\mathbf{V}$  goes at right angles to  $\mathbf{v}$ . Notice, that for strong  $\mathbf{V}$  the scalar part  $v_1$  may be negative, such that  $\mathbf{w}$  may partially or entirely counter-oriented to  $\mathbf{u}$ .

- Because magnetic resonance spectrometers do not allow rf pulses outside of the  $xy$ -plane (i.e.,  $\mathbf{u}, \mathbf{v} \perp \hat{z}$  is always true), it is not possible to move along the *equator of the Bloch sphere* by means of constant (i.e., constant phase, amplitude, and frequency) pulses; the propagator inevitably escapes in  $z$ -direction.
- For the same reason, *on the surface of the Bloch sphere*, constant propagators can only move along the meridians.
- Because of the term  $\mathbf{v} \times \mathbf{u}$ , when *within the equatorial plane*, it is only possible to move along a straight line, if  $\mathbf{v} \parallel \mathbf{u}$  (i.e., along a radial direction).
- Again, because of  $\mathbf{v} \perp \mathbf{z}$  and  $\mathbf{v} \times \mathbf{u}$ , no continuous motion at all is possible *within the equatorial plane* with constant pulses. It is merely possible to make “jumps” starting and ending in the  $xy$ -plane with limited minimum jump distance.

## 3.2 Examples of Visual Pulse Sequence Analysis

In order to demonstrate the utility of the visualization technique described above, two example pulse sequences are analysed in some detail here.

### 3.2.1 Composite $\pi$ -Pulse

To achieve a  $\pi$ -rotation of spins in a sample, an rf pulse of duration  $T = 1/2\nu_1$  is applied, where  $\nu_1 = \gamma B_1/2\pi$  is the Rabi nutation frequency under the rf field with amplitude  $B_1$ . A very typical experimental complication in magnetic resonance lies in the fact that the driving rf field  $B_1$  is inhomogeneous across the extent of the sample. As a result, the Rabi frequency is different for different parts of the spin ensemble. Thus, spins with lower and higher Rabi frequencies than the average experience rotation angles below and above  $\pi$  respectively.

One of the frequently used pulse sequences designed to alleviate the effects of rf inhomogeneity is the *composite  $\pi$ -pulse* [78]. It consists of a  $\pi$ -pulse in  $y$ -direction sandwiched between two  $\pi/2$ -pulses in  $x$ -direction as shown in Figure 3.2. For a resonant spin, the net effect of this pulse is readily calculated:

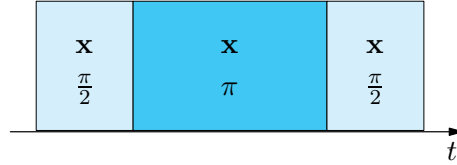


**Figure 3.2:** Composite  $\pi$ -pulse for compensation of  $B_1$  inhomogeneity.

$$U = \exp\left(-i\frac{\pi}{2}\mathbf{I}_x\right) \exp(-i\pi\mathbf{I}_y) \exp\left(-i\frac{\pi}{2}\mathbf{I}_x\right) = -2i\mathbf{I}_y = \exp(-i\pi\mathbf{I}_y) = P_y(\pi) \quad (3.15)$$

Therefore, the composite pulse does indeed produce a transformation equivalent to a single  $\pi$ -pulse in  $y$ -direction. The trajectory of the unitary transformation differs, however, significantly for the two pulses as shown in Figure 3.3. The simple  $\pi$ -pulse corresponds to a straight line extending in the direction of the  $y$ -axis up to the distance  $\pi$ .

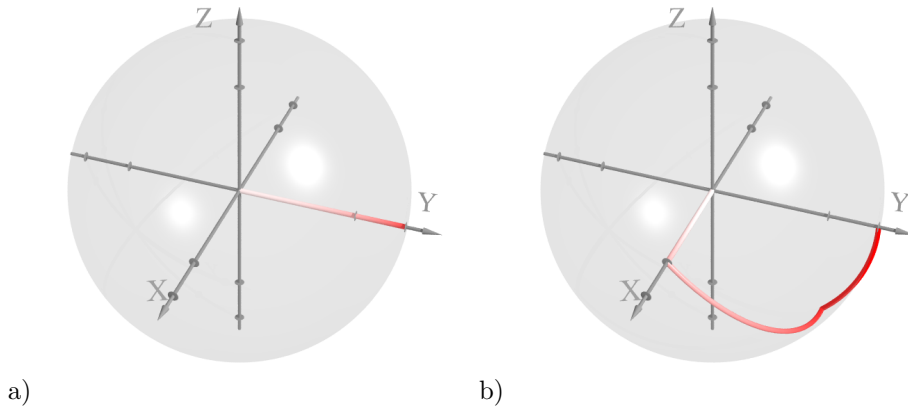


**Figure 3.3:** Trajectories of the unitary transformations for simple (a) and composite (b)  $\pi$ -pulses.

The trajectory of the composite pulse shows the three constituent constant pulses. The fact that trajectories of both pulses end at the same point shows again that the *net transformation* of a *resonant* spin is identical for both types of pulses. The difference in the trajectories, however, has strong effects on the trajectories taken by the spin operator components. Figure 3.4 juxtaposes the paths taken by the different spin components under the two kinds of pulses.

The question is now: How do the two pulses differ in their effect on spins with mismatched Rabi frequencies? To answer this question, the propagator trajectories for both types of pulses have been calculated for a range of Rabi

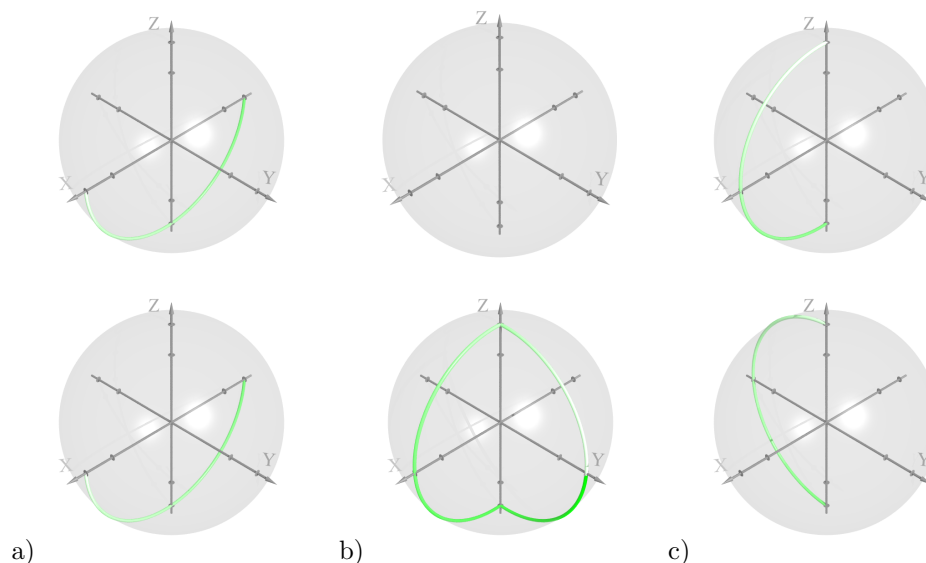


**Figure 3.4:** Comparison of the trajectories taken by  $\mathbf{I}_x$ ,  $\mathbf{I}_y$ , and  $\mathbf{I}_z$  (a, b, and c respectively) under the action of a simple (top row) and a composite (bottom row)  $\pi$ -pulses.

frequencies between 0.7 and 1.3 of the matching value. To make the results more clear, Figure 3.5 a) and b) shows the trajectories taken by  $\mathbf{I}_z$  for mismatches between 1 and 1.3. In the case of the simple pulse the endpoints are situated in the  $zx$ -plane beyond the  $-z$ -direction. For the composite pulse, the endpoints are situated close to the  $zx$ -plane but on the opposite side of the  $-z$ -direction and are less spread out. Figure 3.5 c-e) contains only the endpoints resulting when the spin is initially aligned along  $\mathbf{I}_x$ ,  $\mathbf{I}_y$ , and  $\mathbf{I}_z$ . Here, the entire mismatch range 0.7 – 1.3 is shown.

Figure 3.5 f) shows the *net transformations* for the two pulses. For the simple pulse, the Rabi frequency mismatch spreads the total transformations along the  $y$ -direction halfway between  $\pi/2$  and  $\pi$ , while the axis of rotation remains the same. For the composite pulse, the inverse holds: The amplitude (i.e., the rotation angle) is close to  $\pi$  even for relatively large values of mismatch, while the rotation axis deviates significantly from the  $y$ -axis.

This visual representation, immediately demonstrates the important properties of the two pulses. Due to the spread of rotation angles, the simple pulse shows poor performance with respect to the  $x$ - and  $z$ -component of the spin, while the  $y$ -component is not affected at all by the transformation. The spread of its rotation axes, causes the composite pulse to produce similarly weak results for the  $x$ - and  $y$ -oriented spin components. However, because – independently of the Rabi mismatch – the rotation axis of the composite pulse remains very close to the  $xy$ -plane and the rotation angle close to  $\pi$ , its ability to accurately invert the  $z$ -component of the spin is significantly better than that of the simple pulse.

This analysis shows that the composite pulse described in this section is well suited for the task of inverting  $\mathbf{I}_z$  under large  $B_1$  inhomogeneity. It's usefulness as a universal unitary transformation, however, is limited.

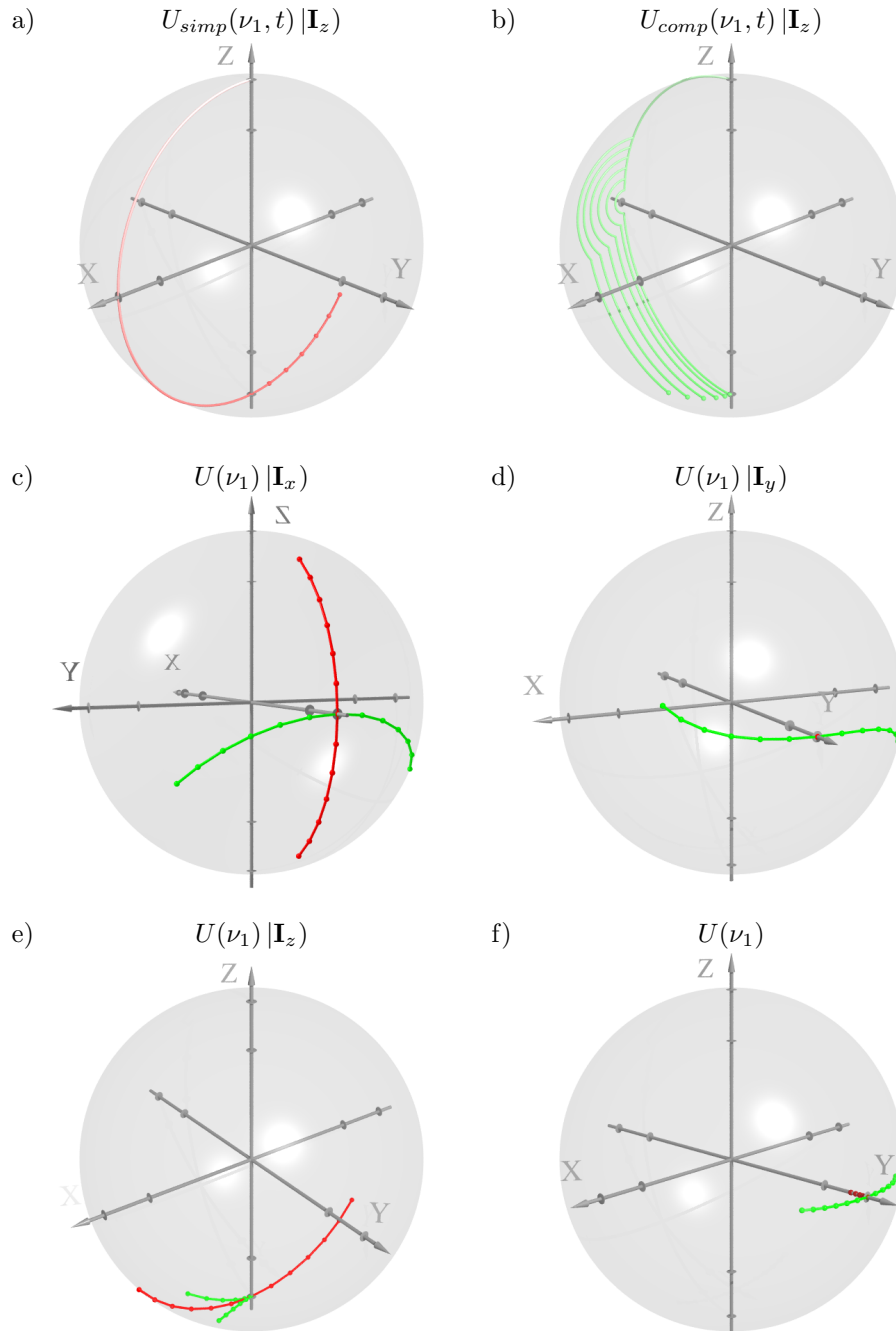


**Figure 3.5:** Dependence of the total transformation on the mismatch of the Rabi frequency for a simple and a composite  $\pi|_y$ -pulse. Red and green indicate data for the simple and the composite pulse respectively. a,b) Trajectories taken by the spin starting at  $I_z$  for a range of Rabi frequency offsets of  $1.05 - 1.3 \nu_1$ . c-e) Endpoints of the evolution of the spin components  $I_x$ ,  $I_y$ , and  $I_z$  for Rabi frequency offsets of  $0.7 - 1.3 \nu_1$ . f) Total unitary transformations.

### 3.2.2 Continuously Shaped Pulses

Various rf pulses are the building blocks of pulse sequences used to implement quantum computing with spins. Even under perfect experimental conditions – such as sufficiently narrow spectral lines, perfectly shaped pulses, etc. – some intrinsic properties of spin systems present substantial difficulties. A typical problem is *cross-excitation*.

Quantum algorithms usually call for well defined one-qubit operations. When several spins of the spin system occupy a narrow spectral region (such as, for instance, in Trifluoroaniline described in Chapter 1), pulses applied to one particular spin can have significant effect on spectrally neighboring spins, thus, causing errors in the algorithm.

In real experiments, the spectral lines being addressed possess finite widths determined by the inhomogeneity of the static field  $B_0$ . This poses another problem, as the excitation properties of pulses typically vary across the linewidth. Such non-uniform excitation is another source of errors. The ideal pulse would produce a perfectly uniform response in a narrow region surrounding the spectral line, while presenting an identity transformation to spins outside of this range.

More demonstratively, these problems are best discussed when considering the usual case of constant rectangular pulses and the alternative *shaped* pulses [88].

#### 3.2.2.1 Constant Rectangular $\frac{\pi}{2}|y\rangle$ -Pulse

To make the discussion more concrete, typical parameters used in our liquid state NMR experiments (see Chapter 1) are used in the following.

The diagram on the upper left in Figure 3.6 shows a constant rectangular rf pulse of 2 ms length. A spin whose Larmor frequency coincides with the rf frequency of the pulse will be rotated by  $\pi/2$  if the amplitude of the rf is such that the Rabi-frequency is, as indicated,  $\nu_1 = 125$  Hz. The phase of the rf is chosen such that its magnetic field vector points in the  $y$ -direction in the rotating frame of reference.

What is now the total transformation experienced by a spin whose Larmor frequency is separated by an offset  $\Delta\nu_0$  from the resonance frequency of the targeted spin? The total transformation effected by the pulse is plotted against  $\Delta\nu_0$  on the upper right in Figure 3.6 for  $0 < \Delta\nu_0 < 1$  kHz =  $8\nu_R$ . This plot is generated by keeping the spin at resonance and moving the excitation frequency by  $-\Delta\nu_0$ . The opposite procedure – namely keeping the excitation constant and moving the test spin – would complicate the results by the presence of the residual precession component.

At  $\Delta\nu_0 = 0$ , the transformation corresponds to a perfect  $\pi/2$ -rotation around the  $y$ -axis, as intended for the resonant spin. As the offset increases, the magnitude of the propagator diminishes and its direction rotates out of the  $xy$ -plane and quickly spirals towards the unity propagator at the coordinate origin. At offsets of a few  $\nu_1$ , the propagator deviates dramatically in magnitude and direction from the intended value. This means that constant rectangular pulses produce propagators of sufficient fidelity only in the region of  $|\Delta\nu_0| < \nu_1/2$ .

The effect for a wide range of offsets is shown in the plot at the bottom of

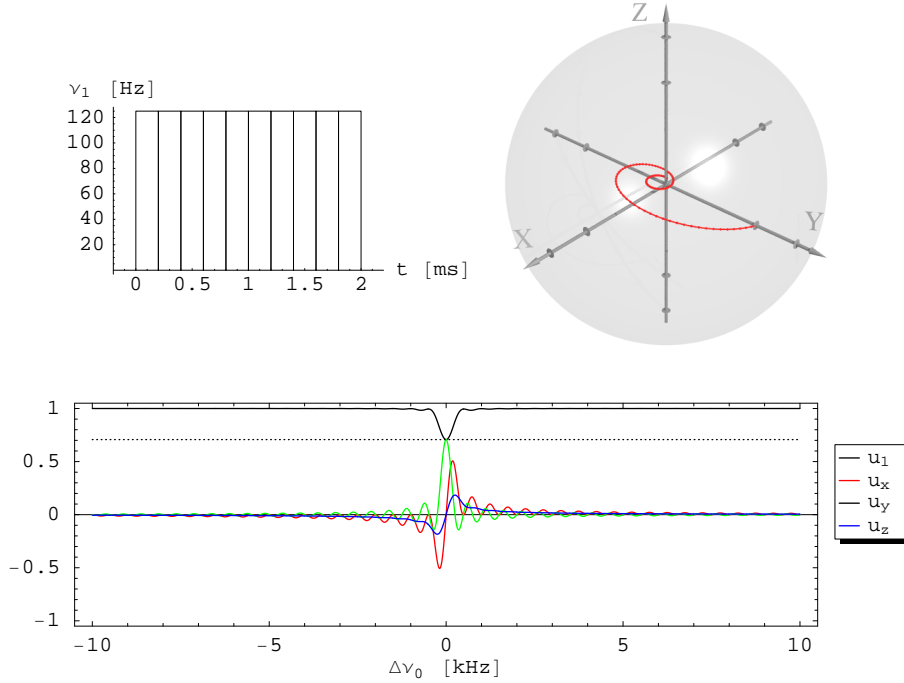


**Figure 3.6:** Selectivity of a rectangular  $\frac{\pi}{2}_y$ -pulse. Upper left: Envelope of the rf applied. Upper right: Ending points of the total transformation effected by the pulse, for resonance frequency offsets between 0 kHz and 1 kHz. Bottom: Dependence of the total propagator on the frequency offset plotted for each component as defined by Equation (3.5). The dashed line indicates the amplitude of  $u_1 = 1/\sqrt{2}$  corresponding to a rotation angle of  $\pi/2$ . The high frequency rf components produce appreciable excitation even for very large ( $\Delta\nu_0 > 20\nu_1$ ) resonance frequency offsets. The region of uniform excitation is narrowly confined around the resonance.

Figure 3.6. The value of  $u_1$  determines the total rotation angle  $\beta$  according to  $\beta = 2 \arccos u_1$ . The plot shows that the rotation angle falls off quickly with increasing offset magnitude resulting in a narrow uniform excitation region. However, even at  $|\Delta\nu_0| > 10\nu_1$  there is a non-negligible effect, mainly in form of a  $z$ -rotation. This phenomenon is a result of *Bloch-Siegert shift* [89].

The spectrum of  $u_y$  (the component parallel to the intended rotation axis) closely resembles the Fourier transform of a symmetric square function around the origin. An often used explanation for the shortcomings of constant square pulses states that high-frequency components arising from the sharp edges of the envelope are responsible for the undesirable excitation of remote spins.<sup>3</sup> The amount of cross-excitation can be reduced by artificially lengthening the pulse and reducing its Rabi frequency to achieve a narrower spectrum. The length of such *soft* pulses is, however, limited by both the requirement of uniform excitation across spectral lines and by the relaxation and interaction time scales.

<sup>3</sup>The spectral view of the cross-excitation problem ignores the fact that rotations do not generally commute. This has important implications as will be shown below.

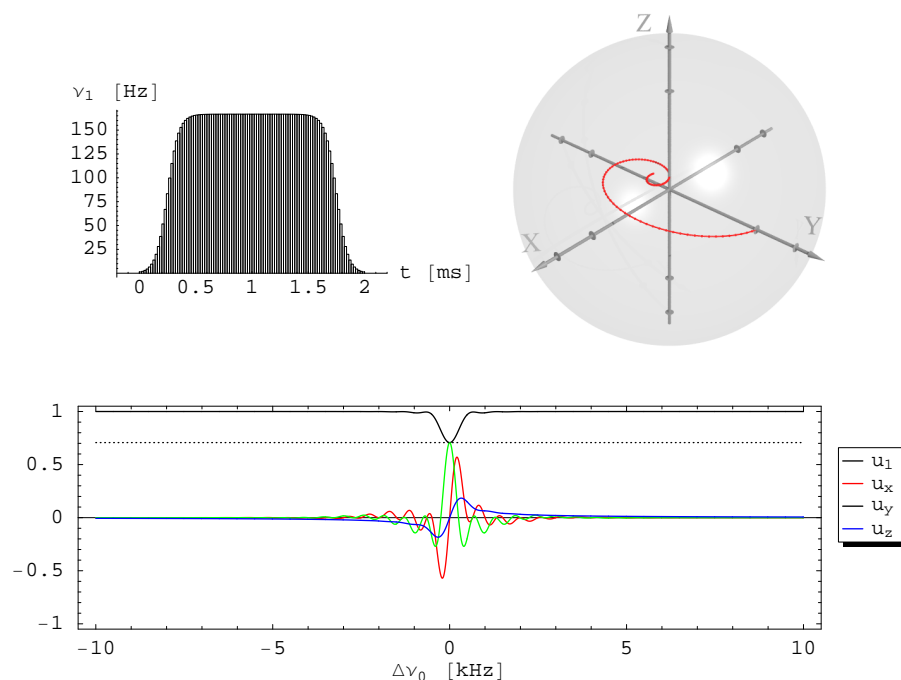


**Figure 3.7:** Selectivity of a  $\frac{\pi}{2}_y$ -pulse with a Fermi-like envelope. Upper left: Rf envelope. Vertical lines show the sampling of the pulse used for simulation. Upper right: Ending points of the total transformation for frequency offsets  $0 \text{ kHz} \leq \Delta\nu_0 \leq 1 \text{ kHz}$ . Bottom: Dependence of propagator components on the frequency offset. Cross-excitation at large offsets is reduced compared to the rectangular pulse, the uniform excitation region is comparable. For more details see Figure 3.6.

### 3.2.2.2 $\frac{\pi}{2}_y$ -Pulse with Fermi-like Envelope

To eliminate the high frequency components, the rectangular envelope can be slightly modified by making the rf amplitude vary more gradually. This is achieved by giving the pulse an envelope based on the Fermi-function:

$$\nu_1(t) = \nu_{1_0} \frac{1}{1 + \exp\left(\frac{|t-t_0|-t_\mu}{t_T}\right)} \quad (3.16)$$

where  $t_0$  is the center of the pulse, and  $t_\mu$  and  $t_T$  control the pulse length and the width of the edges respectively. This type of envelope with  $t_\mu = 750 \mu\text{s}$  and  $t_T = 50 \mu\text{s}$  is shown on the upper left in Figure 3.7. Since the total pulse length is kept the same, a slight increase in Rabi frequency is required to obtain a  $\pi/2$  rotation on resonance.

Again the plot of the trajectory shown on the upper right and of the propagator components at the bottom demonstrates the result most clearly. In the vicinity of the resonance, the behavior resembles closely that of the rectangular pulse. At offsets of  $|\Delta\nu_0| > 2 \text{ kHz} \approx 13\nu_1$ , the difference becomes apparent in the much faster falloff of the propagator amplitude. This envelope was used in the sequences presented in Chapter 1.

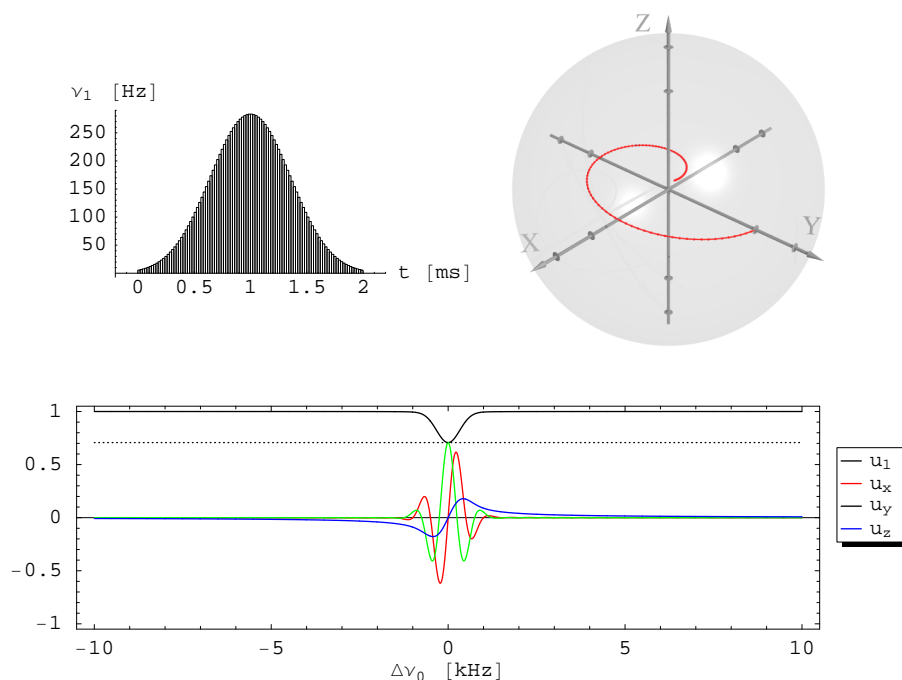


**Figure 3.8:** Selectivity of a  $\frac{\pi}{2}_y$ -pulse with a Gaussian envelope. Upper left: Rf envelope. Upper right: Ending points of the total transformation for frequency offsets  $0 \text{ kHz} \leq \Delta\nu_0 \leq 1 \text{ kHz}$ . Bottom: Dependence of propagator components on the frequency offset. See also Figure 3.6.

### 3.2.2.3 $\frac{\pi}{2}_y$ -Pulse with Gaussian Envelope

Taken to its logical conclusion, the spectral argument leads to an envelope defined by the Gaussian function:

$$\nu_1(t) = \nu_{1_0} \exp \left\{ - \left( \frac{t - t_0}{t_\sigma} \right)^2 \right\} \quad (3.17)$$

where  $t_0$  is, as above, the center of the pulse, and  $t_\sigma$  determines the pulse width. This is the only function which retains its shape under Fourier transform. Again the slow onset is compensated by increased Rabi frequency.

Simulation results for this type of pulse are presented in Figure 3.8. Indeed, the cross-excitation is suppressed even more effectively than with the Fermi-shaped pulse. The performance in the narrow neighborhood of the resonance is slightly better, because the Gaussian function has a flatter top than the Fourier spectrum of the rectangular envelope.

This pulse shape, however, suffers from a problem which hasn't yet been mentioned. At the beginning of the pulse, the rf field is turned on very slowly. In the rotating frame of reference, this results in a very slow change in the direction of the effective field. It can be shown [76,90] that, under such conditions, the magnetization essentially follows the direction of the effective field. This is known as *adiabatic following*. Although relaxation puts an upper limit on this behavior, it is relevant in the context of liquid state NMR.



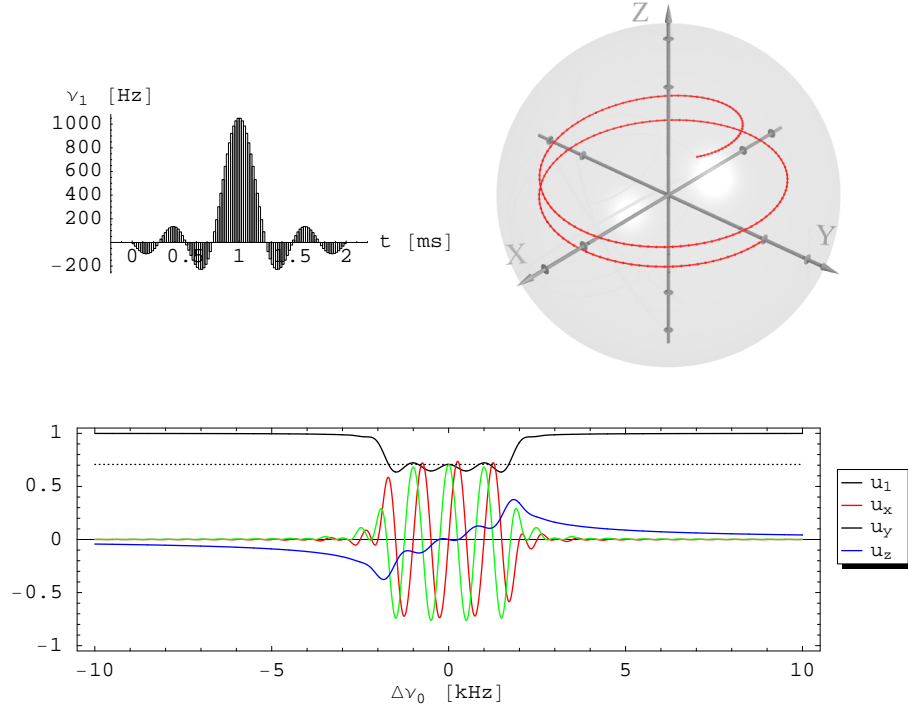


**Figure 3.9:** Selectivity of a  $\frac{\pi}{2}_y$ -pulse with a  $\sin x/x$  envelope. Upper left: Rf envelope. Upper right: Ending points of the total transformation for frequency offsets  $0 \text{ kHz} \leq \Delta\nu_0 \leq 1 \text{ kHz}$ . Bottom: Dependence of propagator components on the frequency offset.

#### 3.2.2.4 $\frac{\pi}{2}_y$ -Pulse with $\sin x/x$ Envelope

To address the problem of non-uniform excitation, one might be tempted to take the Fourier picture too literally by using a pulse envelope which is simply the Fourier transform of the ideal excitation spectrum. A pulse bounded by

$$\nu_1(t) = \nu_{1_0} \frac{\sin(|t - t_0|/t_T)}{t/t_T} \quad (3.18)$$

(shown in Figure 3.9) has a rectangular spectrum centered at the resonance frequency. The pulse shape is even more subject to adiabatic following problems than the Gaussian envelope of previous section. It is, however, instructive to ignore this for the moment and consider the effect of such a pulse.

The component plot partially confirms the expected flat excitation profile. The rotation angle of the propagator does closely follow a rectangular dependence. The fallacy of the Fourier argument becomes immediately apparent, when the propagator trajectory is considered. The direction of the propagator rotates almost four times  $360^\circ$  across the flat excitation region! Apart from adiabatic following, this property renders the  $\sin x/x$  envelope unusable for the purposes of quantum computing. It can, however, be useful for special purposes such as magnetization inversion of strongly inhomogeneous spin ensembles and in magnetic imaging applications.

### 3.2.3 Selective Alternating $\frac{\pi}{2}|_y$ -Pulse

Another approach to creating a spectrally selective pulse is to construct a pulse sequence which by design has no net effect at a given frequency and see, if such a sequence could perform a useful transformation at some other frequency.

One possible ansatz is sketched in Figure 3.10 a). First, a pulse of duration  $t$  is applied in  $y$ -direction with the frequency offset  $\Delta$ . This pulse is followed by another pulse with the same duration and the opposite phase and frequency offset. During the first pulse, the Hamiltonian of a resonant spin is given by

$$\mathcal{H}_1 = \Delta \mathbf{I}_z + \omega_1 \mathbf{I}_y \quad (3.19)$$

where the excitation frequency offset  $\Delta$  and the Rabi frequency  $\omega_1$  are given in units of angular velocity. Therefore, the effect of off-resonant excitation is that, in the rotating frame of reference the resonant spin, the effective field and with it the axis of precession is tilted toward the  $z$ -axis by  $\Delta$ . The resulting rotation axis is labeled  $R_1$  in Figure 3.10 b).

During the second pulse the phase and the offset are inverted, such that the resulting rotation axis  $R_2$  in the rotating frame is exactly opposite to  $R_1$  and the Hamiltonian is given by

$$\mathcal{H}_1 = -\Delta \mathbf{I}_z - \omega_1 \mathbf{I}_y \quad (3.20)$$

The total transformation effected by the two pulses is given by

$$U = \exp \{-it_2 (-\Delta \mathbf{I}_z - \omega_1 \mathbf{I}_y)\} \exp \{-it_1 (\Delta \mathbf{I}_z + \omega_1 \mathbf{I}_y)\} = \mathbf{I}_0 \quad (3.21)$$

Since the durations of the two pulses are equal, the total propagator is an identity transformation. This cancellation is independent of the choice of  $\Delta$  and  $\omega_1$ . Furthermore, any linear combination  $\cos \varphi \mathbf{I}_x + \sin \varphi \mathbf{I}_y$  can be chosen instead of  $\mathbf{I}_y$  as long as the phase  $\varphi$  is inverted between pulses.

For a spin located at some offset  $\Delta\nu_0 \neq 0$ , the offsets of the two pulses with respect to  $\Delta\nu_0$  are no longer equal and the resulting propagators do not cancel out. The maximal effect for such a spin is achieved when  $\Delta\nu_0 = 2\Delta/2\pi$ . When a train of such pulse pairs is applied, this effect can be enhanced or suppressed by varying the phase  $\varphi$ , the offset  $\Delta$ , and the Rabi frequency  $\omega_1$  to obtain pulses with any phase and rotation angle.

As an example, Figure 3.10 c) shows the trajectory of the propagator for a pulse train of three pairs with the phase and rotation angles chosen such that a  $\frac{\pi}{2}|_y$ -rotation is achieved at  $\Delta\nu_0 = 2\Delta/2\pi$ . The consecutive rotations of the spin about the alternating axes resulting from this propagator are demonstrated by the trajectory of the  $z$ -component of the spin is shown in sub-figure d).

The component plot of the total propagator against the excitation offset in Figure 3.10 e) shows that a sequence of three pairs of pulses produces the inverse transformation ( $\frac{\pi}{2}|_{\bar{y}}$ ) at  $\Delta\nu_0 = -2\Delta/2\pi$  as expected from the symmetry.

The two regions around  $\Delta\nu_0 = \pm 2\Delta/2\pi$  show excitation properties similar to that of a simple rectangular pulse with some suppression of cross excitation between the two frequencies. The same plot for a sequence with ten alternations in sub-figure f) shows that the frequency selectivity of the sequence grows with the number of alternations and simulations show that it can be made as selective

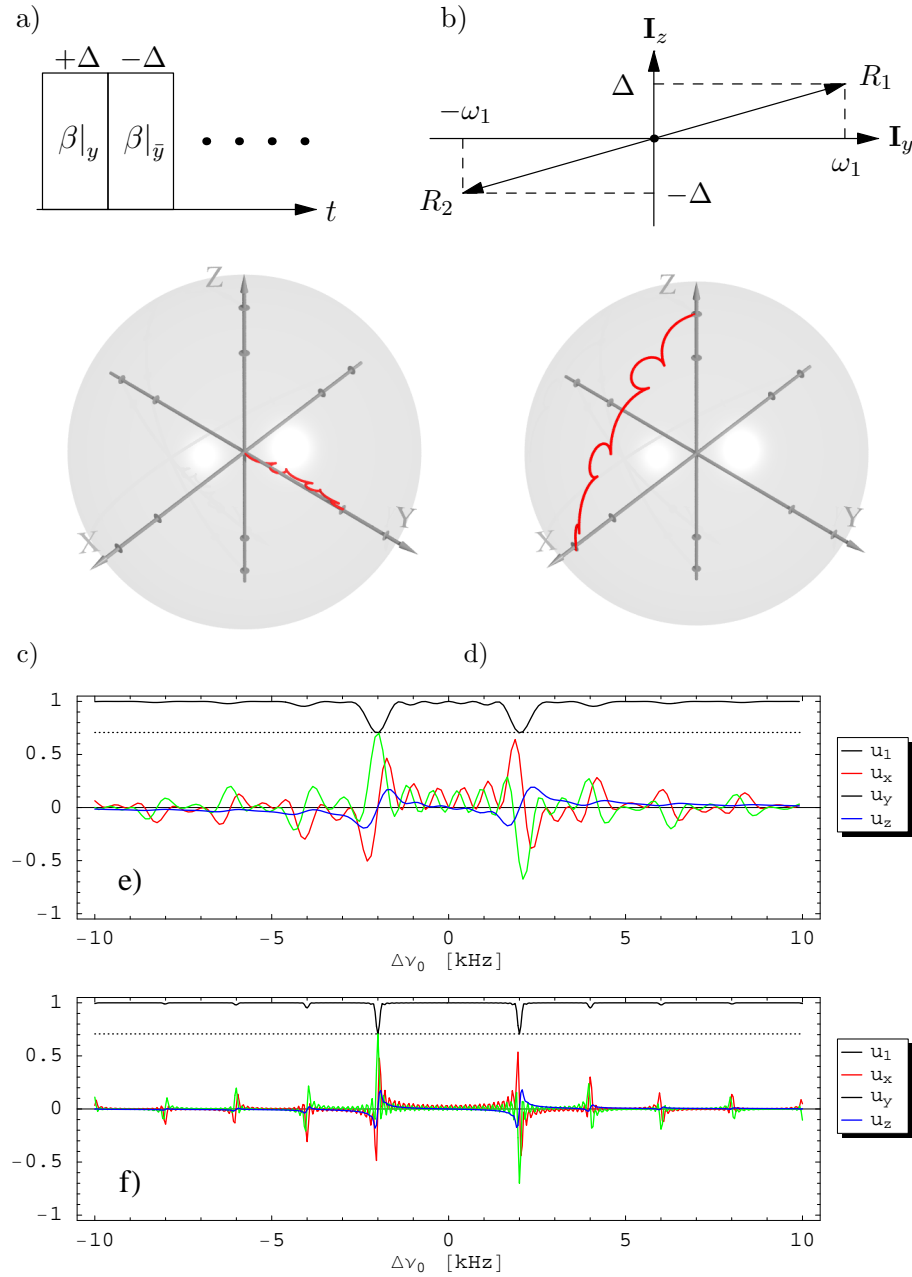


**Figure 3.10:**  $\frac{\pi}{2}|_y$ -pulse with alternating off-resonant excitation. a) Pulse sequence. b) Alternating rotation axes for a resonant spin. c) Trajectory of the propagator for a sequence with three alternation cycles. d) Trajectory of the  $z$ -component of the spin under the sequence. e) Propagator components vs. the resonance offset  $\Delta\nu_0$  for a pulse with three alternation cycles. f) Dito for a pulse with 15 alternations. Sequence length is  $\tau = 1.4$  ms, Rabi frequency  $\nu_1 \approx 280$  Hz. Sequence shows two excitation regions with small cross-excitation at higher harmonics. The selectivity of the excitation increases with the number of alternations per sequence.

as required. The plot also shows the artefact of significant excitation at higher harmonics of  $2\Delta$ .

The utility of this pulse sequence for actual applications in spin quantum computing is limited by the higher harmonic excitation bands, the residual phase errors outside the excitation regions, and some non-uniformity of excitation within the excitation bands. This sequence is described here, merely to demonstrate the use of visual pulse sequence analysis with extended multi-pulse sequences.

## Chapter 4

# Detailed Implementation of the $S$ -Bus Concept with $\text{CaF}_2:\text{Ce}$

The chapter begins with a short introduction of the basic concepts of the  $S$ -bus proposal and its general theoretical treatment. Then, the basic properties of the cerium doped  $\text{CaF}_2$  single crystals essential for its use as a quantum processor are summarized. This system is not described exactly by the general  $S$ -bus theory. Nevertheless, that theory does provide a solid basis for the understanding of the  $\text{CaF}_2:\text{Ce}$  cluster. The quantitative details and precise description can only be gained by further theoretical treatment and experiment. The bulk of the chapter tackles these tasks by means of exact numeric treatment of the paramagnetic Ce-center in  $\text{CaF}_2:\text{Ce}$  and detailed experimental investigations of the evolutions of density matrices of the qubits.

### 4.1 The $S$ -Bus Concept for Spin Quantum Computing

The  $S$ -bus concept for spin quantum computing was developed and theoretically treated by M. Mehring [33,91].

#### 4.1.1 General Features

The proposal assumes a number  $N$  of nuclear spins  $I = \frac{1}{2}$  coupled to a central electron spin  $S = \frac{1}{2}$  via hyperfine interaction. The central  $S$  spin plays the role of a *quantum bus*, in that it mediates the interactions between the single *client qubits*. This scheme has a number of advantageous features.

- In the liquid state, the anisotropic contributions to the interaction between spins are averaged out leaving only the constant isotropic part for the implementation of 2-qubit gates. In an oriented solid state system, such as the  $S$ -bus, the available interactions are typically much stronger, leading

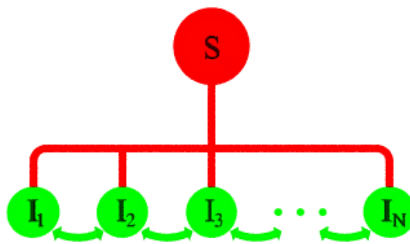


**Figure 4.1:** The  $S$ -bus concept for spin quantum computing. The  $I$ -spins connected to a central  $S$ -spin via the hyperfine interaction serve as a basic building block. Several such clusters may be connected through coupling of their  $S$ -spins.

to potentially much shorter gate times. Also, anisotropic contributions can be conveniently scaled by geometric parameters.

- At temperatures above the absolute zero  $T > 0$  K, any form of ensemble spin quantum computing has to start with the polarization of the spin system arising from the difference of the occupation probability of the two eigenstates of a spin-1/2 system according to the Boltzmann distribution:

$$\exp(-\gamma \hbar B_0 / k_B T)$$

where  $B_0$  is the static external magnetic field and  $\gamma$  is the gyromagnetic ratio of the particle carrying the spin. For electrons, this ratio is typically greater by a factor of  $10^3$  as compared to that of nuclei, resulting in an accordingly larger initial polarization.

- By the same token, the low polarization of the  $I$ -spins makes it non-feasible to observe them directly. Thus, the  $S$ -spin has the second role of a *monitor* spin. The desired information about the quantum state of the client qubits is *encoded* in the state of the monitor spin for readout by appropriate pulse sequences. Direct manipulation of the  $I$ -spins, however, is easily possible and plays an important role in the implementation of quantum computing operations.
- The procedure for the transfer of polarization from the electron spin to the nuclear spins has the side effect of creating a density matrix containing very high-order correlations between the nuclear spins.
- Similarly to other quantum computing proposals [92], the  $S$ -bus arrangement can potentially be scaled by letting the  $S$ -spins of several basic units interact with each other by delocalizing the electron wave function and using spatially selective addressing of each cluster.
- For realistic situations<sup>1</sup>, it is possible to reach the quantum limit for readily achievable temperatures. Therefore, ensembles of truly entangled quantum systems could possibly be obtained.

<sup>1</sup>It has been calculated [91] that for the  $\text{CaF}_2:\text{Ce}$   $S$ -bus cluster (see below) the quantum limit would be reached in a W-band spectrometer ( $B_0 \approx 3.5$  T) at around 2 K.

In its general form, the  $S$ -bus concept permits a number of different implementations. One could, for instance, envisage a large bulk semiconductor containing spatially separated clusters. Spins in such clusters would be manipulated by locally applied rf- and microwave fields and the server spins of different clusters could be brought into interaction by the action of appropriately devised gates. The technology to realize such a device is, of course, not available at present. However, ensembles of isolated  $S$ -bus clusters are available. In fact, single-crystal of  $\text{CaF}_2:\text{Ce}$  has been in use in our lab, as a model system.

### 4.1.2 Density Matrices in the $S$ -Bus

Below, is a summary of the  $S$ -bus theory as developed in [33] and [91]. In the high-field approximation, the general description above translates into the following magnetic Hamiltonian for an isolated  $S$ -bus cluster (in units of angular velocity):

$$\mathcal{H} = \underbrace{\omega_{0_S} \mathbf{S}_z}_{\mathcal{H}_S} + \underbrace{\sum_{j=1}^N \omega_{0_j} \mathbf{I}_{z_j}}_{\mathcal{H}_I} + \underbrace{\sum_{j=1}^N a_j \mathbf{S}_z \mathbf{I}_{z_j}}_{\mathcal{H}_{h_f}} + \underbrace{\sum_{j < k}^N D_{jk} \mathbf{I}_{z_j} \mathbf{I}_{z_k}}_{\mathcal{H}_D} \quad (4.1)$$

Where  $\mathbf{S}_z$  and  $\mathbf{I}_{z_j}$  are the spin operator components of the electron and nuclear spins with the Larmor frequencies  $\omega_{0_S}$  and  $\omega_{0_j}$ ,  $a_j$  is the effective hyperfine coupling of the  $j$ -th nuclear spin,  $D_{jk}$  is the dipole-dipole coupling between spins  $\mathbf{I}_j$  and  $\mathbf{I}_k$  and  $N$  is the number of qubit spins. The constituent terms have the following significance in the context of the  $S$ -bus: The electron spin Zeeman term  $\mathcal{H}_S$  allows the bus spin to be manipulated by means of microwave pulses. The nuclear Zeeman term  $\mathcal{H}_I$  and the hyperfine term  $\mathcal{H}_{h_f}$  provide for the addressability of qubit spins. Hereby, it is necessary that the physical system used for implementation features sufficiently different hyperfine couplings, to enable selective manipulation of the qubits by rf pulses. The dipole-dipole coupling term  $\mathcal{H}_D$  between the qubits can be used to implement two-qubit gates. Thus, all the basic requirements for a quantum processor are present. In addition, the hyperfine term is also responsible for the bulk of the most promising properties of the  $S$ -bus, in that it enables the creation of a highly polarized and correlated nuclear density matrix. Notice, that the Zeeman splitting of the electron spin will commonly be the largest term by three orders of magnitude. Thus, an ensemble of  $S$ -bus clusters can be separated into two sub-ensembles with bus spins in the states  $|m_S = \pm 1/2\rangle$ . The nuclear spins of one set are entirely independent of the other. One could envisage a doubling of the number of qubits based on this separation.

A complete experiment on an isolated  $S$ -bus cluster consists of three basic blocks as indicated in Figure 4.2. First, a preparation sequence  $U_P^{(S)}$  is applied to the bus spin ( $\mathbf{S}$ ) resulting in a density matrix highly correlated with respect to the client spins ( $\mathbf{I}_j$ ). This is the starting point for all quantum computing operations on the qubits. They will typically include the preparation of pseudo-pure states, actual quantum computation, and encoding of the output state for readout. The encoded information is finally made available in the form of a detectable signal by the detection sequence  $U_D^{(S)}$ .

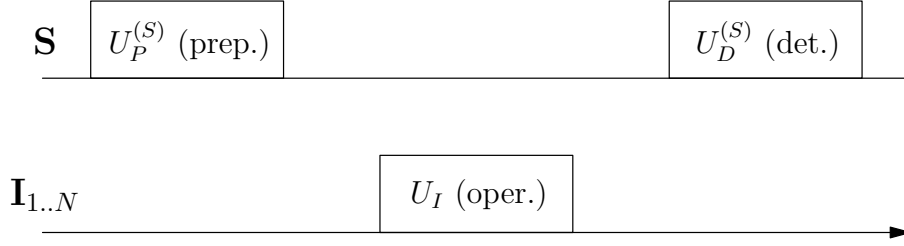


**Figure 4.2:** Block diagram of a general  $S$ -bus pulse sequence.

#### 4.1.2.1 Preparation of a Highly Correlated Nuclear Density Matrix

The goal of a preparation sequence is to transfer the high polarization of the electron spin to the nuclear spins and to create correlations among the them. The basic sequence consists of two  $\pi/2$ -pulses separated by an evolution period  $\tau_S$  as shown in Figure 4.3. It was originally introduced by Mims [93] in the context of pulsed *Electron Nuclear Double Resonance* (ENDOR) [94]. The first

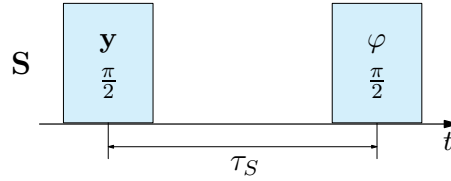


**Figure 4.3:** Basic preparation sequence for the  $S$ -bus. The second pulse can be applied in  $x$ -direction ( $\varphi = 0$ ), in  $y$ -direction ( $\varphi = \pi/2$ ), and with  $\varphi = \pi/4$ . The same variants can also be used for detection.

pulse is applied in the  $y$ -direction and transfers the electron spin into the  $yx$ -plane. During the mixing time  $\tau_S$ , correlations of between the nuclear spins build up under the action of the hyperfine term of the Hamiltonian. The second pulse can be applied in either  $x$ -,  $y$ -, and  $\varphi = \pi/4$ -direction transforming different parts of the created correlations into the  $z$ -direction. After that, all transient components decay on the time scale of the electron spin FID ( $\approx 20$  ns) leaving a purely diagonal density matrix, i.e., one containing only the  $z$ -components of the spin operators.

The initial density matrix of the system is assumed to be

$$\rho_B = \prod_{j=1}^M \left( \frac{1}{2} \mathbf{I}_2 - \Theta \mathbf{S}_{z_j} \right) \approx \frac{1}{2} \mathbf{I}_2 - \Theta \mathbf{S}_z \quad (4.2)$$

where  $M$  is the number of electron spins,  $\mathbf{I}_2$  the  $2 \times 2$  unity matrix and  $\Theta = \tanh(\hbar\omega_0/k_B T)$ .  $T$  denotes the temperature and  $\omega_0$  the Larmor precession frequency of the electron spin. The approximation is valid for  $\Theta \ll 1$ , i.e., for the high temperature and low field case which applies here. Because of the small magneto-gyric ratio of the nuclei,  $\gamma_N/\gamma_S \ll 1$  and the initial polarization of the nuclear spins is negligible. It was shown [33], that the density matrix produced



by any of the preparation sequences can be written as

$$\rho_P^{(S)} = \frac{1}{2^{N+1}} \mathbf{I}_{N+1} - \Theta \mathbf{S}_z \otimes \rho_I \quad (4.3)$$

where  $\mathbf{I}_{N+1}$  is the  $(N+1)$ -dimensional identity matrix and  $\rho_I$  the highly correlated density matrix of  $N$  nuclear spins. These are the qubits carrying the quantum information and this is the density matrix on which the quantum computation represented in Figure 4.2 by  $U_I$  is performed.

The density matrices generated by the three preparation sequences are given by

$$\rho_{yy}^{(S)} = \frac{1}{2^{N+1}} \mathbf{I}_{N+1} - \Theta \mathbf{S}_z \otimes \rho_{yy} \quad (4.4a)$$

$$\rho_{yy} = \text{Re} \left\{ \prod_{j=1}^N (c_j \mathbf{I}_2 + i2s_j \mathbf{I}_{z_j}) \right\} \quad (4.4b)$$

$$\rho_{yx}^{(S)} = \frac{1}{2^{N+1}} \mathbf{I}_{N+1} - \Theta \mathbf{S}_z \otimes \rho_{yx} \quad (4.4c)$$

$$\rho_{yx} = -\text{Im} \left\{ \prod_{j=1}^N (c_j \mathbf{I}_2 + i2s_j \mathbf{I}_{z_j}) \right\} \quad (4.4d)$$

$$\rho_{y\pi/4}^{(S)} = \frac{1}{2^{N+1}} \mathbf{I}_{N+1} - \Theta \mathbf{S}_z \otimes \rho_{y\pi/4} \quad (4.4e)$$

$$\rho_{y\pi/4} = \frac{1}{\sqrt{2}} (\rho_{yx} + \rho_{yy}) \quad (4.4f)$$

where  $c_j = \cos(a_j \tau_S / 2)$  and  $s_j = \sin(a_j \tau_S / 2)$ ,  $a_j$  being the hyperfine coupling constant for spin  $j$ . To give an example, the two density matrices  $\rho_{yy}$  and  $\rho_{yx}$  arising for  $N = 4$  are given by

$$\begin{aligned} \rho_{yy} = & -c_1 c_2 c_3 c_4 \mathbf{I}_4 + 2^2 (s_1 s_2 c_3 c_4 \mathbf{I}_{z_1} \mathbf{I}_{z_2} + s_1 s_3 c_2 c_4 \mathbf{I}_{z_1} \mathbf{I}_{z_3} + \\ & s_1 s_4 c_2 c_4 \mathbf{I}_{z_1} \mathbf{I}_{z_4} + s_2 s_3 c_1 c_4 \mathbf{I}_{z_2} \mathbf{I}_{z_3} + s_2 s_4 c_1 c_3 \mathbf{I}_{z_2} \mathbf{I}_{z_4} + \\ & s_3 s_4 c_1 c_2 \mathbf{I}_{z_3} \mathbf{I}_{z_4}) - 2^4 s_1 s_2 s_3 s_4 \mathbf{I}_{z_1} \mathbf{I}_{z_2} \mathbf{I}_{z_3} \mathbf{I}_{z_4} \quad (4.5) \end{aligned}$$

$$\begin{aligned} \rho_{yx} = & -2^1 (c_2 c_3 c_4 s_1 \mathbf{I}_{z_1} + c_1 c_3 c_4 s_2 \mathbf{I}_{z_2} + c_1 c_2 c_4 s_3 \mathbf{I}_{z_3} + c_1 c_2 c_3 s_4 \mathbf{I}_{z_4}) \\ & + 2^3 (c_4 s_1 s_2 s_3 \mathbf{I}_{z_1} \mathbf{I}_{z_2} \mathbf{I}_{z_3} + c_3 s_1 s_2 s_4 \mathbf{I}_{z_1} \mathbf{I}_{z_2} \mathbf{I}_{z_4} + \\ & c_2 s_1 s_3 s_4 \mathbf{I}_{z_1} \mathbf{I}_{z_3} \mathbf{I}_{z_4} + c_1 s_2 s_3 s_4 \mathbf{I}_{z_2} \mathbf{I}_{z_3} \mathbf{I}_{z_4}) \quad (4.6) \end{aligned}$$

Note that the  $\rho_{yy}$  contains only products of even number of  $\mathbf{I}_z$ -operators, while  $\rho_{yx}$  contains only products with odd number of  $\mathbf{I}_z$ s. The  $y\pi/4$ -sequence produces a mixture of all terms. For  $N = 3$ :

$$\begin{aligned} \rho_{y\pi/4} = & \frac{1}{\sqrt{2}} \{ c_1 c_2 c_3 \mathbf{I}_0 - 2^1 (s_1 c_2 c_3 \mathbf{I}_{z_1} + c_1 s_2 c_3 \mathbf{I}_{z_2} + c_1 c_2 s_3 \mathbf{I}_{z_3}) \\ & - 2^2 (+s_1 s_2 c_3 \mathbf{I}_{z_1} \mathbf{I}_{z_2} + c_1 s_2 s_3 \mathbf{I}_{z_2} \mathbf{I}_{z_3} + s_1 c_2 s_3 \mathbf{I}_{z_1} \mathbf{I}_{z_3}) \\ & - 2^3 s_1 s_2 s_3 \mathbf{I}_{z_1} \mathbf{I}_{z_2} \mathbf{I}_{z_3} \} \quad (4.7) \end{aligned}$$

In general, these density matrices contain correlations of qubits of order up to  $N$  as can be seen by expanding the products:

$$\rho_I = \frac{1}{2^N} p_0 \mathbf{I}_N + \frac{1}{2^{N-1}} \sum_j p_j \mathbf{I}_{z_j} + \frac{1}{2^{N-2}} \sum_{j < k} p_{jk} \mathbf{I}_{z_j} \mathbf{I}_{z_k} + \dots + p_{1\dots N} \prod_j \mathbf{I}_{z_j} \quad (4.8)$$

with the coefficients of each product of  $\mathbf{I}_z$  operators given by

$$p_q = 2^N \prod_{j \in \{q\}} s_j \prod_{k \notin \{q\}} c_k \quad (4.9)$$

#### 4.1.2.2 Reduced Density Matrix

Frequently, only a subset of qubits will be used in a quantum computation. In this case, the nuclear density matrix can be written in a *reduced* form, where the operators of non-participating qubits are not expanded. For instance, for two qubits  $\rho_{yy}$  and  $\rho_{yx}$  will have the form

$$\begin{aligned} \rho_{yy} = & c_1 c_2 \Pi_{N-2}^{(+)} \mathbf{I}_0 - 2s_1 c_2 \Pi_{N-2}^{(-)} \mathbf{I}_{z_1} \\ & - 2c_1 s_2 \Pi_{N-2}^{(-)} \mathbf{I}_{z_2} - 4s_1 s_2 \Pi_{N-2}^{(+)} \mathbf{I}_{z_1} \mathbf{I}_{z_2} \end{aligned} \quad (4.10a)$$

$$\begin{aligned} \rho_{yx} = & -c_1 c_2 \Pi_{N-2}^{(-)} \mathbf{I}_0 - 2s_1 c_2 \Pi_{N-2}^{(+)} \mathbf{I}_{z_1} \\ & - 2c_1 s_2 \Pi_{N-2}^{(+)} \mathbf{I}_{z_2} + 4s_1 s_2 \Pi_{N-2}^{(-)} \mathbf{I}_{z_1} \mathbf{I}_{z_2} \end{aligned} \quad (4.10b)$$

where the contributions of non-participating qubits are accumulated in

$$\Pi_{N-2}^{(+)} = \text{Re} \left( \prod_{j=3}^N (c_j + i2 s_j \mathbf{I}_{z_j}) \right) \quad (4.11a)$$

$$\Pi_{N-2}^{(-)} = \text{Im} \left( \prod_{j=3}^N (c_j + i2 s_j \mathbf{I}_{z_j}) \right) \quad (4.11b)$$

The two operators are orthogonal:

$$\text{tr} \{ \Pi_{N-2}^{+} \Pi_{N-2}^{-} \} = 0 \quad (4.12)$$

because  $\Pi_{N-2}^{(+)}$  contains only products with even numbers of  $\mathbf{I}_{z_j}$ , while  $\Pi_{N-2}^{(-)}$  consists of products with odd numbers of  $\mathbf{I}_{z_j}$ . As will become clear later, this fact has important implications for the use of different preparation and detection sequences.

The operator nature of the non-participating qubits can now be removed by a trace operation over their subspaces, resulting in a representation of the density matrix *reduced* to the subspace of qubits 1 and 2:

$$\rho_{yy}^{(12)} = Q_0^{(yy)} \mathbf{I}_0 - 2Q_1^{(yy)} \mathbf{I}_{z_1} - 2Q_2^{(yy)} \mathbf{I}_{z_2} - 4Q_{12}^{(yy)} \mathbf{I}_{z_1} \mathbf{I}_{z_2} \quad (4.13a)$$

$$\rho_{yx}^{(12)} = -Q_0^{(yx)} \mathbf{I}_0 - 2Q_1^{(yx)} \mathbf{I}_{z_1} - 2Q_2^{(yx)} \mathbf{I}_{z_2} + 4Q_{12}^{(yx)} \mathbf{I}_{z_1} \mathbf{I}_{z_2} \quad (4.13b)$$

with the real coefficients

$$\begin{aligned}
Q_0^{(yy)} &= c_1 c_2 \sqrt{P_{N-2}^{(+)}} & Q_0^{(yx)} &= c_1 c_2 \sqrt{P_{N-2}^{(-)}} \\
Q_1^{(yy)} &= s_1 c_2 \sqrt{P_{N-2}^{(-)}} & Q_1^{(yx)} &= s_1 c_2 \sqrt{P_{N-2}^{(+)}} \\
Q_2^{(yy)} &= c_1 s_2 \sqrt{P_{N-2}^{(-)}} & Q_2^{(yx)} &= c_1 s_2 \sqrt{P_{N-2}^{(+)}} \\
Q_{12}^{(yy)} &= s_1 s_2 \sqrt{P_{N-2}^{(+)}} & Q_{12}^{(yx)} &= s_1 s_2 \sqrt{P_{N-2}^{(-)}}
\end{aligned} \tag{4.14}$$

and

$$P_{N-2}^{(\pm)} = \frac{1}{2^{N-2}} \text{tr} \left\{ \left( \Pi_{N-2}^{(\pm)} \right)^2 \right\} \tag{4.15}$$

The coefficients  $P_{N-2}^{(\pm)}$  have the useful property

$$P_{N-2}^{(\pm)} = \frac{1}{2} (1 \pm M_{N-2}) \quad \text{with} \quad M_{N-2} = \prod_{j=3}^N (c_j^2 - s_j^2) \tag{4.16}$$

### 4.1.2.3 Manipulation and Detection

Equation (4.8) shows that the highly correlated density matrix prepared in the  $S$ -bus system contains *all* base operators necessary to express a *diagonal* pseudo-pure state of  $N$ -qubits (cf. Equation (1.12)). In fact, if all the coefficients  $p_q$  can be adjusted such that  $|p_q| = 1$ , a pseudo-pure base state will be created. This condition would be achieved for all  $c_j = s_j = 1/\sqrt{2}$ . In practice, this would place very stringent requirements on the hyperfine coupling constants  $a_j$ . Any practical system would probably require an additional non-unitary step applied to qubits to prepare pseudo-pure states (cf. Section 4.7.1.2).

After the preparation of the input states, the actual quantum computing algorithm is applied by a series of rf pulses and evolutions. If the resulting nuclear density matrix is given by  $\rho_I$ , then the full density matrix of the system will have the form

$$\rho_I^{(S)} = \frac{1}{2^{N+1}} \mathbf{I}_{N+1} - \Theta \mathbf{S}_z \otimes \rho_I \tag{4.17}$$

The detection proceeds by a second application of one of the preparation sequences. Following the decay of transverse components, again a purely diagonal matrix remains and additional microwave pulses must be used to read out the  $\mathbf{S}_z$  component.<sup>2</sup> As a result of this setup, the detected signal magnitude is given by

$$S_D = \frac{\text{tr} \left( \rho_D^{(S)} \rho_I^{(S)} \right)}{\text{tr} \left( \mathbf{S}_z \mathbf{S}_z \right)} \tag{4.18}$$

with  $\rho_D^{(S)}$  given in Equation (4.4) by the density matrix corresponding to the applied detection sequence variant. Clearly, a single execution of such an experiment will provide only a single piece of information. To obtain a potentially large number of parameters defining the density matrix one- or two-dimensional

<sup>2</sup>A *remote echo detection* (RED) [95] sequence can be used to measure  $\mathbf{S}_z$ .

experiments must be made with the interesting information encoded in some way in the signal amplitude. This can be done successive to the quantum algorithm or during the algorithm itself (see, e.g., Section 4.7.1 and 4.8).

## 4.2 The $S$ -bus cluster in $\text{CaF}_2:\text{Ce}$

### 4.2.1 Crystalline Structure

In our lab, the experimental work on implementing the  $S$ -bus concept was pioneered by J. Mende in the course of his PhD research [35]. From a large number of potentially usable crystalline centers, a suitable candidate was found in  $\text{CaF}_2$  single crystals doped with cerium at concentrations of  $10^{-4} - 10^{-3}$ . Under appropriate growth conditions, the  $\text{Ce}^{3+}$  ion substitutes for a  $\text{Ca}^{2+}$  ion and acquires an interstitial  $\text{F}^-$  at the empty neighboring body centered site for charge compensation as shown in Figure 4.4.

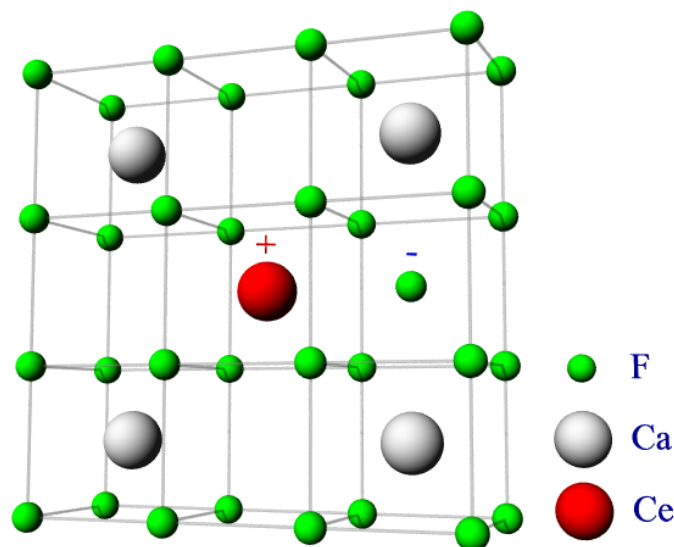


**Figure 4.4:**  $\text{CaF}_2$  lattice with the  $\text{Ce}^{3+}$  ion substituting for a  $\text{Ca}^{2+}$  ion. The charge compensating  $\text{F}^-$  ion is also shown.

The  $\text{Ce}^{3+}$  ion has a complicated electronic configuration but the spin sublevels of the ground state of the unpaired electron spin are sufficiently separated from the next excited states and can serve as an effective spin  $S = \frac{1}{2}$  system. Together with the eight  $^{19}\text{F}$  nuclei next to it and the nucleus of the charge compensating fluorine it comprises an  $S$ -bus cluster with  $N = 9$  client qubits, as shown in Figure 4.5.

The nuclear spins are coupled to the electron spin via hyperfine interaction. Due to the large gyromagnetic ratio of the  $^{19}\text{F}$  nucleus, the coupling for the next neighbors is very strong ( $\approx 10$  MHz) and is comparable to the Zeeman splitting of free  $^{19}\text{F}$  at a magnetic field of  $B_0 = 0.35$  T. The ionic size of  $\text{F}^-$  exceeds the space available at the interstitial site. Thus, the incorporation

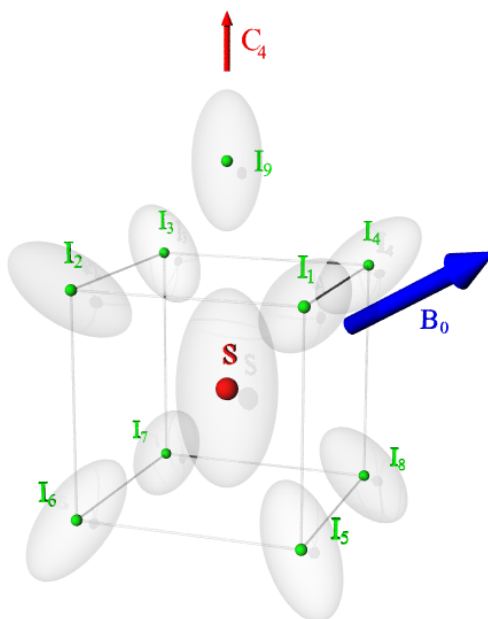


**Figure 4.5:** Structure of the  $S$ -bus cluster in  $\text{CaF}_2:\text{Ce}$ . The spin sublevels of the unpaired electron spin of the electronic ground state of the  $\text{Ce}^{3+}$  ( $S$ ), its eight neighboring lattice fluorines ( $I_1 - I_8$ ) and the charge compensating  $\text{F}^-$  ( $I_9$ ) comprise the  $S$ -bus system. The shaded ellipsoids indicate the anisotropic nuclear hyperfine tensors and the  $g$ -tensor of the electron spin.

of the charge compensating fluorine distorts the lattice by pushing the lattice fluorines radially outward. Also, the strong Coulomb attraction results in a small displacement of the cerium ion. The effect is that the hyperfine tensors of the upper fluorine layer I ( $I_1 - I_4$ ) differ significantly from those in the lower layer II ( $I_5 - I_8$ ). As a whole, the cluster shows four-fold rotational symmetry along the axis connecting the cerium and the charge compensating fluorine. It can, therefore, be expected that the Electron Nuclear Double Resonance (ENDOR) spectrum of the cluster will be fully resolved at appropriate orientations of the external magnetic fields with respect to the crystal axes.

It should be noted, that the  $C_4$  symmetry axis of a given cluster has three possible orientations with respect to the crystal axes resulting in three ensembles of equivalent clusters at a given orientation of the external field. This fact is useful for alignment of the sample with respect to the laboratory frame.

Besides the hyperfine coupling to the electron spin significant dipole-dipole coupling ( $\approx 10$  kHz) amongst the nuclear spins is also present. The strength of the hyperfine interaction of the fluorines falls off quickly with distance and the next-to-next neighbors have very small couplings. However, the dipolar coupling of the nuclear spins within the cluster to the fluorine spins of the surrounding lattice has strong consequences for the relaxation properties and must be taken into account as will be discussed later.

### 4.2.2 The S-Bus Hamiltonian

The magnetic Hamiltonian of the paramagnetic Ce-center in CaF<sub>2</sub> consists of a number of contributions<sup>3</sup>:

$$\mathcal{H} = \mathcal{H}_S + \mathcal{H}_N + \mathcal{H}_{hf} + \mathcal{H}_{dd} \quad (4.19)$$

Where the Zeeman term for the electron is given by the tensor product of the electron spin operator  $\mathbf{S}$ , the anisotropic  $g$ -tensor  $\mathbf{g}$ , and the external magnetic field  $\mathbf{B}_0$ :

$$\mathcal{H}_S = \frac{\mu_B}{h} \mathbf{S} \cdot \mathbf{g} \cdot \mathbf{B}_0 \quad (4.20)$$

The nuclear Zeeman term combines all  $z$ -components of the nuclear spins  $I_{z_i}$  with the magnitude of the external field  $B_0$  and the nuclear  $g$ -factor  $g_N$  and the nuclear magneton  $\mu_N$ :

$$\mathcal{H}_N = \sum_{i=1}^N \frac{\mu_N}{h} g_N B_0 I_{z_i} \quad (4.21)$$

The hyperfine contribution is the sum of the tensor products of all the nuclear spins  $I_i$  with the electron spin and the hyperfine tensors  $\mathbf{a}_i$ :

$$\mathcal{H}_{hf} = \sum_{i=1}^N \mathbf{S} \cdot \mathbf{a}_i \cdot \mathbf{I}_i \quad (4.22)$$

The hyperfine tensors  $\mathbf{a}_i$  can be calculated exactly, when the participating spins may be treated as point-dipoles. However, the bonding in CaF<sub>2</sub>:Ce is not entirely ionic. The covalent contributions to the bonds lead to an extended electron wave function, which leads to large deviations of the hyperfine coupling from the simple dipole-dipole form [96, 97].

Finally, the term describing the through-space dipole-dipole interaction of the nuclear spins amongst each other is given by

$$\mathcal{H}_{dd} = \sum_{i < j}^N \mathbf{I}_i \cdot \mathbf{D}_{ij} \cdot \mathbf{I}_j \quad (4.23)$$

The Cartesian components of the dipolar interaction tensor  $\mathbf{D}_{ij}$  are given by

$$(\mathbf{D}_{ij})_{kl} = \frac{\mu_0}{4\pi r_0^3} h \gamma_F^2 (\delta_{kl} - 3r_k r_l) \quad (4.24)$$

where  $\mu_0$  is the magnetic permeability of vacuum,  $\gamma_F$  the magneto-gyric ratio of the fluorine nucleus,  $\delta_{kl}$  the Kronecker symbol,  $r_0$  the distance between the two spins, and  $r_k$  the Cartesian components of the unit direction vector connecting the spins.

Due to the crystal structure of the paramagnetic center, all the tensors in the found Hamiltonian are strongly anisotropic. Furthermore, an exact *ab initio* calculation of the various couplings is not possible, except for the dipole-dipole tensor. They must be determined experimentally by suitable measurements. This has been done by Baker et al. [96] and the values reported there are used in the present work.

<sup>3</sup>Following the conventions of magnetic resonance the spin operators are assumed to be dimensionless and the Hamiltonian is written in Hz.

### 4.2.3 Manipulation of Spins

In order to implement the  $S$ -bus concept on  $\text{CaF}_2:\text{Ce}$ , an *Electron Paramagnetic Resonance* (EPR) spectrometer was used. It consists of a resistive magnet providing the large external magnetic field  $B_0$  of up to 1 T. The samples are mounted at the center of the magnet in an microwave resonator operating at frequencies around 9.5 GHz (microwave X-band). The magnetic component  $B_1$  of the microwave resonator mode is oriented at right angles to the static field.

The excitation channel is equipped with various analog and digital logic, filters, amplifiers, etc., which allows irradiation of the sample with microwave pulses of 8 ns to several 1  $\mu\text{s}$  length. Full control of phase, amplitude and frequency of these pulses is available through the use of an *Arbitrary Waveform Generator* (AWG). The detection channel allows for quadrature recording of the microwave signal induced by the precessing magnetization of the electron spins in the sample.

The nuclear spins are manipulated by means of rf-pulses. These are produced by an additional coil inside the microwave resonator such that the magnetic component  $B_2$  of the rf-field is perpendicular to  $B_0$  and  $B_1$ . The coil is fed by an high-power, linear rf-amplifier which in turn is driven by another AWG. Again, this allows far-reaching control of all pulse parameters. This arrangement is known as an *Electron Nuclear Double Resonance* (ENDOR) setup.

To allow control of the temperature, the microwave resonator with the sample and the rf-coil is placed inside a flow cryostat, such that temperatures down to 5 K are possible when liquid Helium is used as coolant. The sample is mounted on a one-axis goniometer to facilitate the rotation of the external field with respect to the sample frame of reference.

### 4.2.4 $\text{CaF}_2:\text{Ce}$ as a Testbed for the $S$ -Bus

The general  $S$ -bus theory described in Section 4.1.2 assumes an idealized physical system described by the Hamiltonian in Equation (4.1). The  $\text{CaF}_2:\text{Ce}$  Hamiltonian presented in Section 4.2.2 clearly violates some of the assumptions: Most severely, the large hyperfine coupling – which provides for the selective addressability of the spins and allows fast creation of a highly correlated qubit register – also leads to a strong mixing of states between the electron and the nuclear spins.<sup>4</sup> Furthermore, the  $S$ -bus cluster in  $\text{CaF}_2:\text{Ce}$  is embedded in an extended  $^{19}\text{F}$  spin network which is a powerful source of decoherence.

Nevertheless,  $\text{CaF}_2:\text{Ce}$  can be used as a testbed for the  $S$ -bus concept. The theoretical treatment in Section 4.1.2 can provide a basic description of the experimental situation as, in fact, was shown in experiments by J. Mende. Taking the  $S$ -bus theory as a first approximation, the understanding of  $\text{CaF}_2:\text{Ce}$  must be refined by further theoretical treatment and experimental study. Some of the progress in this direction is detailed below.

<sup>4</sup>This problem could be circumvented by use of higher magnetic fields. Zeeman interaction scales linearly with the field while hyperfine coupling is field-independent. When switching from X band ( $B_0 \approx 0.35$  T) to the W band ( $B_0 \approx 3.5$  T), for instance, the two contributions would be separated by an order of magnitude, making the perturbational approach much more applicable.

## 4.3 EPR Spectra and Sample Alignment

### 4.3.1 Coordinate Transformations

Since no crystallographic procedure (such as X-ray diffractometry) was easily available, the fitting of the angular dependence of the EPR spectrum was used to determine the sample alignment.

The sample was mounted on a goniometer in an *a priori* unknown orientation. The axis of the goniometer was perpendicular to the direction of the external field  $B_0$ . The slotted tube EPR resonator was aligned such that the magnetic component of the alternating field  $B_1$  of the microwave mode was at right angles with the former directions. The axis of the ENDOR coil and the magnetic component  $B_2$  of the rf field coincided with the goniometer axis  $G$ .

For the *laboratory frame* of reference, the direction of the  $z$ -axis was chosen to coincide with the external magnetic field  $B_0$  according to the universal convention of magnetic resonance. The  $x$ -axis was aligned along the  $B_1$  field direction and the  $y$ -axis was chosen along the goniometer axis.

The coordinate transformation from the *lab frame* to the *crystal frame* is described by the  $3 \times 3$  matrix  $\mathbf{R}_{LC}$ :

$$\mathbf{r}^{(c)} = \mathbf{R}_{LC} \mathbf{r}^{(l)} \quad (4.25)$$

According to Euler's theorem, three real numbers are sufficient to fully describe such a rotation matrix. In order to experimentally determine these parameters, the matrix  $\mathbf{R}_{LC}$  was parameterized using Euler angles based on the following elementary rotations around Cartesian axes:

$$x\text{-axis:} \quad \mathbf{R}_x(\alpha) = \begin{pmatrix} 1 & 0 & 0 \\ 0 & \cos \alpha & -\sin \alpha \\ 0 & \sin \alpha & \cos \alpha \end{pmatrix} \quad (4.26a)$$

$$y\text{-axis:} \quad \mathbf{R}_y(\alpha) = \begin{pmatrix} \cos \alpha & 0 & \sin \alpha \\ 0 & 1 & 0 \\ -\sin \alpha & 0 & \cos \alpha \end{pmatrix} \quad (4.26b)$$

$$z\text{-axis:} \quad \mathbf{R}_z(\alpha) = \begin{pmatrix} \cos \alpha & -\sin \alpha & 0 \\ \sin \alpha & \cos \alpha & 0 \\ 0 & 0 & 1 \end{pmatrix} \quad (4.26c)$$

In physics, it is common to parameterize the rotation matrix as  $\mathbf{R}(\alpha, \beta, \gamma) = \mathbf{R}_z(\alpha) \mathbf{R}_y(\beta) \mathbf{R}_z(\gamma)$ . However, with the goniometer axis aligned along the  $y$ -direction, this choice is inconvenient. Thus, for the purpose of fitting the angular dependence of EPR spectra only, the following choice was adopted:<sup>5</sup>

$$\mathbf{R}_{LC} = \mathbf{R}_y(\alpha) \mathbf{R}_z(\beta) \mathbf{R}_y(\gamma) \quad (4.27)$$

Such, that the angle  $\gamma$  is immediately associated with the *goniometer angle*  $\gamma_G$ . Once the rotation matrix is known, the conventional parameterization

$$\mathbf{R}_{LC} = \mathbf{R}_z(\phi) \mathbf{R}_y(\theta) \mathbf{R}_z(\psi) \quad (4.28)$$

is calculated and used for all other modeling.

<sup>5</sup>Here the transformation was chosen heuristically. A more formal treatment of the various frames of reference can be found in [75].



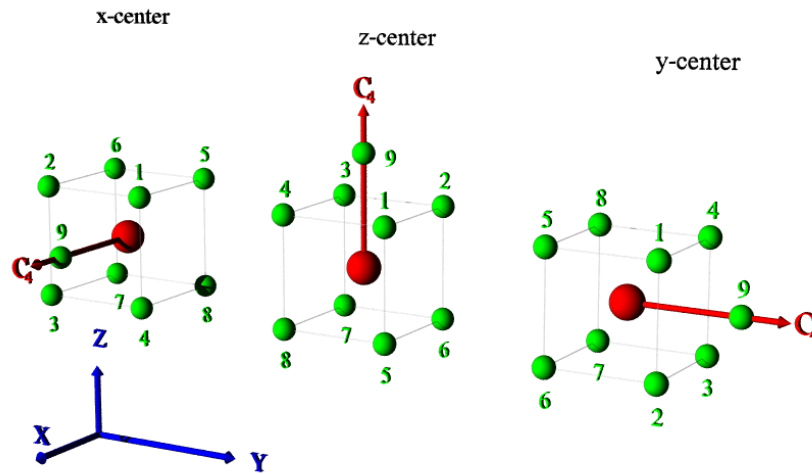


**Figure 4.6:** Crystal frame of reference and three possible orientations of the tetragonal paramagnetic centers present in  $\text{CaF}_2:\text{Ce}$ .

### 4.3.2 Modeling of the EPR Spectra

As mentioned in Section 4.2.1, the interstitial charge-compensating fluorine can assume six different orientations relative to the cerium ion and a coordinate system fixed to the crystal. Every pair of positions, where the fluorine is placed on the same axis (e.g., “above” or “below” the cerium) are equivalent with respect to the spectral properties. The EPR spectra will, therefore, consist of three distinct lines, whose positions are strongly dependent on the orientation of the magnetic field relative to the crystal axes.

The coordinate system fixed to the sample (the “crystal frame”) is defined such that its Cartesian axes coincide with the principal directions of the cubic crystal lattice. Centers will be called  $x$ -,  $y$ - or  $z$ -centers depending on the orientation of their  $C_4$  axis of symmetry with respect to the crystal frame. The numbering of the fluorine nuclei is such that  $I_1$  is found along the  $[111]$  direction and  $I_5$  along the  $[\bar{1}\bar{1}\bar{1}]$  direction in the  $z$ -center as shown in Figure 4.6. The  $x$ - and  $y$ -centers are obtained from the  $z$ -center by rotation around the  $[111]$  direction by  $120^\circ$  and  $240^\circ$  respectively. The charge-compensating fluorine is always labeled  $I_9$ .

It is also possible for the charge-compensating fluorine to occupy the next vacant cube in the  $[111]$  direction with respect to the cerium ion. The concentration of such *trigonal* centers is very low in our samples and they give no significant contribution to the EPR spectra. When the charge-compensating fluorine is situated at a distance from the cerium ion which is greater than the range of the hyperfine interaction, the paramagnetic center retains the cubic symmetry of the host crystal. The EPR line is then independent of the field orientation and can be used for field calibration.

The electron spin Zeeman term of Equation (4.19) is by far the largest contribution to the Hamiltonian. It dominates the next largest interactions (nuclear Zeeman and hyperfine) by a factor of  $10^3$ . In a very good approximation, the

positions of the ESR lines are, therefore, determined by the electron Zeeman contribution, while the rest of the Hamiltonian affects only the shape of those lines.

Because of the  $C_4$  symmetry, the  $g$ -tensor of the electron spin is axially symmetric. In the crystal frame, the  $g$ -tensors of the three types of centers are given by

$$\mathbf{g}_x^{(c)} = \begin{pmatrix} g_{\parallel} & 0 & 0 \\ 0 & g_{\perp} & 0 \\ 0 & 0 & g_{\perp} \end{pmatrix} \quad (4.29a)$$

$$\mathbf{g}_y^{(c)} = \begin{pmatrix} g_{\perp} & 0 & 0 \\ 0 & g_{\parallel} & 0 \\ 0 & 0 & g_{\perp} \end{pmatrix} \quad (4.29b)$$

$$\mathbf{g}_z^{(c)} = \begin{pmatrix} g_{\perp} & 0 & 0 \\ 0 & g_{\perp} & 0 \\ 0 & 0 & g_{\parallel} \end{pmatrix} \quad (4.29c)$$

The magnetic field in the laboratory frame is

$$\mathbf{B}_0^{(l)} = B_0 \mathbf{b}_0^{(l)} = B_0 \begin{pmatrix} 0 \\ 0 \\ 1 \end{pmatrix} \quad (4.30)$$

where  $\mathbf{b}_0^{(l)}$  is the unit vector in the field direction. In the crystal frame the magnetic field is

$$\mathbf{B}_0^{(c)} = \mathbf{R}_{LC}(\alpha, \beta, \gamma) \mathbf{B}_0^{(l)} \quad (4.31)$$

and the magnitude of the *effective* magnetic field in the crystal frame for a given center is

$$B_{x,y,z}^{(eff)} = \left| \mathbf{g}_{x,y,z}^{(c)} \mathbf{B}_0^{(c)} \right| = \left| \mathbf{g}_{x,y,z}^{(c)} \mathbf{R}_{LC}(\alpha, \beta, \gamma) \mathbf{b}_0^{(l)} B_0 \right| = g_{x,y,z}^{(eff)} B_0 \quad (4.32)$$

with the effective  $g$ -factor depending on the Euler angles:

$$g_{x,y,z}^{(eff)}(\alpha, \beta, \gamma) = \left| \mathbf{g}_{x,y,z}^{(c)} \mathbf{R}_{LC}(\alpha, \beta, \gamma) \mathbf{b}_0^{(l)} \right| \quad (4.33)$$

Equations (4.26) - (4.27) and (4.33) allow the angular dependence of the  $g$ -factors for the tetragonal centers to be computed. The fourth line featured in the EPR-spectrum belongs to the cubic center, whose  $g$ -factor  $g_c$  is independent of orientation.

### 4.3.3 Fitting of the EPR Spectra

In order to obtain the EPR-spectra of CaF<sub>2</sub>:Ce, the *Hahn echo* pulse sequence was used. A typical field spectrum is shown in Figure 4.7. It features the four lines arising from the tetragonal and the cubic centers and a broad, unresolved background contribution at around 0.32 T. Because the microwave field  $\mathbf{B}_1$  is at right angles with the static field  $\mathbf{B}_0$ , the anisotropy of the  $g$ -tensor leads to very small transition probabilities and small signal strengths for high values of

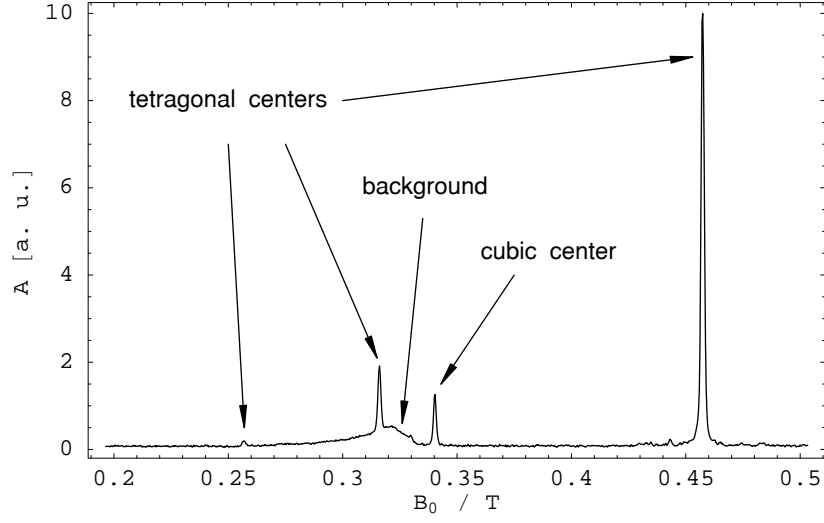


**Figure 4.7:** Typical field spectrum of  $\text{CaF}_2:\text{Ce}$  recorded using the Hahn echo sequence on an X-band spectrometer at  $\nu_0 = 9.350400$  GHz and  $T = 8.0$  K.

the effective  $g$ -factor. This explains the small amplitudes of the resonance lines at the lower end of the spectrum.

EPR-spectra were recorded for a range of goniometer angles  $\gamma_G$  between  $-13^\circ$  and  $360^\circ$ . The line positions were obtained by fitting with Gaussian line shape. Figure 4.8 shows a polar plot of  $1/\sqrt{g^{(eff)}}$  for all fitted lines. The contours of this quantity should be perfect ellipsis reflecting the symmetry properties of the tetragonal centers. Careful analysis, however, shows that  $g(\gamma_G) \neq g(\gamma_G + \pi)$ . This can only be explained by assuming a deviation of the angle between the goniometer axis and the  $B_0$  direction from  $90^\circ$ . To account for this misalignment, the coordinate transformation given in Equation (4.27) was modified:

$$\mathbf{R}_{\text{LC}}(\alpha, \beta, \gamma, \xi) = \mathbf{R}_y(\alpha) \mathbf{R}_z(\beta) \mathbf{R}_y(\gamma) \mathbf{R}_x(\xi) \quad (4.34)$$

Using this expression, the equations for the dependence of the effective  $g$ -factors on the Euler angles and the goniometer tilt can be derived as outlined in Section 4.3.2:

$$\begin{aligned} g_x^{(eff)^2} &= g_{\perp}^2 (\cos \xi \sin \beta \sin \gamma - \cos \beta \sin \xi)^2 + \\ &g_{\parallel}^2 (\cos \gamma \cos \xi \sin \alpha + \cos \alpha (\cos \beta \cos \xi \sin \gamma + \sin \beta \sin \xi))^2 + \\ &g_{\perp}^2 (\cos \alpha \cos \gamma \cos \xi - \sin \alpha (\cos \beta \cos \xi \sin \gamma + \sin \beta \sin \xi))^2 \quad (4.35a) \end{aligned}$$

$$\begin{aligned} g_y^{(eff)^2} &= g_{\parallel}^2 (\cos \xi \sin \beta \sin \gamma - \cos \beta \sin \xi)^2 + \\ &g_{\perp}^2 (\cos \gamma \cos \xi \sin \alpha + \cos \alpha (\cos \beta \cos \xi \sin \gamma + \sin \beta \sin \xi))^2 + \\ &g_{\perp}^2 (\cos \alpha \cos \gamma \cos \xi - \sin \alpha (\cos \beta \cos \xi \sin \gamma + \sin \beta \sin \xi))^2 \quad (4.35b) \end{aligned}$$

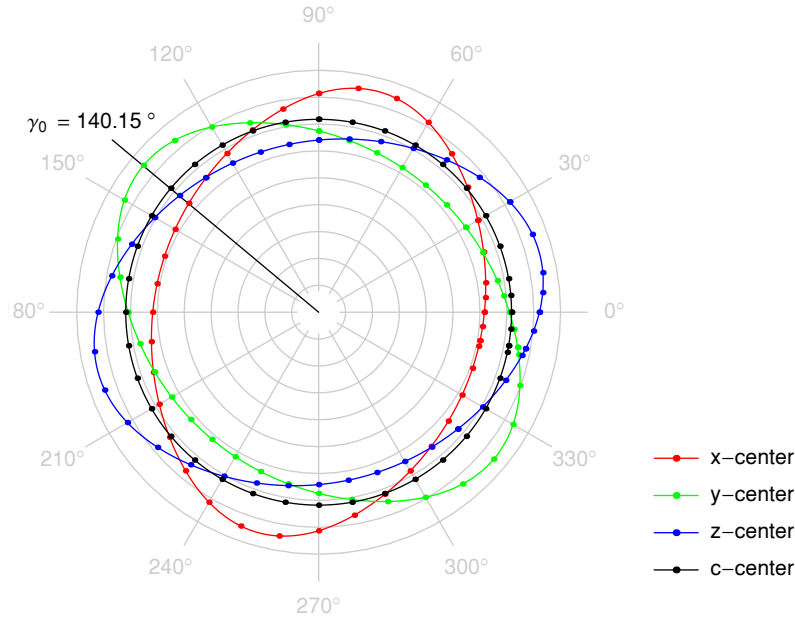


**Figure 4.8:** Polar plot of the dependence of the  $g$ -factors for various centers in  $\text{CaF}_2:\text{Ce}$  on the goniometer angle  $\gamma_0$ . The radial coordinate is given by  $1/\sqrt{g^{(eff)}}$ . The contours for the tetragonal centers have elliptic shape. The circular contour belongs to the cubic center.

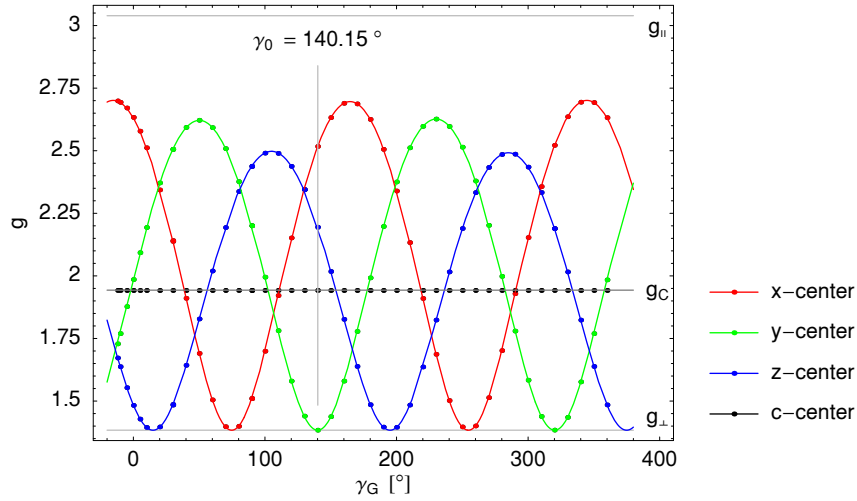


**Figure 4.9:** Fit of the dependence of the effective  $g$ -factors on the goniometer angle. The solid lines are plots of the expressions in Equation (4.33) using the fitted values. Gray horizontal lines indicate the found values of  $g_{\parallel}$ ,  $g_{\perp}$ , and  $g_c$ . The vertical line shows the fitted value of the goniometer scale offset. Experimental details in caption to Figure 4.7.

$$\begin{aligned}
g_z^{(eff)^2} = & g_{\perp}^2 (\cos \xi \sin \beta \sin \gamma - \cos \beta \sin \xi)^2 + \\
& g_{\perp}^2 (\cos \gamma \cos \xi \sin \alpha + \cos \alpha (\cos \beta \cos \xi \sin \gamma + \sin \beta \sin \xi))^2 + \\
& g_{\parallel}^2 (\cos \alpha \cos \gamma \cos \xi - \sin \alpha (\cos \beta \cos \xi \sin \gamma + \sin \beta \sin \xi))^2 \quad (4.35c)
\end{aligned}$$

These expressions and a manual selection of the angles were used to assign data points to particular centers. Latter choice was *a posteriori* found to be consistent with the fit results. A least-square fit to the measured  $g$ -values was performed for all three centers simultaneously. Since the starting value of the goniometer scale was not known the Euler angle  $\gamma$  was replaced by  $\gamma_G - \gamma_0$ . The full set of fitting parameters was thus  $\alpha$ ,  $\beta$ ,  $\gamma_0$ ,  $\xi$ ,  $g_{\parallel}$ , and  $g_{\perp}$ .

It should be noted at this point, that the angles are not independent. Firstly, the Euler theorem states that any three-dimensional rotation can be fully described by a set of three angles. In addition, an examination of the Hamilton operator of the paramagnetic center shows that it is invariant under rotations around the direction of the static field. Thus, only four of the six fit parameters are independent.<sup>6</sup>

In principle, Equation (4.35) could be reexpressed in terms of two such angles plus an additional parameter accounting for the arbitrary starting point of the goniometer scale. Because of the speed of modern computer hardware, such analysis was not required.

The results of the fit are summarized in Table 4.1. Using these parameters the

$\alpha$	51.15°	$g_{\parallel}$	3.0394	(3.038)
$\beta$	55.47°	$g_{\perp}$	1.3836	(1.396)
$\gamma_0$	140.15°			
$\xi$	-0.11°			

**Table 4.1:** Fitted values of the Euler angles and  $g$ -factors for the CaF<sub>2</sub> sample. The values in parentheses were reported in [96]. These angles are determined by the way the sample is attached to the mount. The actual orientation of the sample with respect to the external field depends on the goniometer angle  $\gamma_G$ .

two independent Euler angles of the magnetic field with respect to the crystal frame of reference can be calculated for each sample orientation characterized by the corresponding value of the goniometer angle.

It must be mentioned that because of the nature of the sample mount, the true orientation of the sample varied slightly ( $< 1^\circ$ ) after each weekly cooling cycle. It was, however, possible to find the true current orientation using a fit of the ENDOR spectrum as described below.

## 4.4 ENDOR Spectra

The pervious section dealt with the properties of the  $S$ -bus server spin  $S$ . The second important ingredient of the  $S$ -bus scheme are the client spins  $I_j$ . These were manipulated by rf pulses, applied at their ENDOR transition frequencies.

<sup>6</sup>Since the microwave field was oriented at right angles to the static field, the knowledge of the third Euler angled can, in principle, be gained by measuring the angular dependence of the Rabi precession frequency.

#### 4.4.1 ENDOR Spectra and Hyperfine Parameters

Frequently, the Zeeman interaction is much stronger than the hyperfine coupling. In this *high field approximation*, the hyperfine coupling can thus be treated as perturbation. This commonly encountered case gives a good starting point for the discussion of the energy level diagram:

$$\mathcal{H} = \nu_{0_S} \mathbf{S}_z + \sum_j (\nu_{0_I} + a_j \mathbf{S}_z) \mathbf{I}_{z_j} + \sum_{j < k} D_{jk} \mathbf{I}_{z_j} \mathbf{I}_{z_k} \quad (4.36)$$

The Larmor frequency of the electron spin  $\nu_{0_S} = \mu_B/h g^{(eff)} B_0$  is approximately 9.5 GHz for  $B_0 = 2.5 - 4.5$  T (see Section 4.3.3 for details). The free fluorine nuclear Larmor frequency  $\nu_{0_I} = \gamma_F B_0/2\pi$  is determined by the magneto-gyric ratio of the fluorine nucleus  $\gamma_F = 25.18148 \times 10^7 \text{s}^{-1} \text{T}^{-1}$ . In range of fields of interest,  $\nu_{0_I}$  lies between 11 MHz and 18 MHz. The effective hyperfine couplings  $a_j$  can be as large as 19 MHz. The dipolar couplings constants  $D_{jk}$  are up to approximately 10 kHz.

Since the Hamiltonian in Equation (4.36) is diagonal the resonant frequencies for the energy levels are readily expressed in terms of the spin quantum numbers  $m_S$  and  $m_I$  of the electron and nuclear spins respectively:

$$\nu(m_S, m_I) = m_S \nu_{0_S} + \sum_j (\nu_{0_I} + m_{I_j} a_j) + \sum_{j < k} m_{I_j} m_{I_k} \quad (4.37)$$

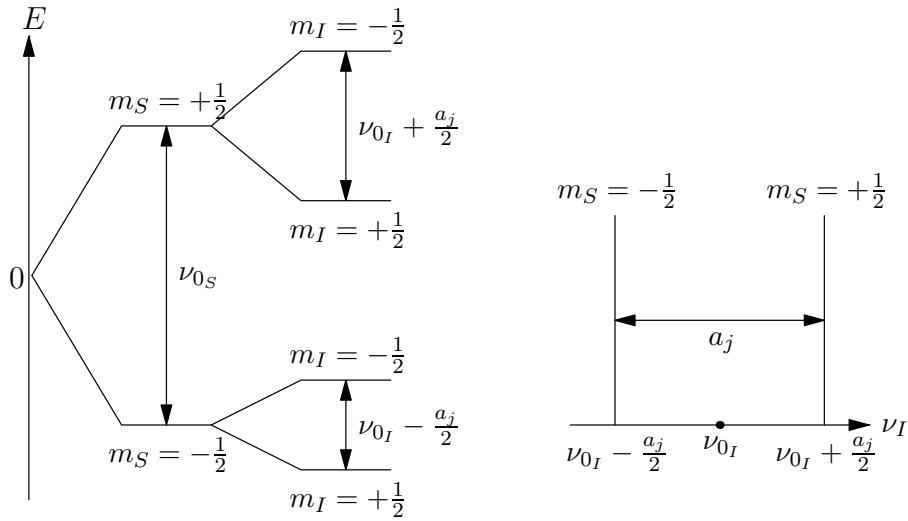


**Figure 4.10:** Energy level diagram (left) and expected ENDOR spectrum (right) of a single nuclear spin coupled to an electron spin in the high field approximation.

The level diagram of a single nuclear spin coupled to the electron spin is shown in Figure 4.10. Under the above mentioned conditions, the two ENDOR transitions corresponding to the two electron spin states  $m_S = \pm 1/2$  are situated symmetrically around the free nuclear Larmor frequency  $\nu_{I_0}$  at a distance of  $a_j$  from each other. Because the dipolar couplings amongst the nuclear spins are

very weak compared to the other contributions to the Hamiltonian, their effect is restricted to small line broadening and all nuclear spins can be considered separately. Thus, the other eight nuclear spins would produce the same pattern with corresponding values of  $a_j$  giving rise to a total of nine lines for  $m_S = -1/2$  and another nine lines for  $m_S = +1/2$ . The lines corresponding to the fluorine nuclei in the second and higher coordination shells can be suppressed (see below).

The ENDOR spectra are obtained by applying the pulse sequence shown in Figure 4.11. After the  $yy$ -preparation sequence on the electron spin and the

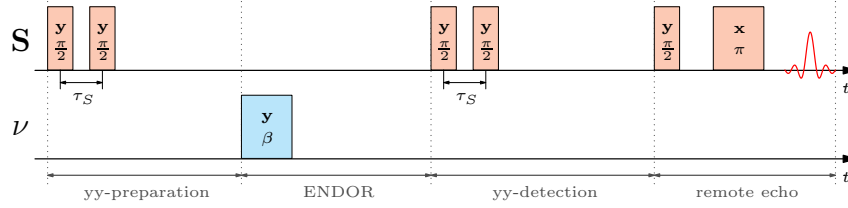


**Figure 4.11:** Pulse sequence for ENDOR experiments. An  $\pi$ -pulse is applied between the preparation and detection sequences for the electron spin. The frequency  $\nu$  of the pulse is scanned to record the ENDOR spectrum.

appropriate decay time of approximately  $100 \mu\text{s}$ , an rf-pulse of length  $t_p$  is applied at a frequency  $\nu$  followed by the  $yy$ -detection sequence and the remote echo sequence for the electron.

When the rf frequency  $\nu$  coincides with an ENDOR transition, the amplitude of the the corresponding operator component  $\mathbf{I}_{z_j}$  is scaled by  $S_j = \cos \beta$ . Where  $\beta = 2\pi \nu_{1_j} t_p$ , with the Rabi frequency  $\nu_{1_j}$  of the spin  $j$ . The  $S$ -bus theory in Section 4.1.2 can be used to calculate the change of the signal relative to off-resonant rf:

$$S_{ENDOR}^{(yy)} = (1 - S_j) s_j^2 P_1^{(-)} \quad (4.38)$$

Since the Rabi frequencies of the individual spins are not known *a priori*, the rotation angles of the frequency-swept pulse will vary. The maximum response with  $S_j = -1$  is reached for a perfect  $\beta = \pi$ -pulse. However, even for rotation angles  $\beta \neq \pi$ , the parameter  $S_j$  will vary significantly when  $\nu$  is swept across an ENDOR resonance making the measurement very robust.

The parameter  $s_j = \sin(a_j \tau_S / 2)$  allows for a certain amount of selectivity with respect to the strength of the hyperfine interaction  $a_j$ . When  $\tau_S$  is kept short, i.e.,  $\tau_S < 100 \text{ ns}$ , nuclei which are far from the electron spin and have small hyperfine couplings fail to build up significant polarization during the preparation time. Their transition lines, which lie close to the free fluorine frequency  $\nu_{0_I}$  have very small amplitudes. The next-neighbor nuclei with large hyperfine couplings, on the other hand, produce very pronounced transition lines.

Figure 4.12 shows an example of a measured ENDOR spectrum. It consists of 18 resolved lines as expected.<sup>7</sup> Full line widths at half of the maximum amplitude (FWHM) are approximately 30 kHz. The ENDOR spectrum is clearly not symmetric with respect to the free fluorine frequency, as would be expected according to the simple model above.

<sup>7</sup>Lines  $L_{12}$  and  $L_{13}$  partially overlap at the indicated sample orientation. It is, however, possible to obtain a fully resolved spectrum at other orientations.

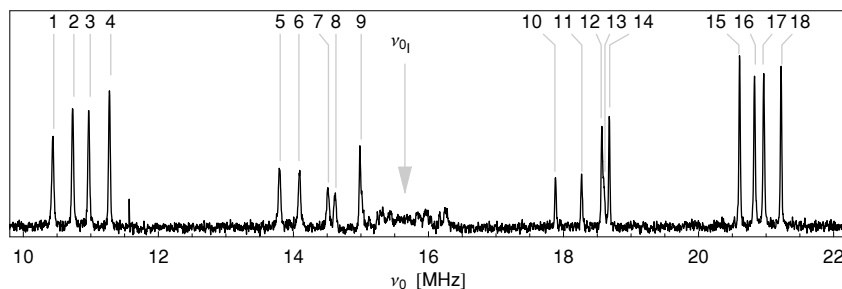


**Figure 4.12:** ENDOR spectrum of CaF<sub>2</sub>:Ce. Lines are numbered left-to-right. All 18 lines except for  $L_{12}$  and  $L_{13}$  are resolved. The arrow indicates the free fluorine resonance frequency  $\nu_{0_I} = 15.651$  MHz. Experimental parameters:  $z$ -center,  $\gamma_G = 346.0^\circ$ ,  $\varphi = -157.75^\circ$ ,  $\vartheta = 111.71^\circ$ ,  $\psi = 134.83^\circ$ ,  $\nu_{0_S} = 9.342206$  GHz,  $B_0 = 0.39052$  T,  $\tau_S = 32$  ns,  $T = 8.0$  K.

This asymmetry is due to the fact that, in CaF<sub>2</sub>:Ce, the hyperfine interaction is in the same order of magnitude as the Zeeman splitting of the nuclear spins, such that the high field approximation is not valid and no closed form solution for the level spectrum can be given. As a result – dependent on the nuclear spin and sample orientation – the ENDOR lines of the next-neighbor nuclear spins corresponding to  $m_S = \pm 1/2$  are, in general, no longer symmetric with respect to  $\nu_{0_I}$  and can even lie to the same side of it. This greatly complicates the modeling of the ENDOR spectra. In particular, at an unknown orientation, it is not possible to tell which pair of lines belongs to the same nuclear spin from the ENDOR spectrum alone.

#### 4.4.2 TRIPLE Spectra and $m_S$ Assignment

A possible way to ascertain which ENDOR lines belong to the same state  $m_S$  of the electron spin is the TRIPLE [98] experiment. It makes no specific assumptions about the energy level system.

The experiment begins with a measurement of a usual pulsed ENDOR spectrum. Once the resonant frequencies and line amplitudes for the ENDOR transitions are known, the experiment proceeds as follows. One of the ENDOR lines ( $j$ ) is saturated by a  $\pi/2$ -pulse followed by a second  $\pi$ -pulse whose frequency is scanned over the positions of the other ENDOR lines, as shown in Figure 4.13. When the frequency of the second pulse matches the resonant frequency of another transition line ( $k$ ) the signal amplitude will be given by

$$S_{TRIPLE}^{(yy)} = (1 - S_k) s_k^2 c_j^2 P_2^{(-)} \quad (4.39)$$

if both lines belong to the same  $m_S$ . Thus, all lines belonging to the same  $m_S$  as the line  $j$  will be attenuated by a factor of  $c_j^2$  when the first pulse is turned on as opposed to when it is off. In praxis, the Rabi frequencies for each ENDOR-line must be known to produce correct  $\pi$ -pulses. In some cases, that measurement is imprecise and Rabi frequencies are not well known. As a result of this and other pulse errors, some variation of the attenuation factor can be expected. In any case, the attenuation factor can be made large by saturating a line at the



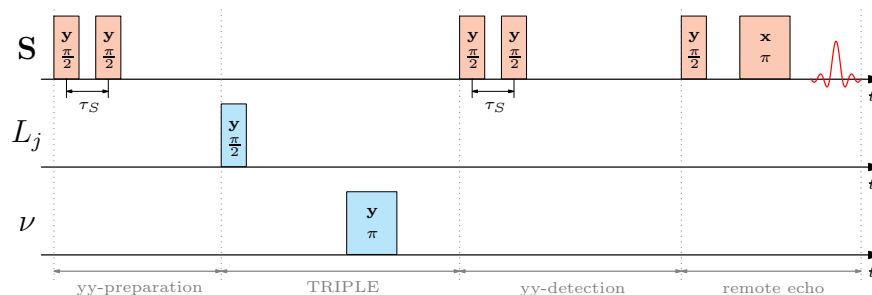


**Figure 4.13:** TRIPLE pulse sequence for assignment of the ENDOR transition lines to different  $m_S$ . A saturation pulse is applied to a selected transition  $L_j$  and an inversion pulse is scanned across the frequency spectrum. Lines unaffected by the saturation pulse belong to a different  $m_S$  than  $L_j$ .

outer extremes of the spectrum. Figure 4.14 compares the ENDOR spectrum from Figure 4.12 with the corresponding TRIPLE spectrum.

The saturation pulse of the TRIPLE sequence was applied to the line number 18. To save measurement time, the second pulse was only scanned through 170 kHz-wide regions around the ENDOR lines. The spectra were fitted with the real part of a Lorentzian line shape:

$$A = \frac{a_0}{1 + (\nu_0 - \nu)^2 / (\Delta\nu/2)^2} \quad (4.40)$$

where  $a_0$  indicates line amplitude,  $\nu_0$  line position, and  $\Delta\nu$  line width. Line intensities were obtained by multiplying line intensity and line width  $a_0 \Delta\nu$ . Table 4.2 summarizes the results. The measurement clearly separates the two line sets belonging to the two electron spin states  $m_S$ , although it does not indicate to *which*  $m_S$  each set belongs. This result can be used as one test of any model of the ENDOR spectra, as it must produce the same  $m_S$ -sets.

line	1	2	5	7	9	10	14	15	17
r	0.97	0.99	0.97	0.98	0.94	0.87	0.98	0.99	0.96
line	3	4	6	8	11	12	13	16	18
r	0.25	0.25	0.48	0.48	0.45	0.45	0.48	0.28	0.07

**Table 4.2:** Ratios  $r$  of line intensities of TRIPLE and ENDOR measurements for all ENDOR transitions (cf. Figure 4.14). Lines are grouped according to  $m_S$ .

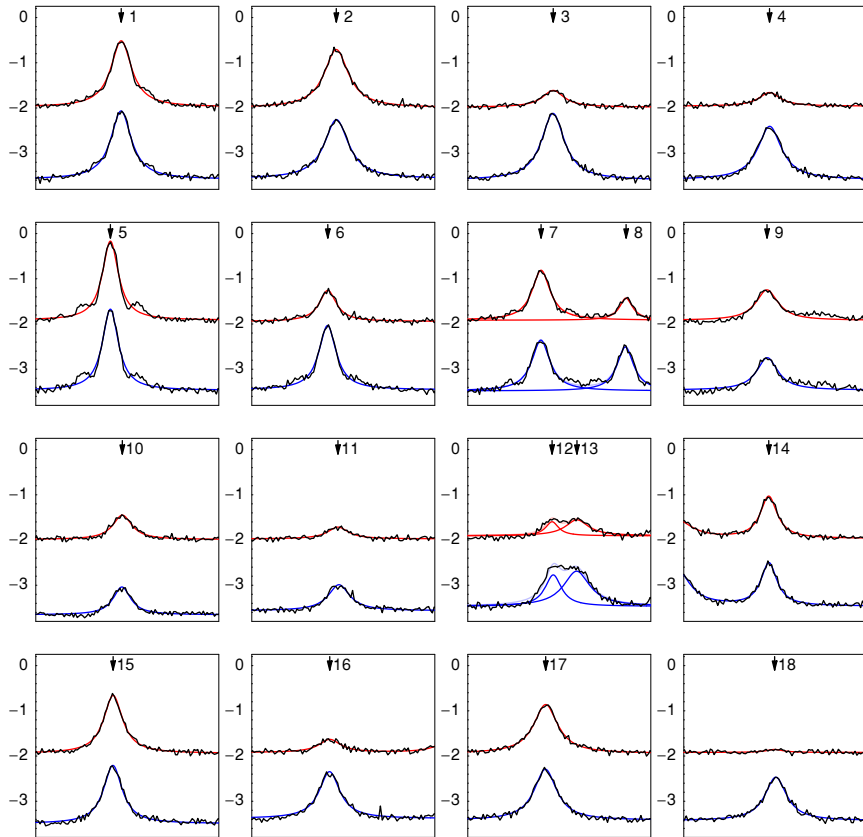


**Figure 4.14:** Assignment of ENDOR lines to different values of  $m_S$  by a TRIPLE measurement. Blue: standard ENDOR spectrum, red: ENDOR spectrum after a saturation pulse. The black lines show experimental data, the colored solid lines indicate fitted Lorentzian line shapes. The saturation pulse of the TRIPLE sequence was applied to line 18. Lines whose intensities are diminished in the presence of the saturation pulse belong to the same electron spin state  $m_S$  as line 18. Unaffected lines belong to the other  $m_S$ -state. For experimental details see Figure 4.12.

## 4.5 Numeric Modeling of the 10-Spin $S$ -Bus System

Although the simple analytic  $S$ -bus model provides qualitative understanding of the system, detailed quantitative description requires a more elaborate modeling effort. Because of the nature of the Hamiltonian and the size of the problem, exact analytic diagonalization is not possible. Therefore, numeric simulation of the cluster was performed.

### 4.5.1 Construction and Diagonalization of the Hamiltonian

Numeric modeling of magnetic properties of the  $\text{Ce}^{3+}$ -center in  $\text{CaF}_2$  begins with the construction of the  $2^{10} \times 2^{10}$  matrix representing the Hamiltonian in Equation (4.19). For operations involving spin component operators, algorithms described in Appendix C were used. The construction of the Hamiltonian is done in the laboratory frame of reference in units of MHz. The latter choice is appropriate, because it is a good compromise between the electron resonance frequencies of approximately 9.5 GHz and nuclear resonances between 10 MHz and 20 MHz and avoids very small and very large numbers, thus reducing the effect of finite precision arithmetics.

#### 4.5.1.1 The Zeeman Terms

First, the Zeeman term for the electron spin is constructed:

$$\mathcal{H}_S = \frac{\mu_B}{h} \mathbf{S} \cdot \mathbf{g} \cdot \mathbf{B}_0 \quad (4.41)$$

The  $g$ -tensor of the chosen type of paramagnetic center is set up in the crystal frame of reference (Section 4.3.2) and transformed to the laboratory frame by the transformation obtained from fitting of EPR spectra (Section 4.3.3):

$$\mathbf{g}_{x,y,z}^{(l)} = \mathbf{R}_{LC}^T \mathbf{g}_{x,y,z}^{(c)} \mathbf{R}_{LC} \quad (4.42)$$

To avoid unnecessary tensor multiplication operations, the local magnetic field of the electron spin  $\mathbf{g}^{(l)} \cdot \mathbf{B}_0$  is constructed prior to the addition of the Zeeman term to the target Hamiltonian.

The calculation of the nuclear Zeeman term

$$\mathcal{H}_N = \sum_{i=1}^N \frac{\mu_N}{h} g_N B_0 I_{z_i} \quad (4.43)$$

is somewhat simpler. Because the anisotropy of the nuclear spin environment is contained in the hyperfine contribution, straight forward addition of the appropriate terms to the diagonal components of the total Hamiltonian is used.

### 4.5.1.2 The Hyperfine Interaction Term

Construction of the hyperfine term

$$\mathcal{H}_{h,f} = \sum_{i=1}^N \mathbf{S} \cdot \mathbf{a}_i \cdot \mathbf{I}_i \quad (4.44)$$

requires the knowledge of the hyperfine tensors  $\mathbf{a}_i$ .

A detailed investigation of the hyperfine properties of tetragonal Ce-centers in CaF<sub>2</sub> has been undertaken by Baker *et al.* [96]. They have used measurements at field orientations along the crystal axes to obtain the hyperfine tensors components from such highly degenerate spectra. Their results are best expressed in terms of a *center frame of reference* where the  $z$  axis is oriented along the line connecting the cerium ion and the charge-compensating fluorine. For the  $z$ -center, this coincides with the crystal frame as shown in Figure 4.6. The nuclei are divided in three layers: I with the spins  $\mathbf{I}_1 - \mathbf{I}_4$ , II with  $\mathbf{I}_5 - \mathbf{I}_8$ , and III with  $\mathbf{I}_9$ . The hyperfine tensors within each layer are connected through simple  $\pi/2$ -rotations around the symmetry axis. Due to lattice distortion by the charge-compensating fluorine, there is no simple correspondence between the values for layers I and II. The form of the hyperfine tensors as required by site symmetry is

$$\mathbf{a}^{(I,II)} = \begin{pmatrix} a_1 & a_2 & a_4 \\ a_2 & a_1 & a_4 \\ a_5 & a_5 & a_3 \end{pmatrix}, \quad \mathbf{a}^{(III)} = \begin{pmatrix} a_1 & 0 & 0 \\ 0 & a_1 & 0 \\ 0 & 0 & a_3 \end{pmatrix}, \quad (4.45)$$

The values of parameters  $a_i$  as reported in [96] are summarized in Table 4.3.

layer	$a_1$	$a_2$	$a_3$	$a_4$	$a_5$
I	2.04	0.95	-5.88	6.25	10.26
II	0.52	-0.56	0.56	-5.70	-9.89
III	-1.20	0.00	19.36	0.00	0.00

**Table 4.3:** Hyperfine parameters of the next-neighbor <sup>19</sup>F nuclei in CaF<sub>2</sub>:Ce reported in [96]. For layers I and II the numbers provided here are valid for spins  $\mathbf{I}_1$  and  $\mathbf{I}_5$  respectively. The tensors for the other sites can be obtained through rotations (see text). Values in MHz.

The hyperfine term in Equation (4.44) can thus be calculated. Its construction is computationally intensive because the hyperfine tensors given in Equation (4.45) in the center frame must be transformed to the laboratory frame and, in this form, have no vanishing elements. Therefore, for each nuclear spin  $j$ , nine expressions of the form  $\mathbf{S}_k a_{kl} \mathbf{I}_{l_j}$  must be evaluated, where Cartesian operator components  $\mathbf{S}_k$  and  $\mathbf{I}_{l_j}$  are represented by  $2^{10} \times 2^{10}$ -matrices. Again, the use of algorithms in Appendix C reduces the execution time for this stage by a factor of 20-30 with respect to full matrix multiplication.

### 4.5.1.3 The Dipole-Dipole Coupling Term

The most computationally expensive contribution are the dipole-dipole couplings between the nuclear spins which also represents the weakest interaction

on the scale of a few kHz.

$$\mathcal{H}_{dd} = \sum_{i < j}^N \mathbf{I}_i \cdot \mathbf{D}_{ij} \cdot \mathbf{I}_j \quad (4.46)$$

The dipolar tensors of Equation (4.24):

$$(\mathbf{D}_{ij})_{kl} = \frac{\mu_0}{4\pi r_0^3} h\gamma_F^2 (\delta_{kl} - 3r_k r_l) \quad (4.47)$$

depend on the internuclear vector  $\mathbf{r}$  whose components are calculated in the crystal frame from nuclear spin coordinates. For the  $z$ -center, these coordinates are given in Table 4.4. Coordinates for the other centers are given by rotations around the [111] direction as described in Section 4.3. The dipolar tensors  $\mathbf{D}_{ij}$

$$\begin{aligned} \mathbf{r}_1 &= a_0 ((1, 1, 1) + \epsilon(1, 1, -1)), & \mathbf{r}_5 &= a_0 (1, 1, -1) \\ \mathbf{r}_2 &= a_0 ((-1, 1, 1) + \epsilon(-1, 1, -1)), & \mathbf{r}_6 &= a_0 (-1, 1, -1) \\ \mathbf{r}_3 &= a_0 ((-1, -1, 1) + \epsilon(-1, -1, -1)), & \mathbf{r}_7 &= a_0 (-1, -1, -1) \\ \mathbf{r}_4 &= a_0 ((1, -1, 1) + \epsilon(1, -1, -1)), & \mathbf{r}_8 &= a_0 (1, -1, -1) \\ & & \mathbf{r}_9 &= a_0 (0, 0, 2) \end{aligned}$$

**Table 4.4:** Positions of the nine next-neighbor nuclear spins in  $\text{CaF}_2:\text{Ce}$  for a  $z$ -center.  $2a_0 = 0.273$  nm is the fluorine-fluorine distance in an undistorted  $\text{CaF}_2$  lattice,  $\epsilon = 0.09$  is the distortion in the fluorine positions in layer I caused by incorporation of the interstitial charge-compensating fluorine. For more details see [96].

are constructed in the crystal frame and transformed to the laboratory frame, as described above for the  $g$ -tensor. This is followed by the tensor multiplication of the appropriate nuclear spin operators. Addition of this term concludes the construction of the total Hamilton operator  $\mathcal{H}^{(l)}$  in the laboratory frame of reference.

#### 4.5.1.4 Diagonalization of the Hamiltonian

For diagonalization of the Hamiltonian, the routine `zheevr`<sup>8</sup> from the standard LAPACK [99] package was used. The result is the list  $\Lambda$  of the 1024 eigenvalues of the system. They represent the energies of the eigenstates of the system in frequency units. The eigenvectors corresponding to these eigenvalues are returned in the matrix  $V$  such that

$$\mathcal{H}^{(l)} = V^\dagger \mathcal{H}^{(d)} V \quad (4.48)$$

With the Hamiltonian represented in the eigenbasis by the empty matrix with the eigenvalues  $\lambda_j$  placed on the main diagonal:

$$\left(\mathcal{H}^{(d)}\right)_{jk} = \lambda_j \delta_{jk} \quad (4.49)$$

Incidentally, Equation (4.48) means that the rows of  $V$  are eigenvectors of  $\mathcal{H}^{(l)}$ .

<sup>8</sup>This routine solves eigenvalue problems of complex double precision Hermitian matrices using ‘‘Relatively Robust Representations’’.

### 4.5.2 The Fictitious Eigenframe Hamiltonian

In its diagonal form, the Hamiltonian is representable by a linear combination of the  $z$ -component operators of the form:

$$\mathcal{H}^{(d)} = \sum_q a_q \prod_{j \in q} \mathbf{I}_{z_j} \quad (4.50)$$

Here,  $\mathbf{I}_{z_j}$  stands for the electron spin or any nuclear spin and  $q$  is a set containing between one and ten spin indices. Different parts of this Hamiltonian represent different properties of the spin system. For instance, the term

$$\mathcal{H}_S^{(d)} \approx a_0 \mathbf{S}_z \quad (4.51)$$

represents the Zeeman interaction of the electron spin modified by the coupling to the nuclear spins. The precession frequency is then given by the coefficient  $a_0$ .

Because the hyperfine couplings are in the same order of magnitude as the Zeeman energy of the nuclear spins and much larger than dipolar couplings between the nuclear spins, the transition frequencies of the nuclear spins will be approximately given by

$$\mathcal{H}_{N_j}^{(d)} \approx (a_j + a_{0,j} \mathbf{S}_z) \mathbf{I}_{z_j} \quad (4.52)$$

Another property, important for the use of the cluster for quantum computing, is the strength of the coupling between two nuclear spins:

$$\begin{aligned} \mathcal{H}_{jk}^{(d)} = & (a_{j,k} + a_{0,j,k} \mathbf{S}_z + \\ & a_{1,j,k} \mathbf{I}_{z_1} + \cdots + a_{9,j,k} \mathbf{I}_{z_9} + \\ & a_{l,m,j,k} \mathbf{I}_{z_l} \mathbf{I}_{z_m} + \cdots \\ & a_{0,l,m,j,k} \mathbf{S}_z \mathbf{I}_{z_l} \mathbf{I}_{z_m} + \cdots) \mathbf{I}_{z_j} \mathbf{I}_{z_k} \end{aligned} \quad (4.53)$$

This representation demonstrates a very interesting fact: Even when the direct dipolar coupling between spins  $j$  and  $k$  vanishes, there still remains a dipolar-like spin-spin interaction mediated by the electron spin and to a much lesser degree by the remaining nuclear spins. These *indirect contributions* may increase or diminish the total spin-spin coupling. This feature is already a demonstration of the “bus”-role which the electron spin assumes in the  $S$ -bus arrangement.

Direct calculation of all these properties requires the ability to represent the diagonal Hamiltonian in the form of Equation (4.50). This, in turn, requires the knowledge of the operators  $\mathbf{I}_{z_j}$  in the eigenframe, which is not readily available.

### 4.5.3 The Sorting Problem

Mathematically, the order in which the eigenvalues and eigenvectors are returned by the computation is arbitrary. Equation (4.48) is still valid, when any two rows of the matrix  $V$  are exchanged, provided the correspondence between eigenvectors and eigenvalues is preserved. The LAPACK routine `zhgeevr` returns the eigenvalues in ascending order.

The eigensystem of the Hamiltonian is defined by its relationship with the Hamiltonian expressed in the laboratory frame (Equation (4.48)). This relation is, in turn, defined by the matrix  $V$ . One would like to probe the properties of the system in connection with the spins of which it is composed. Consider, for instance, a transition of the nuclear spin number seven from the state “spin up” to “spin down”. Which eigenvalues belong to the two states participating in this transition?

In order to answer this question, it would be important to be able to define the  $\mathbf{I}_{z_7}$ -operator in the eigenframe. Because the eigenvectors are returned “scrambled” by the computational routines, this is a non-trivial task. The following example [91] illustrates the problem.

Consider a simple two-spin Hamiltonian given in units of Hz:

$$\mathcal{H} = 4\mathbf{I}_{x_1} + 2\mathbf{I}_{z_2} \quad (4.54)$$

Since the part pertaining to the second spin is already diagonal, it is easy to construct a transformation which diagonalizes the first part and therefore the entire Hamiltonian:

$$V_a = \exp(i\theta\mathbf{I}_{y_1}) = \frac{1}{\sqrt{2}} \begin{pmatrix} 1 & 0 & 1 & 0 \\ 0 & 1 & 0 & 1 \\ -1 & 0 & 1 & 0 \\ 0 & -1 & 0 & 1 \end{pmatrix}, \quad \text{for } \theta = \pi/2 \quad (4.55)$$

The rows of  $V_a$  are the eigenvectors of the Hamiltonian. The eigenvalues are obtained by transforming  $\mathcal{H}$  to its eigenframe:

$$\mathcal{H}_a^{(d)} = V_a \mathcal{H} V_a^\dagger = \begin{pmatrix} 3 & 0 & 0 & 0 \\ 0 & 1 & 0 & 0 \\ 0 & 0 & -1 & 0 \\ 0 & 0 & 0 & -3 \end{pmatrix} \quad (4.56)$$

Now, consider the result of the transformation of base operators from the laboratory frame to the eigenframe:

$$\mathbf{I}_{z_1}^{(d)} = V_a \mathbf{I}_{z_1}^{(l)} V_a^\dagger = -\mathbf{I}_{x_1}^{(e)} \quad \text{and} \quad \mathbf{I}_{z_2}^{(d)} = V_a \mathbf{I}_{z_2}^{(l)} V_a^\dagger = \mathbf{I}_{z_2}^{(e)} \quad (4.57)$$

As one can see, properties attached to any spin in the laboratory frame remain connected to that same spin and only to that spin in the eigenframe. The quantization axes of the two spins are  $\mathbf{I}_{x_1}^{(e)}$  and  $\mathbf{I}_{z_2}^{(e)}$ . This means, that the spin component operator representation for a given spin can be constructed in the eigenframe by the simple tensor multiplication of a Pauli matrix with the unit matrices in appropriate order (see Appendix B).

A numeric solution of the same problem (here done in *Mathematica*) produces the following eigenvectors and eigenvalues:

$$V_n = \frac{1}{\sqrt{2}} \begin{pmatrix} 0 & -1 & 0 & 1 \\ 1 & 0 & 1 & 0 \\ 1 & 0 & -1 & 0 \\ 0 & -1 & 0 & -1 \end{pmatrix} \quad (4.58)$$

and

$$\mathcal{H}_n^{(d)} = \begin{pmatrix} -3 & 0 & 0 & 0 \\ 0 & 3 & 0 & 0 \\ 0 & 0 & -1 & 0 \\ 0 & 0 & 0 & 1 \end{pmatrix} \quad (4.59)$$

Notice, that the eigenvalues and up to a sign the eigenvectors are the same as above, only their order is different. This has a dramatic effect on the transformation properties of the spin component operators:

$$\mathbf{I}_{z_1}^{(d)} = V_n \mathbf{I}_{z_1}^{(l)} V_n^\dagger = 2 \mathbf{I}_{x_1}^{(e)} \mathbf{I}_{x_2}^{(e)}, \quad \text{and} \quad \mathbf{I}_{z_2}^{(d)} = V_n \mathbf{I}_{z_2}^{(l)} V_n^\dagger = -2 \mathbf{I}_{z_1}^{(e)} \mathbf{I}_{z_2}^{(e)} \quad (4.60)$$

The simple correspondence between the spin operator bases in the laboratory frame and in the eigenframe is lost. Since no inter-spin coupling is present in the Hamiltonian, this mixing of the Hilbert spaces of the constituent spins is entirely artificial. In the case of the *S*-bus Hamiltonian, with its strong coupling contributions, the eigenstates are, of course, expected to be mixed to some degree. In particular, states of the nuclear spins will have significant contributions from the electron spin. This further complicates the task of finding the quantization axes.

Furthermore, due to strong anisotropies of the interaction tensors, there is no single quantization axis for all spins. In general, each spin will be quantized along its own direction which is different from that of all other spins. This further aggravates the problem of extracting useful information from the diagonalized Hamiltonian.

Reordering of the eigenvectors can be represented by a sorting matrix  $S$  such that

$$S \mathcal{H}_n^{(d)} S^T = \mathcal{H}_a^{(d)} \quad \text{and} \quad S V_n = V_a \quad (4.61)$$

For the example above, such a matrix is readily given:

$$S = \begin{pmatrix} 0 & 1 & 0 & 0 \\ 0 & 0 & 0 & -1 \\ 0 & 0 & -1 & 0 \\ 1 & 0 & 0 & 0 \end{pmatrix} \quad (4.62)$$

In the case of a large spin system with strong couplings, finding the appropriate sorting matrix is a non-trivial task. I am not aware of any general solution to this problem, as I was unable to locate any reference to this problem at all. One possible attempt at a solution might be to sort the eigenvectors such that their elements of the largest magnitude are located on the diagonal of the transformation matrix  $V$ . Another possibility is to scale the interaction parts of the Hamiltonian starting at very small values and track the energy levels, the latter approach being a very elaborate procedure. Yet another approach would be to transform base operators from the labframe to the eigenframe and “round” their elements to 0 or  $\pm 1/2$ . This might work, if the mixing of states due to coupling is not too strong.

#### 4.5.4 ENDOR Spectrum

The first interesting piece of information which can be learned from the diagonal Hamiltonian are the transition frequencies of the nuclear spins. Experimentally they comprise the ENDOR spectrum of the cluster as described in Section 4.4.



All of the possible  $(N - 1) N/2 = 523776$  differences between the energies of the eigenstates of the system constitute potential transition lines in the spectrum. Most of these transitions are forbidden by selection rules. To calculate the transition probabilities, the transition operator must be constructed. Since the proper form of the transition operators in the eigenframe is not available, the construction begins in the laboratory frame of reference:

$$T^{(l)} = \sum_{j=1}^N \mathbf{I}_{+j}^{(l)} \quad (4.63)$$

$T^{(l)}$  is then transformed to the eigenbasis of the Hamiltonian by

$$T^{(d)} = V T^{(l)} V^\dagger = V \left( \sum_{j=1}^N \mathbf{I}_{+j}^{(l)} \right) V^\dagger = \sum_{j=1}^N \mathbf{I}_{+j}^{(d)} \quad (4.64)$$

The probability of a transition between two levels  $j$  and  $k$  is now given by the modulus squared of the matrix element

$$w_{jk} \approx \left| \left( T^{(d)} \right)_{jk} \right|^2 \quad (4.65)$$

Equation (4.65) would provide exact transition probabilities, if  $\mathbf{I}_{+j}^{(d)}$  were strictly perpendicular to the quantization axes of the spins, which is not necessarily the case.

It is possible to construct the spectrum by placing at every energy difference a Lorentzian line weighted by the corresponding transition probability. Since the line shape and amplitude of the ENDOR lines is of little interest at this point, it is sufficient to select transitions with probabilities above a certain threshold.

The procedure above reproduces the entire ENDOR spectrum at once. In order to be able to assign lines to particular fluorine sites and  $m_S$ -values the following transition operator can be used:

$$T_j^\pm = \left( \frac{1}{2} \mathbf{I}_0 \pm \mathbf{S}_z^{(e)} \right) \mathbf{I}_{+j}^{(d)} \quad (4.66)$$

Because only the transition operator for a *single* nuclear spin  $j$  is taken from the laboratory frame to the eigenframe:

$$\mathbf{I}_{+j}^{(d)} = V \mathbf{I}_{+j}^{(l)} V^\dagger \quad (4.67)$$

only transitions for *that* spin will be found by  $T_j^\pm$ . The use of the electron spin operator  $\mathbf{S}_z$  defined *directly* in the eigenframe selects transitions belonging to  $m_S = \pm 1/2$ . This choice is justified, because the electron Zeeman interaction by far dominates the Hamiltonian and the state of the electron spin is very weakly affected by the nuclear spins. Thus, selecting a spin site and a value for  $m_S$  and repeating the procedure above, produces a single ENDOR line for each combination. Figure 4.15 shows a “stick” spectrum obtained in this way for  $w_{jk} > 10^{-3}$ . Clearly, the numeric solution of the Hamiltonian is in good agreement with the experimental data.

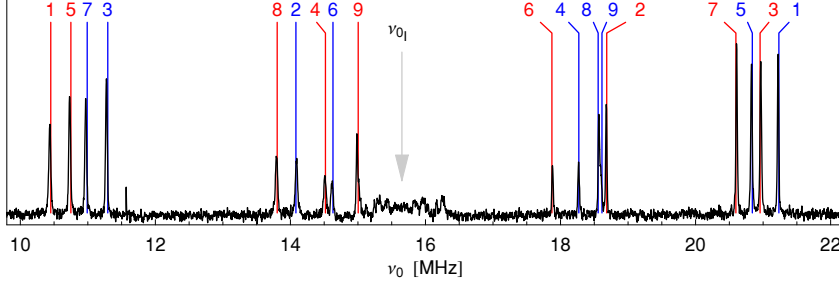


**Figure 4.15:** Exact numeric simulation of the ENDOR spectrum in CaF<sub>2</sub>:Ce. Black: experimental data, red: calculated nuclear Larmor frequencies  $\nu_{0_j}^{(m_S)}$  for  $m_S = +1/2$ , blue: for  $m_S = -1/2$ . The free fluorine resonance frequency  $\nu_{0_I}$  is indicated by the arrow. Numbers show the corresponding fluorine sites. Experimental parameters in Figure 4.12.

Variation of the Euler angles defining the coordinate transformation between the laboratory and the crystal coordinate systems shows that the line positions are very sensitive to these parameters. This allows the uncertainty in the Euler angles due to frequent cooling cycles (see Section 4.3.3) to be eliminated by manually “fitting” the coordinate transformation to a freshly acquired ENDOR spectrum. The range of angle variation, required to align simulated with the measured spectra is within 1° of the values calculated from the goniometer reading and parameters obtained from fitting the EPR spectra.

#### 4.5.5 Spin-Spin Couplings

As mentioned in Section 4.5.2, the coupling constants governing the evolution of two nuclear spins are determined by the through-space dipole-dipole coupling and an additional *indirect* contribution arising from the hyperfine interaction of the two spins with the same electron spin.

According to Equation (4.53), the total coupling can be obtained from the diagonalized Hamiltonian. However, the quantization axes  $\mathbf{I}_{z_j}^{(e)}$  are not known and an approximate calculation of the presumably largest contribution can be attempted by using the  $\mathbf{I}_z^{(l)}$ -operators transformed to the eigenframe:

$$D_{jk}^{\pm} \approx \frac{\text{tr} \left\{ \mathcal{H}^{(d)} \left( \frac{1}{2} \mathbf{I}_0 \pm \mathbf{S}_z^{(e)} \right) \mathbf{S}_z^{(e)} \mathbf{I}_{z_j}^{(d)} \mathbf{I}_{z_j}^{(d)} \right\}}{\text{tr} \left\{ \left( \left( \frac{1}{2} \mathbf{I}_0 \pm \mathbf{S}_z^{(e)} \right) \mathbf{S}_z^{(e)} \mathbf{I}_{z_j}^{(d)} \mathbf{I}_{z_k}^{(d)} \right)^2 \right\}} \quad (4.68)$$

Notice, that due to the indirect contribution, the coupling strength between two nuclear spins depends on the state ( $m_S = \pm 1/2$ ) of the electron spin. Because of the dominant electron spin Zeeman term in the Hamiltonian, the quantization axis of the electron spin can be approximated by the  $\mathbf{S}_z$ -operator in the eigenframe.

To compare the simulation with the experimental findings, spin-spin coupling constants were measured for all possible spin pairs for both values of  $m_S$ . The two measurement methods used were *double spin locking* and *SEDOR* (see

$I_1$	$I_2$	$m_S = -1/2$			$m_S = +1/2$		
		locking	SEDOR	simulation	locking	SEDOR	simulation
1	2	3.6	3.3	3.4	5.8	5.3	5.9
1	3	-	-	1.0	2.4	2.2	2.5
1	4	2.7	-	2.6	2.0	1.7	1.7
1	5	-	3.5	0.6	10.2	10.7	3.9
1	6	-	-	2.0	-	-	3.5
1	7	5.0	4.9	0.7	-	-	2.4
1	8	3.6	-	0.4	2.8	3.0	0.3
1	9	-	-	1.0	-	-	0.5
2	3	-	-	0.5	7.8	7.6	7.3
2	4	-	-	1.7	2.2	2.0	2.0
2	5	-	-	1.8	-	-	2.1
2	6	4.5	-	4.6	16.6	3.8	5.9
2	7	-	-	0.0	4.3	3.9	3.3
2	8	-	-	1.6	-	-	0.7
2	9	4.8	4.2	4.3	-	-	1.2
3	4	5.0	4.9	5.0	-	-	0.2
3	5	-	9.0	4.1	-	-	3.7
3	6	-	-	1.0	4.4	4.2	4.5
3	7	-	3.8	1.7	-	4.4	6.9
3	8	4.5	3.9	3.0	2.5	2.1	1.7
3	9	-	-	2.2	9.8	10.2	8.1
4	5	3.6	-	0.6	3.5	3.4	0.3
4	6	3.8	-	1.0	2.2	-	0.7
4	7	2.8	2.8	1.4	3.5	3.4	0.3
4	8	-	-	2.1	-	-	3.7
4	9	-	-	4.4	19.3	19.4	6.6
5	6	4.2	3.7	3.9	10.3	11.0	10.5
5	7	-	-	0.7	5.0	5.2	5.0
5	8	2.6	2.8	2.5	2.6	2.9	2.4
5	9	2.3	2.4	2.8	-	-	1.0
6	7	3.1	3.0	2.8	6.3	6.3	6.1
6	8	-	2.0	1.9	1.3	-	1.1
6	9	-	-	0.5	-	-	0.6
7	8	6.6	6.5	6.7	3.8	3.8	3.7
7	9	-	-	3.0	-	-	0.0
8	9	-	-	1.6	-	-	1.2

**Table 4.5:** Comparison of measured and numerically simulated spin-spin couplings (all values in kHz). The couplings were measured with two different methods: *double spin locking* and *SEDOR*. These methods are explained in detail in Chapter 5. Dashes indicate measurements where no oscillation was observed. The simulated values correspond to the sample orientation given in Figure 4.12 and include both the dipole-dipole and the indirect interactions.

Chapter 5 for experimental details). Some of the measurements did not produce transients with a clearly recognizable oscillation. This does not necessarily mean, that the coupling between the spins involved is negligible. The amplitude of the oscillation depends on the details of the electron spin preparation sequence. Therefore, a negative result may be due to a too small amplitude.

Table 4.5 presents the measured and computed values. As can be seen, there is some agreement between the experimental findings and the results of the simulation. However, in several cases the discrepancy is very large. Apparently, the approximation in Equation (4.68) is not very good. Until a procedure for finding the quantization axes of nuclear spins is available, the spin-spin couplings can only be reliably obtained by measurement.

### 4.5.6 Computation Time

A note on the computational time required for the calculations described in this section is due. The calculations were performed on a 1.5 GHz Intel Pentium M processor with 512 MB RAM. Program was compiled using the Intel C/C++ Compiler for Linux version 9.0. The Basic Linear Algebra Subroutines (BLAS) and Linear Algebra Package (LAPACK) were provided by Intel Math Kernel Library (MKL) for Linux version 7.2.1.

The running times measured for some subtasks of the numeric modeling are listed in Table 4.6. As one can see, a set of simulations can be performed on

general complex matrix-matrix multiplication <code>zgemm</code>	< 8	s
construction of the electron Zeeman term $\mathcal{H}_S$ :	< 1	ms
construction of the nuclear Zeeman terms $\mathcal{H}_N$ :	4	ms
construction of the hyperfine terms $\mathcal{H}_{hf}$ :	21	s
construction of the dipolar terms $\mathcal{H}_{dd}$ :	84	s
diagonalization of the Hamiltonian:	29	s
computation of the ESR spectrum:	15	s
computation of the total ENDOR spectrum:	15	s
computation of site and $m_S$ selective ENDOR spectrum:	129	s

**Table 4.6:** Computation times for the different parts of numeric modeling of the paramagnetic center in CaF<sub>2</sub>:Ce.

modest hardware in under 5 minutes. Simulations of pulse sequences below can take some 30 s per point depending on the number of matrix multiplications required and on whether diagonalization must be performed in the inner loop. Computational cost for more elaborate simulations, however, e.g., for fitting of the angular dependence, is prohibitive. On the other hand, there is certainly room for improvement in the numeric procedures used.

## 4.6 Simulation of Pulse Experiments

Because of the difficulties described in Section 4.5.3 many interesting properties of the  $S$ -bus cluster are not directly deducible from the diagonalized Hamiltonian. Thus, to gain this information, simulations of actual experiments (i.e., application of pulse sequences) must be performed.

### 4.6.1 Transformation to the Rotating Frame of Reference

Direct use of the diagonalized Hamiltonian is not feasible for use in simulations of pulse experiments, because the time scales involved span six orders of magnitude: The evolution under the electron spin Zeeman term happens at nearly 10 GHz, the evolution under the hyperfine and nuclear Zeeman interaction at 10 – 20 MHz, and the evolution under nuclear spin-spin couplings at less than 10 kHz. Thus, the evolution of the electron spin would need to be sampled at at least 0.1 ns. Since an observation of the evolution under spin-spin couplings takes milliseconds, such a simulation would require at least  $10^7$  steps each potentially taking tens of seconds on commodity hardware.

To avoid such problems, virtually all computations (analytic and numeric) in Magnetic Resonance are done in the *rotating frame of reference* where the fast oscillation due to the Zeeman term is eliminated.

#### 4.6.1.1 Standard Treatment

The task of removing the time dependence from the Hamiltonian is achieved by a time dependent transformation  $U_r(t)$  which shall be specified below. In the moving frame of reference an arbitrary unitary operator  $U(t)$  and the Hamiltonian  $\mathcal{H}$  are given by

$$\tilde{U} = U_r^\dagger U \quad \text{and} \quad \tilde{\mathcal{H}} = U_r^\dagger \mathcal{H} U_r \quad (4.69)$$

As a corollary, the Hamiltonian governing the evolution of the transformed operator  $\tilde{U}$  is derived first. The equation of motion for  $U$  is given by

$$\dot{U}(t) = -i\mathcal{H}U(t) \quad (4.70)$$

Using Equation (4.69), it is found that

$$\begin{aligned} \dot{\tilde{U}} &= \dot{U}_r^\dagger U + U_r^\dagger \dot{U} \\ &= \dot{U}_r^\dagger U - iU_r^\dagger \mathcal{H}U \\ &= \dot{U}_r^\dagger U_r \tilde{U} - iU_r^\dagger \mathcal{H}U_r \tilde{U} \\ &= -i \left( i\dot{U}_r^\dagger U_r + U_r^\dagger \mathcal{H}U_r \right) \tilde{U} \\ &= -i\tilde{\mathcal{H}}\tilde{U} \end{aligned} \quad (4.71)$$

Thus, in the moving frame, the equation of motion for operators has the same form as Equation (4.70) if the Hamiltonian is replaced by

$$\tilde{\mathcal{H}} = U_r^\dagger \mathcal{H}U_r + i\dot{U}_r^\dagger U_r \quad (4.72)$$

Incidentally, the second term is analogous to the pseudo-forces appearing in a non-inertial frame of reference in mechanics.

Now, consider a typical Magnetic Resonance Hamiltonian

$$\mathcal{H} = \omega_0 \mathbf{S}_z + \omega_1 2 \cos(\omega t + \varphi) \mathbf{S}_x = \mathcal{H}_0 + \mathcal{H}_1 \quad (4.73)$$

where  $\mathcal{H}_0$  represents the Zeeman interaction and  $\mathcal{H}_1$  an alternating magnetic field applied in the  $x$ -direction at the angular velocity  $\omega$  with the phase  $\varphi$ . Since it is the precession of the spin around the  $z$ -direction, we wish to compensate for, an appropriate ansatz for  $U_r$  is

$$U_r = \exp(-i\omega t \mathbf{S}_z) \quad (4.74)$$

The transformed Hamiltonian is then given by

$$\begin{aligned} \tilde{\mathcal{H}} &= U_r^\dagger (\mathcal{H}_0 + \mathcal{H}_1) U_r + i \dot{U}_r^\dagger U_r \\ &= \omega_0 \mathbf{S}_z \\ &\quad + \omega_1 \cos \varphi \mathbf{S}_x + \omega_1 \sin \varphi \mathbf{S}_y + \omega_1 \cos(2\omega t + \varphi) \mathbf{S}_x - \omega_1 \sin(2\omega t + \varphi) \mathbf{S}_y \\ &\quad - \omega \mathbf{S}_z \end{aligned} \quad (4.75)$$

The second term (arising from  $\mathcal{H}_1$ ) can be interpreted as follows. The linearly polarized alternating field in Equation (4.73) can be represented as a superposition of two counter-rotating circularly polarized fields. In a reference frame rotating at  $\omega$  with one of these components, that component is stationary, while the other component rotates at twice the frequency. If  $\omega_1 \ll \omega, \omega_0$ , this fast oscillating term has little influence on the spin dynamics and can be eliminated by averaging the Hamiltonian over one rotation period:

$$\bar{\mathcal{H}} = \frac{\omega}{2\pi} \int_0^{2\pi/\omega} dt \tilde{\mathcal{H}} = (\omega_0 - \omega) \mathbf{S}_z + \omega_1 (\cos \varphi \mathbf{S}_x + \sin \varphi \mathbf{S}_y) \quad (4.76)$$

This is known as the *rotating wave approximation*. Its quantum mechanical interpretation is that the counter-rotating component is found at twice the energy splitting of the Zeeman levels and does not induce transitions between them.

At resonance, when  $\omega = \omega_0$ , the  $\mathbf{S}_z$ -term vanishes. The resulting Hamiltonian nicely demonstrates how it is possible to apply pulses along any direction in the  $xy$ -plane, although only a single linearly polarized field is experimentally available. By varying the phase  $\varphi$  of the driving field, its orientation *in the rotating frame* can be varied.

#### 4.6.1.2 Generalized Transformation to the Rotating Frame

The situation in CaF<sub>2</sub>:Ce differs in two ways from the standard arrangement described above. Firstly, due to anisotropy, the quantization axis of the spin is tilted with respect to the external field  $\mathbf{B}_0$  resulting in an unknown tilt between the driving field  $\mathbf{B}_1$  and the quantization axis. Second, in the eigenframe, the appropriate operators are not readily available. The transformation to the rotating frame must, thus, be generalized to suit the present case [91].

We begin with separating the Hamiltonian of the system in a time-independent part  $\mathcal{H}_0$  and a time-dependent part  $\mathcal{H}_1$  due to the driving field:

$$\mathcal{H} = \mathcal{H}_0 + \mathcal{H}_1 \quad (4.77)$$

where

$$\mathcal{H}_1 = \omega_1 2 \cos(\omega t + \varphi) \mathbf{I}_x = \omega_1 f_1(t) \mathbf{I}_x \quad \text{with} \quad f_1(t) = 2 \cos(\omega t + \varphi) \quad (4.78)$$

First, the two parts are transformed to the eigenframe:

$$\mathcal{H}_0^{(d)} = V \mathcal{H}_0 V^\dagger \quad (4.79a)$$

$$\mathcal{H}_1^{(d)} = V \mathcal{H}_1 V^\dagger = \omega_1 f_1 \mathbf{I}_x^{(d)} \quad (4.79b)$$

$$\mathbf{I}_x^{(d)} = V \mathbf{I}_x V^\dagger \quad (4.79c)$$

Since the quantization axes defines the precession direction of the spin, the appropriate choice of the transformation operator is the  $z$ -component of the spin in the eigenframe  $\mathbf{I}_z^{(e)}$ :

$$U_r = \exp(-i \omega t \mathbf{I}_z^{(e)}) \quad (4.80)$$

The rotating frame Hamiltonian can now be calculated according to Equation (4.72). The constant part of the Hamiltonian is not affected by  $U_r$ , because both have diagonal form:

$$\tilde{\mathcal{H}}_0^{(d)} = U_r^\dagger \mathcal{H}_0^{(d)} U = \mathcal{H}_0^{(d)} \quad (4.81)$$

The pseudo-field term is given by

$$\tilde{H}_r^{(d)} = i \dot{U}_r^\dagger U_r = -\omega \mathbf{I}_z^{(e)} \quad (4.82)$$

The time averaged form of the driving Hamiltonian can be found analogous to Equation (4.76):

$$\begin{aligned} \bar{\mathcal{H}}_1^{(d)} &= \omega_1 \frac{\omega}{2\pi} \int_0^{2\pi/\omega} f_1(t) U_r^\dagger \mathbf{I}_x^{(d)} U_r \\ &= \omega_1 \left( Q_1^{(c)} \cos \varphi + Q_1^{(s)} \sin \varphi \right) \end{aligned} \quad (4.83)$$

Again all terms of the type  $\cos n\omega t$  are discarded in the rotating wave approximation. In the choice of  $Q_1^{(c,s)}$ , it is important to consider that only the components perpendicular to the quantization axis of the spin do contribute to the dynamics. Components along the quantization axis only modulate the level separation. This results in the following construction:

$$Q_1^{(s)} = -i [\mathbf{I}_z^{(e)}, \mathbf{I}_x^{(d)}] \quad (4.84a)$$

$$Q_1^{(c)} = -i e^{i \frac{\pi}{2} \mathbf{I}_z^{(e)}} [\mathbf{I}_z^{(e)}, \mathbf{I}_x^{(d)}] e^{-i \frac{\pi}{2} \mathbf{I}_z^{(e)}} \quad (4.84b)$$

The rotating frame Hamiltonian is now given by

$$\tilde{\mathcal{H}}^{(d)} = \mathcal{H}_0^{(d)} - \omega \mathbf{I}_z^{(e)} + \bar{\mathcal{H}}_1^{(d)} \quad (4.85)$$

with

$$\tilde{\mathcal{H}}_0^{(d)} = \mathcal{H}_0^{(d)} - \omega \mathbf{I}_z^{(e)} \quad (4.86)$$

representing the diagonalized system Hamiltonian in the rotating frame in the absence of a driving field, and  $\tilde{\mathcal{H}}_1^{(d)}$  representing the effect of the irradiation.

The resonance condition is found by setting the frequency of excitation to the Larmor frequency of the spin:

$$\omega = \frac{\text{tr} \left( \mathcal{H}_0^{(d)} \mathbf{I}_z^{(e)} \right)}{\text{tr} \left( \mathbf{I}_z^{(e)} \mathbf{I}_z^{(e)} \right)} \quad (4.87)$$

This entire discussion presumes that the operator  $\mathbf{I}_z^{(e)}$  which defines the quantization axis is known. For the electron spin,  $\mathbf{S}_z^{(e)}$  is known to a very good approximation, because of the dominant electron Zeeman term. For the nuclear spins, however, that is not the case.

### 4.6.2 Initial State and Measurement Operators

Experiments, where only the electron spin is directly manipulated and observed can now be simulated with the use of the approximate quantization axis of the electron spin  $\mathbf{S}_z$ . Accordingly, at the Boltzmann equilibrium the electron spin is aligned along  $\mathbf{S}_z$  and the initial density matrix is, unless stated otherwise, given by

$$\rho(t=0) = \mathbf{S}_z^{(e)} \quad (4.88)$$

The observation is performed in the laboratory frame of reference with the measurement operators

$$M_{x,y,z}^{(l)} = \mathbf{S}_{x,y,z}^{(l)} \quad (4.89)$$

Computations are done in the eigenframe of the Hamiltonian, and the measurement operators must be transformed to the that frame:

$$M_{x,y,z}^{(d)} = V M_{x,y,z}^{(l)} V^\dagger, \quad (4.90)$$

so that the signal amplitude is obtained by

$$A_{x,y,z}(t) = \frac{\text{tr} \left( M_{x,y,z}^{(d)} \rho(t) \right)}{\text{tr} \left( M_{x,y,z}^{(d)} M_{x,y,z}^{(d)} \right)} \quad (4.91)$$

### 4.6.3 Rabi Oscillations

The simplest pulsed magnetic resonance experiment that actually produces a result is the observation of the precession of the spin around the effective field in the rotating frame of reference, i.e., the *Rabi precession*. The rf is applied for a period of time  $t$  to the Boltzmann equilibrium spin polarization and the amplitude of the spin components is monitored. The simulation proceeds by applying

$$U(\delta t) = e^{-i\delta t \tilde{\mathcal{H}}^{(d)}} \quad (4.92)$$



with  $\tilde{\mathcal{H}}^{(d)}$  defined by Equation (4.85). The density matrix at time  $t = n \times \delta t$  is then given by

$$\rho(t) = U(\delta t) \rho(t - \delta t) U(\delta t)^\dagger \quad (4.93)$$

Figure 4.16 shows the result of a simulation run with the microwave amplitude (cf. Equation (4.85)) corresponding to  $\omega_1/2\pi = 37$  MHz. The first observation

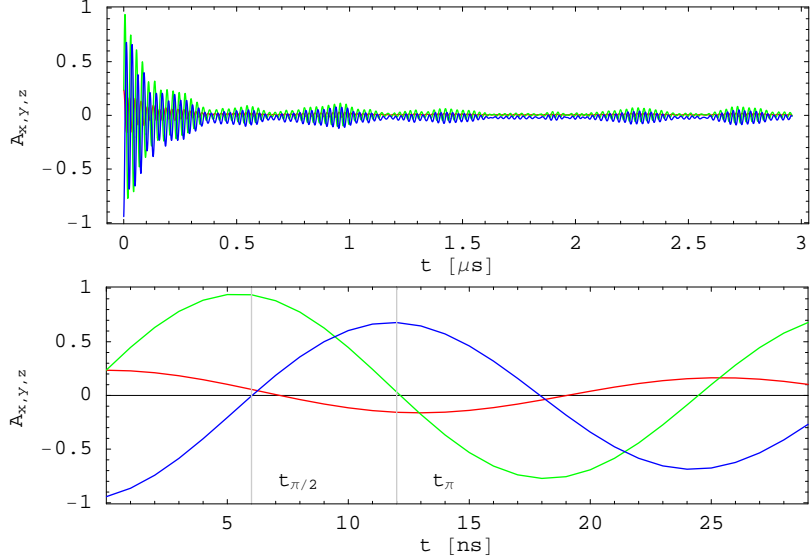


**Figure 4.16:** Simulation of the Rabi oscillation of the electron spin in  $\text{CaF}_2:\text{Ce}$ . Top: Time trace. Red, green, and blue indicate the  $A_x$ ,  $A_y$ , and  $A_z$  respectively. Bottom: Detail of the time trace. Vertical lines indicate durations of  $\pi/2$ - and  $\pi$ -pulse.

is that the starting values of the transverse components  $A_{x,y}$  are not zero and the starting value of  $A_z$  is not one. This is explained by the fact that the quantization axes of the electron spin is tilted with respect to the  $z$ -direction of the laboratory frame, such that the initial electron spin state has a non-vanishing component in the  $xy$ -plane in the laboratory frame. The second interesting finding, is that the Rabi oscillation is modulated by a complicated envelope. This is the result of evolution under the  $z$ -part  $\mathcal{H}_0^{(d)}$  of the rotating frame Hamiltonian in Equation (4.85). To verify this conjecture, a simulation run with the “ $\delta$ -pulse” settings has been done.

The “ $\delta$ -pulse” approximation in Magnetic Resonance is used, when, in the rotating frame, the precession under the driving microwave field is much faster than any evolution under the rest of the Hamiltonian. Here, this situation was implemented by excluding  $\mathcal{H}_0^{(d)}$  from  $\tilde{\mathcal{H}}^{(d)}$ . In this case, the Rabi oscillation shows no envelope modulation, as expected. A direct comparison of the measured and simulated evolution under  $\mathcal{H}_0^{(d)}$  is presented below.

The Rabi simulation was also used to calibrate the evolution time for pulses required for other simulations. In accordance with the experimental practice, the duration of a  $\pi/2$ -pulse was adjusted such that the  $\mathbf{S}_z$ -component vanishes at the end of the pulse. For a  $\pi$ -pulse, the first maximum of  $\mathbf{S}_z$  was taken as indicated in the figure.

#### 4.6.4 Pulse and Free Evolution Propagators

Magnetic Resonance experiments consist mostly of applying rf or microwave pulses and periods of free evolution to spins and observing the resulting magnetization. The rotating frame Hamiltonian in Equation (4.85) together with the simulation of the Rabi precession in the previous section allow one to construct the appropriate propagation operators.

To obtain a  $\pi/2$ -pulse, for instance, the full Hamiltonian in Equation (4.85) is applied for a time  $t_{\pi/2}$  which was calibrated by the Rabi simulation. The direction of the pulse can be selected by setting  $\varphi$  in Equation (4.78) accordingly. A value of  $\varphi = \pi/2$ , for example, produces a pulse in  $y$ -direction. Summarizing, the propagator for  $\pi/2$ -pulse in  $y$ -direction is thus given by

$$P_x\left(\frac{\pi}{2}\right) = e^{-it_{\pi/2}\tilde{\mathcal{H}}^{(d)}(\varphi=\pi/2)} \quad (4.94)$$

Pulses with other rotation angles and rotation axes are obtained analogously.

During the free evolution, the driving field  $B_1$  is off and  $\tilde{\mathcal{H}}_1^{(d)}$  must be omitted. The propagator is fully determined by the diagonalized system Hamiltonian:

$$U(t) = e^{-it\tilde{\mathcal{H}}_0^{(d)}} \quad (4.95)$$

All pulse sequence simulations discussed in the following use these propagators.

#### 4.6.5 Free Induction Decay

The *free induction decay* (FID) is observed, when the magnetization initially has a non-vanishing component perpendicular to the quantization axis and is allowed to evolve freely. Common mechanisms for the decay of the magnetization include decoherence due to field inhomogeneities and interactions with other magnetic moments as well as relaxation due to spin-lattice interaction.

As above, the simulation starts with the density matrix oriented along the quantization axis of the electrons spin:

$$\rho(0) = \mathbf{S}_z \quad (4.96)$$

A  $\pi/2$ -pulse in  $y$ -direction followed by a period of free evolution is applied according to (in Liouville notation)

$$|\rho(t)\rangle = U(t)P_y\left(\frac{\pi}{2}\right)|\rho(0)\rangle \quad (4.97)$$

As  $t$  is incremented, the values of  $A_{x,y,z}$  are computed according to Equation (4.91).

Figure 4.17 shows the result of such a run. As expected after a  $\pi/2$ -pulse in  $y$ -direction, the spin is oriented close to the  $x$ -direction. The deviation is caused by the tilted quantization axis. For the same reason, the baseline after the decay is not zero but has finite values for the transverse spin components and a different finite value for the  $z$ -component.

It is not possible to directly measure the FID due to dead-time effects. However, the time constant of the FID is also found in the rise and fall times of echo

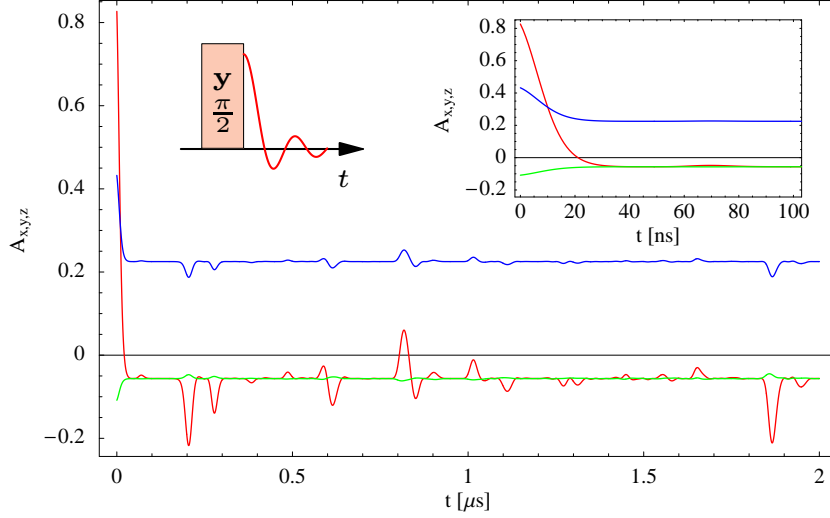


**Figure 4.17:** Simulation of the free induction decay of the electron spin in  $\text{CaF}_2:\text{Ce}$ . Red, green, and blue indicate  $A_{x,y,z}$  respectively. Time  $t = 0$  corresponds to the end of the pulse. The insets show the pulse sequence and the initial decay in detail.

signals. The simulated value of around 15 ns is in good agreement with the experimentally observed echo widths. This indicates that the FID of the electron spin is, in fact, determined by the hyperfine interaction with the nuclear spins of the  $S$ -bus cluster. Notice, that no dissipative relaxation is present in the simulation. True decoherence would require the interaction of the simulated spin system with an external *bath*.

Conceptually, one could consider only the electron spin and treat the nuclear spin as such a bath. The simulation demonstrates impressively, how a bath with only nine nuclear spins can produce an almost total decoherence of the electron spin. However, the small bath size and the coherent nature of the simulation is still found in the partial recovery of the electron spin magnetization during further evolution. Because the “decay” is entirely due to the redistribution of the polarization among the linear and product terms in the cluster, such as  $\mathbf{I}_{z_j}$ ,  $\mathbf{I}_{z_j}\mathbf{I}_{z_k}$ ,  $\mathbf{I}_{z_j}\mathbf{I}_{z_k}\mathbf{I}_{z_l}$ , and so on, the coherence bounces around the spin system due to the evolution of these terms under the various interactions. Occasionally, this produces partial refocussing of one of the linear terms, in this case  $\mathbf{S}_z$ .

#### 4.6.6 Electron Spin Echoes

There is a whole class of pulse sequences designed to deliberately recover the magnetization after the decay caused by different types of decoherence. They are collectively referred to as *spin echo* sequences. To demonstrate, that the simulation does reproduce spin echoes, results of simulating two pulse sequences are presented in this section.

The first is the time-honored *Hahn echo* sequence. It can be shown, that under most circumstances, *any* two pulses will produce an echo. The Hahn echo

sequence is conceptually the easiest. It consists of a  $\pi/2$ -pulse in  $y$ -direction followed, after a period of free evolution  $\tau$ , by a  $\pi$ -pulse in  $x$ -direction. After another period of  $\tau$  an echo in  $x$ -direction appears. The sequence and the simulation result are shown at the top in Figure 4.18. The bottom of the figure shows the result for a sequence consisting of two identical  $\pi/2|_y$ -pulses separated by  $\tau$ . Again the echo is expected at time  $\tau$  after the last pulse. Latter sequence is relevant as a precursor to the simulation described in Section 4.6.7.

Both simulation runs reproduce the features one would expect from the corresponding experiments. Pronounced echoes are found at the expected positions.

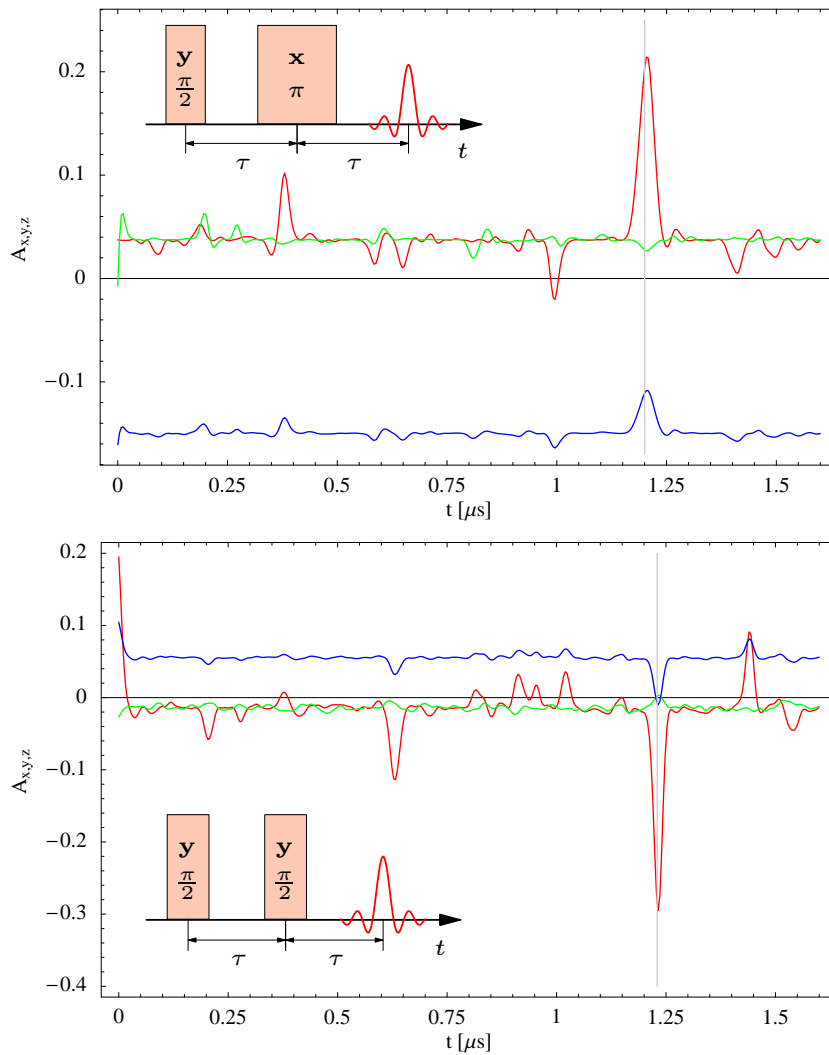


**Figure 4.18:** Simulation of electron spin echoes in CaF<sub>2</sub>:Ce. Gray vertical lines indicate the time  $\tau$  after the last pulse. Top: Hahn echo sequence with  $\tau = 1.2 \mu\text{s}$ . Bottom: Echo sequence with two identical  $\pi/2$ -pulses and  $\tau = 1.23 \mu\text{s}$ . Red, green, and blue correspond to  $A_{x,y,z}$  respectively. Time  $t = 0$  corresponds to the end of the last pulse.

For the Hahn sequence the echo is expected to appear in the  $x$ -direction. This can be seen by setting  $\tau = 0$  and considering the effect of the two pulses on a magnetization along  $z$ . Analogously, the “two-pulse” sequence should produce an echo along  $\bar{x}$ . The initial FID after the last pulse is reproduced in both cases and is more pronounced in the “two-pulse” run. As already seen in the case of the FID, the coherent evolution produces spurious peaks at different times.

Together, the two simulations show that the numeric model is capable of reproducing the formation of spin echoes. Significant magnetization can be recovered even after relatively long evolution times. Also, the amplitude of the echo depends strongly on  $\tau$  via the evolution under the interactions contained in  $\tilde{\mathcal{H}}_0^{(d)}$ .

#### 4.6.7 Electron Spin Echo Envelope Modulation

In most spin echo experiments the echo amplitude depends in various ways on the interactions present in the Hamiltonian. By varying different time parameters in the pulse sequence, it is possible to record the envelope of the echo depending on those parameters. This technique of *Electron Spin Echo Envelope Modulation* (ESEEM) [100,101] can be used to experimentally probe aspects of the system Hamiltonian. Here, an ESEEM experiment is used to test the numeric model of the  $S$ -bus cluster against a non-trivial measurement.

The pulse sequence used for ESEEM is shown in Figure 4.19. It begins with

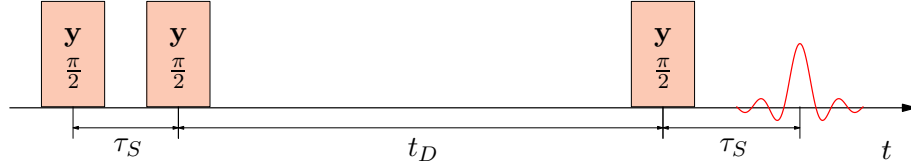


**Figure 4.19:** Stimulated echo sequence used for electron spin echo envelope modulation measurements and simulations in  $\text{CaF}_2:\text{Ce}$ .

two  $\frac{\pi}{2}|y\rangle$ -pulses separated by the time  $\tau_S$ . After an evolution time of  $t_D$ , a third  $\frac{\pi}{2}|y\rangle$ -pulse is applied. An echo along  $x$  is formed at the time  $\tau_S$  after the third pulse. This is also known as the *stimulated echo* [93,102]. In the simple case of a single electron spin  $S = 1/2$  and a single nuclear spin  $I = 1/2$ , the echo amplitude is given by [33,103]

$$S(t_D) = S_0 + C_+ \cos(\omega_+ t_D) + C_- \cos(\omega_- t_D) + S_+ \sin(\omega_+ t_D) + C_- \sin(\omega_- t_D) \quad (4.98)$$

with

$$\begin{aligned} S_0 &= \frac{1}{4} \left( 1 + \sin^2 \vartheta \left( 1 + \frac{1}{2} (\cos(\omega_- \tau_S) + \cos(\omega_+ \tau_S)) \right) \right) \\ C_{\pm} &= \frac{1}{8} \sin^2 \vartheta \cos(\omega_{\pm} \tau_S) (1 - \cos(\omega_{\mp} \tau_S)) \\ S_{\pm} &= \frac{1}{8} \sin^2 \vartheta \sin(\omega_{\pm} \tau_S) (\cos(\omega_{\mp} \tau_S) - 1) \end{aligned} \quad (4.99)$$

The parameters  $\omega_{\pm}$  represent the ENDOR frequencies of the nuclear spins, while

$\vartheta$  is a measure of the anisotropy of the hyperfine interaction:

$$\begin{aligned}\omega_{\pm}^2 &= \left(\frac{A_{xz}}{2}\right)^2 + \left(\frac{A_{yz}}{2}\right)^2 + \left(\omega_{0I} \pm \left(\frac{A_{zz}}{2}\right)\right)^2 \\ \sin \vartheta &= \frac{(A_{xz}^2 + A_{yz}^2)\omega_{0I}^2}{\omega_-^2\omega_+^2}\end{aligned}\quad (4.100)$$

where  $A_{jk}$  are components of the hyperfine tensor and  $\omega_{0I}$  is the Larmor frequency of the free nucleus. The experiment consists of recording the echo amplitude as a function of  $t_D$ . Thus, according to Equation (4.98), the power-spectrum will contain the same two lines corresponding to  $m_S = \pm 1/2$  as the ENDOR spectrum. The line amplitude will depend on the orientation of the hyperfine tensor and the time  $\tau_S$ .

In the case of the *S*-bus cluster with nine strongly coupled nuclear spins, there should be 18 transitions. Because of the dependence on  $\tau_S$ , the ESEEM spectrum would have to be integrated over  $\tau_S$  to produce the ENDOR spectrum. However, for any given  $\tau_S$  most of the ENDOR lines should be visible in the ESEEM spectrum, even though amplitudes would deviate.

Figure 4.20 shows the result of the measurement. The echo envelope modulation was sampled for 8192 points at time increments of  $\delta t_D = 4$  ns. The time trace exhibits a decay with the time constant of around  $25 \mu\text{s}$  which is three orders of magnitude longer than in the case of the FID. The corresponding power-spectrum does, in fact, contain almost all of the lines of the ENDOR spectrum. The latter is indicated for *the same orientation* by the gray vertical lines. One ENDOR line is missing in the ESEEM spectrum in each, the third and the fourth line group. The mixing time for this experiment was  $\tau_S = 352$  ns. This explains, why the nuclei with weak hyperfine couplings produce the most pronounced lines.

Results of a simulation of the same experiment are shown in Figure 4.21. Notice that the simulation can not be expected to reproduce the measurement in all details for two reasons: The simulation does only include the nine nuclei belonging to the cluster and does not consider the next-to-next and further removed neighbors with weaker hyperfine couplings. Neither, does it account for the effects of relaxation. However, all ENDOR lines except for two in the fourth group are reproduced very well. Also, the relative weights of the four groups are roughly the same as in the experiment.

The ESEEM simulation together with the simulations of the FID and spin echoes shows that the numeric model does describe most aspects of the evolution of the electron spin in the *S*-bus cluster in  $\text{CaF}_2:\text{Ce}$  reasonably well. Also, the assumption underlying the choice of the quantization axes of the electron spin in Section 4.6.1 is justified by these results *post factum*.

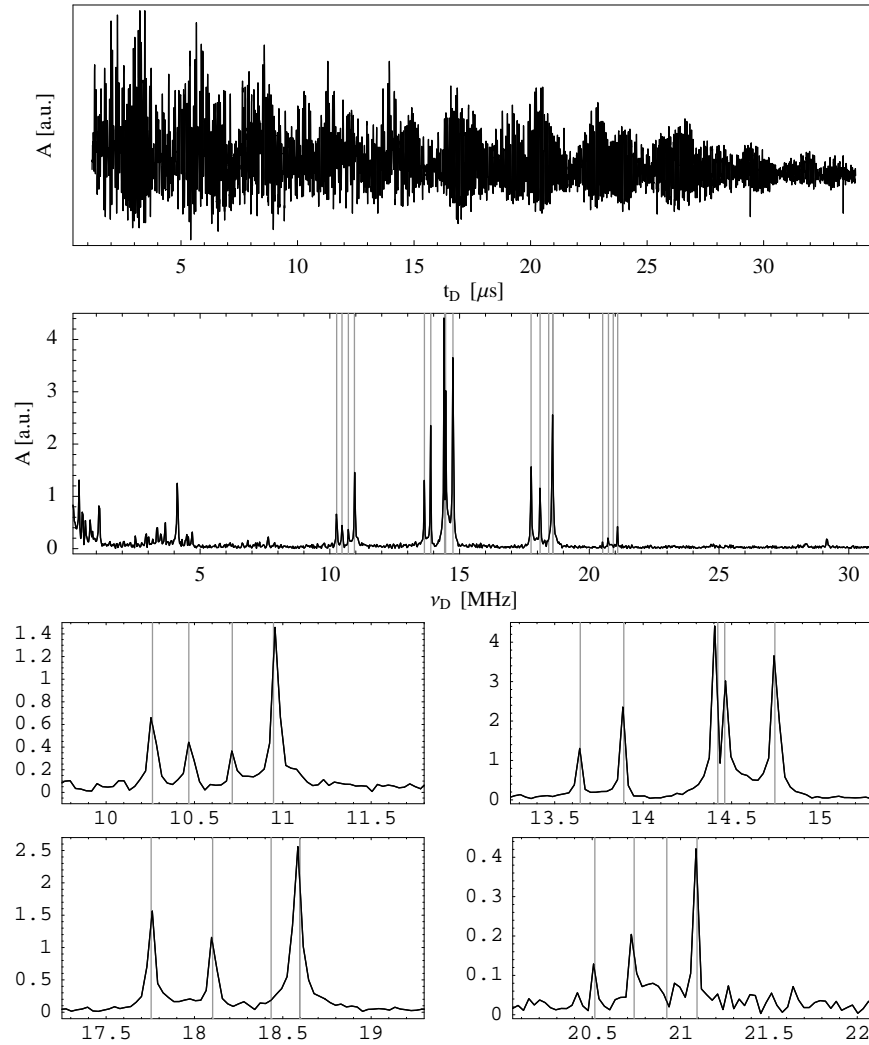


**Figure 4.20:** Envelope modulation measurement of the stimulated echo of the electron spin in  $\text{CaF}_2:\text{Ce}$ . Top: Time trace of the echo amplitude vs. evolution time  $t_D$ . Center: Powerspectrum. Vertical gray lines indicate line positions in the measured ENDOR spectrum for this orientation. Bottom: Detail of the spectrum in the regions of the four line groups of the ENDOR spectrum. See Figure 4.19 for the pulse sequence ( $\tau_S = 352$  ns) and Figure 4.21 for corresponding simulation.

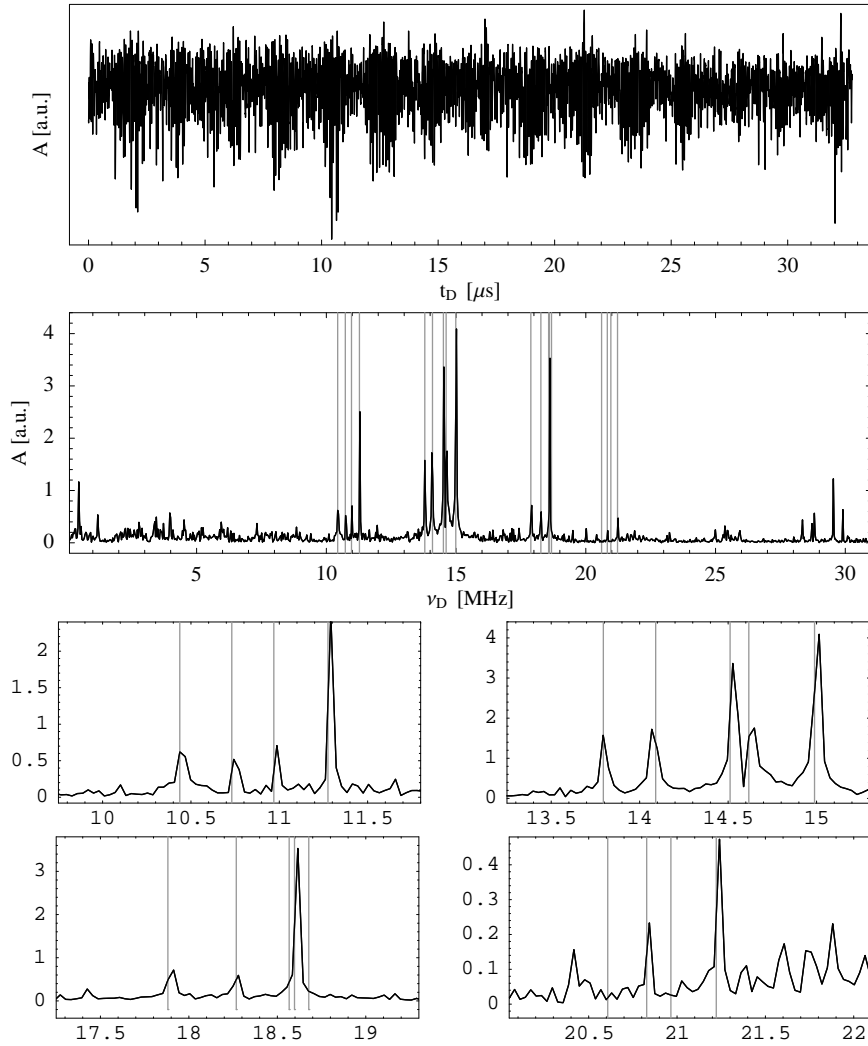


**Figure 4.21:** Simulation of the electron spin simulated echo envelope modulation in  $\text{CaF}_2:\text{Ce}$ . Top: Time trace of the echo amplitude vs. evolution time  $t_D$ . Center: Powerspectrum. Vertical gray lines indicate line positions in the measured ENDOR spectrum for this orientation. Bottom: Detail of the spectrum in the regions of the four line groups of the ENDOR spectrum. Pulse sequence is shown in Figure 4.19 ( $\tau_S = 352$  ns). Notice, that the orientation used for this simulation is slightly different from the one used in the corresponding measurement in Figure 4.20.



## 4.7 Detailed Evolution of Density Matrix Components

Because it is difficult to find the quantization axes of the nuclear spins, a simulation of the evolution of the density matrix under pulse sequences involving the nuclear spins is not feasible. Even if the simulation were doable, experiments would still be needed to verify it. In addition, the measurements detailed below can be used to obtain values of parameters entering quantum computing experiments and the theoretical description of the  $S$ -bus.

### 4.7.1 Multi-Quantum ENDOR and PPS Preparation

#### 4.7.1.1 Phase Encoding of the Nuclear Spin State (MQE)

As mentioned in Section 4.1, the detection of the nuclear spin state through the electron spin affords a large sensitivity enhancement. However, the state of the nuclear spins must be encoded in the state of the electron spin. This is achieved through a pulse sequence derived from the technique of *multiple quantum ENDOR* (MQE) [104–107]. Apart from the basic pulse sequence described in this section, a number of variations is used. For simplicity, they are summarily referred to as “MQE-encoding”.

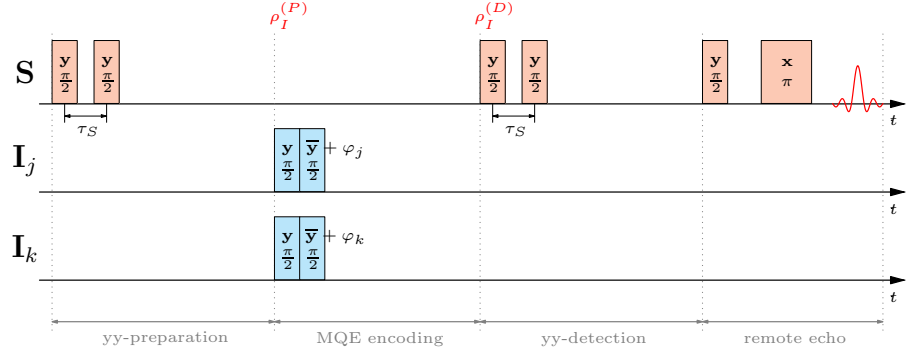


**Figure 4.22:** Pulse sequence for phase encoding of the state of the nuclear qubits onto the state of the electron spin.

Figure 4.22 shows the case of two nuclear spins. The electron spin part of the pulse sequence is made up of the usual  $S$ -bus elements:  $yy$ -preparation and  $yy$ -detection followed by remote echo detection. The MQE sequence proper, is applied to the nuclear spins in between. The nuclear part of the density matrix after the  $yy$  preparation sequence  $U^{(S)}$  is given by  $\rho_{yy}$  in Equation (4.10). Since no transfer between the even and odd products takes place under this pulse sequence, the reduced form of density matrix can be safely used. Thus, the prepared density matrix can be written in the form

$$\rho_I^{(P)} = \frac{1}{4}p_0\mathbf{I}_2 + \frac{1}{2}p_1\mathbf{I}_{z_1} + \frac{1}{2}p_2\mathbf{I}_{z_2} + p_{12}\mathbf{I}_{z_1}\mathbf{I}_{z_2} \quad (4.101)$$

where

$$p_0 = 4Q_0^{(yy)}, \quad p_{12} = -4Q_{12}^{(yy)}, \quad p_1 = -4Q_1^{(yy)}, \quad p_2 = -4Q_2^{(yy)} \quad (4.102)$$

with  $Q_j^{(yy)}$  defined in Equation (4.14).

After application of the MQE sequence and decay of transient components, the coefficients of the  $\mathbf{I}_z$ -terms are modified:

$$\rho_I^{(D)} = \frac{1}{4}p_0\mathbf{I}_2 + \frac{1}{2}p_1 \cos \varphi_1 \mathbf{I}_{z_1} + \frac{1}{2}p_2 \cos \varphi_2 \mathbf{I}_{z_2} + p_{12} \cos \varphi_1 \cos \varphi_2 \mathbf{I}_{z_1} \mathbf{I}_{z_2} \quad (4.103)$$

The signal depends on the phases  $\varphi_j$  in the following way (cf. Section 4.1.2):

$$\begin{aligned} S_D &= \text{tr} \left\{ \rho_{yy}^{(12)} \rho_I^{(D)} \right\} \\ &= \frac{1}{4} \left( p_0^2 + p_1^2 \cos \varphi_1 + p_2^2 \cos \varphi_2 + p_{12}^2 \cos \varphi_1 \cos \varphi_2 \right) \\ &= \frac{1}{4} \left( p_0^2 + p_1^2 \cos \varphi_1 + p_2^2 \cos \varphi_2 + \frac{1}{2}p_{12}^2 \cos(\varphi_1 - \varphi_2) + \frac{1}{2}p_{12}^2 \cos(\varphi_1 + \varphi_2) \right) \end{aligned} \quad (4.104)$$

In order to obtain the sought coefficients  $p_j$ , pulse phases are varied according to  $\varphi_j = 2\pi\nu_j t_\varphi$  and the signal is sampled for a suitable range of  $t_\varphi$ . A Fourier transform of this transient will contain four lines  $L_1, \dots, L_4$  at the frequencies  $\nu_\Delta = \nu_2 - \nu_1$ ,  $\nu_1$ ,  $\nu_2$ , and  $\nu_\Sigma = \nu_1 + \nu_2$  with the amplitudes  $\frac{1}{2}p_{12}^2$ ,  $p_1^2$ ,  $p_2^2$ , and  $\frac{1}{2}p_{12}^2$  respectively. In the parlance of MQE, the lines at  $\nu_1$  and  $\nu_2$  belong to *single quantum transitions* (1Q) while  $\nu_\Delta$  and  $\nu_\Sigma$  arise from *null-quanta* (0Q) and *two-quanta* (2Q) transitions respectively.

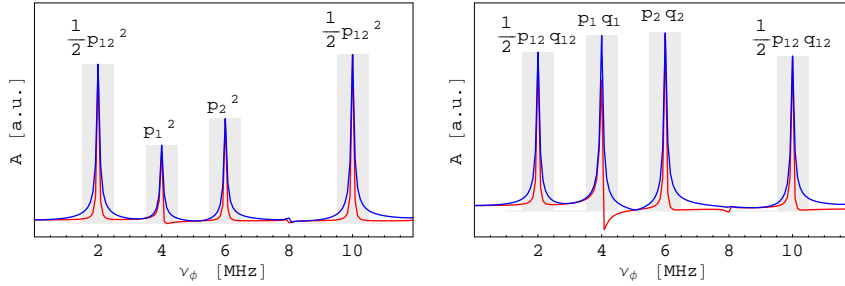


**Figure 4.23:** Encoding of the state of the nuclear spins on the electron spin by phase variation. Red and blue indicate the real part and the modulus of the Fourier transform. The encoding frequencies are  $\nu_1 = 2$  MHz,  $\nu_2 = 6$  MHz,  $\nu_\Delta = 2$  MHz, and  $\nu_\Sigma = 10$  MHz. Left: MQE-spectrum for the unmodified density matrix after *yy*-preparation. Right: MQE-spectrum for a density matrix after a manipulation of the nuclear spins. Experimental details in Figure 4.25.

An example of such an MQE spectrum is shown on the left in Figure 4.23. As indicated in the figure, the coefficients  $p_j$  can be immediately obtained from the line heights in the spectrum. This provides a kind of a calibration for the *yy*-detection sequence.

Once the coefficients of the density matrix produced by an electron spin preparation sequence (in this case *yy*) are known, other density matrices can be tomographed in the same fashion, as long as no conversion between even and odd products takes place. Suppose, the state of the nuclear qubits is modified

through some one-qubit gates after preparation and the density matrix is now:

$$\tilde{\rho}_I^{(P)} = \frac{1}{4}q_0 \mathbf{I}_2 + \frac{1}{2}q_1 \mathbf{I}_{z_1} + \frac{1}{2}q_2 \mathbf{I}_{z_2} + q_{12} \mathbf{I}_{z_1} \mathbf{I}_{z_2} \quad (4.105)$$

When the MQE sequence is applied to such a state, its density matrix becomes

$$\tilde{\rho}_I^{(D)} = \frac{1}{4}q_0 \mathbf{I}_2 + \frac{1}{2}q_1 \cos \varphi_1 \mathbf{I}_{z_1} + \frac{1}{2}q_2 \cos \varphi_2 \mathbf{I}_{z_2} + q_{12} \cos \varphi_1 \cos \varphi_2 \mathbf{I}_{z_1} \mathbf{I}_{z_2} \quad (4.106)$$

Analogously to Equation (4.104) the signal will be given by

$$\begin{aligned} S_D &= \text{tr} \left\{ \rho_I^{(P)} \tilde{\rho}_I^{(D)} \right\} \\ &= \frac{1}{4} (p_0 q_0 + p_1 q_1 \cos \varphi_1 + p_2 q_2 \cos \varphi_2 + p_{12} q_{12} \cos \varphi_1 \cos \varphi_2) \end{aligned} \quad (4.107)$$

The resulting MQE-spectrum is shown on the right in Figure 4.23. Since  $p_j$  are known through the calibration measurement,  $q_j$  can be obtained from the line amplitudes. This technique can be extended to any number of qubits by proper choice of phase encoding sequences  $\nu_{\varphi_j}$

Notice, that the coefficients  $p_j$  and  $q_j$  result from the tracing out of all the products of the nuclear spins not participating in the algorithm (cf. Equation (4.10)). Two qubit gates – most notably the *CNOT* gate – change the order of these products from even to odd and vice versa so that this simple encoding scheme can no longer be used. In such cases, full density matrix must be used in calculations. The tomography procedure is then more elaborate but still based on the same principle.

#### 4.7.1.2 Preparation of Pseudo-Pure States

Many of the measurements below require well defined input states. Preparation of such pseudo-pure states for quantum computing is an interesting operation in its own right and has been demonstrated by J. Mende [35] for two- and three-qubit cases.

Here, the results are presented because a modified pulse sequence was used and much higher fidelities were achieved. Also, pseudo-pure states were later used as input in the demonstration of the *CNOT* operation and the preparation of the *pseudo-entangled states* described below.

The four pseudo-pure states of two qubits have the form:

$$\begin{aligned} \rho_{00} &= \frac{1}{4} \mathbf{I}_0 + \frac{1}{2} \mathbf{I}_{z_1} + \frac{1}{2} \mathbf{I}_{z_2} + \mathbf{I}_{z_1} \mathbf{I}_{z_2} \\ \rho_{01} &= \frac{1}{4} \mathbf{I}_0 + \frac{1}{2} \mathbf{I}_{z_1} - \frac{1}{2} \mathbf{I}_{z_2} - \mathbf{I}_{z_1} \mathbf{I}_{z_2} \\ \rho_{10} &= \frac{1}{4} \mathbf{I}_0 - \frac{1}{2} \mathbf{I}_{z_1} + \frac{1}{2} \mathbf{I}_{z_2} - \mathbf{I}_{z_1} \mathbf{I}_{z_2} \\ \rho_{11} &= \frac{1}{4} \mathbf{I}_0 - \frac{1}{2} \mathbf{I}_{z_1} - \frac{1}{2} \mathbf{I}_{z_2} + \mathbf{I}_{z_1} \mathbf{I}_{z_2} \end{aligned} \quad (4.108)$$

The task of preparing pseudo-pure states thus consists of tailoring the coefficients  $q_j$  in Equation (4.105) such that

$$q_0 = |q_1| = |q_2| = |q_{12}| = 1 \quad (4.109)$$

This is an essentially non-unitary operation. The sequence is shown in Figure 4.25. After the *yy*-preparation and the decay of all transverse components

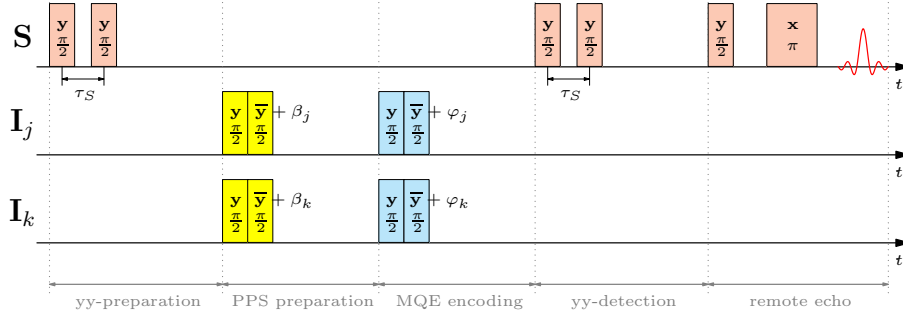


**Figure 4.24:** Pulse sequence for the preparation of pseudo-pure states of two qubits in CaF<sub>2</sub>:Ce.

of the electron spin, the density matrix is purely diagonal (i.e., it contains only *z*-operators). A two-pulse sequence identical to the MQE sequence is now applied. The transverse nuclear density matrix components decay with the time constant of the FID and the resulting density matrix is given by Equation (4.101). When the PPS sequence is applied to such a state, its density matrix becomes (again after the decay of off-diagonal components)

$$\begin{aligned} \rho_I^{(PPS)} &= \\ & \frac{1}{4}q_0 \mathbf{I}_2 + \frac{1}{2}p_1 \cos \beta_1 \mathbf{I}_{z_1} + \frac{1}{2}p_2 \cos \beta_2 \mathbf{I}_{z_2} + p_{12} \cos \beta_1 \cos \beta_2 \mathbf{I}_{z_1} \mathbf{I}_{z_2} \\ &= \frac{1}{4}q_0 \mathbf{I}_2 + \frac{1}{2}p_1 S_1 \mathbf{I}_{z_1} + \frac{1}{2}p_2 S_2 \mathbf{I}_{z_2} + p_{12} S_1 S_2 \mathbf{I}_{z_1} \mathbf{I}_{z_2} \quad (4.110) \end{aligned}$$

with  $S_j = \cos \beta_j$ . Now, the new amplitudes of the operators are:

$$\begin{aligned} q_1 &= p_1 S_1 \\ q_2 &= p_2 S_2 \\ q_{12} &= p_{12} S_1 S_2 \end{aligned} \quad (4.111)$$

In this form, the problem of satisfying the condition in Equation (4.109) will, in general, have no solution. It is, however, still possible to find a set  $\beta_j$  to obtain pseudo-pure states.

Recall that, in *ensemble* spin quantum computing, the density matrix is always almost maximally mixed. Only a small fraction of spins exhibits the operator structure corresponding to pure states. Thus, the magnitude  $q_0$  with which the identity operator is included in the density matrix can be freely chosen to obtain the desired operator structure. In order to be able to satisfy the normalization condition for the density matrix  $\text{tr}(\rho^2) = 1$ , it is more convenient to scale the spin operators instead of the identity operator. Thus the density matrix can be written as

$$\rho_I^{(PPS)} = \frac{1}{4} \mathbf{I}_2 \alpha \left( \frac{1}{2} p_1 S_1 \mathbf{I}_{z_1} + \frac{1}{2} p_2 S_2 \mathbf{I}_{z_2} + p_{12} S_1 S_2 \mathbf{I}_{z_1} \mathbf{I}_{z_2} \right) \quad (4.112)$$

Now the equations for finding the proper  $\beta_j$  become

$$\begin{cases} 1 = \alpha |p_1 S_1| \\ 1 = \alpha |p_2 S_2| \\ 1 = \alpha |p_{12} S_1 S_2| \end{cases} \quad (4.113)$$

And the solution is given by

$$\begin{cases} \alpha = |p_{12}/p_1 p_2| \\ |S_1| = |p_2/p_{12}| \\ |S_2| = |p_1/p_{12}| \end{cases} \quad (4.114)$$

This expression contains four possible sets of  $S_j$  required to produce all four pseudo-pure states  $\rho_{00} - \rho_{11}$  with the normalization condition for the density matrix satisfied by construction. There is even some freedom in the choice of phase angles  $\beta_j$  which implement the desired scaling coefficients  $S_j$ .<sup>9</sup>

Figure 4.25 shows the experimental results. The MQE spectra were obtained by recording signal amplitude for a range of  $t_\varphi$  commensurable with  $1/\nu_1$  and  $1/\nu_2$ , then concatenating a few copies, and applying exponential attenuation to avoid Fourier transform artefacts. Since Equation (4.107) contains only terms of the form  $\cos \varphi_j$ , one would expect the real part of the spectra to contain purely Lorentzian lines. As can be seen in some spectra, the lines in the real part are sometimes shifted in phase. The origin of this phase shift is not clear, it certainly is not related to the phase of the spins themselves. To still be able to account for the full amplitude of the coefficients  $q_j$ , the real part was used to determine their sign while the amplitude was taken from the absolute height of the corresponding line.

The qubits used for this preparation were  $\mathbf{I}_5$  and  $\mathbf{I}_7$  with  $m_S = +1/2$ . The ENDOR frequencies of the two lines were around 5 MHz away from the free fluorine Larmor frequency on the opposite sides of the spectrum. This indicates large and approximately equal effective hyperfine couplings at the given orientation and field. To avoid unnecessary build-up of higher order correlations, the mixing time could thus be chosen relatively short at  $\tau = 16$  ns .

The coefficients  $p_j$  were obtained from the calibration measurement presented on the left in Figure 4.25:

$$p_1 = 0.753, \quad p_2 = 0.872, \quad p_{12} = 1.542$$

These values are already close to the pseudo-pure state  $\rho_{00}$  and satisfy the condition  $p_1, p_2 < p_{12}$  such that Equation (4.114) has real solutions for  $\beta_j$ . This favorable situation is due to the fact that the hyperfine couplings of the two spins are large and similar.

Since the detected states have no off-diagonal components, the three coefficients  $q_j$  and the normalization condition suffice to reconstruct the density matrix and, thus, determine the fidelity of the preparation. An overview of the results are presented in Table 4.7. They show that the pseudo-pure states can be prepared with very high fidelity in  $\text{CaF}_2:\text{Ce}$ .

<sup>9</sup>In this point, the approach used here differs from the one used by J. Mende. In his work he used only one set of  $\beta_j$  to obtain  $\rho_{00}$  and used additional composite  $\pi$ -pulses to create the other states. The use of composite pulses was made necessary because of the much larger rf inhomogeneity caused by significantly larger samples.

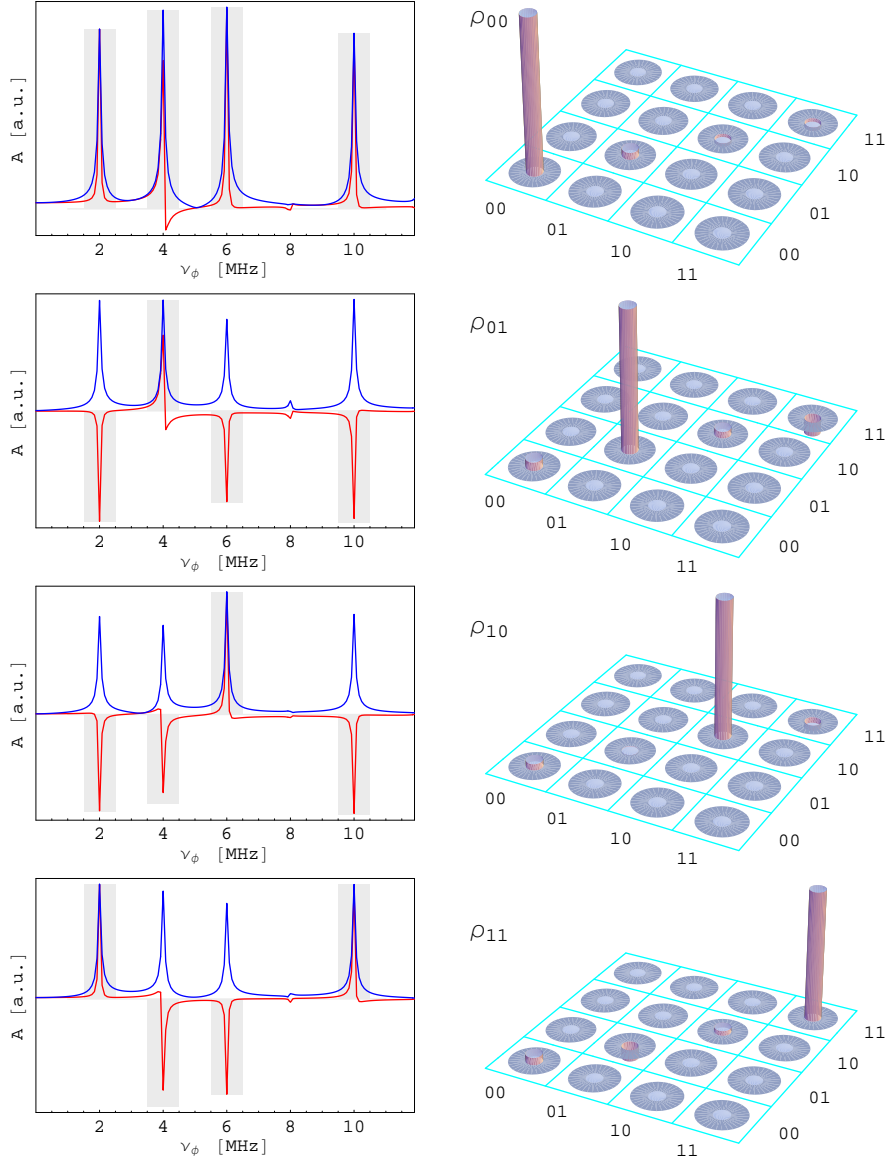


**Figure 4.25:** High fidelity two-qubit pseudo-pure states in CaF<sub>2</sub>:Ce. Left: MQE spectra. Red and blue indicate the real part and the magnitude of the Fourier transform respectively. Gray bars indicate the amplitudes used to calculate the density matrices. Right: Density matrix plots. Experimental: Pulse sequence shown in Figure 4.24; encoding frequencies  $\nu_{\varphi_1} = 2$  MHz,  $\nu_{\varphi_2} = 6$  MHz; qubits  $\mathbf{I}_5$  and  $\mathbf{I}_7$ ;  $m_S = +1/2$ ; ENDOR frequencies  $\nu_5^+ = 10.4538$  MHz, and  $\nu_7^+ = 20.5189$  MHz;  $\tau_S = 16$  ns; Euler angles:  $\{\vartheta = 110.29^\circ, \varphi = -156.23^\circ\}$ ;  $x$ -center;  $B_0 = 0.38186$  T;  $T = 8$  K;  $\nu_S = 9.344742$  GHz;

$\rho$	$\beta_1/2\pi$	$\beta_2/2\pi$	$q_1$	$q_2$	$q_{12}$	$\mathcal{F}$
00	0.155	0.169	1.089	0.955	0.950	0.998
01	0.155	$0.5 + 0.169$	1.103	-0.788	-1.078	0.992
10	$0.5 + 0.155$	0.169	-0.914	1.087	-0.991	0.998
11	$0.5 + 0.155$	$0.5 + 0.169$	-1.061	-0.813	1.102	0.994

**Table 4.7:** Pseudo-pure states in  $\text{CaF}_2:\text{Ce}$ . The four sets of phase angles for the pulse sequence, measured spin operator coefficients, and fidelity of the preparation.

## 4.7.2 Density Matrix Evolution during Two-Qubit Gates

*One-qubit* (i.e., local) gates in the  $S$ -bus cluster are readily implemented by applying simple rf pulses at appropriate ENDOR frequencies. Any interesting quantum computing experiment, however, requires that a *two-qubit* gate be available. One of the most fundamental such gates is the *controlled not* gate (*CNOT*). To implement a two-qubit gate an interaction between the qubits is, of course, required. The effective (i.e., comprised of dipolar and indirect contributions) spin-spin coupling was used for this purpose. The evolution of the density matrix during the pulse CNOT sequence and its precursors were studied in detail.

### 4.7.2.1 The Spin Echo Double Resonance Sequence

The simplest way of utilizing the coupling between two nuclear spins is the *spin echo double resonance* sequence (SEDOR) shown in yellow in Figure 4.27.

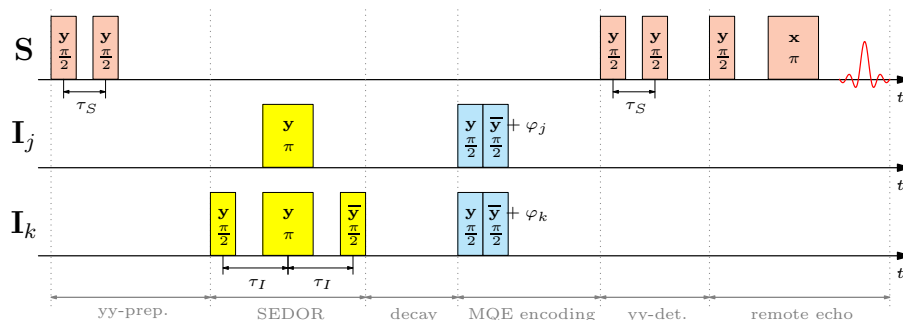


**Figure 4.26:** Pulse sequence for resolved measurement of the density matrix components during their evolution under the SEDOR sequence (*yy*-detection).

The double  $\pi$ -pulse in the middle of the free evolution period has the role of eliminating the effect of different Larmor frequencies of the two qubits as well as decoupling them from the other qubits while maintaining the coupling between the two.

The entire sequence in Figure 4.26 contains the SEDOR part embedded in a *yy*-preparation and *yy*-detection on the electron spin. In order to be able to separate the different components of the density matrix resulting from the SEDOR

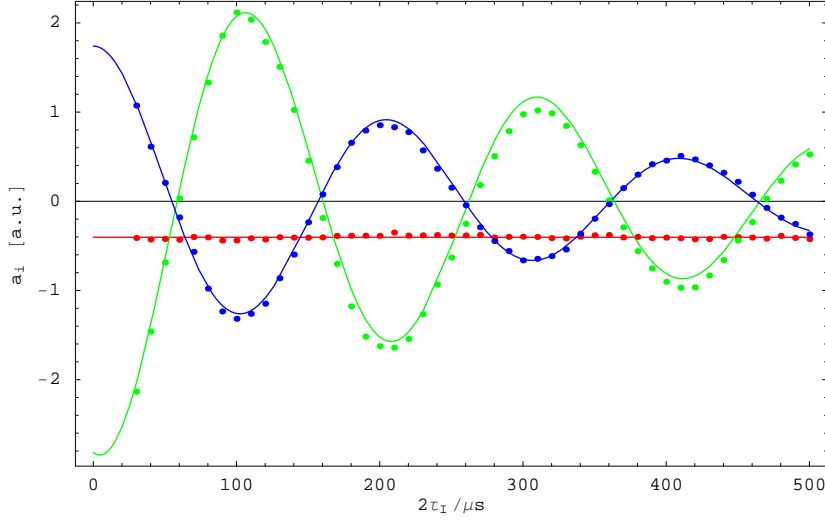


**Figure 4.27:** Evolution of density matrix components during the SEDOR sequence. Red, green, and blue indicate the MQE line heights for  $\nu_1$ ,  $\nu_2$ , and the sum of the heights of the lines at  $\nu_\Delta$  and  $\nu_\Sigma$ . Points show measured values. Solid lines are fits to the data. Experimental: Pulse sequence shown in Figure 4.26; qubits  $\mathbf{I}_9$  and  $\mathbf{I}_3$ ;  $m_S = +1/2$ ; ENDOR frequencies  $\nu_9^+ = 14.7730$  MHz, and  $\nu_3^+ = 20.9203$  MHz;  $\tau_S = 32$  ns;  $T = 8.2$  K; Euler angles  $\{\varphi = -157.75^\circ$ ,  $\theta = 111.71^\circ$ ,  $\psi = 134.83^\circ\}$ ;  $B_0 = 0.38244$  T;  $\nu_S = 9.346600$  GHz.

application, MQE-encoding pulses are also included. Notice that a sufficiently long waiting period decay after the SEDOR sequence must be used to allow for the transverse components of the nuclear part of the density matrix to decay.

The signal dependence on the evolution time  $\tau_I$  and the phase angles  $\varphi_j$  of the MQE-pulses can be calculated from the general  $S$ -bus theory described in Section 4.1.2:

$$\begin{aligned}
 S_{SEDOR} &= \gamma \left( P_2^{(+)} c_1^2 c_2^2 \right. \\
 &\quad - P_2^{(-)} s_1^2 c_2^2 \cos \varphi_1 \\
 &\quad - \cos(D_{12}\tau_I) P_2^{(-)} c_1^2 s_2^2 \cos \varphi_2 \\
 &\quad \left. + \cos(D_{12}\tau_I) P_2^{(+)} s_1^2 s_2^2 \cos \varphi_1 \cos \varphi_2 \right) \\
 &= C_0 + C_1 \cos \varphi_1 + C_2 \cos \varphi_2 + C_{12} \cos \varphi_1 \cos \varphi_2
 \end{aligned} \tag{4.115}$$

where  $D_{12}$  is the total coupling between the qubits. The proportionality constant  $\gamma$  absorbs the effect of sample size and detection sensitivity. Since the absolute values of the  $S$ -bus parameters are of no interest at this point, the value of  $\gamma$  is irrelevant (see also Section 4.7.3).

The measurement consists of recording the MQE transient for a given value of  $\tau_S$  by varying the pulse phases according to  $\varphi_j = 2\pi\nu_j t_\varphi$  as described in Section 4.7.1.1. After the Fourier transformation, the coefficients  $C_1$  and  $C_2$  are found from the height of the lines at  $\nu_1$  and  $\nu_2$ . The coefficient  $C_{12}$  is given by



the sum of the line heights at  $\nu_\Delta$  and  $\nu_\Sigma$ .  $C_0$  does not depend on  $\varphi_j$  and cannot be detected. This procedure is repeated for every value of  $\tau_I$  of interest.

The initial values of the coefficients  $C_j$  were obtained by an MQE measurement without the SEDOR sequence. As expected for the short mixing  $\tau_{\text{mix}} = 32$  ns they were all positive. The results of the SEDOR measurement are presented in Figure 4.27. They reproduce all the important features as expected. The coefficient of  $\mathbf{I}_{z_1}$ ,  $C_1$  is constant and negative. The coefficients of  $\mathbf{I}_{z_2}$  and  $\mathbf{I}_{z_1}\mathbf{I}_{z_2}$ ,  $C_2$  and  $C_{12}$  show the expected *cosinusoidal* dependence on  $\tau_I$  with the correct signs. A fit of the transients with

$$C_j(\tau_I) = A_j e^{-2\tau_I/T} \cos(2\pi D_{12}(2\tau_I + \tau_0)) \quad (4.116)$$

yielded a spin-spin coupling constant of  $D_{12} = 4.9$  kHz. The exponential model for the decay fits the data well and the average time constant is  $T \approx 330$   $\mu\text{s}$ .

Notice the inclusion of the parameter  $\tau_0$  in the fit formula. Equation (4.115) does not account for finite width of the pulses used in the experiment. The length of the  $\pi$ -pulse was, for instance,  $t_\pi = 7.2$   $\mu\text{s}$ . The fitted value was  $\tau_0 \approx 7.6$   $\mu\text{s}$  which is in good agreement with the expectation. It is not easily possible to accurately predict the effects of finite pulse width. Therefore, a measurement like the one presented here must also be used to calibrate the setting of the evolution time.

#### 4.7.2.2 The ‘‘Insensitive Nuclei Enhanced by Polarization Transfer’’ Sequence

The measurement of the evolution during the SEDOR sequence demonstrates that the basic behavior of the spin system under a simple two-qubit gate is correctly described by the theory. However, the unitary transformation effected by the SEDOR sequence deviates significantly from the desired *CNOT* gate.

A sequence which produces the almost correct behavior is known as the ‘‘*insensitive nuclei enhanced by polarization transfer*’’ (INEPT) sequence [108]. As shown in Figure 4.28, it differs from the SEDOR sequence, in that the last  $\pi/2$ -pulse is applied no longer in  $y$  but in  $x$ -direction. This has the dramatic effect, that this sequence now turns some odd product terms in the density matrix to

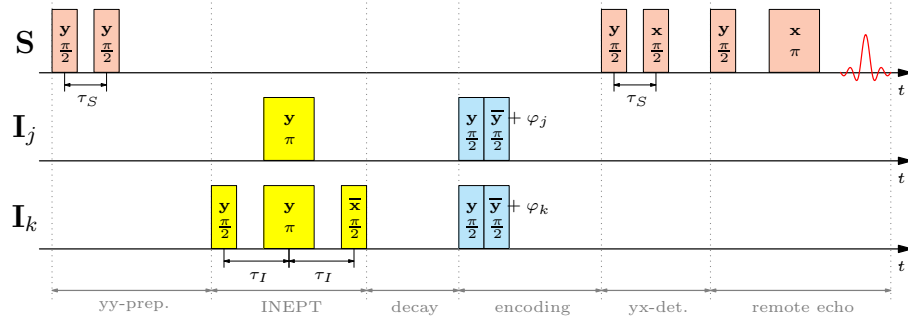


**Figure 4.28:** Pulse sequence for resolved measurement of the density matrix components during their evolution under the INEPT sequence ( $yx$ -detection).

even and vice versa. To detect a thus modified density matrix, the  $yx$ -detection sequence must be used.

Analogously to Equation (4.115), the signal produced by this sequence is given by

$$\begin{aligned} S_{INEPT} &= \gamma \left( \sin(D_{12}\tau_I) c_1 s_1 s_2^2 P_2^{(+)} \cos \varphi_2 \right. \\ &\quad \left. + \sin(D_{12}\tau_I) c_1 s_1 s_2^2 P_2^{(-)} \cos \varphi_1 \cos \varphi_2 \right) \\ &= C_2 \cos \varphi_2 + C_{12} \cos \varphi_1 \cos \varphi_2 \end{aligned} \quad (4.117)$$

The change of the dependence on  $\tau_I$  from *cosinusoidal* for SEDOR to *sinusoidal* for INEPT has to do with the change of the detection sequence: In the case of SEDOR the gradual reduction of an initially existing term is observed. For INEPT, the terms of interest are initially not present and it's their gradual buildup that is detected.

The experimental findings are presented in Figure 4.29. Again, the coefficients

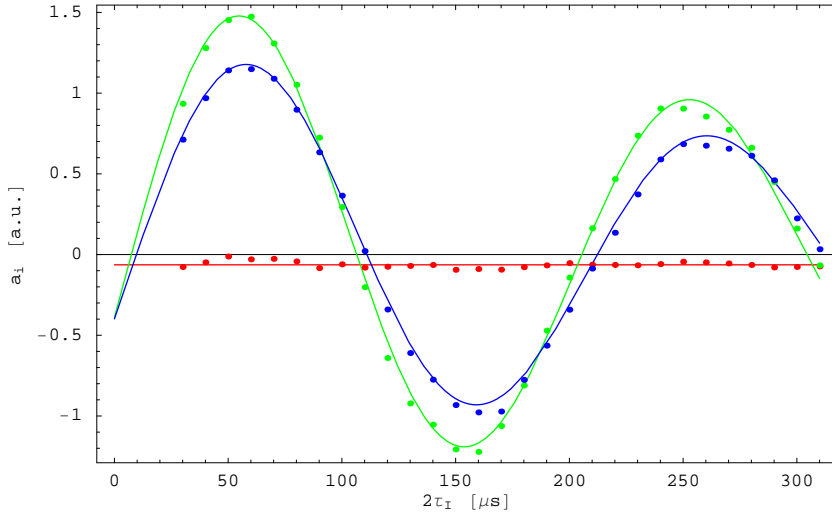


**Figure 4.29:** Evolution of density matrix components during the INEPT sequence. Red, green, and blue indicate the MQE line heights for  $\nu_1$ ,  $\nu_2$ , and the sum of the heights of the lines at  $\nu_\Delta$  and  $\nu_\Sigma$ . Points show measured values. Solid lines are fits to the data. For experimental details see Figure 4.27.

of the  $\mathbf{I}_{z_1}$  and  $\mathbf{I}_{z_1}\mathbf{I}_{z_2}$  terms have the correct signs and do, in fact, depend on  $\tau_I$  sinusoidally.  $C_1$  is nearly zero, as predicted. A fit of  $C_2$  and  $C_{12}$  with

$$C_j(\tau_I) = B_j e^{-2\tau_I/T} \sin(2\pi D_{12}(2\tau_I + \tau_0)) \quad (4.118)$$

produces the same coupling strength of  $D_{12} = 4.9$  kHz and an even longer time constant of  $T = 450$   $\mu\text{s}$ . The finite pulse width effect a  $\tau_0 = 8.1$   $\mu\text{s}$ .

#### 4.7.2.3 The Controlled Not Sequence

A *controlled not* (*CNOT*) operation inverts the controlled bit depending on the state of the control bit. There are four possible *CNOT* gates depending on

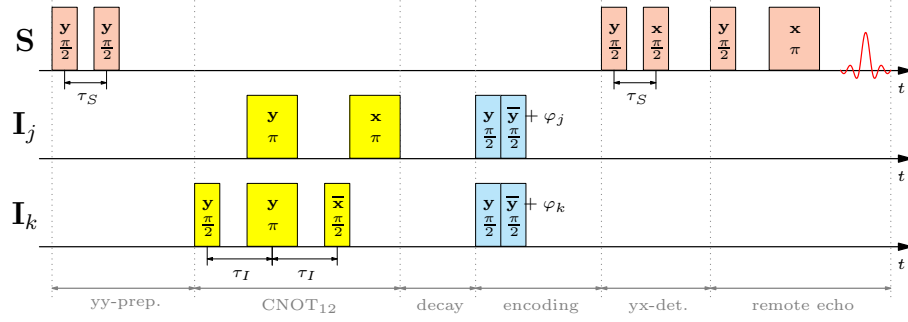


**Figure 4.30:** Pulse sequence for resolved measurement of the density matrix components during their evolution under the  $CNOT_{12}$  sequence (yx-detection).

which of the two qubits is the control bit and which of its two states is the active state<sup>10</sup>:

$$\begin{aligned}
 U_{CNOT_{12}} &= \begin{pmatrix} 0 & 1 & 0 & 0 \\ 1 & 0 & 0 & 0 \\ 0 & 0 & 1 & 0 \\ 0 & 0 & 0 & 1 \end{pmatrix} & U_{CNOT_{23}} &= \begin{pmatrix} 1 & 0 & 0 & 0 \\ 0 & 0 & 1 & 0 \\ 0 & 1 & 0 & 0 \\ 0 & 0 & 0 & 1 \end{pmatrix} \\
 U_{CNOT_{34}} &= \begin{pmatrix} 1 & 0 & 0 & 0 \\ 0 & 1 & 0 & 0 \\ 0 & 0 & 0 & 1 \\ 0 & 0 & 1 & 0 \end{pmatrix} & U_{CNOT_{23}} &= \begin{pmatrix} 0 & 0 & 0 & 1 \\ 0 & 1 & 0 & 0 \\ 0 & 0 & 1 & 0 \\ 1 & 0 & 0 & 0 \end{pmatrix}
 \end{aligned} \tag{4.119}$$

The notation is such that the subscripts designate the rows of the matrix with off-diagonal elements. As an example, the  $U_{CNOT_{12}}$  inverts the second qubit, when the first bit is zero:

$$\begin{array}{ccc}
 & CNOT_{12} & \\
 00 & \longrightarrow & 01 \\
 01 & \longrightarrow & 00 \\
 10 & \longrightarrow & 10 \\
 11 & \longrightarrow & 11
 \end{array} \tag{4.120}$$

A pulse sequence implementing  $CNOT_{12}$  is shown in yellow Figure 4.30. It extends the INEPT sequence by an additional  $\pi$ -pulse on the first qubit to correct its phase. Again, an MQE sequence is included for component-wise encoding. The detection sequence is  $yx$ . Notice that the unitary transformation produced by this sequence is

$$\tilde{U}_{CNOT_{12}} = -\frac{1}{\sqrt{2}} \begin{pmatrix} 0 & 1-i & 0 & 0 \\ 1+i & 0 & 0 & 0 \\ 0 & 0 & 1+i & 0 \\ 0 & 0 & 0 & -1+i \end{pmatrix} \tag{4.121}$$

<sup>10</sup>Note that  $U_{CNOT_{23}}$  is also called a *swap* gate

which differs from the definition in Equation (4.119) in the phases of the elements. To correct these deviations, additional pulses implementing  $z$ -rotations would have to be added to the sequence. This, however, is not necessary because the phase factors cancel out, when the operator is applied to a density matrix:

$$\tilde{U}_{CNOT_{12}} \rho \tilde{U}_{CNOT_{12}}^\dagger \equiv U_{CNOT_{12}} \rho U_{CNOT_{12}}^\dagger \quad (4.122)$$

such that the truth table in Equation (4.120) is still valid for  $\tilde{U}_{CNOT_{12}}$ . Therefore, it was not necessary to introduce additional pulses which would only produce errors due to pulse imperfections.

The signal resulting from the sequence is similar to  $S_{INEPT}$  in Equation (4.117):

$$\begin{aligned} S_{CNOT_{12}} &= \gamma \left( -\sin(D_{12}\tau_I) c_1 s_1 s_2^2 P_2^{(+)} \cos \varphi_2 \right. \\ &\quad \left. + \sin(D_{12}\tau_I) c_1 s_1 s_2^2 P_2^{(-)} \cos \varphi_1 \cos \varphi_2 \right) \\ &= C_2 \cos \varphi_2 + C_{12} \cos \varphi_1 \cos \varphi_2 \end{aligned} \quad (4.123)$$

The experimental procedure is the same as in the case of SEDOR and INEPT measurements. The results are shown in Figure 4.29. The sinusoidal dependence with the correct signs of the two coefficients  $C_2$  and  $C_{12}$  is clearly seen. The fit of the terms dependent to  $\tau_I$  with the model in Equation (4.118) reproduces the coupling strength of  $D_{12} = 4.9$  kHz. The time constant of the decay was  $T \approx 400 \mu\text{s}$  and the time offset due to finite pulse width  $\tau_0 \approx 6.2 \mu\text{s}$ . The values of  $D_{12}$  and  $\tau_0$  can be used to calibrate the value of  $\tau_I$  required to implement a  $CNOT$  operation. It corresponds to the first maximum of the sine wave.

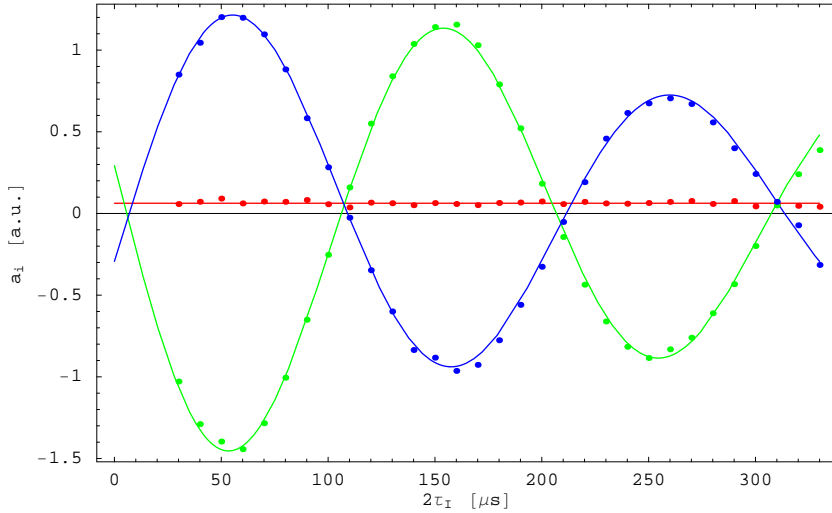


**Figure 4.31:** Evolution of density matrix components during the  $CNOT_{12}$  sequence. Red, green, and blue indicate the MQE line heights for  $\nu_1$ ,  $\nu_2$ , and the sum of the heights of the lines at  $\nu_\Delta$  and  $\nu_\Sigma$  respectively. Points show measured values. Solid lines are fits to the data. For experimental details see Figure 4.27.

### 4.7.3 Quantitative Evaluation of the $S$ -Bus Model

As described in Section 4.1.2, the density matrix of the spin system in  $S$ -bus consists of products of nuclear spin operators. Measurements of the evolution of the density matrix components under two-qubit gates provide a possibility for determining the various coefficients defining the shape of the density matrix.

Both, the SEDOR and the INEPT sequences are required to obtain a full set of values for a pair of spins. The full sequence for the case of the SEDOR gate

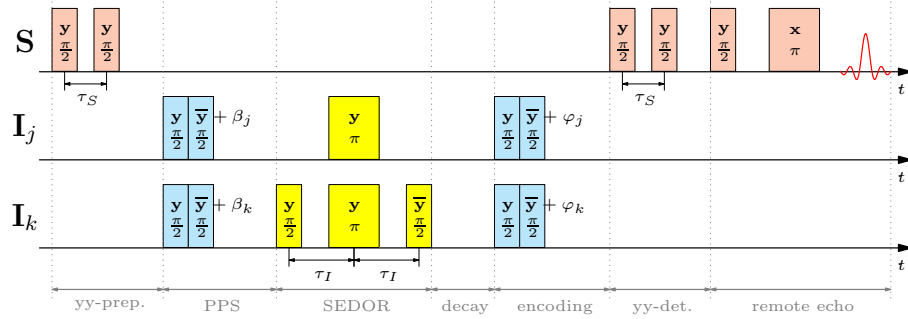


**Figure 4.32:** SEDOR pulse sequence used for measurements for determination of the  $S$ -bus coefficients. The pulses in the “PPS” section are used to scale the operators  $\mathbf{I}_{z_1}$  and  $\mathbf{I}_{z_2}$  by  $S_j = \cos \beta_j$  prior to the application of the two-qubit gate. The other sequence contains an INEPT instead of the SEDOR gate and uses  $yx$ -detection instead of  $yy$ .

is shown in Figure 4.32. The INEPT case is similar except, that  $yx$ -detection is used there. In order to obtain a greater number of controllable parameters a pair of pulses similar to the type used for preparation of pseudo-pure states precedes the actual two-qubit gate. The effect of the  $\frac{\pi}{2}|y_j - \frac{\pi}{2}|y_j + \beta_j$  pulses and the following decay period is to scale the amplitude of the single spin operators  $\mathbf{I}_{z_j}$  by a factor  $S_j = \cos \beta_j$ . The term  $\mathbf{I}_{z_1} \mathbf{I}_{z_2}$  is scaled by  $S_1 S_2 = \cos \beta_1 \cos \beta_2$ .

Analogously to Equation (4.115) and Equation (4.117), the signal amplitude is given by

$$\begin{aligned}
 S_{SEDOR} &= A_0 + A_1 \cos \varphi_1 \\
 &\quad + A_2 \cos(D_{12}\tau_I) \cos \varphi_2 \\
 &\quad + A_{12} \cos(D_{12}\tau_I) \cos \varphi_1 \cos \varphi_2 \\
 S_{INEPT} &= B_0 + B_1 \cos \varphi_1 \\
 &\quad + B_2 \sin(D_{12}\tau_I) \cos \varphi_2 \\
 &\quad + B_{12} \sin(D_{12}\tau_I) \cos \varphi_1 \cos \varphi_2
 \end{aligned} \tag{4.124}$$

where the coefficients

$$\left\{ \begin{array}{l} A_1 = -\alpha P_2^{(-)} s_1^2 c_2^2 S_1^A \\ A_2 = -\alpha P_2^{(-)} c_1^2 s_2^2 S_2^A \\ A_{12} = \alpha P_2^{(+)} s_1^2 s_2^2 S_1^A S_2^A \\ B_2 = \beta P_2^{(+)} c_1 s_1 s_2^2 S_1^B S_2^B \\ B_{12} = \beta P_2^{(-)} c_1 s_1 s_2^2 S_2^B \\ A_0 = B_0 = B_1 = 0 \end{array} \right. \quad (4.125)$$

depend on the sought after parameters  $c_j$ ,  $s_j$ , and  $P_2^{(\pm)}$ . These, are determined by the effective hyperfine couplings for nuclear spins in the cluster (cf. Section 4.1.2). They are, in particular, dependent on the mixing time  $\tau_S$  during the electron spin preparation and detection sequences. Equation (4.125) can be solved for  $c_j$ ,  $s_j$ , and  $P_2^{(\pm)}$  in the following way:

$$\left\{ \begin{array}{l} s_1^2 = 1 / \left( 1 - \frac{A_2}{A_{12}} \frac{B_2}{B_{12}} \frac{S_1^A}{S_1^B} \right) \\ s_2^2 = 1 / \left( 1 - \frac{A_1}{A_{12}} \frac{B_2}{B_{12}} \frac{S_2^A}{S_1^B} \right) \\ P_2^{(+)} = \frac{1}{\alpha} \frac{1}{s_1^2 s_2^2} \frac{1}{S_1^A S_2^A} A_{12} \\ P_2^{(-)} = \frac{1}{\alpha} \frac{1}{s_1^2 s_2^2} \frac{S_1^B}{S_1^A S_2^A} \frac{B_{12}}{B_2} A_{12} \\ c_1 s_1 = \frac{\alpha}{\beta} \frac{S_1^A S_2^A}{S_1^B S_2^B} \frac{B_2}{A_{12}} \end{array} \right. \quad (4.126)$$

The values of  $A_j$  and  $B_j$  can be determined experimentally by SEDOR and INEPT measurements respectively. They correspond to the amplitudes of the  $1Q_1$ -,  $1Q_2$ -, and the sum of the  $0Q$ - and  $2Q$ -lines in the MQE spectrum and can be obtained by fitting the dependence of these amplitudes on  $\tau_I$  as described above. This approach has the advantage of being less sensitive to baseline errors, because most values of interest are obtained from the amplitude of the modulation of line height with  $\tau_I$ .

Note, that Equation (4.124) contains overall proportionality constants  $\alpha$  and  $\beta$ . They depend on the number of clusters in the sample and on any number of ill-defined experimental parameters. For instance, due to the limited power of the microwave pulses, not the entire electron spin transition line can be excited uniformly. The sensitivity of detection varies also, due to temperature dependent losses in the detection chain and gain drift of the various amplifiers etc. A calibration of the detection sensitivity is thus not feasible in the setup used in this work and reliance on the absolute amplitude of the signal must be avoided.

Equation (4.126) shows that  $s_j^2$  only depend on *ratios* of parameters obtained from the *same* measurement. They can be expected to be relatively robust

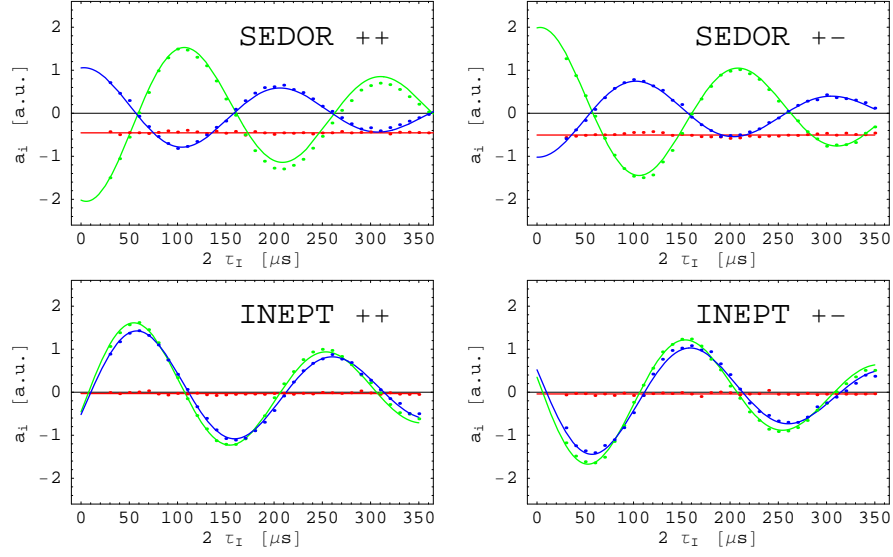


**Figure 4.33:** Example of measurements of the evolution of nuclear density matrix components under the SEDOR (top) and INEPT (bottom) sequence for determination of the  $S$ -bus amplitudes. Pulse sequence shown in Figure 4.32. The labels “ $\pm$ ” indicate the chosen combination of scaling coefficients  $S_1, S_2 = \pm 1$ . Red, green, and blue indicate the MQE line heights for  $\nu_1, \nu_2$ , and the sum of the heights of the lines at  $\nu_\Delta$  and  $\nu_\Sigma$ . Points show measured values. Solid lines are fits to the data. Experimental: Qubits  $\mathbf{I}_9$  and  $\mathbf{I}_3$ ;  $m_S = +1/2$ ; ENDOR frequencies  $\nu_9^+ = 14.7327$  MHz, and  $\nu_3^+ = 20.9030$  MHz;  $\tau_S = 52$  ns;  $T = 8.2$  K; Euler angles  $\{\vartheta = 111.63^\circ, \varphi = -157.73^\circ\}$ ;  $x$ -center;  $B_0 = 0.38162$  T;  $\nu_S = 9.339520$  GHz. Another set of measurement was performed at  $\tau_S = 72$  ns.

against drift of experimental parameters. The values of  $P_2^{(\pm)}$  do depend on the detection efficiency  $\alpha$  which is afflicted by the above stated problems. This dependence can be eliminated when the definition (Equation (4.16))

$$P_2^{(\pm)} = \frac{1}{2} (1 \pm M_{N-2}) \quad (4.127)$$

is used. From it, the relation

$$P_2^{(+)} + P_2^{(-)} = 1 \quad (4.128)$$

follows. The ratio

$$r = \frac{P_2^{(+)}}{P_2^{(-)}} = \frac{1}{S_1^B} \frac{B_2}{B_{12}} \quad (4.129)$$

is independent of  $\alpha$  and the parameters can be calculated according to

$$P_2^{(+)} = \frac{r}{r+1}, \quad \text{and} \quad P_2^{(-)} = \frac{1}{r+1} \quad (4.130)$$

Two sets of measurements were performed at  $\tau_S = 52$  ns and  $\tau_S = 72$  ns. For each value of  $\tau_S$  and for different combinations of the scaling factors  $S_j$ , the dependence of the MQE line heights was recorded for a range of  $\tau_I$  from 30  $\mu\text{s}$

to 360  $\mu$ s. The phase angles  $\beta_j$  of the scaling pulses were chosen such that the scaling coefficients were always of magnitude one:  $S_j = \pm 1$ . Figure 4.33 shows a few examples of  $\tau_I$ -transients. Notice, for instance, how changing the sign of  $S_2$  in the case of the SEDOR measurement inverts the  $\mathbf{I}_{z_2}$  and  $\mathbf{I}_{z_1}\mathbf{I}_{z_2}$  term without affecting the  $\mathbf{I}_{z_1}$  component. In INEPT measurements, both  $\mathbf{I}_{z_2}$  and  $\mathbf{I}_{z_1}\mathbf{I}_{z_2}$  are affected by the switching of  $S_2$ .

The  $\tau_I$ -transients were fitted according to Equation (4.116) and Equation (4.118) to obtain the values of  $A_j$  and  $B_j$ . Table 4.8 contains the summary of performed measurements and fitted values. To demonstrate the consistency of magnitudes

sequence	$\tau_S[ns]$	$S_1^A$	$S_2^A$	$S_1^A A_1$	$S_2^A A_2$	$S_1^A S_2^A A_{12}$
SEDOR	52	+	+	-0.45	-2.09	1.07
		-	+	-0.53	-2.51	1.23
		+	-	-0.51	-2.03	1.03
		-	-	-0.53	-2.10	1.07
	72	+	+	-1.19	-0.79	0.57
		+	-	-1.20	-0.72	0.53
		-	+	-1.35	-0.82	0.64
sequence	$\tau_S[ns]$	$S_1^B$	$S_2^B$	$B_1$	$S_1^B S_2^B B_2$	$S_2^B B_{12}$
INEPT	52	+	+	-0.03	1.88	1.67
		+	-	-0.04	1.99	1.76
		-	+	-0.06	1.66	1.66 <sup>†</sup>
	72	+	+	-0.07	0.59	0.56
		+	-	-0.05	0.60	0.58
		-	+	-0.01	0.65	0.65

**Table 4.8:** Fitted amplitudes of the oscillations of the MQE lines' heights under SEDOR and INEPT sequences. Measurements for different combinations of scaling factors  $S_j$  are listed. To demonstrate the consistency of the different measurements among each other and with the model, the amplitudes are multiplied by appropriate scaling factors. <sup>†</sup>This measurement was aborted after  $\tau_I = 200 \mu$ s due to drift of the detection phase.

between different sets of  $S_j$ , the values of  $A_j$  and  $B_j$  are listed dressed with the values of the scaling factors  $S_j$  chosen for that measurement. In addition, the data shows that the scaling factors enter the different amplitudes in Equation (4.125) correctly. In particular, in the case of the INEPT gate, the term  $\mathbf{I}_{z_2}$  is affected by both  $S_1$  and  $S_2$ , whereas  $\mathbf{I}_{z_1}\mathbf{I}_{z_2}$  only depends on  $S_2$ . With these experimental values, the S-bus parameters can now be calculated according to Equation (4.126) and Equation (4.130).

The results are presented in Table 4.9. As expected, the values of  $s_j^2$  and  $P_2^{(\pm)}$  show relatively little variance. The fact, that the scaling  $\pi/2$ -pulses, which were the only parameters varied between measurements produce such small errors, is an indirect indication of the fidelity of the pulses applied to nuclear spins in general.

The parameters  $P_2^{(\pm)}$  measure the amount of correlations of the other nuclear spins in the cluster. As the initial polarization of the electron spin is converted to such correlations at the time scale of the electron spin FID ( $\approx 20$  ns),  $P_2^{(\pm)}$



quickly approach  $1/2$ . At larger values of  $\tau_S$ , the constructive interference can only occasionally produce noticeable deviations. Thus, the observed situation at  $\tau_S = 52$  ns and  $\tau_S = 72$  ns is in excellent agreement with the expectations.

The parameter  $c_1s_1$  deserves special attention. Its value, by definition cannot exceed  $1/2$ . At least some of the measured values clearly exceed that limit. The reason is found in Equation (4.126).  $c_1s_1$  depends on  $\alpha/\beta$  which is the ratio of detection sensitivities of the  $yy$ - and  $yx$ -detection sequences. Ideally, they should be equal. However, small phase errors and amplitude imbalances apparently lead to deviations from  $\alpha/\beta = 1$ .

To summarize, this section demonstrates a method of experimentally determining the parameters governing the amount of polarization and the correlation structure of the density matrix of nuclear qubits in an  $S$ -bus cluster.

$\tau_S$ [ns]	$S_1^A$	$S_2^A$	$S_1^B$	$S_2^B$	$s_1^2$	$s_2^2$	$P_2^{(-)}$	$P_2^{(+)}$	$c_1s_1$
52	+	+	+	+	0.31	0.68	0.529	0.471	0.55
	+	+	+	-	0.31	0.68	0.531	0.469	0.58
	-	+	+	+	0.30	0.67	0.529	0.471	0.46
	-	+	+	-	0.30	0.67	0.531	0.469	0.49
	+	-	+	+	0.31	0.64	0.529	0.471	0.57
	+	-	+	-	0.31	0.64	0.531	0.469	0.60
	-	-	+	+	0.31	0.64	0.529	0.471	0.55
	-	-	+	-	0.31	0.64	0.531	0.469	0.58
					0.31	0.66	0.530	0.470	0.55
72	+	+	+	+	0.41	0.31	0.515	0.485	0.42
	+	+	+	-	0.41	0.32	0.506	0.494	0.43
	+	+	-	+	0.42	0.33	0.500	0.500	0.48
	+	-	+	+	0.41	0.30	0.515	0.485	0.46
	+	-	+	-	0.42	0.30	0.506	0.494	0.47
	+	-	-	+	0.43	0.31	0.500	0.500	0.52
	-	+	+	+	0.42	0.31	0.515	0.485	0.39
	-	+	+	-	0.43	0.32	0.506	0.494	0.41
	-	+	-	+	0.44	0.32	0.500	0.500	0.45
					0.42	0.31	0.507	0.493	0.45

**Table 4.9:** Values of the  $S$ -bus amplitudes for  $\tau_S = 52$  ns and  $\tau_S = 72$  ns determined from SEDOR and INEPT measurements summarized in Table 4.8. Numbers at the bottom of a column are mean values.

## 4.8 Entanglement of Distant Qubits in the *S*-Bus

The phenomenon of entanglement plays a central role in quantum computing. Creation, manipulation, and detection of entangled states must, thus, be demonstrated in any experimental implementation. In this section, the stepwise procedure to creation of entanglement of two nuclear qubits is reported.

### 4.8.1 Distant Qubits

In the *S*-bus concept of quantum computing, the electron spin is used for readout of the information about the nuclear qubits as well as to connect them via the hyperfine coupling. To emphasize the latter role, two *distant* qubits were selected for entanglement.

The dipole-dipole interaction is highly anisotropic. It is, therefore, possible to choose an orientation of the inter-spin vector such that the direct dipole coupling vanishes. In the high-field approximation this occurs at an angle between the inter-spin vector and the static field defined by  $3 \cos^2 \vartheta_m - 1 = 0$ . In NMR this angle of  $\theta_m \approx 54.74^\circ$  is known as the *magic angle*. At such an orientation, the spins are not directly coupled and in this sense “distant”. The interaction required to implement two-qubit gates is provided by the quantum bus.

The task of finding a pair of distant spins is complicated by the fact that the high-field approximation is not applicable to the *S*-bus cluster in  $\text{CaF}_2:\text{Ce}$  at X-band fields. The approximation assumes that the spins are quantized along the direction of the static field. In  $\text{CaF}_2:\text{Ce}$  the hyperfine coupling is comparable with the Zeeman interaction and the quantization axes are significantly tilted. Therefore, it is not possible to accurately determine the spin-spin coupling theoretically (cf. Section 4.5.5). It is, however, possible to ascertain the contribution of the dipole-dipole interaction to the total spin-spin coupling, because the quantization axes are entirely determined by the hyperfine and Zeeman terms and are thus completely accounted for in the simulation. The Hamiltonian can be constructed with and without the dipole-dipole term. The difference between the coupling constants is then attributed to the dipolar coupling.

Besides negligible dipolar coupling, the orientation must satisfy additional constraints: The ENDOR lines of the two spins must be well separated from all other lines. Also, a strong and approximately equal effective hyperfine couplings are desirable. All reachable sample orientations with one of the inter-site vectors at the magic angle were calculated. For each orientation and spin-pair, the ENDOR spectrum and spin-spin coupling were computed. For promising candidates, the ENDOR spectra in the regions of interest and the actual spin-spin couplings were measured.

The ENDOR spectrum at the orientation used for the measurement in this section is shown in Figure 4.34. The measured value of total spin-spin coupling of the qubits  $\mathbf{I}_4$  and  $\mathbf{I}_6$  for  $m_S = -1/2$  was 4.9 kHz. The values of the spin-spin coupling obtained for the simulation were 4.6 kHz when the dipole-dipole term was included in the Hamiltonian and 4.9 kHz without it. Thus, the direct dipolar interaction with 0.3 kHz contributes only 6% of the total spin-spin coupling and the two qubits can be considered distant in the sense explained above.

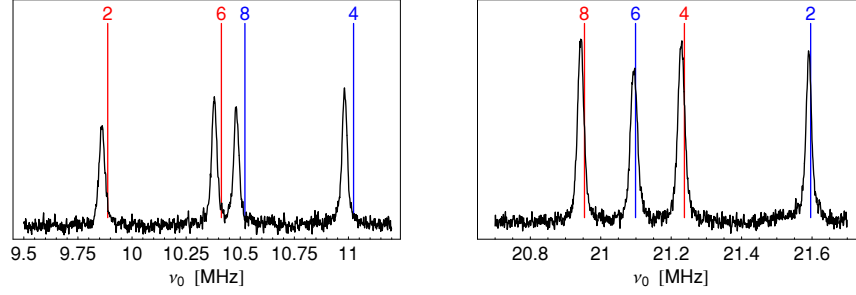


**Figure 4.34:** ENDOR spectrum at an orientation where the qubits  $\mathbf{I}_4^-$  and  $\mathbf{I}_6^-$  are coupled exclusively by the quantum bus. Colored lines indicate simulated transition frequencies. Red: Transitions for  $m_S = +1/2$ . Blue: Transitions for  $m_S = -1/2$ . Experimental:  $x$ -center;  $B_0 = 0.39115$  T;  $\nu = 9.354098$  GHz; ENDOR frequencies  $\nu_4^- = 10.9806$  MHz, and  $\nu_6^- = 21.0928$  MHz;  $\tau_S = 48$  ns;  $T = 8.2$  K; Euler angles:  $\{\varphi = -54.98^\circ, \vartheta = 40.03^\circ, \psi = 95.62^\circ\}$ .

## 4.8.2 Creation of Entanglement

The textbook example of generation of two-qubit entangled states starts with one of the basis states. A *Hadamard* transformation  $H$  is applied to the qubit which is the control bit in the following *CNOT* operation. The Walsh-Hadamard transformation is a special form of discrete Fourier transform. For two points, it is defined by<sup>11</sup>

$$H = \frac{1}{\sqrt{2}} \begin{pmatrix} 1 & 1 \\ 1 & -1 \end{pmatrix} \quad (4.131)$$

In Dirac notation, this corresponds to

$$H = \frac{1}{\sqrt{2}} (|0\rangle\langle 0| + |1\rangle\langle 0| + |0\rangle\langle 1| - |1\rangle\langle 1|) \quad (4.132)$$

When the  $CNOT_{12}$  variant of the *CNOT* gate is chosen, the following entangled states result:

$$\begin{aligned} |00\rangle &\xrightarrow{H} \frac{1}{\sqrt{2}} (|00\rangle + |10\rangle) \xrightarrow{CNOT_{12}} \frac{1}{\sqrt{2}} (|01\rangle + |10\rangle) = |\Psi^+\rangle \\ |01\rangle &\longrightarrow \frac{1}{\sqrt{2}} (|01\rangle + |11\rangle) \longrightarrow \frac{1}{\sqrt{2}} (|00\rangle + |11\rangle) = |\Phi^+\rangle \\ |10\rangle &\longrightarrow \frac{1}{\sqrt{2}} (|00\rangle - |10\rangle) \longrightarrow \frac{1}{\sqrt{2}} (|01\rangle - |10\rangle) = |\Psi^-\rangle \\ |11\rangle &\longrightarrow \frac{1}{\sqrt{2}} (|01\rangle - |11\rangle) \longrightarrow \frac{1}{\sqrt{2}} (|00\rangle - |11\rangle) = |\Phi^-\rangle \end{aligned} \quad (4.133)$$

The four states  $\Psi^\pm$  and  $\Phi^\pm$  are the famous *Bell states*. They are mutually orthogonal and constitute the *entangled basis* for two qubits. Their density

<sup>11</sup>Notice that the  $2 \times 2$  matrix must be extended to  $4 \times 4$ , when applied to a two-qubit density matrix. For instance, a Hadamard gate on the first qubit is given by  $U_{H_1} = H \otimes \mathbf{I}_0$ .

matrices are

$$\begin{aligned}
\rho_{\Psi^+} &= \frac{1}{2} \begin{pmatrix} 0 & 0 & 0 & 0 \\ 0 & 1 & 1 & 0 \\ 0 & 1 & 1 & 0 \\ 0 & 0 & 0 & 0 \end{pmatrix} = \frac{1}{4} \mathbf{I}_0 + \mathbf{I}_{x_1} \mathbf{I}_{x_2} + \mathbf{I}_{y_1} \mathbf{I}_{y_2} - \mathbf{I}_{z_1} \mathbf{I}_{z_2} \\
\rho_{\Phi^+} &= \frac{1}{2} \begin{pmatrix} 1 & 0 & 0 & 1 \\ 0 & 0 & 0 & 0 \\ 0 & 0 & 0 & 0 \\ 1 & 0 & 0 & 1 \end{pmatrix} = \frac{1}{4} \mathbf{I}_0 + \mathbf{I}_{x_1} \mathbf{I}_{x_2} - \mathbf{I}_{y_1} \mathbf{I}_{y_2} + \mathbf{I}_{z_1} \mathbf{I}_{z_2} \\
\rho_{\Psi^-} &= \frac{1}{2} \begin{pmatrix} 0 & 0 & 0 & 0 \\ 0 & 1 & -1 & 0 \\ 0 & -1 & 1 & 0 \\ 0 & 0 & 0 & 0 \end{pmatrix} = \frac{1}{4} \mathbf{I}_0 - \mathbf{I}_{x_1} \mathbf{I}_{x_2} - \mathbf{I}_{y_1} \mathbf{I}_{y_2} - \mathbf{I}_{z_1} \mathbf{I}_{z_2} \\
\rho_{\Phi^-} &= \frac{1}{2} \begin{pmatrix} 1 & 0 & 0 & -1 \\ 0 & 0 & 0 & 0 \\ 0 & 0 & 0 & 0 \\ -1 & 0 & 0 & 1 \end{pmatrix} = \frac{1}{4} \mathbf{I}_0 - \mathbf{I}_{x_1} \mathbf{I}_{x_2} + \mathbf{I}_{y_1} \mathbf{I}_{y_2} + \mathbf{I}_{z_1} \mathbf{I}_{z_2}
\end{aligned} \tag{4.134}$$

An implementation of the Hadamard transform, as defined by Equation (4.131), with the means of magnetic resonance is cumbersome. Fortunately, a simple  $\frac{\pi}{2}|_y$ -pulse can be used instead:

$$\tilde{H} = P_y \left( \frac{\pi}{2} \right) = \frac{1}{\sqrt{2}} \begin{pmatrix} 1 & -1 \\ 1 & 1 \end{pmatrix} \tag{4.135}$$

With the use of this alternative Hadamard transform, Equation (4.133) is slightly modified:

$$\begin{aligned}
&\tilde{H} - CNOT_{12} \\
|00\rangle &\longrightarrow |\Psi^+\rangle \\
|01\rangle &\longrightarrow |\Phi^-\rangle \\
|10\rangle &\longrightarrow |\Psi^-\rangle \\
|11\rangle &\longrightarrow |\Phi^+\rangle
\end{aligned} \tag{4.136}$$

### 4.8.3 Implementation and Tomography of the *CNOT* gate

The first step to creation of entanglement is the implementation of a *CNOT*-gate and the tomography of its output states. The pulse sequence is shown in Figure 4.35. It begins with the *yy*-preparation sequence applied to the electron spin. The resulting density matrix  $\rho_0$  is the same as  $\rho_{yy}$  in Equation (4.10). The preparation sequence for pseudo-pure states (PPS) introduces the scaling factors  $S_j = \cos \beta_j$ :

$$\begin{aligned}
\rho_1 &= c_1 c_2 \Pi_{N-2}^{(+)} \mathbf{I}_0 - 2s_1 c_2 S_1 \Pi_{N-2}^{(-)} \mathbf{I}_{z_1} \\
&\quad - 2c_1 s_2 S_2 \Pi_{N-2}^{(-)} \mathbf{I}_{z_2} - 4s_1 s_2 S_1 S_2 \Pi_{N-2}^{(+)} \mathbf{I}_{z_1} \mathbf{I}_{z_2} \tag{4.137}
\end{aligned}$$

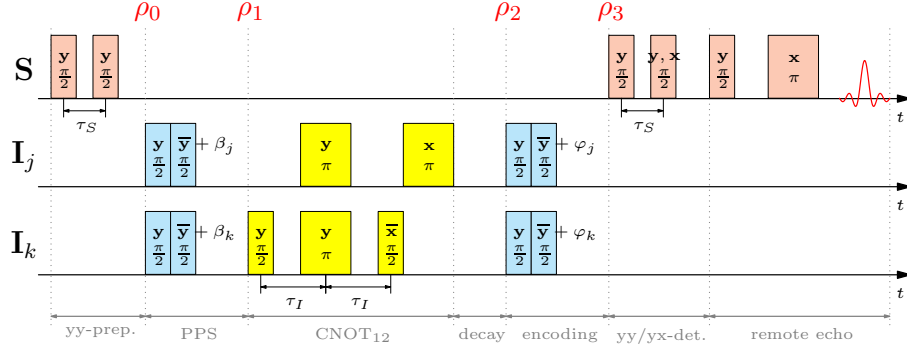


**Figure 4.35:** Pulse sequence for creation and tomography of the output states of the  $CNOT_{12}$  operation.

or – reduced to the subspace of the qubits of interest:

$$\begin{aligned} \rho_1^{(12)} &= Q_0^{(yy)} \mathbf{I}_0 - 2Q_1^{(yy)} S_1 \mathbf{I}_{z_1} - 2Q_2^{(yy)} S_2 \mathbf{I}_{z_2} - 4Q_{12}^{(yy)} S_1 S_2 \mathbf{I}_{z_1} \mathbf{I}_{z_2} \\ &= q_0 \mathbf{I}_0 + 2q_1 \mathbf{I}_{z_1} + 2q_2 \mathbf{I}_{z_2} + 4q_{12} \mathbf{I}_{z_1} \mathbf{I}_{z_2} \end{aligned} \quad (4.138)$$

where

$$\begin{aligned} q_1 &= -Q_1^{(yy)} S_1, & q_0 &= Q_0^{(yy)} \\ q_2 &= -Q_2^{(yy)} S_2, & q_{12} &= -Q_{12}^{(yy)} S_1 S_2 \end{aligned} \quad (4.139)$$

The phase angles  $\beta_j$  of the scaling pulses must be chosen such that

$$|q_1| = |q_2| = |q_{12}| = 1 \quad (4.140)$$

to obtain one of the pseudo-pure basis states. The experimental procedure is described in Section 4.7.1.2. These states then serve as input to the following  $CNOT$ -gate.

The  $CNOT_{12}$  has no effect on  $\mathbf{I}_{z_1}$  and exchanges  $\mathbf{I}_{z_2}$  and  $\mathbf{I}_{z_1} \mathbf{I}_{z_2}$ :

$$\begin{aligned} \mathbf{I}_{z_1} &\xleftarrow{U_{CNOT_{12}}} \mathbf{I}_{z_1} \\ \mathbf{I}_{z_2} &\xleftarrow{U_{CNOT_{12}}} -2\mathbf{I}_{z_1} \mathbf{I}_{z_2} \end{aligned} \quad (4.141)$$

Applying it to  $\rho_1$  produces (after the decay of transient components)

$$\begin{aligned} \rho_2 &= c_1 c_2 \Pi_{N-2}^{(+)} \mathbf{I}_0 - 2s_1 c_2 S_1 \Pi_{N-2}^{(-)} \mathbf{I}_{z_1} \\ &\quad + 4c_1 s_2 S_2 \Pi_{N-2}^{(-)} \mathbf{I}_{z_1} \mathbf{I}_{z_2} + 2s_1 s_2 S_1 S_2 \Pi_{N-2}^{(+)} \mathbf{I}_{z_2} \end{aligned} \quad (4.142)$$

This is the density matrix we wish to detect. In the reduced form it is given by

$$\begin{aligned} \rho_2^{(12)} &= Q_0^{(yy)} \mathbf{I}_0 - 2Q_1^{(yy)} S_1 \mathbf{I}_{z_1} + 4Q_2^{(yy)} S_2 \mathbf{I}_{z_1} \mathbf{I}_{z_2} + 2Q_{12}^{(yy)} S_1 S_2 \mathbf{I}_{z_2} \\ &= \tilde{q}_0 \mathbf{I}_0 + 2\tilde{q}_1 \mathbf{I}_{z_1} + 2\tilde{q}_2 \mathbf{I}_{z_2} + 4\tilde{q}_{12} \mathbf{I}_{z_1} \mathbf{I}_{z_2} \end{aligned} \quad (4.143)$$

The new coefficients are

$$\begin{aligned} \tilde{q}_1 &= -Q_1^{(yy)} S_1, & \tilde{q}_0 &= Q_0^{(yy)} \\ \tilde{q}_2 &= -Q_{12}^{(yy)} S_1 S_2, & \tilde{q}_{12} &= -Q_2^{(yy)} S_2 \end{aligned} \quad (4.144)$$

If the  $CNOT$ -operation works correctly,  $\rho_2$  will represent an output state corresponding to the chosen input state according to the truth table in Equation (4.120).

To detect the coefficients  $\tilde{q}_j$ , the terms in Equation (4.142) are phase-encoded by the now following MQE pulses. The resulting density matrix is

$$\begin{aligned} \rho_3 = & c_1 c_2 \Pi_{N-2}^{(+)} \mathbf{I}_0 - 2s_1 c_2 S_1 \cos \varphi_1 \Pi_{N-2}^{(-)} \mathbf{I}_{z_1} \\ & + 4c_1 s_2 S_2 \cos \varphi_1 \cos \varphi_2 \Pi_{N-2}^{(-)} \mathbf{I}_{z_1} \mathbf{I}_{z_2} + 2s_1 s_2 S_1 S_2 \cos \varphi_2 \Pi_{N-2}^{(+)} \mathbf{I}_{z_2} \end{aligned} \quad (4.145)$$

From  $\rho_3$ , the signal amplitude for the  $yy$ - and  $yx$ -detection sequences can be calculated:

$$\begin{aligned} S_{yy} &= \frac{1}{2^N} \text{tr} \{ \rho_{yy} \rho_3 \} \\ &= c_1^2 c_2^2 P_{N-2}^{(+)} + s_1^2 c_2^2 P_{N-2}^{(-)} S_1 \cos \varphi_1 \\ &= \left( Q_0^{(yy)} \right)^2 + \left( Q_1^{(yy)} \right)^2 S_1 \cos \varphi_1 \end{aligned} \quad (4.146)$$

and

$$\begin{aligned} S_{yx} &= \frac{1}{2^N} \text{tr} \{ \rho_{yx} \rho_3 \} \\ &= c_1 s_1 s_2^2 P_{N-2}^{(-)} S_2 \cos \varphi_1 \cos \varphi_2 - c_1 s_1 s_2^2 P_{N-2}^{(+)} S_1 S_2 \cos \varphi_2 \\ &= \left( Q_2^{(yy)} \right)^2 S_2 \cos \varphi_1 \cos \varphi_2 - Q_{12,2}^{(yy,yx)} S_1 S_2 \cos \varphi_2 \end{aligned} \quad (4.147)$$

with

$$Q_{12,2}^{(yy,yx)} = Q_{12}^{(yy)} Q_2^{(yx)} = Q_{12}^{(yy)} Q_2^{(yy)} \sqrt{\frac{P_{N-2}^{(+)}}{P_{N-2}^{(-)}}} \quad (4.148)$$

From which it follows that

$$Q_{12}^{(yy)} = \frac{Q_{12,2}^{(yy,yx)}}{Q_2^{(yy)}} \sqrt{\frac{P_{N-2}^{(-)}}{P_{N-2}^{(+)}}} \quad (4.149)$$

Notice, that orders of operator products of the third and fourth terms of the density matrix are switched from even to odd between  $\rho_1$  and  $\rho_2$ . This is reflected in the expressions for the signal detected with the two detection sequences:  $yy$  only detects the even while  $yx$  only the odd products. Because of this property of the  $S$ -bus, both detection sequences must be used to determine the coefficients of the output density matrix of the  $CNOT$ -gate.

Prior to actual  $CNOT$  measurements, the four pseudo-pure basis states were created and tomographed according to the procedure presented in Section 4.7.1. The experimental parameters are found in the caption to Figure 4.36 and the results in Table 4.10 and on the left in Figure 4.37. The fidelities of these preparations are lower than the ones achieved at more favorable orientations. This is due to the fact that, at the magic angle, the ENDOR line of one of the selected qubits ( $\mathbf{I}_6$ ) was flanked closely ( $< 100$  kHz) by lines belonging to

non-participating qubits (cf. Figure 4.34). The cross-excitation of these spins had detrimental effects on the fidelity of the pulses. It was possible to somewhat alleviate the problem by adjusting the Rabi frequency of the affected spin such that the neighboring lines would experience  $2\pi$ -rotations during a single pulse on the intended line.

The optimal evolution time  $\tau_I$  for the *CNOT* gate, was calibrated as described in Section 4.7.2.3. For each of the four input states, the dependence of the signal in Equations (4.146) and (4.147) on  $\varphi_j$  was recorded. Figure 4.36 shows an example of *yx*- and *yy*-detected MQE spectra for the input state  $\rho_{01}$ .

The lines corresponding to the  $Q_{12}^{(yy)}$ -,  $Q_2^{(yy)}$ -, and  $Q_1^{(yy)}$ -terms in  $S_{yx}$  and  $S_{yy}$  are highlighted. A separate measurement of  $P_{N-2}^{(\pm)}$  was not performed for technical reasons. At the chosen mixing time of  $\tau_S = 48$  ns, their values can be safely assumed to be very close to  $1/2$  (cf. Section 4.7.3). Thus, Equations (4.149), (4.147), (4.146), and (4.144) together with the normalization condition  $\text{tr}\{\rho_3\} = 1$  allow the coefficients  $\tilde{q}_j$  to be determined.

Table 4.10 summarizes the experimental parameters and results. The truth table of the *CNOT*<sub>12</sub>-gate is obviously reproduced. The fidelities of the implementation at 82% to 96% are not very high. However, the output states are unambiguously the expected basis states. This is most clearly seen in Figure 4.37 where the density matrices of the input and the corresponding output states are presented side by side.

With this working *CNOT*-gate, preparation of entangled states can be attempted.

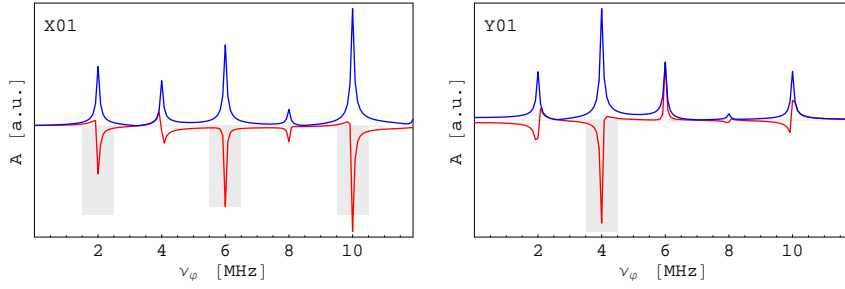


**Figure 4.36:** Example of MQE spectra taken for tomography of the output states of the  $CNOT_{12}$  operation. The relevant MQE lines are at  $\nu_{\Delta}$ ,  $\nu_{\Sigma}$ , and  $\nu_2$  for  $yx$ -detection (left) and  $\nu_1$  for  $yy$ -detection (right). Red and blue correspond to the real part and the modulus respectively, gray bars indicate line amplitudes used for further evaluation. Experimental: Pulse sequence in Figure 4.35; encoding frequencies  $\nu_{\varphi_1} = 4$  MHz,  $\nu_{\varphi_2} = 6$  MHz; qubits  $\mathbf{I}_4$  and  $\mathbf{I}_6$ ;  $m_S = -1/2$ ;  $\tau_I = 50$   $\mu$ s; further details in caption to Figure 4.34.

input	$\rho$	00	01	10	11
	$\beta_1/2\pi$	+0.154	-0.154	0.5 + 0.154	0.5 + 0.154
	$\beta_2/2\pi$	+0.152	0.5 - 0.152	+0.152	0.5 - 0.152
	$S_1$	0.567	0.567	-0.567	-0.567
	$S_2$	0.577	-0.577	0.577	-0.577
	$q_1$	0.913	1.040	-0.747	-0.997
	$q_2$	0.978	-0.581	1.180	-0.626
	$q_{12}$	1.100	-1.250	-1.030	1.270
	$\mathcal{F}$	0.998	0.970	0.988	0.973
output	$\rho$	01	00	10	11
	$\tilde{q}_1$	1.420	1.360	-1.160	-1.150
	$\tilde{q}_2$	-0.157	0.385	0.534	-0.154
	$\tilde{q}_{12}$	-0.982	1.000	-1.170	1.280
	$\mathcal{F}$	0.889	0.937	0.966	0.821

**Table 4.10:** Experimental parameters and measurement results of the demonstration of the  $CNOT$ -gate in CaF<sub>2</sub>:Ce (see also Figures 4.36 and 4.37).



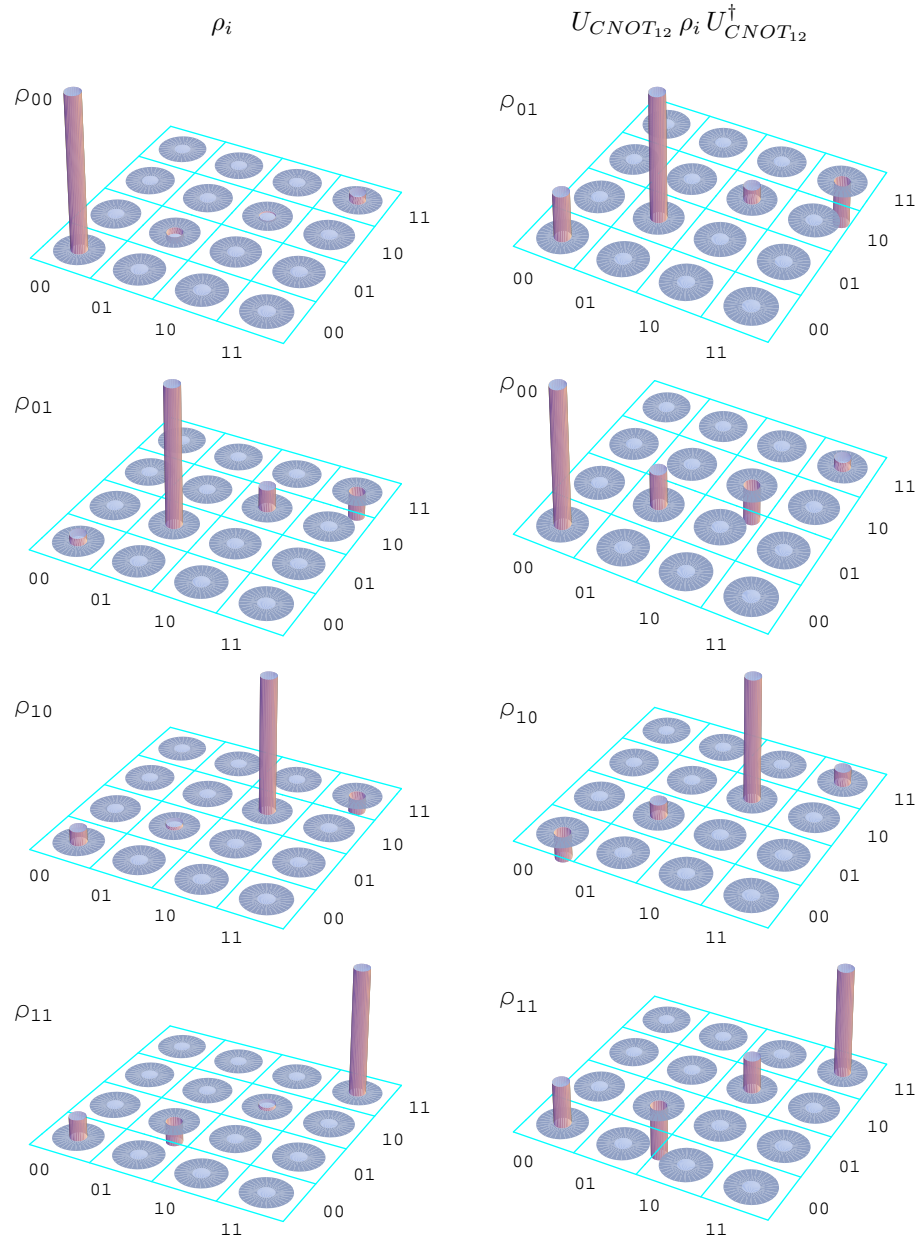


**Figure 4.37:** Demonstration of the  $CNOT_{12}$  gate in  $\text{CaF}_2:\text{Ce}$ . Left: Pseudo-pure input states. Right: Corresponding output states of the  $CNOT_{12}$  gate. Experimental details in caption to Figure 4.36.

#### 4.8.4 Creation and Direct Detection of Entangled States in CaF<sub>2</sub>:Ce

Figure 4.38 shows a pulse sequence for creation and detection of entangled two-qubit states. It consists of the familiar  $yy$ -preparation pulses applied to the electron spin followed by pulses for preparation of pseudo-pure input states. The actual entanglement is achieved by a  $\frac{\pi}{2}|y_1\rangle$ -pulse implementing the Hadamard transformation and a  $CNOT_{12}$  gate. Immediately after the  $CNOT$  the density

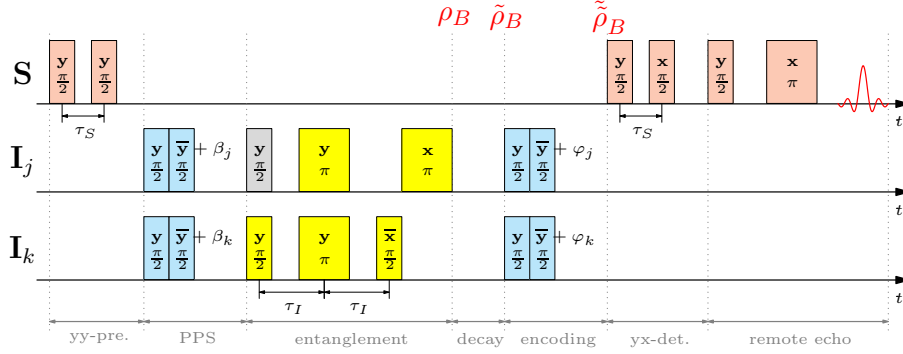


**Figure 4.38:** Sequence for creation and direct detection of entangled states. Pulses used to generate the pseudo-pure base states and to perform phase encoding are shown in blue. The entanglement sequence proper consists of a Hadamard transform (gray) and a  $CNOT_{12}$ -gate (yellow).

matrix  $\rho_B$  is given by

$$\begin{aligned} \rho_B &= c_1 c_2 \Pi_{N-2}^{(+)} \\ &\quad - 4s_1 s_1 s_2 S_2 \Pi_{N-2}^{(+)} \mathbf{I}_{x_1} \mathbf{I}_{x_2} - 4c_2 s_1 S_1 \Pi_{N-2}^{(-)} \mathbf{I}_{y_1} \mathbf{I}_{y_2} \\ &\quad + 4c_1 s_2 S_2 \Pi_{N-2}^{(-)} \mathbf{I}_{z_1} \mathbf{I}_{z_2} \\ &= \frac{1}{4} b_0 \mathbf{I}_0 + b_x \mathbf{I}_{x_1} \mathbf{I}_{x_2} + b_y \mathbf{I}_{y_1} \mathbf{I}_{y_2} + b_z \mathbf{I}_{z_1} \mathbf{I}_{z_2} \quad (4.150) \end{aligned}$$

If the coefficients of all terms satisfy the condition

$$|b_j| = 1 \quad (4.151)$$

then  $\rho_B$  will represent one of the four Bell states given in Equation (4.134). This condition is automatically fulfilled, by the choice of  $S_j$  for the preparation of the input states as given in Equation (4.114).

Detection of this density matrix is not a trivial task. The density matrices of the Bell states are essentially non-diagonal. The off-diagonal components are subject to decay on the time-scale of the nuclear FID ( $\approx 40 \mu s$ ). Even, if they should decay much slower, the phase encoding sequence is only capable of consistently detecting the diagonal components of the density matrix.

Still, this measurement is interesting as a first attempt at implementing the entanglement sequence. After the decay period, the density matrix is reduced to

$$\tilde{\rho}_B = c_1 c_2 \Pi_{N-2}^{(+)} - 4c_1 s_2 S_2 \Pi_{N-2}^{(-)} \mathbf{I}_{z_1} \mathbf{I}_{z_2} = \frac{1}{4} b_0 \mathbf{I}_0 + b_z \mathbf{I}_{z_1} \mathbf{I}_{z_2} \quad (4.152)$$

The MQE pulses and another decay period produce

$$\begin{aligned}\tilde{\rho}_B &= c_1 c_2 \Pi_{N-2}^{(+)} - 4c_1 s_2 S_2 \Pi_{N-2}^{(-)} \cos \varphi_1 \cos \varphi_2 \mathbf{I}_{z_1} \mathbf{I}_{z_2} \\ &= \frac{1}{4} b_0 \mathbf{I}_0 + b_z \cos \varphi_1 \cos \varphi_2 \mathbf{I}_{z_1} \mathbf{I}_{z_2}\end{aligned}\quad (4.153)$$

which can be detected by the  $yx$ -sequence. The signal amplitude is given by

$$\begin{aligned}S_{yx}^{(H+CNOT+MQE)} &= 4c_1 s_1 s_2^2 S_2 P_{N-2}^{(-)} \cos \varphi_1 \cos \varphi_2 \\ &= b_z \cos \varphi_1 \cos \varphi_2\end{aligned}\quad (4.154)$$

Thus, the  $\mathbf{I}_{z_1} \mathbf{I}_{z_2}$ -component produces equally high  $0Q$ - and  $2Q$ -lines, while the  $1Q_1$ - and  $1Q_2$ -lines ideally should disappear.

Starting with the pseudo-pure state  $\rho_{00}$  characterized in the previous section, MQE spectra were taken at  $\tau_I$  between  $20 \mu\text{s}$  and  $210 \mu\text{s}$ . Figure 4.39 shows the obtained transients. The fact, that the  $1Q$  amplitudes remain small for all values of  $\tau_I$  proves that, at no point, significant linear  $z$ -components  $\mathbf{I}_{z_j}$  are created. The  $\mathbf{I}_{z_1} \mathbf{I}_{z_2}$  term, on the other hand, shows the expected sinusoidal dependence on  $\tau_I$ .

Although this measurement does not conclusively prove creation of entanglement, it shows the absence of linear terms in the prepared state and is thus in full agreement with the theoretical expectations. Detection of the off-diagonal components of the Bell states requires a rather more elaborate approach.

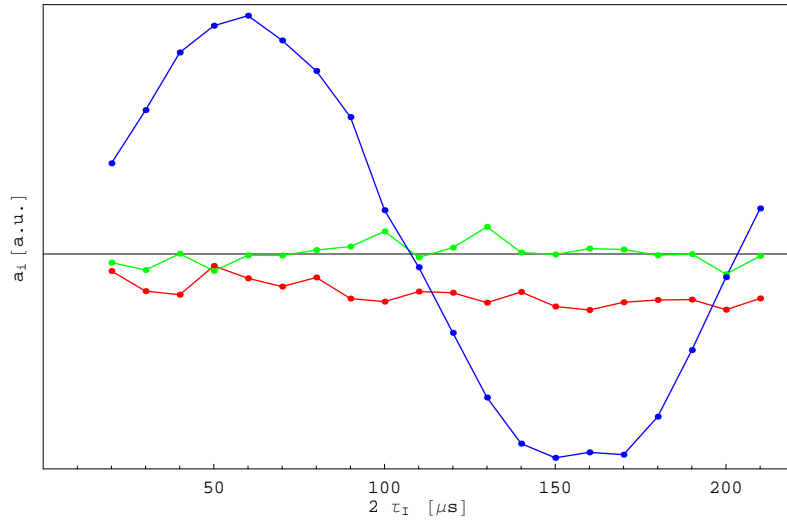


**Figure 4.39:** Creation and direct detection of Bell states in  $\text{CaF}_2:\text{Ce}$ . Evolution of diagonal density matrix components with  $\tau_I$  (cf. Figure 4.38) was measured. Red, green, and blue indicate the MQE line heights for  $\nu_1$ ,  $\nu_2$ , and the sum of the heights of the lines at  $\nu_\Delta$  and  $\nu_\Sigma$ . For experimental details, see caption to Figure 4.36 and text.

### 4.8.5 Detection of Entanglement through “Disentanglement”

One way to design a measurement, whose signature is sensitive to the entangled states is as follows: Once the entangled states have been created with a Hadamard-gate – *CNOT*-gate combination, an inverse sequence (*CNOT*-gate – Hadamard-gate) is immediately applied (see Figure 4.40). This reverses the effect of the “forward” sequence, thus “disentangling” the entangled state and producing a purely diagonal density matrix. To encode the information about the entangled state in the signal, the entire “reverse” sequence is subjected to an MQE-like phase rotation.

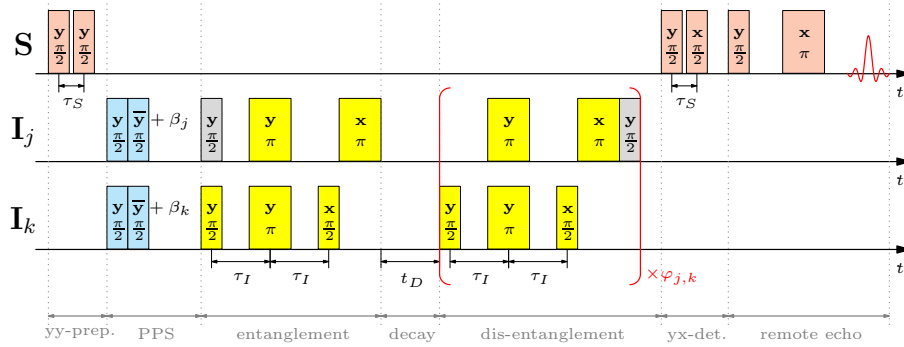


**Figure 4.40:** Pulse sequence for creation and indirect detection of Bell states in CaF<sub>2</sub>:Ce. For detection of the created states  $t_D = 0$  must be chosen. Incrementing  $t_D$  allows the decay of entangled states to be observed.

The experimentally obtained signatures for the four entangled states are shown in Figure 4.41. They show that only the 0Q-line is present in the signature of the  $\Psi^\pm$ -states, while the  $\Phi^\pm$ -states produce only the 2Q-line. Furthermore, the “+” and “-”-versions of the Bell states can be distinguished by the sign of the characteristic line. If the Hadamard transform and the *CNOT* gate function correctly and a Bell state is indeed prepared, the sequence in Figure 4.40 provides a means to unambiguously distinguishing them.

A first attempt at understanding these findings can be made by considering only that part of the density matrix which is restricted to the subspace of two qubits. When the phase-rotated reverse sequence is applied to the Bell states given in Equation (4.134), the following density matrices result after the decay of off-diagonal components:

$$\begin{aligned}
 & \left( CNOT_{12} - \tilde{H} \right)_{\varphi_{j,k}} \\
 | \Psi^+ \rangle & \longrightarrow \frac{1}{4} \mathbf{I}_0 + \frac{1}{2} \mathbf{I}_{z_2} - \sin(\varphi_1 - \varphi_2) \left( \frac{1}{2} \mathbf{I}_{z_1} + \mathbf{I}_{z_1} \mathbf{I}_{z_2} \right) \\
 | \Phi^- \rangle & \longrightarrow \frac{1}{4} \mathbf{I}_0 - \frac{1}{2} \mathbf{I}_{z_2} + \sin(\varphi_1 + \varphi_2) \left( \frac{1}{2} \mathbf{I}_{z_1} - \mathbf{I}_{z_1} \mathbf{I}_{z_2} \right) \\
 | \Psi^- \rangle & \longrightarrow \frac{1}{4} \mathbf{I}_0 + \frac{1}{2} \mathbf{I}_{z_2} + \sin(\varphi_1 - \varphi_2) \left( \frac{1}{2} \mathbf{I}_{z_1} + \mathbf{I}_{z_1} \mathbf{I}_{z_2} \right) \\
 | \Phi^+ \rangle & \longrightarrow \frac{1}{4} \mathbf{I}_0 - \frac{1}{2} \mathbf{I}_{z_2} - \sin(\varphi_1 + \varphi_2) \left( \frac{1}{2} \mathbf{I}_{z_1} - \mathbf{I}_{z_1} \mathbf{I}_{z_2} \right)
 \end{aligned} \tag{4.155}$$

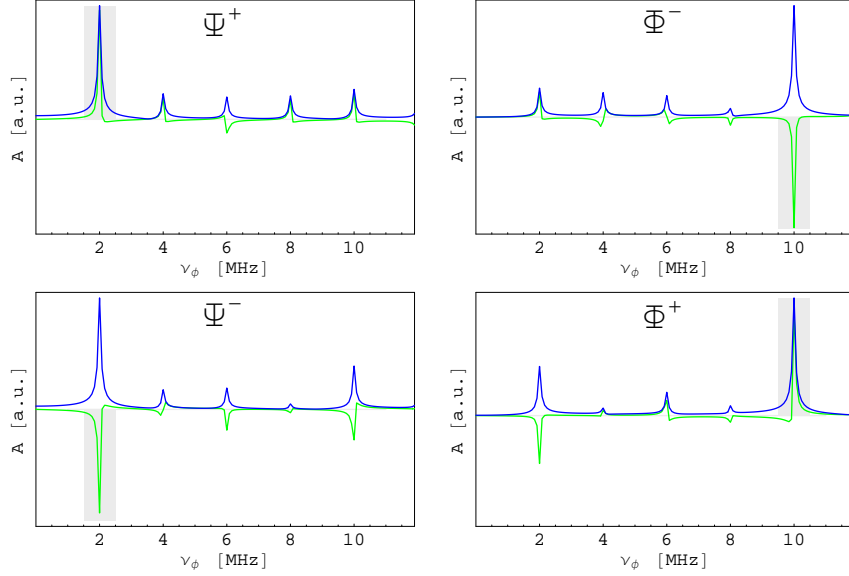


**Figure 4.41:** Signatures of Bell states in  $\text{CaF}_2:\text{Ce}$ . Green and blue indicate imaginary part and modulus. Gray bars indicate lines characteristic of the particular Bell state. Plots are labeled with the Bell states resulting from the chosen input state according to Equation (4.133). For experimental details, see caption to Figure 4.36.

Thus, this simple calculation does capture the fact that either the  $0Q$ - or the  $2Q$ -line dominates the MQE-spectrum and that the sign of the dominant line changes between the “+”- and “-”-versions of the Bell states. However, it disregards the influence of the other seven qubits in the cluster in conjunction with the preparation and the detection sequences. The basic *S*-bus theory above, cannot describe these measurements quantitatively and a full theoretical treatment is still missing.

#### 4.8.6 Decay of Entangled States

One of the interesting properties of entangled states is their behavior with respect to the environment. There have been studies indicating that some of the Bell states are especially resistant to decoherence [109]. In particular, it has been known for a long time that, in molecules in solution, the states spanning zero-quanta transitions are insensitive to decoherence under field inhomogeneities. In the context of spin quantum computing in the solid state, it is intriguing to know, whether the interaction of a state with the environment significantly depends on its operator structure.

The decay of the Bell states in  $\text{CaF}_2:\text{Ce}$  was studied by introducing a variable decay time  $t_D$  between the entangling and the disentangling sequences as shown in Figure 4.40. MQE spectra were recorded for a range of  $t_D$  between 0 and  $85 \mu\text{s}$  for each of the four Bell states. For each state, the fits of an exponential decay to the difference between the amplitudes of the dominant line ( $0Q$  for  $\Psi^\pm$  and  $2Q$  for  $\Phi^\pm$ ) and the respectively other multi-quanta line ( $2Q$  for  $\Psi^\pm$  and

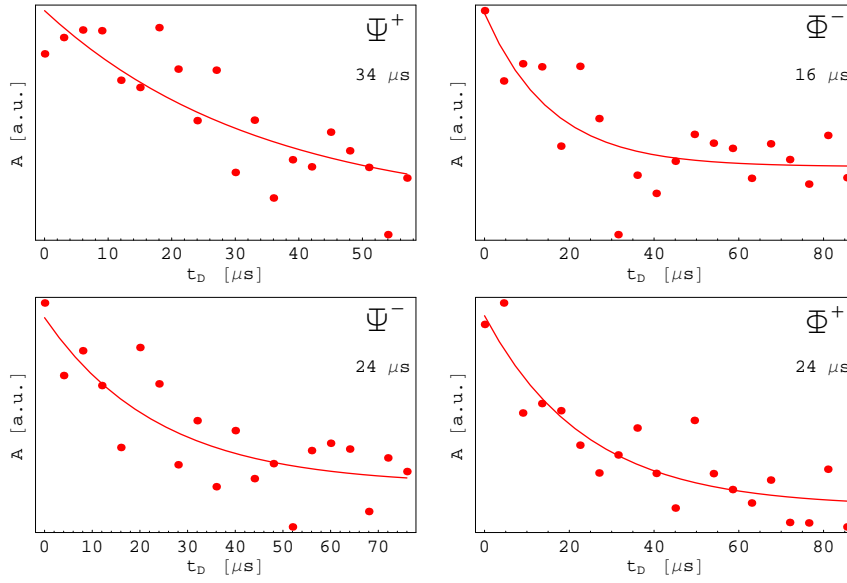


**Figure 4.42:** Decay of entangled states of distant qubits. The decay of the modulus of the difference between the  $\nu_2 - \nu_1$  and  $\nu_2 + \nu_1$  MQE lines fitted by an exponential function is shown. For experimental details, see caption to Figure 4.36.

$0Q$  for  $\Phi^\pm$ ) are shown in the Figure 4.42.

The observed decay constants are summarized in Table 4.11. The states  $\Psi^-$  and  $\Phi^+$  decay approximately at the rate of the nuclear spin FID. The states  $\Psi^+$  and  $\Phi^-$  deviate significantly from that average. With the latter decaying twice as fast as the former. A detailed model of the relaxation would be required to understand this finding. Also, studies of possible dependence of decay rates on orientation and other parameters might prove illuminating.

state	T [ $\mu s$ ]
$\Psi^+$	$34 \pm 12$
$\Psi^-$	$24 \pm 11$
$\Phi^+$	$24 \pm 8$
$\Phi^-$	$16 \pm 7$

**Table 4.11:** Decay constants of the Bell states in CaF<sub>2</sub>:Ce.

## Chapter 5

# Measurement and Use of Spin-Spin Interactions in a Hostile Environment

### 5.1 Spin-Spin Couplings

Pairwise inter-qubit couplings are a necessary prerequisite for the use of a particular physical system for implementation of quantum computing. In the  $S$ -bus system  $\text{CaF}_2:\text{Ce}$ , these are realized by direct dipole-dipole interaction between the nuclear  $^{19}\text{F}$ -spins as well as by an indirect coupling mediated by the central electron spin. In addition, all qubits within the cluster couple via the dipolar interaction to the abundant  $^{19}\text{F}$ -spins of the host lattice. This dense coupling network is a powerful source of decoherence and as such presents a problem for quantum computing with the  $S$ -bus.

Already in the very early applications of solid state NMR, the dipole-dipole interaction among nuclear spins was a subject of interest [90, 110] and has later been utilized in a number of advanced concepts of multiple quantum NMR [105–107, 111, 112] and more recently in the context of quantum computing [113, 114].

Decoherence and buildup of correlations in extended dipolarly coupled networks are governed by many-body dynamics. Quantitative description of these phenomena is a challenging theoretical problem. In the framework of this thesis, a practical solution to the decoherence problem was needed.

The techniques discussed below make the coupling between two spins observable by effecting an evolution of the spins under its action. This makes these methods useful for implementing two-spin gates in quantum computing experiments in addition to their utility for accurate measurement of the coupling constants. Most of the results, in this chapter were published in [37].

To simplify the discussion, consider the Hamiltonian of a pair of nuclear spins coupled by the dipole-dipole interaction. In the rotating frame of reference, it

can be written as

$$\mathcal{H} = \delta\nu_{jk} (\mathbf{I}_{z_j} - \mathbf{I}_{z_k}) + \frac{1}{2} D_{jk} \left( 2\mathbf{I}_{z_j} \mathbf{I}_{z_k} - \frac{1}{2} (\mathbf{I}_{+j} \mathbf{I}_{-k} + \mathbf{I}_{-j} \mathbf{I}_{+k}) \right) \quad (5.1)$$

The reference frequency is chosen halfway between the resonance frequencies of the two spins and  $\delta\nu_{jk}$  is their difference.  $D_{jk}$  is the dipolar coupling constant. The interaction part of the Hamiltonian

$$\mathcal{H}_D = \mathcal{H}_D^{(s)} + \mathcal{H}_D^{(ns)} \quad (5.2)$$

can be separated into two contributions: the secular part

$$\mathcal{H}_D^{(s)} = D_{jk} \mathbf{I}_{z_j} \mathbf{I}_{z_k} \quad (5.3)$$

and the non-secular part

$$\mathcal{H}_D^{(ns)} = -\frac{1}{4} D_{jk} (\mathbf{I}_{+j} \mathbf{I}_{-k} + \mathbf{I}_{-j} \mathbf{I}_{+k}) \quad (5.4)$$

If the frequency separation of the two spins is much larger than the characteristic strength of the coupling Hamiltonian

$$\delta\nu_{jk} \gg \sqrt{\text{tr} \{ \mathcal{H}_D^2 \}} \quad (5.5)$$

then spins  $\mathbf{I}_j$  and  $\mathbf{I}_k$  are called *hetero*-spins.

## 5.2 Single Nuclear Spin Decoherence

The simplest manifestation of spin dynamics under the action of a Hamiltonian in Equation (5.1) is the free induction decay (FID). The nuclear spin pulse sequence for measuring the FID of a single spin in  $\text{CaF}_2:\text{Ce}$  is shown at the top Figure 5.1. The two pulses are applied selectively to a single spin. In the actual experiment, this sequence (and all other sequences shown in this chapter) is sandwiched between the familiar *S*-bus preparation and detection sequences as shown in Figure 4.2.

A typical result is shown at the bottom of the Figure. The decay constant of the FID is around 20  $\mu\text{s}$ . This fast decay is caused by the multitude of interaction partners and the strength of the couplings. Both the secular and the non-secular parts of the interaction Hamiltonian contribute to the dynamics. However, the contribution of the non-secular flip-flop terms depends on how far apart the two spins are in the spectrum. It can be shown [75] that the effective non-secular Hamiltonian is scaled by the ratio of the coupling strength to the frequency separation:

$$\tilde{\mathcal{H}}_D^{(ns)} = \frac{\sqrt{\text{tr} \{ \mathcal{H}_D^2 \}}}{\delta\nu_{jk}} \mathcal{H}_D^{(ns)} \quad (5.6)$$

Nuclear spins within the *S*-bus cluster in  $\text{CaF}_2:\text{Ce}$  are typically separated by  $\delta\nu_{jk} \approx 200 \text{ kHz} - 10 \text{ MHz}$  from each other and from the lattice spins. The coupling constants do not exceed 10 kHz such that the non-secular terms are



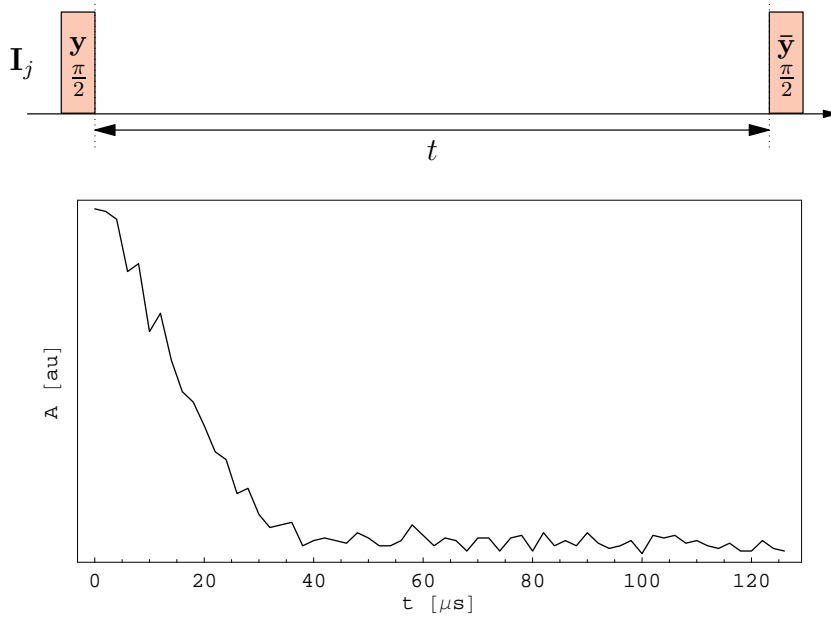


**Figure 5.1:** Single nuclear spin free induction decay (FID) in  $\text{CaF}_2:\text{Ce}$ . Top: nuclear spin part of the pulse sequence (cf. Figure 4.2). Bottom: Typical measured FID. The decay constant is approximately  $20 \mu\text{s}$ .

diminished by  $10^{-1} - 10^{-3}$  with respect to the secular part. Such that the bulk of decoherence is due to the secular part.

The need to combat decoherence now becomes apparent: With the coupling strength of a few kHz, typical two-qubit gates take tens of microseconds and measures must be taken reduce the speed of decoherence. To show that this is possible, a number of well known sequences was applied. They are shown in Figure 5.2 along with the experimental results.

The simplest way of decoupling a single spin is the Hahn-echo sequence. It eliminates the secular part of the dipolar Hamiltonian in the 0-th order of average Hamiltonian theory such that the evolution under this term is fully refocused. The measurement shows that decay time of the echo is now beyond  $400 \mu\text{s}$ . This decoherence is now caused by the flip-flop terms  $\tilde{\mathcal{H}}_D^{(ns)}$  during the long free evolution periods. Also, the free evolution time increases during the measurement. This results in increasing contributions of higher order average Hamiltonian terms. The non-exponential decay under the Hahn sequence is explained by this fact.

To further improve the decoupling, the non-secular part of the interaction Hamiltonian must be suppressed. The spin locking sequence [115] in Figure 5.2(b) is suitable for this task. Under the action of continuous irradiation, the non-secular terms are further reduced. In terms of the average Hamiltonian theory, the cycle time is now equal to a full Rabi-oscillation:  $t_c = 1/\nu_1$ . The 0-th order average Hamiltonian is then scaled by a factor  $\sqrt{\text{tr}\{\tilde{\mathcal{H}}_D^{(ns)2}\}}/\nu_1$ . The decay time achieved by spin locking is on the order of 2 ms providing a further

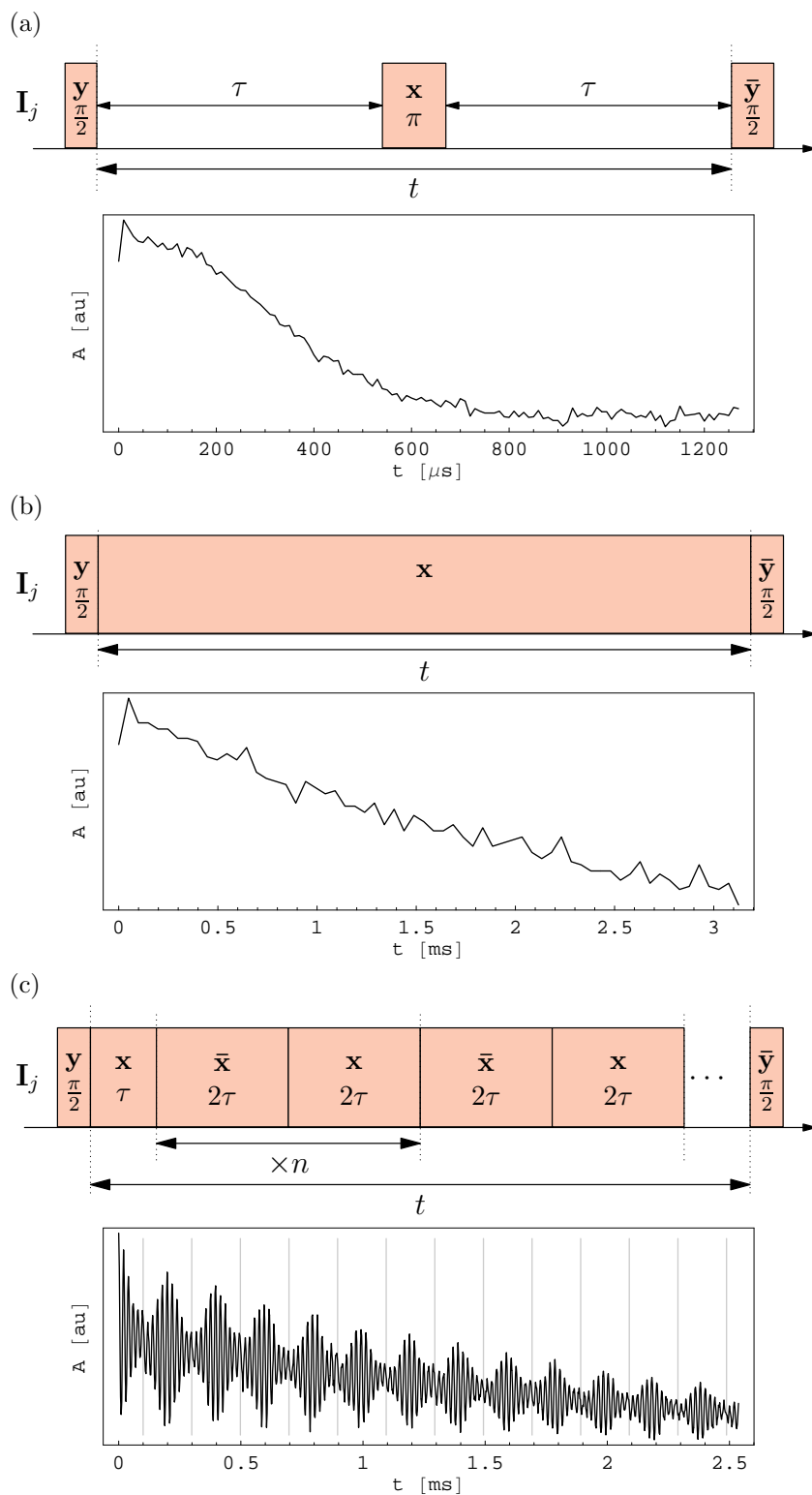


**Figure 5.2:** Single nuclear spin decoherence in  $\text{CaF}_2:\text{Ce}$ . (a) Hahn echo. (b) The Spin-locking sequence. (c) The rotary echo sequence. See text for details.

five-fold improvement of decoherence suppression.

The spin-locking sequence provides the best decoupling for a given strength of the driving field. However, it suffers from the problem of dephasing due to the inhomogeneity of the driving rf field  $\mathbf{B}_2$ . Who's detrimental effect can be compensated by periodically inverting the rf phase. The resulting *rotary echo* [116] sequence is shown in Figure 5.2(c). In the rotating frame, the spin is quantized along the direction of the rf field and the magnetization experiences a dephasing process analogous to an FID in an inhomogeneous static field. After a period  $\tau$ , the phase of the rf field is reversed. This inverts the direction of the driving field in the rotating frame. The effect of  $\mathbf{B}_2$  inhomogeneity is therefore reversed and the dephased magnetization refocuses until a *rotary echo* appears at  $t = 2\tau$ . This is followed by another period of dephasing until the phase is switched again at  $t = 3\tau$  giving rise to an echo at  $t = 4\tau$ . Thereafter, the phase is periodically alternated at  $t = (2n + 1)\tau$  producing a train of echoes at  $t = (2n)\tau$ . Additionally, it is observed that refocusing becomes increasingly better, with decreasing  $\tau$  (see also discussion of the CPMG sequence below). For the measurement in Figure 5.2(c) the choice was  $\tau = 200 \mu\text{s}$ . Phase alternation times are indicated by vertical lines.

These single nuclear spin decoherence experiments show that it is possible to maintain the coherence of the qubits sufficiently long for implementation of quantum computing algorithms.

## 5.3 Recoupling of Selected Spin-Pairs

The sequences discussed in the previous section indiscriminately suppress all couplings of a nuclear qubit to its neighbors. In order to be able to measure or generally utilize a particular spin-spin coupling for two-qubit quantum gates, it must be reintroduced while keeping the decoupling of the rest as good as possible. In the following, a selection of sequences serving this purpose is presented.

### 5.3.1 Spin-Echo Double Resonance

The conceptually simplest case is the *spin-echo double resonance* (SEDOR) sequence [117, 118] shown in Figure 5.3. It extends the Hahn-echo sequence by a  $\pi$ -pulse on the second spin. This results in an additional sign inversion and the coupling between the two spins is reintroduced, while the coupling to all other spins is still averaged out. The 0-th order secular average Hamiltonian for the SEDOR sequence is

$$\bar{\mathcal{H}}_{\text{SEDOR}}^D = D_{jk} \mathbf{I}_{z_j} \mathbf{I}_{z_k} \quad (5.7)$$

Couplings to all other spins are averaged out. Results of application of this sequence to a selected pair of nuclear spins are shown in Figure 5.3. The oscillation under the spin-spin coupling is clearly seen in the transient. The decay time is around  $450 \mu\text{s}$  and is similar to the one found in a single spin decoherence measurement with the analogous Hahn-echo sequence. A spectrum of this oscillation can be obtained by a Fourier transform. A fit with a Lorentzian line produces a center frequency of  $f_{\text{SEDOR}} = 4.55 \text{ kHz}$  and a full line width at half maximum (FWHM) of  $\Delta f_{\text{FWHM}} = 2.24 \text{ kHz}$ . Notice that the oscillation goes through three full cycles before coherence is completely lost. This means that

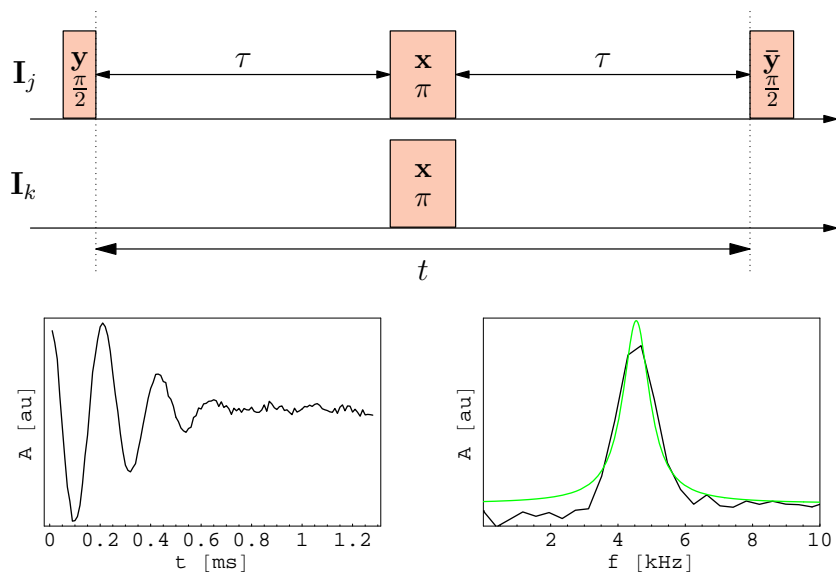


**Figure 5.3:** Spin-echo double resonance (SEDOR) measurement on two nuclear spins in  $\text{CaF}_2\text{:Ce}$ . Top: Pulse sequence. Bottom: Measured echo decay and the corresponding spectrum. Center frequency:  $f_{\text{SEDOR}} = 4.55$  kHz, line width:  $\Delta f_{\text{FWHM}} = 0.96$  kHz, decay constant:  $1/\pi \Delta f_{\text{FWHM}} = 0.33$  ms.

up to 10 two qubit gates can, in principle, be implemented for this spin pair with the SEDOR sequence. In practice, this number can be significantly lower due to the fine width of pulses.

As discussed in the previous section for the Hahn echo, the suppression of unwanted spin-spin couplings is insufficient during long periods of free evolution and can be improved.

### 5.3.2 Carr-Purcell-Meiboom-Gill Sequence

To shorten the time when the spins evolve freely, the Carr-Purcell-Meiboom-Gill (CPMG) sequence [119] introduces additional  $\pi$ -pulse pairs as shown in Figure 5.4. The sequence can be treated as a periodic repetition of the  $\tau - \pi - \tau$  block. As such it has the same first-order average Hamiltonian as the SEDOR sequence. However, the CPMG-sequence suppresses spin diffusion much better, because the free evolution periods – and with them the cycle time  $t_c$  – can be made arbitrarily short, limited only by finite pulse width.

The effect of reduced cycle time is seen explicitly when comparing the results for three different settings of  $\tau$  as shown in the figure. Line width of the oscillation under the spin-spin coupling are significantly reduced with shorter cycle time: tripling  $t_c$  almost doubles the linewidth. For quantitative analysis, the slow baseline decay has been fitted with an exponential function and subtracted from the time-domain data prior to the Fourier transform. The spectra were then fitted with Lorentzian line shapes to yield the data shown in Table 5.1. At the shortest tested setting of the cycle time, the CPMG sequence gives an three-fold improvement in decoherence suppression over the SEDOR sequence.

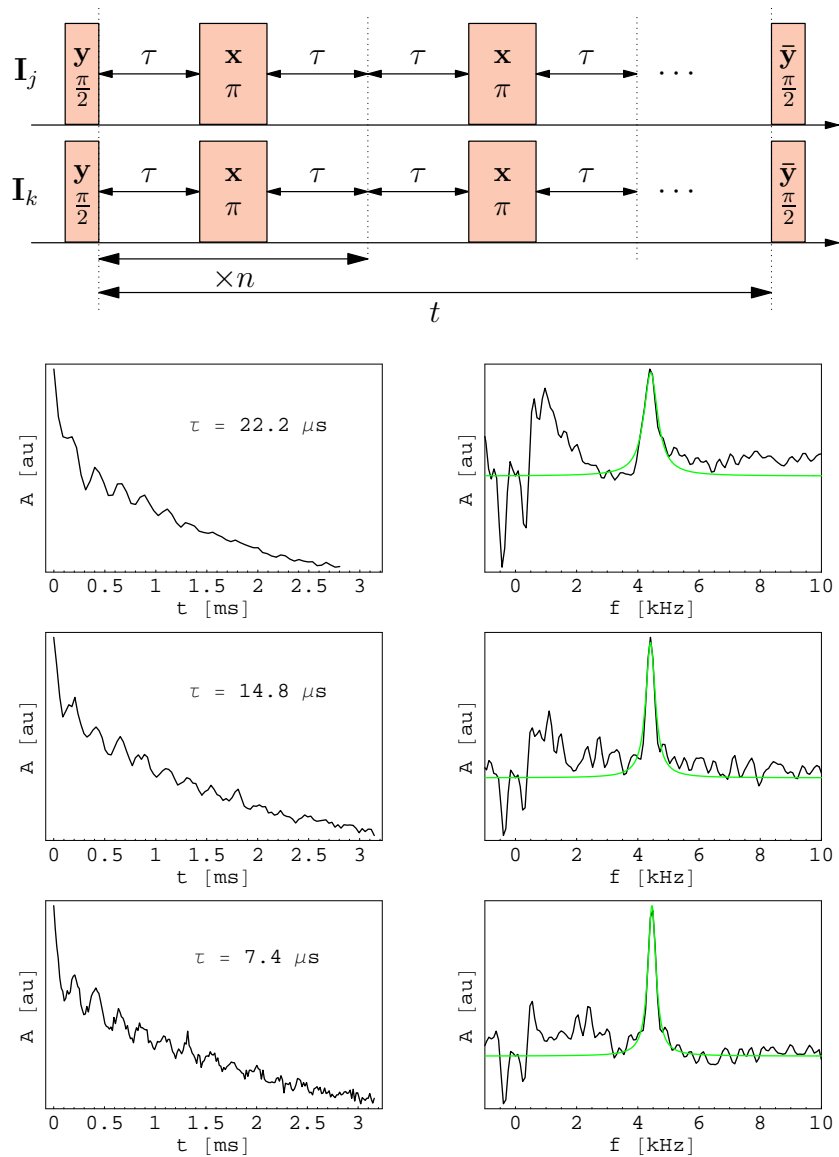


**Figure 5.4:** Carr-Purcell-Meiboom-Gill sequence on two nuclear spins in  $\text{CaF}_2:\text{Ce}$ . Top: Pulse sequence. Bottom: Time traces and corresponding spectra for progressively shorter cycle times. The green line indicates a fit of a Lorentzian line to the spectrum. The slow baseline decay has been removed from the spectra by subtracting a fitted exponential decay from the transients prior to Fourier transform.

$\tau$ [ $\mu$ s]	$f_{\text{CPMG}}$ [kHz]	$\Delta f_{\text{FWHM}}$ [kHz]	$1/\pi \Delta f_{\text{FWHM}}$ [ms]
22.2	4.42	0.55	0.58
14.8	4.41	0.37	0.86
7.4	4.46	0.32	0.99

**Table 5.1:** Results of spin-spin coupling measurement with the CPMG sequence for different cycle times.

### 5.3.3 Simultaneous Spin-Locking

The next logical step in the quest for decoherence suppression is to eliminate free evolution altogether. In its simplest form, this is achieved by applying the spin-locking sequence to two spins simultaneously. To compute the average Hamiltonian [120] one starts again with the time dependent version:

$$\mathcal{H}_{2\text{lock}}^D(t) = \frac{1}{2} D_{jk} (\mathbf{I}_{z_j} \cos \omega_1 t - \mathbf{I}_{y_j} \sin \omega_1 t) (\mathbf{I}_{z_k} \cos \omega_1 t - \mathbf{I}_{y_k} \sin \omega_1 t) \quad (5.8)$$

and arrives at the average value of

$$\bar{\mathcal{H}}_{2\text{lock}}^D = \frac{1}{2} D_{jk} (\mathbf{I}_{z_j} \mathbf{I}_{z_k} + \mathbf{I}_{y_j} \mathbf{I}_{y_k}) \quad (5.9)$$

Notice the tilted quantization axis in this case. The pulse sequence and the experimental result are shown in Figure 5.5. Although decoupling from other

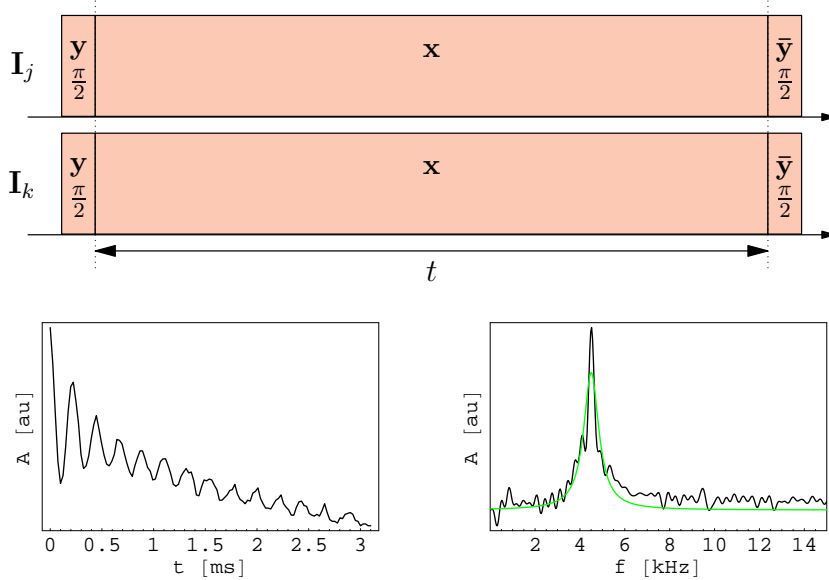


**Figure 5.5:** Simultaneous spin locking on two nuclear spins in  $\text{CaF}_2:\text{Ce}$ . Top: Pulse sequence. Bottom: Time trace and corresponding spectrum. The slow baseline decay was removed prior to Fourier transform. Center frequency:  $f_{2\text{lock}} = 4.50$  kHz, line width:  $\Delta f_{\text{FWHM}} = 0.81$  kHz, decay constant:  $1/\pi \Delta f_{\text{FWHM}} = 0.39$  ms.

spins should now be optimal, the line width does not achieve values found with the CPMG sequence. As mentioned above, this can be attributed to the inhomogeneity of the driving rf field  $\mathbf{B}_2$ . This dephasing effect must be addressed by appropriate phase alternation.

### 5.3.4 The $8\pi$ -Sequence

The phase alternation which is required to counter the rf inhomogeneity, can also be used for another purpose. The tilted quantization axis of the average Hamiltonian of the spin-locking sequence differs from the situation encountered in standard INEPT [16] and *CNOT* [13] implementations and presents a problem for the use of that sequence in quantum information processing. For a straight forward implementation of gates, a Hamiltonian quantized along the  $z$ -direction is much more useful. To address this problem the sequence shown in Figure 5.6 was devised. It consists of four consecutive  $2\pi$ -rotations with the phase alternating in each section on one spin and in every second section on the other spin (hence the name “ $8\pi$ -block”). The average Hamiltonian for each section can be calculated in the same way as in the case of spin-locking:

$$\bar{\mathcal{H}}_{xy} = \bar{\mathcal{H}}_{\bar{x}\bar{y}} = \frac{1}{2}D_{jk} (\mathbf{I}_{z_j}\mathbf{I}_{z_k} - \mathbf{I}_{y_j}\mathbf{I}_{x_k}) \quad (5.10a)$$

$$\bar{\mathcal{H}}_{\bar{x}y} = \bar{\mathcal{H}}_{x\bar{y}} = \frac{1}{2}D_{jk} (\mathbf{I}_{z_j}\mathbf{I}_{z_k} + \mathbf{I}_{y_j}\mathbf{I}_{x_k}) \quad (5.10b)$$

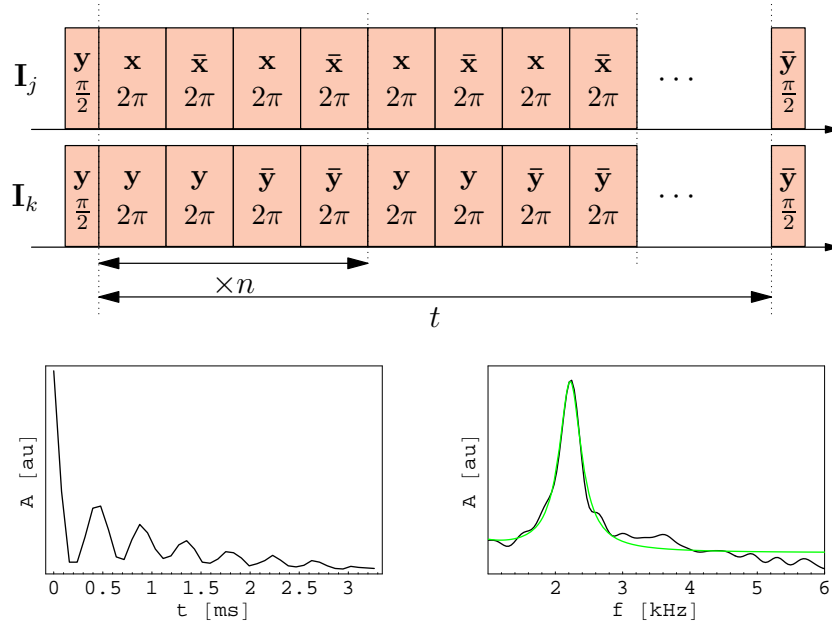


**Figure 5.6:** Evolution of two nuclear spins in  $\text{CaF}_2:\text{Ce}$  under the  $8\pi$ -block. Top: Pulse sequence. Bottom: Time trace and corresponding spectrum. Center frequency:  $f_{8\pi} = 2.22$  kHz, line width:  $\Delta f_{\text{FWHM}} = 0.40$  kHz, decay constant:  $1/\pi \Delta f_{\text{FWHM}} = 0.80$  ms

The Hamiltonian for the entire block is then given by

$$\bar{\mathcal{H}}_{8\pi}^D = \frac{1}{4} (\bar{\mathcal{H}}_{xy} + \bar{\mathcal{H}}_{\bar{x}y} + \bar{\mathcal{H}}_{x\bar{y}} + \bar{\mathcal{H}}_{\bar{x}\bar{y}}) = \frac{1}{2} \mathbf{I}_{z_j} \mathbf{I}_{z_k} \quad (5.11)$$

The factor 1/2 demonstrates that the straight quantization axis comes at the cost of halving the usable coupling strength. This is reflected by measurement in Figure 5.6. The linewidth of 400 Hz shows that the full potential of this sequence is not realized in our measurements as compared for instance to the CPMG data. This can be attributed to experimental problems, such as sample heating during long periods of rf irradiation, amplifier droop, etc.

## 5.4 Conclusions

This section has demonstrated that the coherence can be kept in the nuclear qubits of the  $S$ -bus cluster for time periods sufficient for simple quantum computing algorithms to be performed. The techniques described here, also, allow the pairwise spin couplings to be measured accurately as well as used to implement two-qubit gates. This can be achieved in the face of a very “hostile” environment rife with decoherence and dephasing paths.

The CPMG sequence yields the narrowest coupling spectra, especially when the cycle time of the sequence is kept short. For the use in quantum computing experiments, the use of the CPMG sequence can be problematic. The average Hamiltonian calculation does not take into account the finite width of the rf pulses and thus neglects some tilting of the quantization axes. Especially because the minimum pulse width is limited both technically and by the requirement of selective excitation.

Here, the  $8\pi$ -block shows the most promise, because it produces the desired Hamiltonian without the approximation of  $\delta$ -pulses while retaining good dephasing suppression properties. Its disadvantages lie in the potential sample heating by prolonged rf irradiation and in the reduction of the usable coupling strength by a factor of two.



# Summary

This thesis presents my work on improving existent and developing new methods for preparation, manipulation, and observation of quantum states in the context of spin quantum computing. Three quite different types of quantum systems were used for this purpose: One consisted of nuclear spins of small molecules in the liquid state. The second was comprised of similar molecules aligned in a liquid crystal matrix. The third combined nuclear spins with electron spins in a single crystal environment. Experimental methods ranged from high resolution Nuclear Magnetic Resonance (NMR) to Electron Spin Resonance (ESR). Theoretical methods and computer simulations were used to deepen the understanding and aid in the work with pulse sequences.

## **Entanglement in the Three-Qubit Deutsch-Josza Algorithm**

The main result of the work done with high-resolution liquid state NMR was the use of local operations to reveal the entanglement content of the output states of the Deutsch-Josza algorithm.

The modern Collins-version of the Deutsch-Josza algorithm was implemented in cooperation with O. Mangold during his Diploma thesis work. The three nuclear  $^{19}\text{F}$ -spins of the liquid 2,3,4-Trifluoroaniline were used as qubits. One of the notable properties of this compound is the absence of  $J$ -coupling between two of the three qubits resulting in a linear coupling topology. The pseudo-pure state  $\rho_{000}$  prepared with fidelity close to 1 was used as an input. Full tomography of the output states was employed to obtain exhaustive knowledge of the corresponding density matrices. The method used to bridge the missing link is applicable to other linear topology systems.

It was shown that the possible oracle transformations of the Deutsch-Josza algorithm can be divided into several classes according to their operator structure such that the oracles within a class are equivalent under exchange of qubits. The linear topology of our quantum processor partially lifts this equivalence. Nine oracles covering the interesting cases (including the one which uses correlations across the non-existent coupling) were selected for implementation. Starting with three qubits the Deutsch-Josza algorithm can produce entanglement in the course of its execution. The entanglement content of the output states, however, is not immediately obvious. Using the fact that *local* (i.e., one-qubit) operations do not modify the entanglement contained in a given quantum state, a set of such transformations for each of the implemented oracles was found, which immediately reveals the entanglement of the output states produced by

those oracles. In this way, it was shown that some of the output states can be locally mapped onto states entangled in the subspace of two qubits. One of the oracles was found to produce a state equivalent to the maximally entangled Greenberger-Horne-Zeilinger (GHZ) state under local transformations.

### Selective Excitation under Continuous Averaging

Qubit-qubit couplings are an indispensable prerequisite for quantum computing. Many physical systems proposed for experimental implementation contain such couplings in their native Hamiltonian. This “always on” nature of interactions frequently poses difficulties for implementation of two-qubit gates. In NMR, it is possible to effectively eliminate such interactions through appropriate pulse sequences.

Small organic molecules aligned in a liquid crystal matrix were used to test the feasibility of this idea. In a series of basic proof-of-principle experiments, the magic echo pulse sequence was used to switch off the dipolar coupling of nuclear spins. Most importantly, it was shown that it is still possible to selectively address individual qubits while the averaging sequence is in effect.

### Visual Analysis of Pulse Sequences

A method for visualization of unitary transforms of spin- $\frac{1}{2}$  was devised to aid in the analysis and design of pulses and pulse sequences. It was shown that such transformations can be represented by a vector in  $\mathbb{R}^3$  with the expected properties of representing the axis and angle of a rotation. This type of visualization presents all important features of a unitary transformation in a single picture. Especially plots of variation of this vector with experimental parameters allow the merits of a pulse sequence to be easily and intuitively judged. The advantages of this method were demonstrated by analysing and comparing a number of simple pulses with respect to their selectivity and phase fidelity. A sequence of alternating off-resonance pulses was constructed, which could be used to implement a highly selective  $\frac{\pi}{2}$ -pulse.

### Details of Spin Quantum Computing with the *S*-Bus System $\text{CaF}_2:\text{Ce}$

The *S*-bus concept for spin quantum computing was developed by M. Mehring. First implementation was performed by J. Mende in single crystal  $\text{CaF}_2$  weakly doped with cerium. My work on this system was focused on improving quantitative understanding and experimental methods.

The general theory of the *S*-bus given by Mehring provides a good fundamental understanding of  $\text{CaF}_2:\text{Ce}$ . It does, however, contain a number of parameters which can only be obtained from measurements. In addition, some of the assumptions underlying the analytic model are not well met by this system.

An exact numeric modeling of the 10-spin magnetic Hamiltonian of the paramagnetic cluster in  $\text{CaF}_2:\text{Ce}$  was undertaken. A problem for the utilization of the diagonalized Hamiltonian arises from the fact that the numeric routines return the eigenvalues and eigenvectors in arbitrary order thus artificially scrambling the Hilbert spaces of the constituent spins. To circumvent this obstacle, the

measurement operators had to be constructed in the laboratory frame of reference and transformed to the eigenframe of the Hamiltonian. In this way the ESR and ENDOR spectra were calculated. They show excellent agreement with experimental results. Furthermore they allow accurate assignment of the ENDOR transitions to the fluorine sites and to the  $m_S = \pm\frac{1}{2}$  states of the electron spin. The mentioned scrambling problem together with the mixing of states due to strong hyperfine coupling make finding the quantization axes of the nuclear spins difficult. Because of the large Zeeman splitting of the electron, its quantization axis can be determined accurately. The standard procedure for rotating frame transformation was extended to account for the complicated transformation to the eigenframe. This allowed simulations of ESR pulse sequences to be performed.

A free induction decay (FID) simulation showed that the  $T_2$  decoherence of the electron spin can be almost entirely attributed to its coupling with the nuclear spins *within* the cluster. The obtained value of the time constant of the FID is in good agreement with the experimental finding. Simulations of a Hahn echo and a two-pulse sequences demonstrated the ability of the numeric model to reproduce the refocusing of the electron spin magnetization. Finally an envelope modulation of the stimulated echo (ESEEM) was computed. The simulation correctly reflects the spectrum produced by this non-trivial experiment.

The evolution of the two-qubit density matrix components was studied under the action of the *CNOT*-gate and its precursor sequences (SEDOR and INEPT) with two main goals: to compare the general predictions of the theory about such evolutions and to experimentally determine the parameters entering the model.

Measurements towards creation of pseudo-entangled states of two *distant* qubits were performed. A pair of nuclear spins in  $\text{CaF}_2\text{:Ce}$  can be made distant by aligning the sample such that their dipole-dipole coupling vanishes. The interaction is then mediated by the electron spin emphasizing its role as a quantum bus. As a first step, the *CNOT*-gate was implemented and tested by applying it to pseudo-pure states. Because of special properties of the preparation and detection sequences in the *S*-bus, an elaborate procedure had to be devised for the measurement of the output states. With the working *CNOT*-gate and the four pseudo-pure states as basic ingredients, preparation of the four Bell-states of two qubits was attempted. Their off-diagonal structure again presents a problem in their detection. In a first step, the standard tomography procedure was used to show that the prepared states did not, in fact, contain any linear components. Secondly, a pulse sequence was devised which allows the four entangled states to be distinguished using their signatures.

Finally, the interesting question of whether entangled states are especially resistant to decoherence was studied by measuring their decay constants. The obtained relaxation times states can differ by a factor of two. However, no spectacular resistance to decoherence was found in the Bell-states in  $\text{CaF}_2\text{:Ce}$ .

### Measurement of Spin-Spin Interactions in Hostile Environments

The main disadvantage of  $\text{CaF}_2\text{:Ce}$  for the purpose of quantum computing is the fact that the cluster carrying the qubits is embedded in an extended  $^{19}\text{F}$ -

spin network which is a powerful source of decoherence. A number of existing sequences were applied to  $\text{CaF}_2:\text{Ce}$  and compared with respect to their fitness for one of two purposes: the accurate measurement of the coupling strength between two qubits and the use of this coupling for quantum gates. Both uses, require all other couplings to neighboring spins to be suppressed.

The sequences studied were SEDOR, CPMG, and spin locking. The SEDOR sequence is the simplest variant and has the additional advantage of producing an average Hamiltonian which is usable for quantum computing. However, it produces only insufficient decoupling because of the long evolution periods, where the non-secular parts of the interactions are not averaged out. The CPMG sequence produces the correct Hamiltonian and much better decoupling, especially with short cycle times. However, with the decreasing cycle time, the effects of finite pulse width, which cannot easily be accounted for, make an accurate measurement of the coupling strength difficult. Although the spin locking sequence might be expected to produce the best decoupling, its decay constant is dominated by the inhomogeneity of the driving field. Also, its average Hamiltonian's quantization axis is tilted, making it less useful for quantum computing.

As a compromise, an  $8\pi$ -pulse sequence was devised, which consists of four successive  $2\pi$ -rotations whose phases are alternated such that  $B_1$ -inhomogeneities are refocused and the average Hamiltonian is aligned along the  $z$ -direction.

Additionally, these methods are useful for accurate measurement of spin-spin couplings in the presence of strong relaxation sources. They can be applied outside of the realm of quantum computing and in systems other than  $\text{CaF}_2:\text{Ce}$ .

## Outlook

The potential of the  $S$ -bus concept implemented in  $\text{CaF}_2:\text{Ce}$  is certainly not yet exhausted. Especially its use at higher magnetic fields (in particular in the W-band) warrants more attention. A sufficiently high field would clearly separate the Zeeman energy of the nuclear spins from the hyperfine interaction. This would greatly simplify the theoretical understanding of the experimental situation. Furthermore, the higher Boltzmann polarization of the electron spin would, at low temperature, place the quantum limit within reach and enable the transition of ensemble spin quantum computing from pseudo-pure to pure states.

---

# Zusammenfassung

Quantencomputing, d.h. Rechnen mit Quantensystemen, ist eine der aufregendsten Entwicklungen der letzten Jahre in der Physik. Die Faszination gründet sich sowohl in den theoretischen Aspekten dieses Forschungsgebiets als auch in den experimentellen Herausforderungen, die mit der Umsetzung der abstrakten Algorithmen verbunden sind.

Den Theoretiker reizt die Möglichkeit, Objekte der Quantenwelt, deren Verhalten dem gesunden Menschenverstand trotz, in den Dienst der Informationsverarbeitung zu zwingen. Dabei stößt man unweigerlich auf ganz fundamentale Fragen der Interpretation der Quantenmechanik. Insbesondere das Phänomen der Verschränkung, das schon die Pioniere der Quantenmechanik beschäftigte, steht hier im Mittelpunkt.

Die theoretischen Fortschritte im Feld der Quanteninformationsverarbeitung sind in der Tat enorm. Eine Vielzahl von Algorithmen zur Lösung rechnerisch schwieriger Aufgaben, zur Simulation von Quantensystemen mit Quantensystemen, zur abhörsicheren Informationsübertragung, zur Quantenfehlerkorrektur und mehr ist entwickelt worden. Es gibt sogar Vorschläge, die sich von der prozeduralen Methode der Turing-Maschinen ganz lösen und eine ganz neuartige Nutzung von großen verschränkten Qubitregistern anstreben. Auch das Verständnis der Verschränkung ist inzwischen deutlich vertieft worden.

Für den Experimentator bietet Quantencomputing eine Gelegenheit die Grenzen des machbaren zu erweitern. Experimentelle Umsetzung erfordert einen bis jetzt nicht dagewesenen Grad an Kontrolle über Quantensysteme. Die so entstehenden Verfahren zur Präparation, Manipulation und Vermessung der Quantenzustände bereichern das Instrumentarium der experimentellen Grundlagenforschung.

Naturgemäß kann das Experiment nicht mit dem Tempo der theoretischen Entwicklung Schritt halten. Jedoch sind auch bei der Implementierung entscheidende Fortschritte gemacht worden. Viele der theoretischen Konzepte sind an kleinen Systemen demonstriert worden. Dabei kommt eine große Bandbreite an physikalischen Systemen zum Einsatz: von den Kernspins in Molekülen, über gefangene Atome und Ionen, über Quantenpunkte und supraleitende Inseln bis hin zu einzelnen Moden des elektromagnetischen Feldes in Resonatoren hoher Güte.

Die schnellsten Erfolge wurden seit Ende der 90er Jahre mit den Mitteln der hochauflösenden Kernspin Resonanz (NMR, engl. *Nuclear Magnetic Resonance*) erzielt worden. Dies ist vor allem zwei Tatsachen geschuldet. Erstens ist der Spin- $\frac{1}{2}$ ein ideales Qubit. Zweitens, hat die magnetische Resonanz im Hinblick

auf die Möglichkeiten seinen Zustand zu manipulieren einen sehr hohen Entwicklungsstand erreicht. Diese ersten Bemühungen haben das Teilgebiet des Spin-Quantencomputing begründet.

Sicherlich ist Quantencomputing mit NMR an Flüssigkeiten in seiner Skalierbarkeit grundsätzlich begrenzt. Jedoch soll der Spin in vielen Quantencomputingvorschlägen als Qubit verwendet werden. Deshalb bleibt magnetische Resonanz eine wichtige Testumgebung für die Entwicklung von experimentellen Methoden. Gleichzeitig, verlagert sich das Interesse von Flüssigkeiten zu orientierten Systemen und insbesondere zu Festkörpern, die eine höhere Skalierbarkeit versprechen.

Der Schwerpunkt meiner Arbeit lag an der Entwicklung und Verfeinerung von Methoden zur Präparation, Manipulation und Vermessung von Quantenzuständen. Dabei wurden sowohl Moleküle in Lösung und in einer Flüssigkristallmatrix als auch Festkörpersysteme verwendet. Auf apparativer Seite kamen Methoden der NMR und Elektron Spin Resonanz (ESR) zum Einsatz. In einigen Fällen wurden numerische Simulationen durchgeführt, um das Verständnis der Experimente zu verbessern. Auf diese Weise gliedert sich die Arbeit in die nun folgenden Abschnitte.

## Verschränkung im Drei-Qubit Deutsch-Josza Algorithmus

David Deutsch war der erste, der zeigte, dass Quantencomputing in der Lage ist klassisch unlösbare Probleme zu lösen. In der Folge, hat sich der Deutsch-Josza Algorithmus zu einer beliebten Methode entwickelt, die Praktikabilität von Vorschlägen zur Implementierung von Quantencomputing zu testen. Auch in unserem Labor wurde der Deutsch-Josza Algorithmus mit drei Qubits im Rahmen der Diplomarbeit von O. Mangold implementiert. Dabei ging es uns vor allem um die Frage der Entstehung von Verschränkung im Ablauf des Algorithmus und insbesondere um die experimentelle Darstellung solcher verschränkter Zustände.

## Experimentelle Durchführung

**Der Quantenprozessor** Zur Implementierung mit der Flüssigkeits-NMR wurde das Molekül 2,3,4-Trifluoroanilin verwendet. Seine drei  $^{19}\text{F}$ -Kernspins sind durch ihre chemischen Verschiebungen hinreichend spektral getrennt und können somit selektiv angeregt und als Qubits verwendet werden. Einer der Spins ist durch skalare Wechselwirkung an jeden der beiden Anderen gekoppelt. Die dritte Kopplung ist vernachlässigbar. Ihr Fehlen hat interessante Auswirkungen auf das Design der Pulssequenzen.

**Präparation und Tomographie** Beim Ensemble-Quantumcomputing mit Flüssigkeits-NMR startet man naturgemäß mit dem nahezu maximal gemischten Boltzmann-Zustand. Zur Durchführung von Algorithmen muß daraus zunächst ein *pseudo-reiner* Zustand erzeugt werden. Die Präparation muss vor allem

Korrelationen zwischen den Qubits erzeugen, die in pseudo-reinen Zuständen vorhanden sind aber im Boltzmann-Zustand fehlen. Dabei liegt eine besondere Herausforderung darin, die zwei Qubits zu korrelieren, die nicht miteinander gekoppelt sind. Das Verfahren dazu ist auch in anderen Systemen mit linearer Qubit-Topologie einsetzbar. Die nicht-unitäre Natur der Präparationssequenz bietet auch die Möglichkeit Fehler durch nicht-perfekte Pulse zu korrigieren und Verluste durch Relaxation während der freien Evolution zu berücksichtigen. Auf diese Weise konnten pseudo-reine Zustände mit einer Güte von über 99.9% präpariert werden. Um die Güte der Präparation überhaupt bestimmen zu können, wurde eine *vollständige Tomographie* der Dichtematrix vorgenommen. Diese verwendet im Wesentlichen die gleichen Bausteine wie die Präparationssequenz.

## Verschränkung im Deutsch-Josza Algorithmus

**Das Deutsch-Problem** Das Deutsch-Problem betrachtet Funktionen, die  $N$  Bits auf ein Bit abbilden. Es werden zwei Klassen von getesteten Funktionen zugelassen; diese werden als *ausgeglichene* und *konstante* bezeichnet. Die eigentliche Rechnung wird durch eine physikalische Vorrichtung bewerkstelligt. Da die innere Beschaffenheit dieser Vorrichtung dem Auswerter vorenthalten bleibt, nennt man sie ein Orakel für die getestete Funktion. Die Aufgabe besteht nun darin, eine Funktion in eine der zwei Klassen einzuteilen und dabei das Orakel möglichst selten zu betätigen. In der modernen Version des Deutsch-Josza Algorithmus nach Collins löst ein Quantencomputer das Problem mit einer einzigen Anwendung des Orakels. Ab  $N = 3$  Qubits kann dabei Verschränkung entstehen.

**Auswahl und Implementierung der Orakel** Aus den 72 erlaubten Funktionen musste eine sinnvolle Auswahl getroffen werden. Dazu wurden die entsprechenden unitären Transformationen, die die Orakel verwirklichen, in der Spinoperator-Basis dargestellt. Es stellt sich heraus, dass die Orakel auf natürliche Weise in sieben Klassen zerfallen. Die Transformationen innerhalb einer Klasse zeigen die gleiche Operatorstruktur und können durch Vertauschung von Qubits ineinander überführt werden. Weil das Kopplungsnetzwerk unseres Quantenprozessors nicht unter allen Vertauschungen symmetrisch ist, wurden neun Orakel implementiert, die alle interessanten Fälle abdecken. Insbesondere auch das Orakel, für welches die fehlende Kopplung überbrückt werden muss. Als Eingangszustand diente der pseudo-reine Zustand  $\rho_{000}$ . Die Ausgangszustände wurden wiederum tomographiert und analysiert.

**Darstellung des Verschränkungsgrades der Endzustände** Da das Problem der Verschränkung ab drei Qubits nachwievorn theoretisch nicht vollständig gelöst ist, ist es nicht ohne Weiteres klar, ob und wie stark die Ausgangszustände des Algorithmus verschränkt sind. Andererseits ist es bekannt, dass *lokale* Transformationen, d.h. solche, die nur einzelne Spins betreffen, den Verschränkungsgrad eines Zustandes nicht ändern. Es stellt sich heraus, dass es möglich ist diesen Grad für die Endzustände des Algorithmus durch einige wenige lokale Transformationen offensichtlich zu machen.

Für jedes Orakel wurde ein solcher Satz gefunden. Manche Orakel erzeugen keine Verschränkung. Andere ergeben Zustände, die im Subraum zweier Qubits verschränkt sind, sodass der Gesamtzustand ein Produkt aus einem Bell-Zustand dieser Qubits mit einem reinen Zustand des dritten Qubits bildet. Es gibt auch Orakel mit einem Endzustand, der lokal auf den vollständig verschränkten Greenberger-Horne-Zeilinger Zustand abgebildet werden kann. Die Erzeugung von Verschränkung durch ein Orakel ist so mit der Operatorstruktur der Orakeltransformation korreliert.

## Maßschneidern des Hamilton-Operators

Wechselwirkungen zwischen den Qubits sind eine unabdingbare Voraussetzung für Quantencomputing. Viele Quantensysteme beinhalten solche Kopplungen in ihren Hamilton-Operatoren. Dabei ist es oft wünschenswert diese Kopplungen temporär außer Kraft setzen zu können. Die magnetische Resonanz bietet die Möglichkeit den Hamilton-Operator durch Verwendung von geeigneten Pulssequenzen zu modifizieren. Um diese Idee zu testen, wurden kleine organische Moleküle in einer Flüssigkristall-Matrix mit den Mitteln der NMR untersucht. Diese Systeme nehmen eine Zwischenposition zwischen den Flüssigkeiten und Einkristallen ein, weil die Flüssigkristalle durch Ausrichtung der Moleküle die Ausmittelung der anisotropen Dipol-Dipol-Wechselwirkung teilweise aufheben. Die Magic-Echo-Sequenz erlaubt es diese Wechselwirkung zu unterdrücken. Die theoretische erwarteten Eigenschaften (Unterdrückung der Dipol-Dipol-Kopplung und Skalierung der chemischen Verschiebung) wurden experimentell demonstriert. Es wurde auch gezeigt, dass es möglich ist, während der Mittelungssequenz die einzelnen Qubits selektiv anzusprechen, was für das Quantumcomputing von entscheidender Bedeutung ist.

## Visualisierung Unitärer Transformationen

Design von Pulssequenzen ist ein wesentlicher Bestandteil bei der Arbeit am Spin-Quantumcomputing. Über die Jahre ist eine Vielzahl von Verfahren entwickelt worden, die verschiedene Aufgaben in der magnetischen Resonanz lösen. Meist geht es dabei darum, die Magnetisierung aus einer gegebenen Richtung in eine andere Richtung zu überführen. Quantumcomputing mit Spins bringt nun die Komplikation mit sich, dass hier weder der Anfangszustand noch der Endzustand spezifiziert sind. Vielmehr geht es darum, die Transformation selbst möglichst getreu zu verwirklichen. Die Schwierigkeit besteht nun darin, dass man dabei nicht die Bahnen der drei Spinkomponenten verfolgen, sondern sich die Evolution der unitären Transformation selbst vorstellen muss. Ich habe ein Verfahren angewendet, das diese Aufgabe wesentlich erleichtert.

Ein Spin- $\frac{1}{2}$  wird üblicherweise in der Bloch-Konstruktion durch einen Vektor im  $\mathbb{R}^3$  visualisiert. Nun sind unitäre Transformationen von Einzelspins nichts weiter als Drehungen solcher Vektoren<sup>1</sup> und können im wesentlichen auch durch Vektoren im  $\mathbb{R}^3$  visualisiert werden. Die Richtung eines solchen Vektors entspricht

---

<sup>1</sup>Bis auf einige Details, die mit den Spinoreigenschaften der Spins zusammenhängen.



dabei der Drehachse und seine Länge dem Drehwinkel. Eine rechnergestützte Austragung eines solchen Vektors macht es möglich, die Entwicklung der unitären Transformation während eines Pulses mit einem komplizierten Phasen-, Amplituden- und Frequenzverlauf visuell zu erfassen. Es konnten auch einige hilfreiche Vorschriften angegeben werden, wie aufeinander folgende Pulse zusammenzufügen sind.

Weiterhin kann man mit Hilfe von Computersimulationen die Abhängigkeit eines solchen Vektors von verschiedenen experimentellen Parametern (wie z.B. der Inhomogenität der statischen oder der RF-Felder) auftragen. Eine solche Spur fasst die wesentlichen Eigenschaften eines Pulses auf einen Blick zusammen.

An Beispielen von einigen einfachen in der NMR üblichen Pulsen wurde die Anwendung dieser Methode demonstriert. Diese Demonstrationen verdeutlichen sehr schön das Problem der Mitanregung spektral benachbarter Spins bei selektiven Pulsen. Es stellt sich auch heraus, dass ein häufiger Schwachpunkt der Pulse darin besteht, dass sie zwar über große Bandbreiten von Parametern die richtigen Drehwinkel haben, dass ihre Drehachsen allerdings in einem nicht annehmbaren Maß variieren.

Mit Hilfe dieser Werkzeuge wurde eine aus alternierenden off-resonanten Pulsen bestehende Sequenz entwickelt. Diese Sequenz implementiert einen selektiven  $\frac{\pi}{2}$ -Puls, der potentiell im Spin-Quantencomputing verwendet werden kann.

## **Detaillierte Untersuchung der Dichtematrizen im $S$ -Bus-System $\text{CaF}_2:\text{Ce}$**

Von der Vielzahl der existierenden Vorschläge zum Quantencomputing mit Spins sind diejenigen am aussichtsreichsten, die auf Festkörpersystemen basieren. Dabei sollen Elektronen- wie Kernspins Verwendung finden. Das Studium der Kopplungen und Manipulationsmöglichkeiten ihrer Wechselwirkungen ist also von allgemeinem Interesse. Das von M. Mehring entwickelte  $S$ -Bus-Konzept ist ein ideales Testfeld für solche Untersuchungen. In unserer Gruppe hat J. Mende im Rahmen seiner Doktorarbeit seine Machbarkeit anhand von einkristallinem mit Cer dotiertem  $\text{CaF}_2$  eindrucksvoll vorgeführt. Seine wesentlichsten Erfolge waren unter Anderem, die Präparation von pseudo-reinen Zuständen von zwei und drei Qubits, die Durchführung des 2-Qubit-Deutsch-Josza-Algorithmus und erste Versuche zur Herstellung verschränkter Zustände.

Das Ziel meiner Beschäftigung mit  $\text{CaF}_2:\text{Ce}$  bestand darin, das Verständnis dieses Systems zu vertiefen und auch auf eine quantitative Basis zu stellen. Dazu habe ich eine exakte numerische Simulation dieses 10-Spin-Systems durchgeführt. Auf experimenteller Seite, habe ich die Evolution der Dichtematrizen unter der Wirkung verschiedener 2-Qubit-Gatter im Detail studiert um die in die Theorie eingehenden Parameter messtechnisch zu bestimmen. Anhand einer vollständigen Tomographie wurde die Implementierung des  $CNOT$ -Gatters gezeigt mit dessen Hilfe dann die Bell-Zustände zweier Qubits erzeugt wurden. Auch der Frage der Zerfallseigenschaften dieser verschränkten Zustände wurde nachgegangen.

## Das $S$ -Bus-Konzept für Spin-Quantencomputing

Das Spin-Bus-Konzept für Quantencomputing basiert auf einem Elektronenspin ( $S$ ) der mit einer Anzahl von Kernspins ( $I$ ) durch die Hyperfeinwechselwirkung verbunden sind. Die  $I$ -Spin sind die Informationsträger (Qubits). Der  $S$ -Spin wird verwendet, um einen hochkorrelierten Zustand der Qubits zu erzeugen und um ihren Zustand auszulesen. Er dient somit als ein *Quantenbus*. Zusätzlich können die Kernspins untereinander durch die Dipol-Dipol-Wechselwirkung gekoppelt sein. Das System kann im Prinzip skaliert werden, indem einzelne  $S$ -Bus-Cluster über die großen Dipolmomente ihrer Bus-Spins kontrolliert miteinander in Wechselwirkung gebracht werden.

Das  $S$ -Bus-Konzept hat eine Reihe von Vorteilen:

- Durch das  $10^3$ -fach größere gyromagnetische Verhältnis ist im thermischen Gleichgewicht die Polarisation der Elektronenspins wesentlich höher als die der Kernspins. Somit steht diese Ressource in einem viel größerem Umfang für Quantenalgorithmen zur Verfügung.
- Die starke Aufspaltung der Zeeman-Niveaus des Elektronenspins bewirkt, dass bereits bei heute verfügbaren Temperaturen und Feldstärken die Quantengrenze überschritten werden kann, was einen Übergang von pseudo-reinen zu reinen Quantenzuständen möglich ist.
- Aus dem gleichen Grund, ist die Nachweisempfindlichkeit bei Beobachtung des Elektronenspins um Größenordnungen höher.
- Die starke Hyperfeinkopplung und die sternförmige Topologie erlauben eine rasche Erzeugung eines hochkorrelierten Zustands des Qubit-Registers. Dieser Zustand enthält bereits *alle* Korrelationen, die zur Herstellung pseudo-reiner Zustände benötigt werden.

Eine der wesentlichen Schwierigkeiten des Konzepts besteht in der indirekten Beobachtung des Zustands der Qubits. Als Konsequenz, kann diese Information nur in ein- oder höherdimensionalen Messungen gewonnen werden.

## $\text{CaF}_2:\text{Ce}$ als Quantenprozessor

Das in unserem Labor verwendete System zur Implementierung des  $S$ -Bus-Konzeptes ist ein mit Cer dotierter  $\text{CaF}_2$ -Einkristall. Das  $\text{Ce}^{3+}$ -Ion ersetzt im Kristallgitter ein  $\text{Ca}^{2+}$ -Ion. Zur Kompensation der überschüssigen Ladung wird an benachbarter raumzentrierter Position ein  $\text{F}^-$ -Ion eingebaut. Aufgrund seiner Größe verzerrt es merklich das Gitter in seiner Umgebung und reduziert damit die Symmetrie des Zentrums auf  $C_4$ . Das  $\text{Ce}^{3+}$  hat ein ungepaartes Elektron, dessen Spin als der Bus-Spin dienen kann. Die  $^{19}\text{F}$ -Kernspins des ladungskompensierenden Ions und der acht nächsten Nachbarn sind durch starke Hyperfeinwechselwirkung an das zentrale paramagnetischen Ion gekoppelt. Aufgrund der starken Anisotropie der Hyperfeintensoren sind bei bestimmten Orientierungen alle Resonanzen der  $I$ -spins aufgelöst, sodass diese selektiv adressiert werden können. Damit sind alle Ingredienzien für ein  $S$ -Bus-Cluster vorhanden. Der wesentlicher Nachteil des  $S$ -Bus-Clusters in  $\text{CaF}_2$  liegt darin, dass es in

ein ausgedehntes Netzwerk von Dipol-Dipol-gekoppelten Fluor-Kernspins eingebettet ist, die eine starke Quelle der Dekohärenz für die Qubits darstellen. Besondere Verfahren mussten entwickelt werden, um diesen Dekohärenzpfad zu unterdrücken.

Experimentelle Umsetzung erfolgte mit einem ENDOR-fähigen X-Band Puls-ESR-Spektrometer bei Temperaturen um 8 K. Der Elektronenspin wurde durch Mikrowellenpulse (9.5 GHz) angesprochen und mit Quadraturdetektion beobachtet. Zur Manipulation der Kernspins dienten RF-Pulse (10 – 20 MHz).

### Exakte numerische Behandlung des paramagnetischen Cer-Zentrums in $\text{CaF}_2$

Die durch Mehring gegebene theoretische Behandlung des  $S$ -Bus liefert ausgehend von einem idealisierten System ein grundsätzliches Verständnis der Verhältnisse. Jedoch, weicht das paramagnetische Zentrum im  $\text{CaF}_2$  in mancher Hinsicht stark von der Idealisierung ab. Insbesondere, liegt die Zeeman-Energie der Kernspins in der gleichen Größenordnung wie die Hyperfeinkopplung. Deshalb, kann das Problem störungstheoretisch nicht befriedigend behandelt werden. Um ein quantitatives Modell zu erhalten, wurde eine exakte numerische Simulation des Clusters durchgeführt.

**Das 10-Spin-Problem** Der Hamilton-Operator des Systems wurde im Laborsystem aufgesetzt. Die benötigten Werte des  $g$ -Tensors und der Hyperfeintensoren sowie die Gitterparameter sind aus der Literatur bekannt. Die Diagonalisierung wurde mit den Standardroutinen aus dem LAPACK-Paket auf einem üblichen PC durchgeführt.

Die Matrizen, die die benötigten Operatoren in diesem System aus 10 Spins- $\frac{1}{2}$  beschreiben aus  $2^{10} \times 2^{10}$  komplexen Zahlen. Die Anzahl der Basisoperatoren, die in den Hamilton-Operator eingehen würde also den verfügbaren Speicher sprengen. Deshalb mussten diese Basisoperatoren für jede Operation neu konstruiert werden. Eine solche Konstruktion erfordert bis zu 10 Tensor-Multiplikationen, deren rechnerischer Aufwand mit der Anzahl der Spins sehr schnell wächst. Unter ausnutzung der Eigenschaften von Pauli-Matrizen konnte die benötigte Rechenzeit in vielen Fällen um den Faktor 10–20 reduziert werden.

Mit Hilfe von speziell konstruierten Messoperatoren liefert die Simulation ESR und ENDOR-Spektren, die in hervorragender Übereinstimmung mit den gemessenen Daten stehen. In der Tat, eine manuelle Anpassung konnte genutzt werden, um die genauen Werte der Euler-Winkel nach kleinen Orientierungsänderungen zu bestimmen.

**Bestimmung der Quantisierungsachsen** Durch die starke Anisotropie und Größe der Wechselwirkungstensoren sind die Quantisierungsachsen aller Spins stark verkippt und unterscheiden sich auch von Spin zu Spin. Die Kenntnis ihrer Lage ist allerdings erforderlich für die Konstruktion vieler Operatoren, die insbesondere für die Simulation von Puls-Experimenten erforderlich sind. Die Quantisierungsachse des Elektronenspins ist leicht zu finden, da seine Zeeman-Aufspaltung den Rest des Hamilton-Operators um den Faktor  $10^3$  übersteigt. Die Quantisierungsachsen der Kernspins sind allerdings nicht ohne Weiteres

erhältlich bedingt durch die starke Mischung der Zustände und durch ein numerisches Problem. Es ist nämlich so, dass die Diagonalisierungsroutinen die Eigenwerte und Eigenvektoren in willkürlicher Reihenfolge liefern. Das führt zu einer künstlichen Vermischung der Hilbert-Räume der einzelnen Spins. Obwohl es mehrere Lösungsansätze gibt, wurde das Problem der Bestimmung der Quantisierungsachsen der Kernspins letztendlich nicht befriedigend gelöst.

### **Verallgemeinerte Transformation ins rotierende Koordinatensystem**

Die Zeitskalen, die die Evolution des  $S$ -Bus-Hamilton-Operators in  $\text{CaF}_2:\text{Ce}$  bestimmen erstrecken sich über mehrere Größenordnungen: Der Elektronspin präzediert mit ca. 9.5 GHz, die Zeeman-Aufspaltung der Kernspins und die Hyperfeinkopplungen liegen zw. 10 – 20 MHz, die Spin-Spin-Kopplungen unter 10 kHz. Zur numerischen Simulation von Experimenten muss diese Bandbreite deutlich reduziert werden.

In der magnetischen Resonanz wird dies mit der Transformation in ein mit den Spins rotierendes Koordinatensystem bewerkstelligt. Allerdings berücksichtigt das Standardverfahren zur Transformation ins rotierende System nicht die Verkippung der Quantisierungsachsen und die Mischung der Zustände durch starke Wechselwirkungen. Es wurde eine Methode verwendet, die es doch erlaubt das rotierende System bei bekannten Quantisierungsachsen zu finden.

**Simulation von ESR-Pulssequenzen** Durch die Transformation ins rotierende Koordinatensystem wurde die Simulation von ESR-Puls-Experimenten ermöglicht. Eine Reihe von solchen Rechnungen wurde durchgeführt.

Die Simulation der Rabi-Oszillation wurde durchgeführt, um die Pulsdauern von  $\frac{\pi}{2}$ - und  $\pi$  Pulsen zu bestimmen, die für weitere Simulationen benötigt werden. Aufgrund der vielen im System vorhandenen Kopplungen und vor allem wegen der Anisotropie und Verkippung der Quantisierungsachsen ist eine direkte Berechnung der Rabi-Frequenz nicht möglich.

Eine Simulation des freien Induktionszerfalls (FID) (*engl. free induction decay*) zeigt die gleiche Zeitkonstante für den Zerfall der Elektron-Spin-Magnetisierung wie die, die experimentell aus der Echo-Breite bestimmt wurde. Dies ist ein Hinweis darauf, dass der  $T_2$ -Zerfall beim Elektron-Spin vorwiegend durch die Kopplung an die nächsten Nachbarn bestimmt wird, da weiter entfernte Spins in der Simulation nicht berücksichtigt wurden. Da keine Kopplung an ein Spin-Bad in die Simulation eingeht, bleibt die simulierte Evolution der Spins vollständig kohärent. Dies zeigt sich darin, dass die FID-Spur zu verschiedenen Zeiten eine teilweise Echo-artige Refokussierung der linearen Elektron-Spin-Terme aufweist. Nichtsdestoweniger, ist es bemerkenswert, dass bereits ein Bad mit neun Wechselwirkungspartner ausreichen um eine schnelle und scheinbar vollständige Dephasierung eines Spins zu bewirken.

Auch die Fähigkeit der Simulation echte Spin-Echos nachzubilden wurde getestet. Das Hahn-Echo und ein Zwei-Spin-Echo zeigen dabei alle wichtigen Eigenschaften wie z.B. die Modulation durch die Hyperfein-Kopplungen. Mit der Berechnung von Echo-Modulation (ESEEM) (*engl. electron spin echo envelope modulation*) wurde das Modell an einem nicht-trivialen Puls-Experiment getestet. Die gemessenen Modulationsspektren konnten numerisch sehr gut reproduziert werden.

## Evolution der Dichtematrizen unter 2-Qubit-Gattern

Eine der wesentlichen Aufgaben bei der experimentellen Umsetzung von Quantencomputing ist die Realisierung von 2-Qubit-Gattern. Im *S*-Bus-Konzept wird bis jetzt die Spin-Spin-Kopplung der Qubits untereinander dafür verwendet. Die generelle *S*-Bus-Theorie kann dazu herangezogen werden quantitative Aussagen über die Entwicklung der Quantenzustände unter 2-Qubit-Gattern zu erhalten. Allerdings, enthält sie eine Reihe von Parametern, die nur aus Messungen bestimmt werden können. Zur Bestimmung dieser Parameter und zur Überprüfung der allgemeinen Aussagen wurde die Evolution der Dichtematrizen während einiger 2-Qubit-Gatter experimentell untersucht.

**Tomographie durch Phasenkodierung** Wie bereits erwähnt, wird der Zustand der Qubits im *S*-Bus indirekt, über den Bus-Spin ausgelesen. Zur Bestimmung der einzelnen Elemente der Kern-Spin-Dichtematrix muss diese Information in den Zustand des Elektron-Spins kodiert werden. Dazu dient eine Pulssequenz, die auf der Multiquanten-Resonanz basiert. Sie besteht aus zwei Pulsen gleichen Drehwinkels, wobei der Zweite gegenüber dem Ersten phasenverschoben ist. Die Sequenz wird gleichzeitig aber selektiv auf jeden Kern-Spin angewandt dabei wird die Phasenverschiebung mit einer Frequenz die für jeden Spin anders ist von Schuss zu Schuss inkrementiert. In der Fourier-Transformation einer solchen fiktiven Zeitspur ergeben die linearen Terme der Dichtematrix Linien bei den jeweiligen Phasenfrequenzen, während die Korrelationsterme sich in Linien bei Summen- und Differenzenfrequenzen manifestierten. Die Analyse des Spektrums erlaubt also die Bestimmung der Amplituden der einzelnen Terme.

**Präparation der Eingangszustände** Die Präparation von Zwei- und Drei-Qubit pseudo-reinen Zuständen wurde bereits von Mende gezeigt. Hier wurden sie verwendet als Eingangszustände für die Demonstration des *CNOT*-Gatters. Dabei wurde eine vereinfachte Pulssequenz verwendet. Es konnten alle vier pseudo-reine Zustände von zwei Qubits mit Güten von über 95% hergestellt werden.

**Parameterbestimmung durch Evolution unter 2-Qubit Operationen** Das wichtige *CNOT*-Gatter enthält als wesentlichen Baustein eine freie Evolution des Spinsystems, die in der Mitte durch einen  $\pi$ -Puls an den beiden teilnehmenden Spins geteilt wird. Zwei andere Sequenzen, nämlich die "Spin-Echo Double-Resonance"- (SEDOR) und die "Insensitive Nuclei Enhanced by Polarisation Transfer"-Sequenz (INEPT), basieren auf dem gleichen Prinzip. Der Verlauf einzelner Dichtematrix-Terme mit wachsender Evolutionszeit wurde für die drei Sequenzen in 2D-Experimenten vermessen. Dadurch konnten die im Modell enthaltenen Parameter aus den experimentell bestimmt werden.

## Präparation pseudo-verschränkter Zustände "entfernter" Qubits

Erzeugung von Verschränkung ist das eigentliche Gütesiegel einer jeden experimentellen Realisierung von Quantencomputing. In mehreren Schritten wurden die Bell-Zustände von nicht direkt gekoppelten Qubits in  $\text{CaF}_2:\text{Ce}$  präpariert.

**“Entfernte” Qubits** Normalerweise sind die Kernspins im  $S$ -Bus-Cluster miteinander durch Dipol-Kopplungen verknüpft. Bei gewissen Orientierungen verschwinden diese Kopplungen. In diesem Fall, können die beiden Qubits im Sinne des Kopplungsnetzwerks als *entfernt* betrachtet werden. Die für Quantengatter benötigte Wechselwirkung wird dann ausschließlich durch den Bus-Spin vermittelt.

**Implementierung und Tomographie der  $CNOT$ -Operation** Zum Nachweis eines funktionsfähigen  $CNOT$ -Gatters muss neben der Präparation wohl definierter Eingangszustände auch eine Tomographie der Ausgangszustände vorgenommen werden. Die oben beschriebene Phasenkodierung kann wegen einer Besonderheit des Detektionsverfahrens im  $S$ -Bus nicht direkt verwendet werden. Mit einer modifizierten Phasenkodierung konnte jedoch die gewünschte Information über die Dichtematrix der beiden beteiligten Qubits erhalten werden. Die Daten entsprechen eindeutig die Wahrheitstabelle des  $CNOT$ -Gatters.

**2-Qubit-Bell-Zustände** Auch der Nachweis verschränkter Zustände ist aufgrund ihrer besonderen Operatorstruktur umständlich. Als erster Test wurden die Endzustände direkt Phasenkodiert. Bell-Zustände enthalten keine linearen Operatoren, was so auch für die präparierten Dichtematrizen gezeigt werden konnte. Eine direkte Detektion der nicht-diagonalen Terme ist allerdings nicht möglich. Deshalb wurde die inverse Pulssequenz ( $CNOT$ -Gatter und Hadamard-Transformation) angewandt und dabei Phasenkodiert. Es stellt sich heraus, dass die vier Bell-Zustände anhand des resultierenden Phasenspektrums eindeutig voneinander unterschieden werden können. Eine erschöpfende theoretische Beschreibung dieses Experiments steht allerdings noch aus.

**Zerfall verschränkter Zustände** Es ist gelegentlich darüber berichtet worden, dass verschränkte Zustände besondere Eigenschaften bezüglich ihrer Empfindlichkeit gegenüber dephasierenden Einflüssen haben können. Um dieser interessanten Frage nachzugehen, wurde der Zerfall der Bell-Zustände Vermessen. Dazu genügt es, eine variable Zerfallszeit zwischen die beiden Teile der oben beschriebenen Sequenz einzufügen. In der Tat unterscheiden sich die Zerfallszeiten um einen Faktor von bis zu 2. Eine außergewöhnliche Resistenz gegenüber Dekohärenz liegt im  $\text{CaF}_2:\text{Ce}$  aber nicht vor.

## Beobachtung von Spin-Spin Wechselwirkungen in einer feindlichen Umgebung

Die experimentelle Bestimmung der Kopplungsstärke zwischen den einzelnen Kernspins des  $S$ -Bus-Clusters in  $\text{CaF}_2:\text{Ce}$  ist dadurch erschwert, dass diese Spins untereinander und auch mit den übrigen Spins des Gitters ähnlich stark gekoppelt sind. Die Vielzahl der Kopplungen führt zu einer vollständigen Dekohärenz innerhalb weniger  $10 \mu\text{s}$ . Es werden also Verfahren benötigt, die einerseits *alle* Kopplungen zwischen den Spins unterdrücken und andererseits *eine* der Kopplungen wirksam lassen. Dieselbe Anforderung besteht auch bei der Nutzung der Kopplungen für Quantengatter. Eine Reihe von bekannten Methoden wurde

---

hinsichtlich ihrer Eignung für diesen Zweck in  $\text{CaF}_2:\text{Ce}$  überprüft. Es wurde, weiterhin, eine Sequenz entwickelt, die sich besonders für Quantengatter eignet. Zunächst wurde in SEDOR und und anderen Echo-Experimenten gezeigt, dass die Kohärenz-Zeit für einzelne Kernspins durch effektive Entkopplung um den Faktor 100 gesteigert werden kann.

Zum Herauspräparieren einzelner Kopplungen wurden folgende Sequenzen herangezogen: SEDOR, gleichzeitiges Spin-Locking und Carr-Purcell-Meiboom-Gill-Sequenz (CPMG). Alle Sequenzen haben ihre Vor- und Nachteile. Die SEDOR-Sequenz ist besonders einfach zu realisieren und liefert den im Quantencomputing benötigten mittleren Hamilton-Operator. Allerdings zeigt sie auch die schwächste Entkopplungswirkung. Dies kann auf die langen Perioden der freien Evolution während derer nicht-säkulare Anteile der Wechselwirkungen wirksam sind.

Die CPMG-Sequenz reduziert die Zykluszeit gegenüber der SEDOR-Sequenz und zeigt eine höhere Entkopplungseffizienz. Sie leidet jedoch unter den Effekten der endlichen Pulsbreite, die für eine genaue Bestimmung der Kopplungskonstanten von Nachteil sind. Spin-Locking eliminiert freie Evolution vollständig und erzielt auch die beste Entkopplung. Allerdings werden hier die Linienbreiten durch den Effekt der Wechselfeld-Inhomogenität nach unten begrenzt. Zusätzlich, verkippt diese Sequenz die Quantisierungsachse des mittleren Hamilton-Operators was für die Nutzung in Quantengattern ungünstig ist.

Aufgrund dieser Beobachtungen wurde schließlich eine neue Sequenz entwickelt. Sie enthält keine freie Evolution und ist somit wirksame gegen nicht-säkulare Terme und Effekte der endlichen Pulsdauer. Sie wirkt der Wechselfeld-Inhomogenität durch Phasen-Alternierung entgegen und sie erzeugt einen Hamilton-Operator, der in  $z$ -Richtung quantisiert ist. Nachteilig ist, dass dabei die Kopplungsstärke um den Faktor  $\frac{1}{2}$  reduziert wird.

Es bleibt zu bemerken, dass diese Verfahren auch außerhalb von Quantencomputing und in anderen Systemen als  $\text{CaF}_2:\text{Ce}$  nützlich sein können.

## Ausblick

Mit dem bis dato erreichten ist das  $S$ -Bus-Konzept noch lange nicht ausgereizt. Insbesondere, eine Übertragung auf ein höheres Feld erscheint vielversprechend. Dies hätte zweierlei Vorteile. Erstens, würde die hohe Polarisierung der Elektronen in hohen Feldern bei tiefen Temperaturen die Quantengrenze für Ensemble-Quantencomputing in greifbare Nähe rücken. Zweitens, könnten die Zeeman-Wechselwirkung der Kernspins und die Hyperfein-Kopplung deutlich voneinander getrennt werden, was den experimentellen und vor allem den theoretischen Zugang erheblich vereinfachen würde. In fernerer Zukunft (und mit einem stark erhöhten Aufwand) könnte man daran denken isolierte Cluster zu adressieren und miteinander quantenmechanisch zu verschalten.

---





# Appendix A

## Basics of Magnetic Resonance

This section summarizes the principles of magnetic resonance for the convenience of the reader. For simplicity, the discussion is limited to particles with spin quantum number  $I = 1/2$ . More detailed and general introduction can be found in [76, 90, 121].

### A.1 Spin Evolution

#### A.1.1 Spin Hamiltonian

Most elementary particles and nuclei carry an intrinsic angular momentum called *spin*. It is quantized in units of  $\hbar/2$ . In this work the letter ‘ $S$ ’ is used to refer to *electron* spin and the letter ‘ $I$ ’ to *nuclear* spin. When both types are meant ‘ $I$ ’ is used.

Spin is represented by a vector operator  $\mathbf{I}$  with three Cartesian components  $\mathbf{I}_x$ ,  $\mathbf{I}_y$ , and  $\mathbf{I}_z$ .<sup>1</sup> These components obey the usual commutator relations of the angular momentum algebra.

The magnetic moment associated with the spin of a nucleus is given by

$$\boldsymbol{\mu}_I = g_N \mu_N \mathbf{I} = \gamma_I \hbar \mathbf{I} \quad (\text{A.1})$$

where  $g_N$  is *g-factor* of this specific nucleus and  $\mu_N = 5.050783 \times 10^{-27}$  J/T. The coefficient  $\gamma_I = g_N \mu_N / \hbar$  is the *gyromagnetic ratio*<sup>2</sup>.

For the spin of an electron, the magnetic moment is given by

$$\boldsymbol{\mu}_S = -g \mu_B \mathbf{S} \quad (\text{A.2})$$

where  $\mu_B = 927.400949 \times 10^{-26}$  J/T is the Bohr magneton and  $g$  is the *g-factor* of the electron spin.

---

<sup>1</sup>Throughout this thesis the *dimensionless* form of spin operators is used as described in Section B.2.

<sup>2</sup>Since  $\gamma_I$  is defined by  $|\boldsymbol{\mu}|/|\hbar\mathbf{I}|$ , the more consistent term *magneto-gyric ratio* is also used infrequently.

When placed in an static homogeneous magnetic field  $\mathbf{B}_0$  the Hamilton operator of a nuclear spin is given by

$$\mathcal{H}_I = -\boldsymbol{\mu}_I \mathbf{B}_0 = -\gamma_I \hbar \mathbf{I} \mathbf{B}_0 \quad (\text{A.3})$$

and for an electron spin by

$$\mathcal{H}_S = -\boldsymbol{\mu}_S \mathbf{B}_0 = g \mu_B \hbar \mathbf{S} \mathbf{B}_0 \quad (\text{A.4})$$

When the  $z$ -direction of the coordinate system is chosen along the magnetic field the two Hamiltonians assume the form

$$\mathcal{H}_I = -\gamma_I \hbar B_0 \mathbf{I}_z \quad (\text{A.5a})$$

$$\mathcal{H}_S = g \mu_B \hbar B_0 \mathbf{S}_z \quad (\text{A.5b})$$

It is convenient to express the spin Hamiltonian in units of angular velocity  $\text{s}^{-1}$  by dividing it by  $\hbar$ . The Hamiltonian is then written

$$\mathcal{H} = \omega_0 \mathbf{I}_z \quad (\text{A.6})$$

with  $\omega_0 = -\gamma_I B_0$  for nuclear and  $\omega_0 = g \mu_B B_0 / \hbar$  for electron spins.

The eigenvalue problem of the spin Hamiltonian

$$\omega |\psi\rangle = \mathcal{H} |\psi\rangle \quad (\text{A.7})$$

has two solutions described by the *spin quantum number*  $m_I$

$$\omega_{m_I} = m_I \omega_0 \quad (\text{A.8a})$$

$$m_I = -\frac{1}{2} : \quad \omega_{\downarrow} = -\frac{\omega_0}{2}, \quad |\downarrow\rangle = \begin{pmatrix} 0 \\ 1 \end{pmatrix} \quad (\text{A.8b})$$

$$m_I = +\frac{1}{2} : \quad \omega_{\uparrow} = +\frac{\omega_0}{2}, \quad |\uparrow\rangle = \begin{pmatrix} 1 \\ 0 \end{pmatrix} \quad (\text{A.8c})$$

corresponding to the famous “spin down” and “spin up” states.

### A.1.2 Evolution in a Static Magnetic Field

Suppose the spin is in a superposition state

$$|\psi(t=0)\rangle = a |\uparrow\rangle + b |\downarrow\rangle = \begin{pmatrix} a \\ b \end{pmatrix}, \quad \text{with } a a^* + b b^* = 1 \quad (\text{A.9})$$

at time  $t = 0$ . The general solution of the time dependent Schrödinger equation with the Hamilton operator in Equation (A.6) is given by

$$|\psi(t)\rangle = a e^{-i\frac{\omega_0}{2}t} |\uparrow\rangle + b e^{+i\frac{\omega_0}{2}t} |\downarrow\rangle \quad (\text{A.10})$$

The expectation values for the Cartesian components of the spin operator are then

$$\langle \mathbf{I}_x \rangle = \frac{1}{2} ab \cos(\omega_0 t) \quad (\text{A.11a})$$

$$\langle \mathbf{I}_y \rangle = \frac{1}{2} ab \sin(\omega_0 t) \quad (\text{A.11b})$$

$$\langle \mathbf{I}_z \rangle = \frac{1}{2} (|a|^2 - |b|^2) \quad (\text{A.11c})$$

This corresponds to a precession of a classical angular momentum around the direction of the field which can be described by a classical equation of motion for the expectation values:

$$\frac{d}{dt}\langle\mathbf{I}\rangle = \omega_0 \langle\mathbf{I}\rangle \times \mathbf{b}_0 \quad (\text{A.12})$$

where  $\mathbf{b}_0$  is the direction of the magnetic field. Since the expectation values of the spin operator are directly linked to magnetic moment by Equations (A.1) - (A.2), this is also the equation of motion for a *macroscopic magnetization of an ensemble* of spins.

The precession frequency  $\omega_0$  is called *Larmor* frequency and is found from the separation  $\hbar\omega_0$  between the energy levels of a spin  $I = 1/2$ .

### A.1.3 Evolution in a Static and an Oscillating Magnetic Fields

To manipulate a spin precessing in a static magnetic field the following approach is used almost universally in magnetic resonance. A second magnetic field  $\mathbf{B}_1$  rotating with the frequency  $\omega$  in the  $xy$ -plane is applied. The Hamiltonian of the spin then becomes

$$\mathcal{H} = \omega_0 \mathbf{I}_z + \omega_1 (\cos(\omega t) \mathbf{I}_x + \sin(\omega t) \mathbf{I}_y) \quad (\text{A.13})$$

where  $\omega_1 = -\gamma B_1$  for a nuclear and  $\omega_1 = g\mu_B B_1/\hbar$  for an electron spin. At  $t = 0$  the vector of the rotating field points in the  $x$ -direction:

$$\mathbf{B}_1(t = 0) \parallel \hat{x} \quad (\text{A.14})$$

In the case of *resonant excitation* when  $\omega = \omega_0$  a solution to the Schrödinger equation is readily obtained:

$$|\psi(t)\rangle = \cos(\omega_1 t) e^{-i\frac{\omega_0}{2}t} |\uparrow\rangle + i \sin(\omega_1 t) e^{+i\frac{\omega_0}{2}t} |\downarrow\rangle \quad (\text{A.15})$$

The expectation values of the spin components are now

$$\langle\mathbf{I}_x\rangle = \frac{1}{2} \sin(\omega_1 t) \cos(\omega_0 t) \quad (\text{A.16a})$$

$$\langle\mathbf{I}_y\rangle = \frac{1}{2} \sin(\omega_1 t) \sin(\omega_0 t) \quad (\text{A.16b})$$

$$\langle\mathbf{I}_z\rangle = \frac{1}{2} \cos(\omega_1 t) \quad (\text{A.16c})$$

The effect of an additional oscillating field, therefore, is to superimpose a nutation motion upon the precession around the static field. In particular the expectation value of the  $z$ -component of the spin operator oscillates between  $+1/2$  and  $-1/2$  with the angular frequency  $\omega_1$ . This phenomenon is known as *Rabi oscillation* and  $\omega_1$  as *Rabi frequency*.

### A.1.4 Empiric Approach to Relaxation: Bloch Equation

According to Equation (A.12), a spin set in motion around the field  $\mathbf{B}_0$  would precess with the same value of the  $z$ -component indefinitely. In practice, no spin ensemble is isolated from its environment and evolves toward a thermal equilibrium with it. In equilibrium, the population difference between the two eigenstates  $|\uparrow\rangle$  and  $|\downarrow\rangle$  must obey the Boltzmann distribution which links the expectation value of the  $z$ -component of the spin operator to the temperature.

To account for this, Bloch extended Equation (A.12) by the empirical relaxation terms to obtain the equation known by his name:

$$\frac{d}{dt}\langle\mathbf{I}\rangle = \omega_0 \langle\mathbf{I}\rangle \times \mathbf{b}_0 + \begin{pmatrix} -\frac{1}{T_2}\langle\mathbf{I}_x\rangle \\ -\frac{1}{T_2}\langle\mathbf{I}_y\rangle \\ \frac{I_0 - \langle\mathbf{I}_z\rangle}{T_1} \end{pmatrix} \quad (\text{A.17})$$

Here,  $I_0$  is the expectation value of the  $z$ -component of the spin operator dictated by the Boltzmann distribution and  $T_1$  is time constant of the relaxation into the equilibrium state. It describes the rate at which the spin system exchanges energy with its surroundings (collectively called “lattice”) until they reach thermal equilibrium. This type of relaxation process is known as *longitudinal* relaxation. Its effectiveness basically depends on the strength of the magnetic field fluctuations felt by the spin at the Larmor frequency.

The terms containing  $T_2$  account for the fact that, in a spin ensemble, coherence between individual spins is generally lost with time. As a result, the expectation values of the  $x$ - and  $y$ -components of spin operator must vanish in the steady-state limit.  $T_2$  is therefore known as the *transverse* relaxation time.

The most prominent mechanism of transverse relaxation is due to the fact that the Larmor frequency of a given spin depends on its position in the sample (due, e.g., to a slight inhomogeneity of the magnetic field). In this case, different spins will precess at slightly different angular velocities and fan out from their initial direction until they become equally distributed in all directions in the  $xy$ -plane. This mechanism gives rise to *inhomogeneous broadening* of spectral lines.

Another prominent source of transverse relaxation is found in extended spin networks. If the spins contained in a sample are coupled (e.g., by dipole-dipole interaction), two neighboring particles can spontaneously exchange their spins. After such an event, the phase of the two spins will be distributed randomly, which diminishes the transverse magnetization of the sample.

Depending on the specifics of the relaxation mechanism, the relaxation dynamics frequently deviate from the exponential decay implied by the Bloch equation. Detailed treatment of spin relaxation is can be found elsewhere [75].

## A.2 The Principle of Pulsed Magnetic Resonance

### A.2.1 Rotating Frame of Reference

The dynamics of spin under a static and an oscillating magnetic field described in Section A.1.3 contains both the precession around the static field and the nutation under the rotating field. Spin motion becomes much clearer when considered in a frame of reference fixed to the rotating field  $\mathbf{B}_1$ .

The unitary operator of the transformation is

$$R(\omega t) = e^{-i \omega t \mathbf{I}_z} \quad (\text{A.18})$$

and the Hamiltonian in Equation (A.13) becomes, in the rotating frame,

$$\begin{aligned} \mathcal{H}_{rot} &= R^\dagger(\omega t) \mathcal{H} R(\omega t) - \omega \mathbf{I}_z \\ &= (\omega_0 - \omega) \mathbf{I}_z + \omega_1 \mathbf{I}_x \end{aligned} \quad (\text{A.19})$$

The term  $\omega \mathbf{I}_z$  is due to the non-inertial nature of the *rotating frame* of reference. It represents a fictitious magnetic field analogous to the fictitious forces in classical mechanics.

In the rotating frame, the time dependence of the Hamilton operator is thus completely removed and the spin precesses around an *effective* magnetic oriented along

$$\mathbf{B}_{eff} \parallel \begin{pmatrix} \omega_1 \\ 0 \\ \omega_0 - \omega \end{pmatrix} \quad (\text{A.20})$$

with the effective angular frequency

$$\omega_{eff} = \sqrt{\omega_1^2 + (\omega_0 - \omega)^2} \quad (\text{A.21})$$

The situation is further simplified, when the angular frequencies of field rotation and spin precession in the laboratory frame coincide. Under this condition of *resonant excitation*

$$\omega = \omega_0 \quad \text{and} \quad \mathcal{H}_{rot}^{res} = \omega_1 \mathbf{I}_x \quad (\text{A.22})$$

so that the spin precesses around the  $x$ -direction:

$$|\psi(t)\rangle = \cos(\omega_1 t) \mathbf{I}_z - \sin(\omega_1 t) \mathbf{I}_y \quad (\text{A.23})$$

At resonance, Rabi oscillation occurs around the direction of the rotating field.

### A.2.2 Rotation Pulses

Equation (A.23) shows, how spin can be manipulated in a magnetic resonance apparatus. Initially, the rotating field is off ( $\omega_1 = 0$ ) and the spin in the rotating frame points in the  $z$ -direction. Then, the driving field is switched on for a time  $t_{\pi/2} = \pi/(2\omega_1)$  and switched off again. The spin now points in the  $-y$ -direction having been turned by an angle of  $\pi/2$  around the  $x$ -axis. This constitutes a

$\pi/2$ -pulse in  $x$ -direction. If the field is kept on for  $t_\pi = \pi/\omega_1$ , the rotation angle of the spin is  $\pi$ . After such a  $\pi$ -pulse the spin points in the  $-z$ -direction.

If the phase of the rotating field is chosen such that it points in the  $y$ -direction when it is turned on, the rotation of the spin proceeds in the  $zx$ -plane. Thus, selecting the phase, strength, and duration of application of the rotating field a spin rotation through any angle around any axis in the  $xy$ -plane can be effected.

### A.2.3 FID

The most basic and common experiment in pulsed magnetic resonance begins with the spin ensemble in thermal equilibrium with its environment, such that the total magnetization of the sample points in the  $z$ -direction. A  $\pi/2$ -pulse in  $y$ -direction is applied next. The magnetization now points in  $x$ -direction and begins to precess around the  $z$ -direction.

According to Equation (A.17), various relaxation processes now begin to drive the magnetization towards its equilibrium value along  $z$  and the magnitude of the transverse magnetization decays to zero. This – often exponential – decay is superimposed upon the harmonic oscillation of the transverse components due to Larmor precession and is known as the *free induction decay* (FID).

### A.2.4 Hahn Echo

The second most prominent experiment in magnetic resonance is the *spin echo* observation. If the dominating mechanism of transverse relaxation is due to field inhomogeneity as described in Section A.1.4, then the coherence of the spins is not lost after the FID. A  $\pi$ -pulse applied at a time  $\tau$  after the  $\pi/2$  pulse effectively inverts the time for the Zeeman Hamiltonian, so that the dephased spins gradually come together again giving a maximum of magnetization at  $t = 2\tau$ . After that another FID takes place. This phenomenon was first observed by Hahn and is commonly known as *Hahn echo*.

In many situations, any two successive pulses will produce a spin echo. Many types of experiments and echoes have been introduced for measurement of a large array of material properties especially in solid-state systems [57, 75].

## A.3 Pulsed Nuclear Magnetic Resonance

Over the last decades Nuclear Magnetic Resonance (NMR) has become a ubiquitous tool in physics, chemistry and life sciences. A modern NMR-instrument usually consists of a superconducting magnet providing the static magnetic field. The field strength of NMR magnets is usually specified in terms of the proton resonance frequency; spectrometers up to 900 MHz are commercially available today. Another important characteristic of an NMR magnet is the homogeneity, which can reach  $10^{-7}$  in modern systems.

The magnet typically has a room temperature bore into which a cryostat containing the probe head can be inserted. In common use are cryostats and probes

which allow measurement between 4.2 K and some 400 K. The probe head contains a small coil placed at the center of the magnet's field. The sample is placed into the coil. For high resolution liquid state NMR a *magic angle spinning* unit is used to average out unwanted interactions through sample rotation at up to 50 kHz.

The spectrometer is equipped with electronics which allow to synthesize rf pulses with the desired frequency, phase, amplitude, and timing and a number of high-power amplifiers for excitation of nuclei in different spectral regions. Great freedom in choice of all these parameters is today available to the experimentalist.

The excitation coil is also used for the detection of the signal induced by the precessing magnetization of the sample. The detection channel consists of filters, low noise amplifiers, etc. to provide for very sensitive detection of the NMR signal. Since the coil only captures one linear component of the rf signal, a special *quadrature detection* scheme is used to detect both the  $x$ - and the  $y$ -component of the sample magnetization.

Finally, the received signal is digitized and recorded as a complex amplitude of the sample response versus time. In this form, it is available for any number of numerical methods of enhancement and analysis. Ultimately, the recorded data are subjected to a Fourier transformation to obtain an excitation spectrum.

## A.4 Electron Spin Resonance

Because the gyromagnetic ratio of electrons in most environments is around  $10^3$  times larger than that of nuclei, the experimental equipment of electron spin resonance (ESR) differs from that of NMR. First of all, the frequencies of excitation at feasible field strengths are much higher; the most commonly used frequencies are 9.5 GHz (microwave X band) and 95 GHz (W band).

At these frequencies, coils can no longer be used for efficient excitation and detection, therefore various types of resonators are employed. These are only tunable in a small frequency range, thus, the magnetic field is varied instead of the excitation frequency in order to establish the resonance condition.

Due to the usually very fast relaxation times for electron spins, ESR, in its early years, operated almost exclusively in the cw regime where the excitation frequency is kept constant and the magnetic field is slowly scanned across the resonance while the microwave absorption of the sample is monitored. To this day, this is the most common use of ESR spectrometers.

With the advances in electronics, it became feasible to apply the pulsed approach which is standard in NMR to the study of electron spins. The major components of a pulsed ESR spectrometer are essentially the same as in an NMR machine, although the technical details differs significantly.





## Appendix B

# Density Matrix Formalism and Notation

This appendix summarizes the basics of the density matrix formalism [122, 123] which are relevant to this thesis. The notation used throughout this work – particularly the use of *spin component operators* – is also described.

### B.1 Fundamental Properties of the Density Operator

If the probability of finding a system in a quantum state  $|\psi_m\rangle$  is given by  $p_m$ , then the density operator is defined by

$$\hat{\rho} = \sum_m p_m |\psi_m\rangle \langle \psi_m| \quad (\text{B.1})$$

To find an explicit representation of the density operator, i.e., the *density matrix*, consider a basis of the Hilbert space of the quantum states of the system:

$$B : \{|\varphi_j\rangle\} \quad (\text{B.2})$$

As implied by the properties of a Hilbert space, the basis vectors  $|\varphi_j\rangle$  are assumed to be orthonormal<sup>1</sup>

$$\langle \varphi_j | \varphi_k \rangle = \delta_{jk} \quad (\text{B.3})$$

and complete

$$\sum_j |\varphi_j\rangle \langle \varphi_j| = \mathbf{1} \quad (\text{B.4})$$

where  $\mathbf{1}$  is the unit operator.

---

<sup>1</sup>The orthogonality of the basis is not strictly required.

The density operator can be expressed in terms of this basis as

$$\begin{aligned}\hat{\rho} &= \sum_m p_m \left( \sum_j |\varphi_j\rangle\langle\varphi_j| \right) |\psi_m\rangle\langle\psi_m| \left( \sum_k |\varphi_k\rangle\langle\varphi_k| \right) \\ &= \sum_{jk} \left( \sum_m p_m \langle\varphi_j|\psi_m\rangle\langle\psi_m|\varphi_k\rangle \right) |\varphi_j\rangle\langle\varphi_k| \\ &= \sum_{jk} \rho_{jk} |\varphi_j\rangle\langle\varphi_k|\end{aligned}\quad (\text{B.5})$$

where

$$\rho_{jk} = \sum_m p_m \langle\varphi_j|\psi_m\rangle\langle\psi_m|\varphi_k\rangle \quad (\text{B.6})$$

are the elements of the *density matrix* of the system represented in the basis  $B$ . From this definition, a number of properties of the density matrix follow:

- The expectation value of any observable  $\hat{A}$  can be calculated from the density matrix by

$$\langle\hat{A}\rangle = \text{tr}(\hat{A}\hat{\rho}) = \text{tr}(A\rho) \quad (\text{B.7})$$

where  $A$  is the matrix representation of the operator  $\hat{A}$  in the basis  $B$ . This means that all physical information about a state of the system is contained in the density matrix.

- The definition of the density matrix involves two distinct types of statistical averaging: the fundamental quantum mechanical average arising from the uncertainty of measurement and the classical statistic average due to the incomplete knowledge of the observer.

If the knowledge of the system state is complete, i.e., a full set of observables has been measured, the system is said to be in a *pure state*  $|\psi_m\rangle$ . The trace of the square of the density matrix of a pure state is unity

$$\text{tr}(\rho_{\text{pure}}^2) = 1 \quad (\text{B.8})$$

Incompletely known states represent statistical mixtures. The trace of the square of the density matrix of such *mixed states* is less than one:

$$\text{tr}(\rho_{\text{mixed}}^2) < 1 \quad (\text{B.9})$$

This ability to describe pure states and statistical mixtures in a unified way is the chief advantage of the density matrix formalism.

- The density operator is Hermitian (aslef-adjoint)

$$\hat{\rho} = \hat{\rho}^\dagger \quad (\text{B.10})$$

meaning that the density matrix itself is an observable and that its eigenvalues are non-negative, real numbers:

$$0 \leq \rho_{jj} \quad (\text{B.11})$$

In particular, the diagonal elements of the density matrix  $\rho_{jj}$  give the probability of finding the system in the state  $|\varphi_j\rangle$ . In the context of ensembles, this corresponds to the *population* of that state.

- The trace of the density matrix is normalized to unity:

$$\text{tr}(\rho) = 1 \quad (\text{B.12})$$

in accordance with the probability interpretation.

- In the case of pure states, the off-diagonal elements of the density matrix  $\rho_{jk}$  with  $j \neq k$  are complex amplitudes of coherent superpositions of states  $|\varphi_j\rangle$  and  $|\varphi_k\rangle$ .
- The evolution of the density matrix with time is described by the *Liouville equation*

$$i\hbar \frac{d\rho(t)}{dt} = [\mathcal{H}(t), \rho(t)] \quad (\text{B.13})$$

where  $\mathcal{H}(t)$  is the matrix representation of the Hamilton operator.<sup>2</sup>

## B.2 Spin Operator Component Basis

The most natural choice of basis vectors  $|\varphi_j\rangle$  of the Hilbert space of a spin  $I = 1/2$  particle in an external magnetic field are the eigenstates of the Hamilton operator. They are known as the *Zeeman states* and are commonly labeled as  $|\downarrow\rangle$  and  $|\uparrow\rangle$  or  $|-1/2\rangle$  and  $|+1/2\rangle$  or  $|1\rangle$  and  $|0\rangle$ . The corresponding density matrices according to Equation (B.6) are

$$|0\rangle\langle 0|: \quad \rho_0 = \begin{pmatrix} 1 & 0 \\ 0 & 0 \end{pmatrix} \quad (\text{B.14a})$$

$$|1\rangle\langle 1|: \quad \rho_1 = \begin{pmatrix} 0 & 0 \\ 0 & 1 \end{pmatrix} \quad (\text{B.14b})$$

These density matrices represent two pure states of a spin  $I = 1/2$  system. The remaining two basis matrices are

$$|0\rangle\langle 1|: \quad \begin{pmatrix} 0 & 1 \\ 0 & 0 \end{pmatrix} \quad (\text{B.15a})$$

$$|1\rangle\langle 0|: \quad \begin{pmatrix} 0 & 0 \\ 1 & 0 \end{pmatrix} \quad (\text{B.15b})$$

These four elementary matrices constitute a basis in which any density matrix can be expressed.

The most prominent objects in the field of Magnetic Resonance are the magnetic moment associated with the spin and its components. Because of that, the basis used almost exclusively is the basis of the spin operator components. Their

<sup>2</sup>If the Hamiltonian of the system is written in units of angular velocity  $s^{-1}$ , the factor  $\hbar$  is omitted.

matrix representation is based on the *Pauli matrices*. The full basis is given by

$$\mathbf{I}_0 = \begin{pmatrix} 1 & 0 \\ 0 & 1 \end{pmatrix} \quad (\text{B.16a})$$

$$\mathbf{I}_x = \frac{1}{2} \begin{pmatrix} 0 & 1 \\ 1 & 0 \end{pmatrix} \quad (\text{B.16b})$$

$$\mathbf{I}_y = \frac{1}{2} \begin{pmatrix} 0 & -i \\ i & 0 \end{pmatrix} \quad (\text{B.16c})$$

$$\mathbf{I}_z = \frac{1}{2} \begin{pmatrix} 1 & 0 \\ 0 & -1 \end{pmatrix} \quad (\text{B.16d})$$

The identity operation is denoted by  $\mathbf{I}_0$ . Notice, that this is the *dimensionless* form of the spin component operators. The usual form given in units of angular momentum is obtained by multiplying the given expressions by  $\hbar$ . In addition to the Cartesian components, the “ladder” operators

$$\mathbf{I}_{\pm} = \mathbf{I}_x \pm i\mathbf{I}_y \quad (\text{B.17})$$

are also occasionally used.

The expressions in Equation (B.16) satisfy the usual commutator relations of the spin operators:

$$[\mathbf{I}_j, \mathbf{I}_k] = \frac{i}{2} \mathbf{I}_l \quad (\text{B.18})$$

where  $\{j, k, l\}$  are cyclic permutations of  $\{x, y, z\}$ . Additionally, spin component operators are orthogonal:

$$\text{tr}(\mathbf{I}_j \mathbf{I}_k) = 0, \quad \text{for } j \neq k \quad (\text{B.19})$$

The pure states in Equation (B.14) can now be expressed in terms of spin operator components:

$$\rho_0 = \frac{1}{2} \mathbf{I}_0 + \mathbf{I}_z \quad (\text{B.20a})$$

$$\rho_1 = \frac{1}{2} \mathbf{I}_0 - \mathbf{I}_z \quad (\text{B.20b})$$

### B.3 Density Matrices of Multi-Particle Systems

Any non-trivial quantum computation requires more than one qubit. Thus, several aspects of the density matrix formalism particular to multi-particle systems become relevant.

Consider a set of  $N$  spin  $I = 1/2$  particles. The Hilbert space  $H_S$  of the combined system is said to be a *tensor product* of the Hilbert spaces of the individual particles  $H_j$ .

$$H^{(S)} = H^{(1)} \otimes H^{(2)} \otimes \dots \otimes H^{(N)} \quad (\text{B.21})$$

Commonly, the tensor product of two tensors with ranks  $n$  and  $m$  produces a tensor of rank  $n + m$ . A direct translation of this procedure to density matrices

would, in our case, produce a  $2^N$ -dimensional “matrix”. To retain the representation with two-dimensional matrices, the following definition of tensor product – also known as *Kronecker product* is used. Given two matrices  $A$  and  $B$ , their tensor product is defined by

$$A \otimes B = \begin{pmatrix} a_{11}B & a_{12}B & \cdots \\ a_{21}B & a_{22}B & \cdots \\ \vdots & & \ddots \end{pmatrix} = \begin{pmatrix} a_{11}b_{11} & a_{11}b_{12} & a_{11}b_{13} & \cdots & a_{1n}b_{11} & a_{1n}b_{12} & a_{1n}b_{13} & \cdots \\ a_{11}b_{21} & a_{11}b_{22} & a_{11}b_{23} & \cdots & a_{1n}b_{21} & a_{1n}b_{22} & a_{1n}b_{23} & \cdots \\ a_{11}b_{31} & a_{11}b_{32} & a_{11}b_{33} & & a_{1n}b_{31} & a_{1n}b_{32} & a_{1n}b_{33} & \\ \vdots & \vdots & & \ddots & \vdots & \vdots & & \\ a_{m1}b_{11} & a_{m1}b_{12} & a_{m1}b_{13} & & a_{mn}b_{11} & a_{mn}b_{12} & a_{mn}b_{13} & \\ a_{m1}b_{21} & a_{m1}b_{22} & a_{m1}b_{23} & \cdots & a_{mn}b_{21} & a_{mn}b_{22} & a_{mn}b_{23} & \cdots \\ a_{m1}b_{31} & a_{m1}b_{32} & a_{m1}b_{33} & & a_{mn}b_{31} & a_{mn}b_{32} & a_{mn}b_{33} & \\ \vdots & \vdots & & & \vdots & \vdots & & \ddots \end{pmatrix} \quad (\text{B.22})$$

With this definition, the density matrix  $\rho^{(S)}$  of the entire system is obtained from the density matrices  $\rho^{(j)}$  describing individual particles by the tensor product

$$\rho^{(S)} = \rho^{(1)} \otimes \rho^{(2)} \otimes \cdots \otimes \rho^{(N)} \quad (\text{B.23})$$

A density matrix constructed in this fashion represents a *separable state* or *product state*, in that it can be expressed as a tensor product of density matrices describing individual subsystems. Coherent superpositions between degrees of freedom belonging to different subsystems are manifestations of *entanglement* between the subsystems involved.

## B.4 Notation of Pulses

In Magnetic Resonance the state of the spin system is manipulated by means of rf or microwave pulses. The straight forward interpretation of a pulse is the rotation of the magnetization through a particular angle around a particular axis. Thus one frequently speaks of a  $\pi/2$ -pulse in  $x$ -direction, meaning that the magnetization is rotated by  $\pi/2$  around the  $x$ -axis of the rotating frame of reference. In text this may be symbolized by  $\frac{\pi}{2}|_x$ . In calculations, the operator associated with a pulse around the axes at an angle  $\varphi$  to the  $x$ -axis and a rotation angle  $\beta$  is represented by the symbol  $P_\varphi(\beta)$ . The  $\frac{\pi}{2}|_x$  above would be written  $P_x(\frac{\pi}{2})$ . The matrix representing such an operator is given by

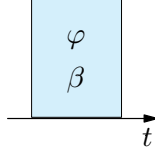
$$P_\varphi(\beta) = e^{-i\beta(\cos\varphi \mathbf{I}_x + \sin\varphi \mathbf{I}_y)} \quad (\text{B.24})$$

To calculate the effect of a pulse on a density matrix  $\rho$ , the latter must be multiplied by the pulse’s matrix representation according to

$$\rho' = P_\varphi(\beta) \rho P_\varphi(\beta)^\dagger \quad (\text{B.25})$$

In pictorial representations of pulse sequences, pulses are depicted as rectangular blocks with the orientation of the rotation axis given above the rotation angle

such as this:



## B.5 Useful Formulae

This section lists some expressions useful for calculations on spin systems.

Firstly,

$$\text{tr}(\mathbf{I}_j^2) = \frac{1}{4} \text{tr}(\mathbf{I}_0) = 2^{N-2} \quad (\text{B.26})$$

where  $N$  is the number of spin  $I = 1/2$  particles comprising the system. Notice, that this is not true for spin quantum numbers larger than  $1/2$ .

Also, for spin  $I = 1/2$  particles,

$$\mathbf{I}_j \mathbf{I}_k = \frac{i}{2} \mathbf{I}_l \quad (\text{B.27})$$

irrespective of the number of spins in the system. Again  $\{j, k, l\}$  are cyclic permutations of  $\{x, y, z\}$ . For non-cyclic permutations the right-hand side changes sign.

In the computation of the evolution of spin systems, it is frequently necessary to evaluate the exponential function of spin operators. For an operator  $\mathbf{R}$  with

$$\mathbf{R}^2 = \left(\frac{r}{2}\right)^2 \mathbf{I}_0 \quad (\text{B.28})$$

it can be shown that

$$\begin{aligned} \exp(i\alpha \mathbf{R}) &= \\ &= \sum_{n=0}^{\infty} \frac{(i\alpha)^{2n}}{(2n)!} \mathbf{R}^{2n} + \sum_{n=0}^{\infty} \frac{(i\alpha)^{2n+1}}{(2n+1)!} \mathbf{R}^{2n+1} \\ &= \mathbf{I}_0 \sum_{n=0}^{\infty} \frac{(-1)^n}{(2n)!} \left(\frac{r\alpha}{2}\right)^{2n} + i\mathbf{R} \left(\frac{2}{r}\right) \sum_{n=0}^{\infty} \frac{(-1)^n}{(2n+1)!} \left(\frac{r\alpha}{2}\right)^{2n+1} \quad (\text{B.29}) \\ &= \cos \frac{r\alpha}{2} \mathbf{I}_0 + \frac{2i}{r} \sin \frac{r\alpha}{2} \mathbf{R} \end{aligned}$$

In particular, the special case of evolution under static and varying fields and simple space rotations is useful:

$$\exp(i\alpha \mathbf{I}_j) = \cos \frac{\alpha}{2} \mathbf{I}_0 + 2i \sin \frac{\alpha}{2} \mathbf{I}_j \quad (\text{B.30})$$

and for evolutions under spin-spin couplings:

$$\exp(i\alpha \mathbf{I}_j \mathbf{I}_k) = \cos \frac{\alpha}{4} \mathbf{I}_0 + 4i \sin \frac{\alpha}{4} \mathbf{I}_j \mathbf{I}_k \quad , \quad \text{for } j \neq k \quad (\text{B.31})$$

## Appendix C

# Tensor Product Algorithms for Large Sparse Matrices

In numeric modeling of multi-spin systems, it is frequently necessary to construct matrices representing the single-spin operators and product operators for multiple spins. Conceptually this is done by computing corresponding tensor products as described in Section B.3. For instance, the matrix  $\mathbf{I}_{x_j}$  representing the  $\mathbf{I}_x$  operator for spin  $j$  is given by

$$\mathbf{I}_{x_j} = \mathbf{I}_0 \otimes \mathbf{I}_0 \otimes \cdots \otimes \mathbf{I}_0 \otimes \mathbf{I}_x \otimes \mathbf{I}_0 \otimes \cdots \otimes \mathbf{I}_0 \otimes \mathbf{I}_0 \quad (\text{C.1})$$

1      2                                   $j-1$        $j$        $j+1$                                    $N-1$        $N$

In large spin systems the costs of storage of and computation with these matrices become prohibitive.

Consider, for example, the  $S$ -bus cluster in  $\text{CaF}_2$  described in Chapter 4, which consists of  $N = 10$  spins  $I = 1/2$ . A matrix representation of an operator in this system consists of  $2^N \times 2^N$  complex numbers with real and imaginary part each represented by a double precision floating-point number. Thus, a single operator requires  $2^{10} \times 2^{10} \times 2 \times 64 \text{ Bit} = 16 \text{ MB}$  of storage. Simply to provision the three Cartesian component operators for all ten spins – and this is only a small part of the full basis – would thus require in excess of 480 MB of storage. Together with workspaces required for various operations, this quickly exceeds the limits of commodity hardware. In addition, the time required for construction of simple tensor products already grows exponentially with the size of the spin system.

Fortunately, some of the properties of the tensor product and the base spin operators allow the requirements to be greatly reduced. The improvement achieved by the algorithms described below is sufficient to allow the task at hand to be performed in feasible time on commodity hardware. However, no claim of optimal efficiency either in terms of storage or running time is implied, since no rigorous analysis of computational complexity was performed.

## C.1 Tensor Product of General Matrices

Consider two matrices  $A$  and  $B$  with sizes  $h_A \times w_A$  and  $h_B \times w_B$  respectively. The tensor product  $C = A \otimes B$  will have size  $h_A h_B \times w_A w_B$ . The elements of this matrix will be given by

$$c_{i,j} = a_{\lfloor i/h_B \rfloor, \lfloor j/w_B \rfloor} b_{(i \bmod h_B), (j \bmod w_B)} \quad (\text{C.2})$$

where element indices  $i, j$  start with 0 and “ $\lfloor x/y \rfloor$ ” (meaning floor) is the integer part and “ $x \bmod y$ ” the remainder of integer division of  $x$  by  $y$ . To simplify the formulae, a notation akin to those used in many computer programming languages can be used:

$$c[i, j] = a[i/h_B, j/w_B] \cdot b[i \% h_B, j \% w_B] \quad (\text{C.3})$$

with square brackets enclosing the element indices and “/” and “%” denoting the quotient and the remainder of integer division.

With this notation, Equation (C.3) can be extended to the case of  $N$  arbitrarily shaped matrices  $M_k$ :

$$P = M_1 \otimes M_2 \otimes \cdots \otimes M_N \quad (\text{C.4a})$$

$$p[i, j] = \prod_{k=1}^N m_k[i_k, j_k] \quad (\text{C.4b})$$

The indices  $[i_k, j_k]$  of the matrix elements  $m_k$  contributing to  $p[j, k]$  can be calculated as follows. To make the expression legible, the parentheses are omitted. The integer division must be executed successively *left-to-right*, i.e., in the expression for  $i_l$ , first,  $i$  is divided by the product with  $k = 2 \dots N$ , then the result is divided by the product with  $k = 3 \dots N$  and so on.

$$i_1 = i / \left( \prod_{k=2}^N h_k \right) \quad (\text{C.5a})$$

$$i_l = i \% \left( \prod_{k=2}^N h_k \right) \% \left( \prod_{k=3}^N h_k \right) \% \dots \% \left( \prod_{k=l}^N h_k \right) / \left( \prod_{k=l+1}^N h_k \right) \quad (\text{C.5b})$$

$$i_N = i \% \left( \prod_{k=2}^N h_k \right) \% \left( \prod_{k=3}^N h_k \right) \% \dots \% \left( \prod_{k=N-1}^N h_k \right) \% h_N \quad (\text{C.5c})$$

where  $h_k$  is the number of rows in the matrix  $M_k$ . The formula for  $j_k$  is analogous and involves the number of columns  $w_k$  of the matrices being multiplied.

To give an example, consider the case of  $N = 4$ :

$$P = \begin{pmatrix} m_0[0,0] & m_0[0,1] \\ m_0[1,0] & m_0[1,1] \end{pmatrix} \otimes \begin{pmatrix} m_1[0,0] & m_1[0,1] & m_1[0,2] \\ m_1[1,0] & m_1[1,1] & m_1[1,2] \\ m_1[2,0] & m_1[2,1] & m_1[2,2] \end{pmatrix} \otimes \begin{pmatrix} m_2[0,0] & m_2[0,1] & m_2[0,2] \\ m_2[1,0] & m_2[1,1] & m_2[1,2] \end{pmatrix} \otimes \begin{pmatrix} m_3[0,0] & m_3[0,1] \\ m_3[1,0] & m_3[1,1] \\ m_3[2,0] & m_3[2,1] \end{pmatrix} \quad (\text{C.6})$$



The matrix  $P$  has  $h_P = h_0 \cdot h_1 \cdot h_2 \cdot h_3 = 2 \cdot 3 \cdot 3 \cdot 2 = 36$  rows and  $w_P = w_0 \cdot w_1 \cdot w_2 \cdot w_3 = 2 \cdot 3 \cdot 2 \cdot 3 = 36$  columns. Which elements of  $M_k$  contribute to the element  $p[i, j]$  of  $P$  with  $i = 23$  and  $j = 11$ ? According to Equation (C.4):

$$p[i, j] = m_0[i_0, j_0] \cdot m_1[i_1, j_1] \cdot m_2[i_2, j_2] \cdot m_3[i_3, j_3] \quad (\text{C.7})$$

The indices  $i_k$  can be calculated according to Equation (C.5):

$$\begin{aligned} i_0 &= i / (h_1 \cdot h_2 \cdot h_3) = 23 / 18 = 1 \\ i_1 &= i \% (h_1 \cdot h_2 \cdot h_3) / (h_2 \cdot h_3) = 23 \% 18 / 6 = 5 / 6 = 0 \\ i_2 &= i \% (h_1 \cdot h_2 \cdot h_3) \% (h_2 \cdot h_3) / h_4 = 23 \% 18 \% 6 / 2 = 5 \% 6 / 2 = 5 / 2 = 2 \\ i_3 &= i \% (h_1 \cdot h_2 \cdot h_3) \% (h_2 \cdot h_3) \% h_4 = 23 \% 18 \% 6 \% 2 = 5 \% 2 = 1 \end{aligned} \quad (\text{C.8})$$

Analogously, for  $j_k$ :  $j_0 = 0$ ,  $j_1 = 1$ ,  $j_2 = 1$ ,  $j_3 = 2$ . And the end result is

$$p[23, 11] = m_0[1, 0] \cdot m_1[0, 1] \cdot m_2[2, 1] \cdot m_3[1, 2] \quad (\text{C.9})$$

Based on the general expression in Equation (C.5) a number of simplified procedures can be constructed. They are briefly described in the following sections.

## C.2 Tensor Multiplication Algorithms

For simplicity and completeness, the algorithms are explained with the help of actual C routines. *GNU Scientific Library* (GSL) [124] was used for basic storage and access of matrices and complex numbers. The names of functions and types beginning with the prefix “gsl\_” are self-explanatory.

### C.2.1 Addition of Single Spin Operators

In the construction of Hamiltonians with several contributions, it is convenient start with an empty matrix and adds various terms successively. To save space, it is, therefore, useful to be able to add operators directly to the already completed portion of the Hamiltonian. For example, adding the Zeeman term for the spin  $j$  requires

$$\mathcal{H} = \mathcal{H} + \omega_{0j} \mathbf{I}_{z_j} \quad (\text{C.10})$$

The following procedure achieves just that. It is a straight forward implementation of the algorithm described by Equations (C.4) and (C.5). It performs the operation of adding a single-spin base operator  $\mathbf{I}_d$  for spin  $j$  multiplied by a real factor  $f$  to the matrix  $M$ :

$$\begin{aligned} M &= M + f \mathbf{I}_{d_j} \\ &= M + f \mathbf{I}_0 \otimes \mathbf{I}_0 \otimes \cdots \otimes \mathbf{I}_d \otimes \cdots \otimes \mathbf{I}_0 \end{aligned} \quad (\text{C.11})$$

The matrix  $M$  describes the full  $N$ -spin system. This procedure iterates over all elements of the target matrix. For each element, it successively calculates the intermediate indices given in Equation (C.5) using the base operator  $\mathbf{I}_d$  for  $M_k$  at the requested spin number.

No special assumptions about the structure of the base operators are necessary. However, for *every* element of the matrix  $M$ , *every* element of the single-spin matrices is tested for *all*  $N$  spins. The only optimization is that the iteration over the spins is aborted once a null-factor is found in Equation (C.4b).

---

```

/*
matrix_add_op( m, fac, type, num )

Adds the spin-1/2 operator 'op' for the spin number 'num' to matrix 'm'.
m: target complex matrix;
fac: the spin operator is multiplied by this factor;
op: 2x2 base operator
num: number of the spin (0-based).

Example: matrix_add_op( H, g, 1, 3) implements  $H = H + g S_y^3$ 
*/
void
matrix_add_op( gsl_matrix_complex* m, double f, gsl_matrix_complex* op, size_t num )
{
    size_t dim = 2;          /* dimension of the spin operators */
    size_t i,j,k;           /* iterators */
    size_t iC, jC;          /* current element indices */
    size_t iR, jR;          /* remaining divisors */
    size_t iN, jN;          /* starting indices for next spin */
    gsl_complex c;          /* accumulator */
    size_t n_spins = 0;     /* number of spins */
    /* Get number of spins. */
    i = m->size1;
    while ( ( i = i >> 1 ) ) {
        n_spins++;
    }
    for ( i = 0; i < m->size1; i++ ) { /* For all elements of the matrix... */
        for ( j = 0; j < m->size2; j++ ) {
            iR = m->size1; /* Start with dimensions of all spins. */
            jR = m->size2;
            iN = i;        /* Indices for next spin. */
            jN = j;
            GSL_SET_COMPLEX( &c, f, 0 );
            for ( k = 0; k < n_spins; k++ ) { /* For all spins... */
                iR = iR / dim; /* ! integer operations ! */
                jR = jR / dim;
                iC = iN / iR;
                iN = iN % iR;
                jC = jN / jR;
                jN = jN % jR;
                if ( k == num ) { /* Operator op used for this spin. */
                    c = gsl_complex_mul( c, gsl_matrix_complex_get( op, iC, jC ) );
                } else { /* Identity used for this spin: delta(i,j) */
                    if ( iC == jC ) {
                        c = gsl_complex_mul_real( c, 1.0 );
                    } else {
                        c = gsl_complex_mul_real( c, 0.0 );
                    }
                }
            }
            if ( GSL_REAL(c)==0 && GSL_IMAG(c)==0 ) { /* Skip null elements. */
                break;
            }
        }
        gsl_matrix_complex_set(
            m, i, j, gsl_complex_add( c, gsl_matrix_complex_get(m, i, j) ) );
    }
}
return;
}/* ENDOF matrix_add_op() */

```

---

## C.2.2 Addition of a Spin $I = 1/2$ Operator

This algorithm inverts the procedure described in Section C.2.1. Instead of starting at each element of the target matrix and finding the operator elements contributing to it, it starts at the elements of the base operators and finds the elements of the target matrix to which the former contribute. Thus, the number of elements of the target matrix touched by this procedure is reduced. Also, since a large proportion of the elements of the target matrix is independent of a given base operator, this approach immediately profits from the null-elements in the base operator.

---

```

/*
  matrix_add_2op( m, fac, op, num )

  Adds the spin-1/2 operator 'op' for the spin number 'num' multiplied by
  'fac' onto the matrix 'm'.

  In effect, adds the tensor product to m:
  m += fac * 1 x ... x 1 x op x 1 x ... x 1 .

  NOTE: The other elements of the matrix are not referenced.
*/
void
matrix_add_2op( gsl_matrix_complex* m, double fac,
               gsl_matrix_complex* op, int num )
{
  int i,j,k;           /* iterators */
  int n_spins = 0;     /* number of spins */
  gsl_complex c;       /* operator element */
  int occ;             /* number of occurrences of each op element */
  int dims;            /* width of dimensions to the right of the spin */
  /* Compute number of spins. */
  i = m->size1; while ( ( i = i >> 1 ) ) { n_spins++; }
  if ( n_spins <= num ) {
    fprintf( stderr, "oops: spin number %d out of range [0,%d]\n", num, n_spins-1 );
    exit(1);
  }
  /* Compute number of occurrences of each operator element in the matrix. */
  occ = 1 << ( n_spins-1 );

  /* Compute the width of the dimensions to the right of the spin. */
  dims = 1 << ( n_spins-num-1 );

  for ( i = 0; i < 2; i++ ) { /* For all components of the spin operator. . . */
    for ( j = 0; j < 2; j++ ) {
      c = gsl_matrix_complex_get( op, i, j );
      if ( GSL_REAL(c)==0 && GSL_IMAG(c)==0 ) { /* Skip null elements. */
        continue;
      }
      c = gsl_complex_mul_real( c, fac );
      for ( k = 0; k < occ; k++ ) {
        int ic = k + dims * ( i + k/dims );
        int jc = k + dims * ( j + k/dims );
        gsl_matrix_complex_set( m, ic, jc,
                               gsl_complex_add( c, gsl_matrix_complex_get( m, ic, jc ) ) );
      }
    }
  }
}
} /* END OF matrix_add_2op() */

```

---

### C.2.3 Addition of a Product of Operators

This algorithm extends the one described in Section C.2.1 in a different way. It allows a *product* of base operators multiplied by a real factor to be added to the target matrix:

$$\begin{aligned} M &= M + f \mathbf{I}_{a_j} \mathbf{I}_{b_k} \cdots \mathbf{I}_{n_l} \\ &= M + f \mathbf{I}_0 \otimes \mathbf{I}_0 \otimes \cdots \mathbf{I}_a \cdots \mathbf{I}_b \cdots \mathbf{I}_n \cdots \otimes \mathbf{I}_0 \end{aligned} \quad (\text{C.12})$$

In this case, the forward search starting at the base operators is not feasible and every element of the target matrix is touched.

---

```

/*
matrix_add_ops( m, fac, ops, nums )

Adds the spin-1/2 operators listed in 'ops' multiplied by 'fac' to
matrix 'm'.

m += fac * ops[0] x ops[1] x ... x ops[N].
*/
void
matrix_add_ops( gsl_matrix_complex* m, double f,
                gsl_matrix_complex* ops[] )
{
    size_t dim = 2;          /* dimension of the spin operators */
    size_t i,j,k;           /* iterators */
    size_t iC, jC;          /* current indices */
    size_t iR, jR;          /* remaining divisors */
    size_t iN, jN;          /* starting indices for next spin */
    gsl_complex c;          /* accumulator */
    size_t n_spins = 0;      /* number of spins */
    /* Get number of spins. */
    i = m->size1; while ( (i = i >> 1) ) { n_spins++; }

    for ( i = 0; i < m->size1; i++ ) { /* For all elements of the matrix... */
        for ( j = 0; j < m->size2; j++ ) {
            iR = m->size1; /* Start with dimensions of all spins. */
            jR = m->size2;
            iN = i;        /* Indices for next spin. */
            jN = j;
            GSL_SET_COMPLEX( &c, f, 0 );
            for ( k = 0; k < n_spins; k++ ) { /* For all spins... */
                iR = iR / dim; /* ! integer operations ! */
                jR = jR / dim;
                iC = iN / iR;
                iN = iN % iR;
                jC = jN / jR;
                jN = jN % jR;
                c = gsl_complex_mul( c, gsl_matrix_complex_get( ops[k], iC, jC ) );
                /* Skip the remaining dimensions if c = 0 already. */
                if ( GSL_REAL(c) == 0 && GSL_IMAG(c) == 0 ) { break; }
            }
            gsl_matrix_complex_set(
                m, i, j, gsl_complex_add( c, gsl_matrix_complex_get(m, i, j) ) );
        }
    }
    return;
} /* END OF matrix_add_ops() */

```

---

# Bibliography

- [1] A. Einstein, B. Podolski, and N. Rosen. Can quantum-mechanical description of physical reality be considered complete? *Phys. Rev.*, 47:777, 1935.
- [2] R. P. Feynman. Simulating physics with computers. *Int. J. Theor. Phys.*, 21:467, 1982.
- [3] D. Deutsch. Quantum theory, the Church-Turing principle and the universal quantum computer. *Proc. R. Soc. Lond. A*, 400:97–117, 1985.
- [4] D. Deutsch. Quantum computational networks. *Proc. R. Soc. Lond. A*, 425:73–90, 1989.
- [5] D. Deutsch and R. Jozsa. Rapid solutions of problems by quantum computation. *Proc. R. Soc. Lond. A*, 439:553–558, 1992.
- [6] C. H. Bennett. Quantum information and computation. *Phys. Today*, 48:24–30, 1995.
- [7] A. Barenco, C. H. Bennett, R. Cleve, D. P. DiVincenzo, N. Margolus, P. Shor, T. Sleator, John A. Smolin, and H. Weinfurter. Elementary gates for quantum computation. *Phys. Rev. A*, 52:3457, 1995.
- [8] L. K. Grover. Quantum mechanics helps in searching for a needle in a haystack. *Phys. Rev. Lett.*, 79:325–328, 1997.
- [9] L. K. Grover. Quantum computers can search arbitrarily large databases by a single query. *Phys. Rev. Lett.*, 79:4709–12, 1997.
- [10] P. W. Shore. Polynomial-time algorithms for prime factorisation and discrete logarithms on a quantum computer. In *Proc. 35th annual symposium on foundations of computer science*, Los Alamitos, 1994. IEEE Computer Society Press.
- [11] D. P. DiVincenzo and D. Loss. Quantum information is physical. *Superlattices and Microstructures*, 23:419–32, 1998.
- [12] D. P. DiVincenzo. The physical implementation of quantum computation. *Fortschr. Phys.*, 48:771–83, 2000.
- [13] J. A. Jones and M. Mosca. Implementation of a quantum algorithm on a Nuclear Magnetic Resonance quantum computer. *J. Chem. Phys.*, 109:1648–53, 1998.

- 
- [14] I. L. Chuang, L. M. K. Vandersypen, X. Zhou, D. W. Leung, and S. Lloyd. Experimental realization of a quantum algorithm. *Nature*, 393:143–6, 1998.
- [15] K. Dorai, Arvind, and A. Kumar. Implementating quantum-logic operations, pseudopure states, and the deutsch-jozsa algorithm using non-commuting selective pulses in NMR. *Phys. Rev. A*, 61:042306/1–7, 2000.
- [16] N. Linden, H. Barjat, and R. Freeman. An implementation of the Deutsch-Jozsa algorithm on a three-qubit NMR quantum computer. *Chem. Phys. Lett.*, 296:61–7, 1998.
- [17] R. Marx, A. F. Fahmy, J. M. Myers, W. Bermel, and S. J. Glaser. Approaching five-bit nmr quantum computing. *Phys. Rev. A*, 62:012310, 2000.
- [18] I. L. Chuang, N. A. Gershenfeld, and M. Kubinec. Experimental implementation of fast quantum searching. *Phys. Rev. Lett.*, 80:3408–11, 1998.
- [19] J. A. Jones, M. Mosca, and R. H. Hansen. Implementation of a quantum search algorithm on a quantum computer. *Nature*, 393:344–6, 1998.
- [20] C.S. Yannoni, M.H. Sherwood, L.M.K. Vandersypen, M.G. Kubinec, D.C. Miller, and I. Chuang. Nuclear magnetic resonance quantum computing using liquid crystal solvents. *Appl. Phys. Lett.*, 75:3563 – 5, 1999.
- [21] S. Zühlsdorff. Durchführung von Quantenalgorithmien mit Kernspinresonanz. Master’s thesis, Universität Stuttgart, Stuttgart, Germany, 2000.
- [22] Y. S. Weinstein, S. Lloyd, and D. G. Cory. Implementation of the quantum Fourier transform. *Phys. Rev. Lett.*, 86:1889–91, 2001.
- [23] Liping Fu, Jun Luo, Li Xiao, and Xizhi Zeng. Experimental realization of discrete Fourier transformation on NMR quantum computer. *Applied Magnetic Resonance*, 19:153–9, 2000.
- [24] C. H. Tseng, S. Somaroo, Y. Sharf, E. Knill, R. Laflamme, T. F. Havel, and D. G. Cory. Quantum simulation of a three-body-interaction Hamiltonian on an NMR quantum computer. *Phys. Rev. A*, 61:012302/1–6, 2000.
- [25] S. Somaroo, C. H. Tseng, T. F. Havel, R. Laflamme, and D. G. Cory. Quantum simulations on a quantum computer. *Phys. Rev. Lett.*, 82:5381–5384, 1999.
- [26] N. Boulant, E. M. Fortunato, M. A. Pravia, G. Teklemariam, D. G. Cory, and T. F. Havel. Entanglement transfer experiment in NMR quantum information processing. *Phys. Rev. A*, 65:024302, 2002.
- [27] D. G. Cory, M. D. Price, W. Maas, E. Knill, R. Laflamme, W. H. Zurek, T. F. Havel, and S. S. Somaroo. Experimental quantum error correction. *Phys. Rev. Lett.*, 81:2152–5, 1998.

- [28] L. M. K. Vandersypen, M. Steffen, G. Breyta, C. S. Yannoni, M. H. Sherwood, and I. L. Chuang. Experimental realization of Shor's quantum factoring algorithm using nuclear magnetic resonance. *Nature*, 414:883, 2001.
- [29] D. G. Cory, R. Laflamme, E. Knill, L. Viola, T. F. Havel, N. Boulant, G. Boutis, E. Fortunato, S. Lloyd, R. Martinez, C. Negrevergne, M. Pravia, Y. Sharf, G. Teklemariam, Y. S. Weinstein, and W. H. Zurek. NMR based quantum information processing: Achievements and prospects. *Fortschr. Phys.*, 48:875, 2000.
- [30] O. Mangold. *Implementierung des Deutsch Algorithmus mit drei  $^{19}\text{F}$ -Kernspins*. PhD thesis, Universität Stuttgart, 2003.
- [31] O. Mangold, A. Heidebrecht, and M. Mehring. NMR tomography of the three-qubit Deutsch-Jozsa algorithm. *Phys. Rev. A*, 70:042307, 2004.
- [32] M. Mehring, J. Mende, and W. Scherer. Novel NMR and EPR techniques. volume Novel NMR and EPR Techniques of *Lecture Notes in Physics*, chapter On Route to Solid State Spin Quantum Computing, pages 87–114. Springer Frankfurt, 2005.
- [33] M. Mehring and J. Mende. Spin-bus concept of spin quantum computing. *Phys. Rev. A*, 73:052303, 2006.
- [34] M. Mehring, W. Scherer, and A. Weidinger. Pseudoentanglement of spin states in the multilevel  $^{15}\text{N}@\text{C}_{60}$  system. *Phys. Rev. Lett.*, 93:206603, 2004.
- [35] J. Mende. *Festkörper-Spin-Quantencomputing nach dem S-Bus-Konzept in  $\text{CaF}_2 : \text{Ce}$* . PhD thesis, Universität Stuttgart, Stuttgart, Germany, 2005.
- [36] A. Heidebrecht, J. Mende, and M. Mehring. Quantum state engineering with spins. *Fortschritte der Physik*, 54:788 – 803, 2006.
- [37] A. Heidebrecht, J. Mende, and M. Mehring. Indirect detection of selective nuclear spin-spin interactions in a hostile environment. *Solid State Nucl. Magn. Reson.*, 29:90–94, 2006.
- [38] D. G. Cory, A. E. Dunlop, T. F. Havel, S. S. Somaroo, and W. Zhang. The effective Hamiltonian of the Pound-Overhauser controlled-NOT gate. quant-ph/9809045, 1998.
- [39] M. Marjanska, I.L. Chuang, and M.G. Kubinec. Demonstration of quantum logic gates in liquid crystal Nuclear Magnetic Resonance. *J. Chem. Phys.*, 112:5095 – 9, 2000.
- [40] M. D. Price, S. S. Somaroo, C. H. Tseng, J. C. Gore, A. F. Fahmy, T. F. Havel, and D. G. Cory. Construction and implementation of NMR quantum logic gates for two spin systems. *J. Magn. Reson.*, 140:371–378, 1999.

- [41] T. S. Mahesh, K. Dorai, Arvind, and A. Kumar. Implementing logic gates and the deutsch-jozsa quantum algorithm by two-dimensional NMR using spin- and transition-selective pulses. *J. Magn. Resonance*, 148:95–103, 2000.
- [42] D. Collins, K. W. Kim, W. C. Holton, H. Sierzputowska-Gracz, and E. O. Stejskal. NMR quantum computation with indirectly coupled gates. *Phys. Rev. A*, 62:022304, 2000.
- [43] Jaehyun Kim, Jae-Seung Lee, and Soonchil Lee. Implementation of the refined Deutsch-Jozsa algorithm on a three-bit NMR quantum computer. *Phys. Rev. A*, 62:022312, 2000.
- [44] Arvind, Kavita Dorai, and Anil Kumar. Quantum entanglement in the nmr implementation of the deutsch-jozsa algorithm. *Pramana*, 56:L705–L713, 2001.
- [45] J. Kim, J. Seung, and S. Lee. Experimental realization of a target-accepting quantum search by NMR. *Phys. Rev. A*, 65:054301–4, 2002.
- [46] R. R. Ernst, G. Bodenhausen, and A. Wokaun. *Principles of Nuclear Magnetic Resonance in One and Two Dimensions*. Clarendon Press, Oxford, 1987.
- [47] N. A. Gershenfeld and I. L. Chuang. Bulk spin-resonance quantum computation. *Science*, 275:350–356, 1997.
- [48] W. S. Warren, N. Gershenfeld, and I. Chuang. The usefulness of NMR quantum computing. *Science*, 277:1688, 1997.
- [49] N. A. Gershenfeld and I. L. Chuang. Response to warren. *Science*, 277:1689, 1997.
- [50] R. Schack and C. M. Caves. Classical model for bulk-ensemble nmr quantum computation. *Phys. Rev. A*, 60:4354–62, 1999.
- [51] S. L. Braunstein, C. M. Caves, R. Josza, N. Linden, S. Popescu, and R. Schack. Separability of very noisy mixed states and implications for NMR quantum computing. *Phys. Rev. Lett.*, 83:1054–7, 1999.
- [52] G. L. Long, H. Y. Yan, Y. s. Li, C. C. Tu, s. J. Zhu, D. Ruan, Y. Sun, J. X. Tao, and H. M. Chen. On the quantum mechanical nature in liquid NMR quantum computing. e-print quant-phy/0007077, 2000.
- [53] Yakir Aharonov, David Z. Albert, and Lev Vaidman. How the result of a measurement of a component of the spin of a spin-1/2 particle can turn out to be 100. *Phys. Rev. Lett.*, 60:1351–1354, 1988.
- [54] I. M. Duck, P. M. Stevenson, and E. C. G. Sudarshan. The sense in which a "weak measurement" of a spin-1/2 particle's spin component yields a value 100. *Phys. Rev. D*, 40:2112–2117, 1989.
- [55] I.L. Chuang, N. A. Gershenfeld, M.G. Kubinec, and D.W. Leung. Bulk quantum computation with Nuclear Magnetic Resonance: theory and experiment. *Proc. Roy. Soc. A*, 454:447–467, 1998.



- [56] J. Jeener, R. Du Bois, and P. Broekaert. "Zeeman" and "dipolar" spin temperatures during a strong rf irradiation. *Phys. Rev.*, 139:A1959–A1961, 1965.
- [57] M. Mehring and V. A. Weberruß. *Object Oriented Magnetic Resonance*. Academic Press, 2001.
- [58] D. G. Cory, M. D. Price, and T. F. Havel. Nuclear magnetic resonance spectroscopy: An experimentally accessible paradigm for quantum computing. *Physica D*, 120:82–101, 1998.
- [59] Z. L. Mádi, R. Brüschweiler, and R. R. Ernst. One and two-dimensional ensemble quantum computing in spin Liouville space. *J. Chem. Phys.*, 109:10603, 1998.
- [60] R. Cleve, A. Ekert, C. Macchiavello, and M. Mosca. Quantum algorithms revisited. *Proc. R. Soc. Lond. A*, 454:339–54, 1998.
- [61] D. Collins, K. W. Kim, and W. C. Holton. Deutsch-Jozsa algorithm as a test of quantum computation. *Phys. Rev. A*, 58:R1633–6, 1998.
- [62] A. Peres. Separability criterion for density matrices. *Phys. Rev. Lett.*, 77:1413–1415, 1996.
- [63] M. Horodecki, P. Horodecki, and R. Horodecki. Separability of mixed states: necessary and sufficient conditions. *Phys. Lett. A*, 223:1, 1996.
- [64] M. Lewenstein, B. Kraus, J. I. Cirac, and P. Horodecki. Optimization of entanglement witnesses. *Phys. Rev. A*, 62:052310–26, 2000.
- [65] Dagmar Bruss. Characterizing entanglement. *J. Math. Phys.*, 43:4237, 2002. quant-ph/0110078.
- [66] O. Gühne, P. Hyllus, D. Bruš, A. Ekert, M. Lewenstein, C. Macchiavello, , and A. Sanpera. Detection of entanglement with few local measurements. *Phys. Rev. A*, 66:062305–5, 2002.
- [67] J. S. Bell. *Physics*, 1:195, 1964.
- [68] D. M. Greenberger, M. A. Horne, and A. Zeilinger. Bell's theorem without inequalities. *Am. J. Phys.*, 58:1131, 1990.
- [69] U. Haeberlen and J. S. Waugh. Coherent averaging effects in magnetic resonance. *Phys. Rev.*, 175:453–467, 1968.
- [70] W.-K. Rhim, A. Pines, and J. S. Waugh. Violation of the spin-temperature hypothesis. *Phys. Rev. Lett.*, 25:218–220, 1970.
- [71] W.-K. Rhim and H. Kessemeier. Transverse-magnetization recovery in the rotating frame. *Phys. Rev. B*, 3:3655–3661, 1971.
- [72] Jr. J. D. Ellett and J. S. Waugh. Chemical-shift concertina. *J. Chem. Phys.*, 51:2851–2858, 1969.
- [73] W.-K. Rhim, A. Pines, and J. S. Waugh. Time-reversal experiments in dipolar-coupled spin systems. *Phys. Rev. B*, 3:684–696, 1971.

- [74] K. Takegoshi and C. A. McDowell. A magic echo pulse sequence for the high-resolution NMR spectra of abundant spins in solids. *Chem. Phys. Lett.*, 116:100–104, 1985.
- [75] M. Mehring. *Principles of High Resolution NMR in Solids*. Springer, Berlin, 2nd edn., 1983.
- [76] C. P. Slichter. *Principles of Magnetic Resonance*. Springer-Verlag, 1978.
- [77] B. M. Fung. Pair of pseudopure states for 4- and 5-qubit nuclear magnetic resonance systems. *J. Chem. Phys.*, 63:8044–8048, 2001.
- [78] M. H. Levitt and R. Freeman. NMR population inversion using a composite pulse. *J. Magn. Reson.*, 33:473476, 1979.
- [79] R. Tycko. Broadband population inversion. *Phys. Rev. Lett.*, 51:775–777, 1983.
- [80] M. S. Silver, R. I. Joseph, C.-N. Chen, V. J. Sank, and D. I. Hoult. Selective population inversion in NMR. *Nature*, 310:681 – 683, 1984.
- [81] L. Emsley and G. Bodenhausen. Gaussian pulse cascades: New analytical functions for rectangular selective inversion and in-phase excitation in NMR. *Chem. Phys. Lett.*, 165:469–476, 1990.
- [82] M. A. Smith, H. Hu, and A. J. Shaka. Improved broadband inversion performance for NMR in liquids. *J. Magn. Reson.*, 151:269–283, 2001.
- [83] N. Khaneja, T. Reiss, C. Kehlet, T. Schulte-Herbrüggen, and S. J. Glaser. Optimal control of coupled spin dynamics: design of NMR pulse sequences by gradient ascent algorithms. *J. Magn. Reson.*, 172:296–305, 2005.
- [84] T. Schulte-Herbrueggen, A. Spoerl, N. Khaneja, and S.J. Glaser. Optimal control for generating quantum gates in open dissipative systems. *quant-ph/0609037*, 2006.
- [85] B. Blumich B and H.W. Spiëß. Quaternions as a practical tool for the evaluation of composite rotations. *J. Magn. Reson.*, 61:356–62, 1985.
- [86] L. Emsley and G. Bodenhausen. Optimization of shaped selective pulses for NMR using a quaternion description of their overall propagators. *J. Magn. Reson.*, 97:135–48, 1992.
- [87] J. Shen. A simple quaternion analysis of selective decoupling pulses. *J. Magn. Reson.*, 117:98–102, 1995.
- [88] R. Freeman. Selective excitation in high resolution NMR. *Chem. Rev.*, 91:1397–1412, 1991.
- [89] L. Emsley and G. Bodenhausen. Phase shifts induced by transient Bloch-Siegert effects in NMR. *Chem. Phys. Lett.*, 168:297–303, 1990.
- [90] A. Abragam. *The Principles of Nuclear Magnetism*. Clarendon Press Oxford, 1961.
- [91] M. Mehring. private communication.

- [92] B. E. Kane. A silicon-based nuclear spin quantum computer. *Nature*, 393:133, 1998.
- [93] W. B. Mims. Pulsed ENDOR experiments. *Proc. R. Soc. London*, 283:452, 1965.
- [94] E. R. Davies. A new pulse ENDOR technique. *Phys. Lett. A*, 47 A:1, 1974.
- [95] H. Cho, S. Pfenninger, C. Gemperle, A. Schweiger, and R. R. Ernst. Zero deadtime pulsed ESR by remote echo detection. *Chem. Phys. Lett.*, 160:391–395, 1989.
- [96] J. M. Baker, E. R. Davies, and J. P. Hurrell. Electron nuclear double resonance in calcium fluoride containing  $\text{Yb}^{3+}$  and  $\text{Ce}^{3+}$  in tetragonal sites. *Proc. Roy. Soc. A*, 308:403, 1968.
- [97] D. N. Chambers. EPR of trigonal centres in  $\text{CaF}_2:\text{Ce}^{3+}$ . *Phys. Lett. A*, 37:77–78, 1971.
- [98] M. Mehring, P. Höfer, , and A. Grupp. *Ber. Bunsenges. Phys. Chem.*, 91:1132–1137, 1987.
- [99] E. Anderson, Z. Bai, C. Bischof, S. Blackford, J. Demmel, J. Dongarra, J. Du Croz, A. Greenbaum, S. Hammarling, A. McKenney, and D. Sorensen. *LAPACK Users' Guide*. Society for Industrial and Applied Mathematics, third edition, 1999.
- [100] L. Kevan. Modulation of electron spin-echo decay in solids. In L. Kevan and R. N. Schwartz, editors, *Time Domain Electron Spin Resonance*. John Wiley, New York, 1979.
- [101] S. A. Dikanov and Y. D. Tsvetkov. *Electron spin echo envelope modulation (ESEEM) spectroscopy*. CRC Press, Boca Raton, 1992.
- [102] E. L. Hahn. Spin echoes. *Phys. Rev.*, 80:580–594, 1950.
- [103] J. Mende and M. Mehring. The qubyte S-bus system  $\text{CaF}_2 : \text{Ce}$ . *unpublished*, 2006.
- [104] G. Drobny, A. Pines, S. Sinton, D. Weitekamp, and D. Wemmer. Fourier transform multiple quantum nuclear magnetic resonance. *Faraday Division of the Chemical Society Symposium*, 13:49–174, 1979.
- [105] W.S. Warren, S. Sinton, D. P. Weitekamp, and A. Pines. Selective excitation of multiple-quantum coherence in nuclear magnetic resonance. *Phys. Rev. Lett.*, 43:1791, 1979.
- [106] M. Munowitz, A. Pines, and M. Mehring. Multiple-quantum dynamics in NMR: A directed walk through Liouville space. *J. Chem Phys.*, 86:3172, 1987.
- [107] J. Baum, M. Munowitz, A. N. Garroway, and A. Pines. Multiple-quantum dynamics in solid state NMR. *J. Chem. Phys.*, 83:2015, 1985.

- 
- [108] G. A. Morris and R. Freeman. *J. Am. Chem. Soc.*, 101:760, 1979.
- [109] D.A. Lidar, I.L. Chuang, and K.B. Whaley. Decoherence-free subspaces for quantum computation. *Phys. Rev. Lett.*, 81:2594 – 97, 1998.
- [110] I. J. Lowe and R. E. Norberg. Free-induction decays in solids. *Phys. Rev.*, 107:46, 1957.
- [111] D.P. Weitekamp, J.R. Garbow, and A. Pines. Determination of dipole-dipole couplings using heteronuclear multiple-quantum NMR. *J. Chem. Phys.*, 77:2870, 1982.
- [112] P. Höfer, A. Grupp, and M. Mehring. High-resolution time-domain electron-nuclear-sublevel spectroscopy by pulsed coherence transfer. *Phys. Rev. A*, 33:3519, 1986.
- [113] H. Cho, T. D. Ladd, J. Baugh, D. G. Cory, and C. Ramanathan. Multispin dynamics of the solid-state NMR free induction decay. *Phys. Rev. B*, 72:054427, 2005.
- [114] H. G. Krojanski and D. Suter. Scaling of decoherence in wide nmr quantum registers. *Phys. Rev. Lett.*, 93:090501–1, 2004.
- [115] E. D. Ostroff and J. S. Waugh. Multiple spin echoes and spin locking in solids. *Phys. Rev. Lett.*, 16:1097–1098, 1966.
- [116] I. Solomon. Rotary spin echoes. *Phys. Rev. Lett.*, 2:301–302, 1959.
- [117] M. Emschwiller, E. L. Hahn, and D. Kaplan. Pulsed nuclear resonance spectroscopy. *Phys. Rev.*, 118:414, 1960.
- [118] H. Thomann and M. Bernardo. Indirect detection of internuclear dipolar interaction in paramagnetic solids. *J. Am. Chem. Soc.*, 118:5806, 1996.
- [119] S. Meiboom and D. Gill. Modified spin-echo method for measuring nuclear relaxation times. *Rev. Sci. Inst.*, 29:688, 1958.
- [120] U. Haeberlen and J. S. Waugh. Spin-lattice relaxation in periodically perturbed systems. *Phys. Rev.*, 185:420, 1969.
- [121] H. Haken and H. C. Wolf. *Atom- und Quantenphysik*. Springer, Berlin, 2003.
- [122] K. Blum. *Density matrix theory and applications*. Physics of atoms and molecules. Plenum Press, New York, 1981.
- [123] W. Nolting. *Grundkurs: Theoretische Physik*, volume 5 Quantenmechanik, Teil 1: Grundlagen. Zimmermann-Neufang, Ulmen, 1992.
- [124] B. Gough, editor. *GNU Scientific Library Reference Manual*. Network Theory Ltd., 2003.

# List of Figures

1.1	Molecular structure and FID-Spectrum of 2,3,4-Trifluoroaniline. . .	6
1.2	Two-dimensional echo modulation on 2,3,4-Trifluoroaniline . . .	7
1.3	Pulse sequence for preparation of 3-qubits pseudo-pure states in 2,3,4-Trifluoroaniline. . . . .	13
1.4	Spectral signature of the pseudo-pure state $\rho_{001}$ in 2,3,4-Trifluoroaniline . . . . .	14
1.5	Real part of the density matrix of the pseudo-pure state $\rho_{000}$ . . .	15
1.6	Block diagram of the CEMM version of the Deutsch-Jozsa algorithm for $N$ qubits. . . . .	16
1.7	Partially and fully entangled output states of the three-qubit Deutsch-Jozsa algorithm. . . . .	24
2.1	Magic echo pulse sequence for the suppression of direct dipolar couplings between spins. . . . .	28
2.2	Magic echo pulse train used to demonstrate the scaling of the chemical shift part of the Hamilton operator . . . . .	31
2.3	Scaling of the chemical shift part of the Hamiltonian under the magic echo pulse train. . . . .	31
2.4	Chemical structure of 2,3-Difluoroaniline. Fluorine NMR-spectra of Difluoroaniline in a liquid crystal matrix. . . . .	32
2.5	Suppression of the dipole-dipole coupling under the magic echo sequence. . . . .	33
2.6	Pulse sequence for selective excitation under magic echo averaging. . . . .	34
2.7	Selective excitation of a single spin under continuous action of the magic echo sequence. . . . .	35
2.8	FID under magic echo averaging after selective $\pi/2$ pulse . . . . .	36
3.1	Visual representation of a $\pi$ -pulse in $y$ -direction. . . . .	39
3.2	Composite $\pi$ -pulse for compensation of $\mathbf{B}_1$ inhomogeneity. . . . .	42
3.3	Trajectories of the unitary transformations for simple and composite $\pi$ -pulses. . . . .	42
3.4	Comparison of the trajectories of the spin operator components under a simple and a composite $\pi$ -pulse. . . . .	43

3.5	Dependence of the total transformation on the mismatch of the Rabi frequency for a simple and a composite $\pi _y$ -pulse. . . . .	44
3.6	Selectivity of a rectangular $\frac{\pi}{2} _y$ -pulse . . . . .	46
3.7	Selectivity of a $\frac{\pi}{2} _y$ -pulse with Fermi-like envelope . . . . .	47
3.8	Selectivity of a $\frac{\pi}{2} _y$ -pulse with a Gaussian envelope . . . . .	48
3.9	Selectivity of a $\frac{\pi}{2} _y$ -pulse with a $\sin x/x$ envelope . . . . .	49
3.10	$\pi/2 _y$ -pulse with alternating off-resonant excitation . . . . .	51
4.1	The $S$ -bus concept for spin quantum computing. . . . .	54
4.2	Block diagram of a general $S$ -bus pulse sequence in $\text{CaF}_2:\text{Ce}$ . . .	56
4.3	Basic preparation/detection sequences for the $S$ -bus. . . . .	56
4.4	$\text{CaF}_2$ lattice with the $\text{Ce}^{3+}$ substituting for a $\text{Ca}^{2+}$ . . . . .	60
4.5	Structure of the $S$ -bus cluster in $\text{CaF}_2:\text{Ce}$ . . . . .	61
4.6	Three types of paramagnetic centers in $\text{CaF}_2:\text{Ce}$ . . . . .	65
4.7	Typical field spectrum of $\text{CaF}_2:\text{Ce}$ . . . . .	67
4.8	Polar plot of the angular dependence of the $g$ -factor. . . . .	68
4.9	Fit of the angular dependence of the effective $g$ -factors. . . . .	68
4.10	Energy level diagram and ENDOR spectrum in absence of anti-symmetric hyperfine contributions. . . . .	70
4.11	Pulse sequence for ENDOR experiments . . . . .	71
4.12	ENDOR spectrum of $\text{CaF}_2:\text{Ce}$ . . . . .	72
4.13	TRIPLE ENDOR pulse sequence . . . . .	73
4.14	Line Assignment to different values of $m_S$ by a TRIPLE measurement. . . . .	74
4.15	Exact numeric simulation of the ENDOR spectrum in $\text{CaF}_2:\text{Ce}$ . .	82
4.16	Simulation of the Rabi oscillation of the electron spin in $\text{CaF}_2:\text{Ce}$ . 89	
4.17	Simulation of the free induction decay of the electron spin in $\text{CaF}_2:\text{Ce}$ . . . . .	91
4.18	Simulation of electron spin echoes in $\text{CaF}_2:\text{Ce}$ . . . . .	92
4.19	Stimulated echo sequence for ESEEM in $\text{CaF}_2:\text{Ce}$ . . . . .	93
4.20	Electron spin echo envelope modulation measurement in $\text{CaF}_2:\text{Ce}$ . 95	
4.21	Simulation of the electron spin echo envelope modulation in $\text{CaF}_2:\text{Ce}$ . . . . .	96
4.22	Pulse sequence for phase encoding of the state of nuclear spins. .	97
4.23	Encoding of the state of the nuclear spins by MQE . . . . .	98
4.24	Sequence for the preparation of pseudo-pure states in $\text{CaF}_2:\text{Ce}$ . .	100
4.25	High fidelity two-qubit pseudo-pure states in $\text{CaF}_2:\text{Ce}$ . . . . .	102
4.26	SEDOR with $yy$ -detection. . . . .	103
4.27	Evolution of density matrix components during the SEDOR sequence . . . . .	104
4.28	INEPT sequence with $yx$ -detection . . . . .	105
4.29	Evolution of density matrix components during the INEPT sequence . . . . .	106

---

4.30	<i>CNOT</i> <sub>12</sub> sequence with <i>yx</i> -detection . . . . .	107
4.31	Evolution of density matrix components during the <i>CNOT</i> <sub>12</sub> sequence . . . . .	108
4.32	SEDOR sequence for determination of <i>S</i> -bus amplitudes. . . . .	109
4.33	Measurements for determination of the <i>S</i> -bus coefficients. . . . .	111
4.34	ENDOR spectrum of qubits coupled exclusively by the quantum bus. . . . .	115
4.35	Pulse sequence for tomography of the output states of the <i>CNOT</i> <sub>12</sub> operation. . . . .	117
4.36	Example of MQE spectra measured for tomography of the output states of <i>CNOT</i> <sub>12</sub> . . . . .	120
4.37	Input and output states for the CNOT operation. . . . .	121
4.38	Sequence for creation and direct detection of entangled states. . . . .	122
4.39	Creation and direct detection of Bell states in CaF <sub>2</sub> :Ce . . . . .	123
4.40	Pulse sequence for creation and detection of Bell states. . . . .	124
4.41	Signatures of Bell states in CaF <sub>2</sub> :Ce. . . . .	125
4.42	Decay of entangled state components at the magic angle. . . . .	126
5.1	Single spin nuclear FID in CaF <sub>2</sub> :Ce . . . . .	129
5.2	Single nuclear spin decoherence in CaF <sub>2</sub> :Ce . . . . .	130
5.3	Spin-echo double resonance (SEDOR) measurement on two nuclear spins in CaF <sub>2</sub> :Ce. . . . .	132
5.4	CPMG on two nuclear spins in CaF <sub>2</sub> :Ce . . . . .	133
5.5	Double spin-locking on two nuclear spins in CaF <sub>2</sub> :Ce . . . . .	134
5.6	Evolution of two nuclear spins in CaF <sub>2</sub> :Ce under the 8 $\pi$ -block . . . . .	135





# List of Tables

1.1	Chemical shifts and $J$ -couplings of the $^{19}\text{F}$ in 2,3,4-Trifluoroaniline.	8
1.2	Parameters for the preparation of 3-qubit pseudo-pure states in 2,3,4-Trifluoroaniline . . . . .	14
1.3	Definitions of the implemented Deutsch-Josza test functions. . .	19
1.4	Fidelity and decision parameter for the Deutsch-Josza algorithm.	19
4.1	Euler angles and $g$ -factors for the $\text{CaF}_2$ sample. . . . .	69
4.2	TRIPLE to ENDOR ratios of line intensities for all ENDOR lines.	73
4.3	Hyperfine parameters of $^{19}\text{F}$ nuclei in $\text{CaF}_2:\text{Ce}$ . . . . .	76
4.4	Positions of the nuclear spins in $\text{CaF}_2:\text{Ce}$ . . . . .	77
4.5	Comparison of measured and numerically simulated spin-spin couplings in $\text{CaF}_2:\text{Ce}$ . . . . .	83
4.6	Computation times for $\text{CaF}_2:\text{Ce}$ modeling. . . . .	84
4.7	Pseudo-pure states in $\text{CaF}_2:\text{Ce}$ . . . . .	103
4.8	Amplitudes of the oscillations of the MQE lines under the SE-DOR and INEPT sequences. . . . .	112
4.9	Experimentally determined values of the $S$ -bus coefficients. . . .	113
4.10	Parameters and results for the $CNOT$ -gate measurement in $\text{CaF}_2:\text{Ce}$ . . . . .	120
4.11	Decay constants of the Bell states in $\text{CaF}_2:\text{Ce}$ . . . . .	126
5.1	Results of CPMG experiments in $\text{CaF}_2:\text{Ce}$ . . . . .	134



# Lebenslauf

## Persönliche Daten

Name: Andreas Heidebrecht  
Geburtsdatum: 10.07.1971  
Geburtsort: Alma-Ata, Kasachstan  
Eltern: Helmut Heidebrecht und Maria Heidebrecht, geb. Högele  
Familienstand: verheiratet

## Schulbildung

Sept. 78 – Mai 88 Schulbesuch in Saran, Zelinograd und Alma-Ata in Kasachstan  
Juni 88 Reifeprüfung an der Physikalisch-Mathematischen Internatsschule der Republik Kasachstan in Alma-Ata  
Sept. 88 – Nov. 88 Beginn des Physikstudiums an der Staatsuniversität in Moskau  
April 1989 Einwanderung in die Bundesrepublik Deutschland  
Dez. 89 – Mai 90 Sprachkurs „Deutsch als Fremdsprache“ bei GFBA e.V., Heilbronn  
Sept. 90 – Mai 92 Besuch des Zeppelin-Gymnasiums in Stuttgart  
Mai 1992 Abitur

## Wissenschaftliche Ausbildung

Okt. 92 – Feb. 00 Physikstudium an der Universität Stuttgart  
Februar 2000 Studienabschluss Diplom-Physiker, Diplomarbeit „ESR Untersuchungen an einem bakteriellen Lichtsammelkomplex“  
Sept. 95 – Jan. 98 Studium im Fach „Applied Optics“ am Rose-Hulman Institute of Technology in Terre Haute, Indiana, USA  
Januar 1998 Abschluss Master of Science, Abschlussarbeit „Fabrication and testing of a photorefractive polymer composite“  
Jul. 00 – Dez. 06 Doktorarbeit am 2. Physikalischen Institut der Universität Stuttgart  
Dezember 2006 Promotion zum Thema „Quantum-State-Engineering for Spin-Quantum-Computer“



# Dank

An dieser Stelle möchte ich mich bei all denen bedanken, die direkt oder indirekt zum Gelingen meiner Arbeit beigetragen haben. Mein besonderer Dank gilt ...

- ... Herrn Prof. Dr. Mehring für die Aufnahme am 2. Physikalischen Institut, die stete Unterstützung und für viele interessante und anregende Diskussionen.
- ... Herrn Prof. Dr. Wrachtrup für die Übernahme des Mitberichts.
- ... der Landesstiftung Baden-Württemberg für die finanzielle Unterstützung.
- ... Frau Ulrike Offenbeck für ihre unfehlbar gute Laune.
- ... den Laborkollegen für eine schöne Arbeitsatmosphäre, vor allem Dr. Jürgen Rahmer mit dem wir schon durch das ganze Studium zusammen gegangen waren, Dr. Stefan Knorr, der mich in das ESR-Labor einführte, Dr. Arthur Grupp für viele gute Ratschläge und interessante Gespräche.
- ... Dr. Bernd Nebendahl, Hermann Neuman und Heinz Erhardt, die mir bei meinen Kämpfen mit den aufmüpfigen Rechnern zur Seite standen, Dr. Hans-Jürgen Kümmerer unserem Lüfter-Papst und Computerspezialisten.
- ... Dr. Steffen Krämer für die Einführung in die Geheimnisse der NMR, Oliver Mangold für mancherlei elektronische Kniffe und Dr. Michael Schmid dem schnellsten Experimentator auf der nördlichen Hemisphäre.
- ... Meinen Quantumcomputing-Kollegen Drs. Werner Scherer und Jens Mende für konstruktive Zusammenarbeit.
- ... Valentin Blickle für seinen ungebrochenen Optimismus und Jörg Baumgartl für tiefgründige Gespräche und allen „Konstanzer“ Kollegen für die belebenden Kaffee-Runden und ÖZ-Besuche.
- ... Herrn Dietrich und Quack für die geduldige Aufklärung darüber, was man mit ihren Stoffen (Metall und Glas) alles machen kann oder eben nicht.
- ... dem „Team Tieftemperatur“ Herren Maurer, Titz, Schobel und Lefèvre, die mir halfen meinen Helium-Hunger zu stillen.
- ... meinen Eltern für ihre bedingungslose Unterstützung während meiner langen universitären Laufbahn.
- ... meiner Frau Suzana, ohne die mein Leben inzwischen unvorstellbar geworden ist.



